High Pressure Synthesis, Structure and Multiferroic Properties of Doubly Ordered Perovskites ($AA'BB'O_6$) and other Polar Oxides

A Thesis

Submitted for the Degree of

Doctor of Philosophy

by

Ravi Shankar P N

Chemistry and Physics of Materials Unit

Jawaharlal Nehru Centre for Advanced Scientific Research

(A Deemed University)

Bengaluru – 560064

September 2021

Dedicated to my parents and brother…...

DECLARATION

I hereby declare that the matter embodied in the thesis entitled **"High Pressure Synthesis, Structure and Multiferroic Properties of Doubly Ordered Perovskites (*AA′BB′*O_6) and other Polar Oxides"** is the result of investigations carried out by me at the Chemistry and Physics of Materials Unit, Jawaharlal Nehru Centre for Advanced Scientific Research, Bangalore, India under the supervision of Prof. A. Sundaresan and it has not been submitted elsewhere for the award of any degree or diploma.

In keeping with the general practice in reporting the scientific observations, due acknowledgements have been made whenever the work described is based on the findings of other investigators. Any omission that might have occurred due to oversight or error in judgement is regretted.

Bengaluru

07/09/2021

Ravi Shankar P N

CERTIFICATE

I hereby certify that the matter embodied in this thesis entitled **"High Pressure Synthesis, Structure and Multiferroic Properties of Doubly Ordered Perovskites (*AA′BB′*O_6) and other Polar Oxides"** has been carried out by Mr. Ravi Shankar P N at the Chemistry and Physics of Materials Unit, Jawaharlal Nehru Centre for Advanced Scientific Research, Bangalore, India under my supervision and it has not been submitted elsewhere for the award of any degree or diploma.

Prof. A. Sundaresan

(Research Supervisor)

ACKNOWLEDGEMENTS

I express my sincere gratitude to my research supervisor Prof. A. Sundaresan for giving me the opportunity to work under his guidance and introducing me to the field of multiferroics. I sincerely thank him for his invaluable guidance, enormous support, and constant encouragement throughout my research career. I am extremely grateful to him for providing me with good collaborations, which enhanced my research experience. I am also grateful to him for giving me enough freedom to carry my research work. I thank him for his patience, belief, and positive attitude towards me in various aspects of my research work.

I would like to thank Prof. C. N. R. Rao, FRS, for providing me various experimental facilities and for being a constant source of inspiration.

I would like to thank Prof. S. Balasubramanian, Prof. Chandrabhas Narayana, and Prof. A. Sundaresan, past and present chairperson, respectively, for allowing me to utilize various facilities in the unit.

I acknowledge International Centre for Materials Science (ICMS) and Sheikh Saqr Laboratory (SSL) at JNCASR for providing various experimental facilities.

I would like to thank Prof. A. Sundaresan, Prof. U V Waghmare, Prof. S M Shivaprasad, Prof. Vidhyadhiraja, Prof. Shobhana Narasimhan, and Prof. T. N. Guru Row (IISc) for their informative course works.

It is my great pleasure to thank my collaborators. My sincere thanks to Dr. Fabio Orlandi, Dr. Pascal Manuel from WISH, and Dr. Ivan da Silva from GEM, RAL, UK, for neutron diffraction experiments. I especially thank Prof. Myung-Hwan Whangbo from North Carolina State University, USA and Prof. Hyun-Joo Koo from Kyung Hee University, Republic of Korea for theoretical studies. I would like to thank Prof. P. S. Halasyamani, Dr. Weiguo Zhang from University of Houston, USA for SHG measurements. I also want to thank Sinay Simanta Behera and Prof. K. S. Narayanan, JNCASR, Bengaluru for SHG measurements.

I thank the technical staff, namely Mr. Srinath, Mr. Anil, Mr. Vasu, Mr. Mahesh, Mr. Rahul, Ms. Pavana, Ms. Radha, and Balaraju for their help in various aspects of research and academics.

I would like to thank the Council of Scientific and Industrial Research (CSIR) and JNCASR for providing fellowship during my Ph.D. tenure. I would like to thank JNCASR and DST-RAL project for financial support to attend conferences and to visit RAL, UK, for performing neutron diffraction experiments, respectively.

I thank Complab, Library, Academics, Administration, Dhanvantari, Housekeeping, Garden, Dining hall, and Hostel for providing and maintaining different facilities.

I must thank all my past and present lab mates, Dr. Pranab Mondal, Dr. Rana Saha, Dr. Somnath Ghara, Dr. Chandan De, Dr. Abhijit Sen, Dr. Chandriah, Dr. Madhu, Dr. Rambabu, Dr. Shivani, Dr. Anzar, Mr. Amit, Mr. Prem, Ms. Pavitra, Ms. Swarnamayee, Mr. Debendra, Mr. Rahul, and Mr. Souvik for their various helps and useful discussions during my tenure and maintain a friendly atmosphere in the lab. My special thanks to Mr. Prem, Dr. Somnath, and Dr. Chandan for fruitful discussions and helping in measurements.

I thank all my friends at JNCASR, especially Prem, Priyanka, Divya, Dr. Pradeep, Shivaram, Rajendra, Madhu, Dr. Archana, Pavitra, and Suhas, for their company in various activities and always being there for me. I also thank Deepak, Ganesh, Dr. Usha, Malay, Anusha, Dr. Shashi, Vybhav, Dr. Pramod for making my journey memorable. I would like to thank all my sports friends from badminton. I would like to thank my friends and well wishers outside JNCASR, especially Dr. Manjunath, Sachin, Silpa, Harshith, Dada, Saraswathi, Ranjitha, and Salma.

Finally, I would like to thank my parents, Mr. Narayana Swamy P R and Mrs. Nalini H S, and my brother, Sunil Kumar P N, for their unconditional love, support and for giving me this life.

Preface

The thesis aims to explore new polar compounds for multiferroic properties. Thus, the thesis presents a detailed study on the structural, magnetic and multiferroic properties of polar doubly ordered perovskites synthesized at high pressure and high temperature and on the other polar oxides.

Chapter 1 is an introductory chapter that briefly highlights the various origins of ferroelectricity, multiferroicity and symmetry aspects of these properties. A detailed discussion on polar magnetic oxides resulting from inversion symmetry breaking by chemical ordering and responsible for multiferroic properties are explained with examples. Apart from that, the background of doubly ordered perovskites is given.

Chapter 2 describes the various experimental techniques used in the present work.

Chapter 3 deals with the multiferroic properties of doubly ordered perovskites Na*Ln*NiWO$_6$ (*Ln* = Dy-Lu and Y). These compounds crystallize in a polar monoclinic ($P2_1$) structure and exhibit a combination of unusual layered *A*-site cation ordering and *B*-site rock-salt ordering. Long-range antiferromagnetic ordering of Ni^{2+} spins at T_N ~ 18 – 23 K is accompanied by a dielectric anomaly and a change in electric polarization (ΔP). Analysis of neutron diffraction data for NaYNiWO$_6$ at 20 K revealed an unconventional spin density wave with $\mathbf{k_i}$ = (0.471(2), 0, 0.491(4)) and a commensurate collinear spin structure with $\mathbf{k_c}$ = (½, 0, ½) below 18 K. The observed polarization at T_N could be due to the possible enhancement of high temperature polarization expected from the magnetoelastic coupling.

Chapter 4 deals with the magnetodielectric properties of Na*Ln*NiWO$_6$ (*Ln* = La, Pr-Tb) with larger sized rare-earth cations. These compounds undergo a long-range antiferromagnetic ordering in the temperature range of 23 – 30 K, depending on the *Ln*-ion. Observed dielectric anomaly demonstrates the magnetodielectric behavior. Further, the electric polarization was not observed for all the compounds within the experimental detection limit. A simple collinear magnetic structure with the propagation vector, $\mathbf{k}$ = (½, 0, ½) is found for NaLaNiWO$_6$.

Chapter 5 contains the studies on doubly ordered perovskites with different transition metals such as Co, Mn, and Fe holding the same double ordered structure. DC magnetization and heat capacity measurements indicate long-range antiferromagnetic ordering (T_N ~ 6-8 K)

in Na*Ln*$CoWO_6$ (*Ln* = Y, Er, Tm, Yb, and Lu) and $NaLuMnWO_6$, which is accompanied by the dielectric anomaly. A nonswitchable polarization is realized below T_N for Na*Ln*$CoWO_6$ (*Ln* = Y, Er, Tm, and Yb) and $NaLuMnWO_6$. In contrast, the polarization is switchable in $NaLuCoWO_6$ by changing the direction of the electric field (*E*), indicating the ferroelectric nature of this compound. The magnetic structure of $NaYCoWO_6$ is collinear with the propagation vector **k** = (½, 0, ½). Magnetic, heat capacity and dielectric measurements of $NaYFeWO_6$ and $NaHoFeWO_6$ have signified antiferromagnetic ordering (T_N) coupled with the dielectric peak. However, the pyroelectric current anomalies for $NaYFeWO_6$ and $NaHoFeWO_6$ were overshadowed by leakage currents.

Chapter 6 gives a detailed account of investigations of the structural, magnetic and multiferroic properties of two new polar compounds $LiFeV_2O_7$ and $LiCrAs_2O_7$. These compounds crystallize in the monoclinic *Cc* ($LiFeV_2O_7$) and *C*2 ($LiCrAs_2O_7$) space groups and exhibit super-super-exchange interactions between transition metal cations. A magnetic anomaly was found around 5 K for both the compounds. Neutron diffraction data for the $LiFeV_2O_7$ at 2 K revealed a collinear spin structure with the propagation vector **k** = (0, 1, 0). Interestingly, the magnetization plateau is observed with one-third of the saturation moment at 4.3 T for $LiFeV_2O_7$. This compound exhibits a significant magnetocaloric effect around T_N with a maximum magnetic entropy change ($-\Delta S$ ~ 9 J/kg.K) at 7 T. Further, a multiferroic behavior at the magnetic transition was found in $LiFeV_2O_7$. In contrast, the dielectric anomaly was not observed for $LiCrAs_2O_7$ at the magnetic ordering temperature.

List of Publications

From the thesis

1. "A-site and B-site cation ordering induces polar and multiferroic behavior in the perovskite $NaLnNiWO_6$ (Ln = Y, Dy, Ho, and Yb)". **Ravi Shankar P N**, Fabio Orlandi, Pascal Manuel, Weiguo Zhang, P. Shiv Halasyamani, and A. Sundaresan, **Chem. Mater. 32, 5641 (2020)**.

2. "On ferro- and antiferro-spin-density waves describing the incommensurate magnetic structure of $NaYNiWO_6$". Hyun-Joo Koo, **Ravi Shankar P N**, Fabio Orlandi, Athinarayanan Sundaresan, and Myun-Hwan Whangbo, **Inorg. Chem. 59, 17856 (2020).**

3. "Structural, magnetic, and electrical properties of doubly ordered perovskites $NaLnNiWO_6$ (Ln = La, Pr, Nd, Sm, Eu, Gd, and Tb)". **Ravi Shankar P N,** Fabio Orlandi, Pascal Manuel, Weiguo Zhang, P. Shiv Halasyamani, and A. Sundaresan, **J. Phys. Chem. C, 125, 6749 (2021).**

4. "Switchable and nonswitchable polarization in doubly ordered perovskites Na*Ln*$CoWO_6$ (*Ln* = Er, Tm, Yb, and Lu)". **Ravi Shankar P N,** Debendra Prasad Panda, and Athinarayanan Sundaresan, **J. Phys. Chem. C, 125, 10803 (2021).**

5. "Synthesis, characterization and multiferroic properties of the doubly-ordered polar perovskite $NaLnNiWO_6$ (Ln = Er, Tm, and Lu)". **Ravi Shankar P N** and A. Sundaresan, **J. Magn. Magn. Mater. 540, 168412 (2021).**

6. "Magnetization plateau and multiferroicity in the frustrated antiferromagnet $LiFeV_2O_7$". **Ravi Shakar P N**, Ivan da Silva, Sinay Simanta Behera, and A. Sundaresan, to be communicated (2021).

7. "Structural and Magnetodielectric properties of $NaLnFeWO_6$ (Ln = Y, Ho)". **Ravi Shankar P N** and A. Sundaresan, manuscript under preparation (2021).

Perspective

8. “Polar magnetic oxides from chemical ordering: A new class of multiferroics”, **Ravi shankar P N,** Swarnamayee Mishra, and Sundaresan Athinarayanan, **APL Mater. 8, 040906 (2020).**

Miscellaneous Publications

9. “Factors governing the propagation direction and spin-rotation plane of noncollinear magnetic structures: A helix vs. cycloid in doubly ordered perovskites $NaYMnWO_6$ and $NaYNiWO_6$”. **Ravi Shankar P N**, Fabio Orlandi, Pascal Manuel, Hyun-Joo Koo, Myun-Hwan Whangbo, and Athinarayanan Sundaresan, **Inorg. Chem. 60, 15124 (2021).**

10. “Structural and magnetic properties of $R_{0.5}Sr_{0.5}Fe_{0.5}Mn_{0.5}O_3$ (R = Gd, Nd or Pr) perovskites”. Antara Sarkar, Anirban Das, Soumen Ash, **Ravi Shankar P N**, Kaustava Bhattacharya, Ashok K. Ganguli, **J. Alloys Comd. 540, 168412 (2021).**

Contents

Chapter 1

Introduction to multiferroics and polar magnetic oxides

Summary

This chapter presents a brief introduction to ferroelectricity, multiferroics, and polar magnetic oxides, including their definition, importance, and possible applications. Starting from the introduction and different origins of ferroelectricity and various ways by which magnetism and ferroelectricity can be combined for multiferroic properties in single-phase materials are thoroughly discussed. A brief discussion on the symmetry requirement for multiferroic materials is presented here. Further, inversion symmetry breaking by chemical ordering for polar structure and multiferroic properties is explained. Following this, inversion symmetry breaking in doubly ordered perovskites is discussed. Finally, the scope of the thesis is provided.

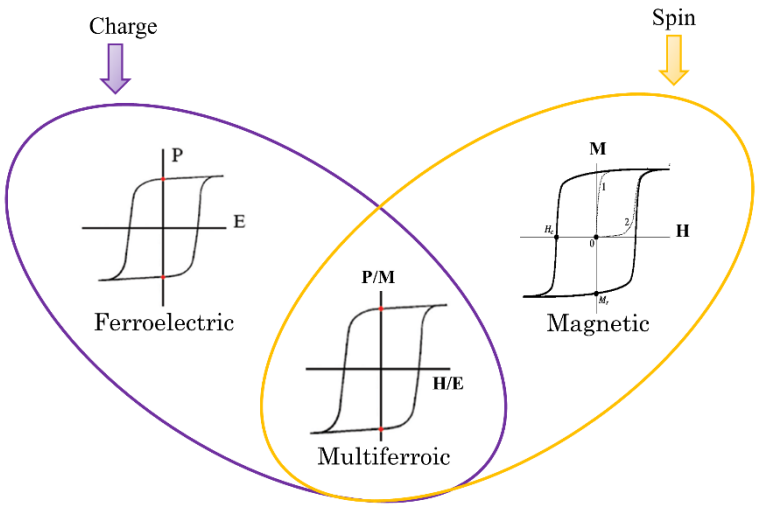

1.1 Ferroelectricity

Last year 2020 was celebrated as the 100th anniversary of the discovery of ferroelectricity. Although ferroelectricity was identified 100 years ago in the 1920s in Rochelle salt by the graduate student Joseph Valasek, at that time, its importance was seldom realized [1]. Ferroelectricity is a characteristic of particular materials which exhibits spontaneous polarization and can be switched by reversing the direction of the electric field. Before this, some physicists anticipated and even predicted the feasibility of an electrical behavior in some materials similar to the long-known analogous hysteresis behavior of magnetic materials. The concept of Curie temperature was used in some solids by Peter Debye in 1912. Later in the same year, Erwin Schrödinger assigned the term ferroelectricity [2]. The names ferroelectrics, ferroelectricity, etc., are referred to the hysteresis loop, which is originally observed in the magnetic materials. Also, related terminologies, e.g., Curie constant, Curie temperature, etc., that characterize the ferroelectricity are inherited from magnetic materials.

The ferroelectric hysteresis loop between electric polarization (*P*) *vs*. the electric field (*E*) of Rochelle salt was published in Physical Review in April 1921 [1]. After this, less attention was paid to the scientific observation of ferroelectricity. In the late 1940s, ferroelectricity was discovered in barium titanate ($BaTiO_3$), and it triggered the understanding and development of ferroelectric behavior in materials [3,4]. By that time, the Landau theory (1937) [5] and later Landau-Ginzburg's (1950) lattice dynamics approach [6] were in place to explain the mechanisms of material phase transition. Further, the role of crystallographic point group symmetry was understood to design the new functional materials.

Rochelle salt (sodium potassium tartrate tetrahydrate $NaKC_4H_4O_6{\cdot}4H_2O$) displays ferroelectric properties between 255 and 297 K (ferroelectric region), and the spontaneous polarization (*P*) arises along the *a*-axis. The symmetry of the crystal structure of Rochelle salt is orthorhombic ($P2_12_12$) in paraelectric phases and monoclinic ($P2_1$) in the ferroelectric phase. The crystal structure of Rochelle salt is shown in Figure 1.1(a), and hydrogen bonds between tartrate molecules and water molecules are accounted for ferroelectricity. The well-known ferroelectric material $BaTiO_3$ undergoes a phase transition at 403 K from cubic paraelectric phase ($Pm\bar{3}m$) to tetragonal ferroelectric phase ($P4mm$) with an accompanying displacement of atoms. The titanium (Ti) atom inside the TiO_6 octahedra is displaced significantly by second-order Jahn-Teller (SOJT) distortion and is responsible for the net

polarization, as shown in Figure 1.1(b). Upon cooling, $BaTiO_3$ undergoes a phase transition to ferroelectric orthorhombic phase (*Amm*2) at 278 K and further to ferroelectric rhombohedral phase (*R*3*m*) below 183 K.

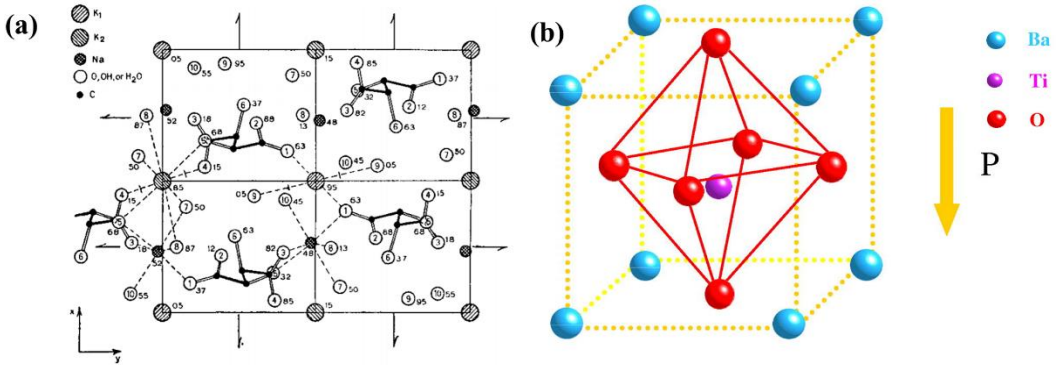

Figure 1.1 (a) Structure of Rochelle salt on (001) plane (adapted from Ref. [7]). (b) Crystal structure of $BaTiO_3$ in tetragonal ferroelectric phase (adapted with permission from Ref. [8], © (2008) by the Elsevier Ltd).

Some ferroelectric materials have ions with lone-pair of electrons (e.g., Pb^{2+}, Bi^{3+}, Sn^{2+}, Te^{4+}, I^{5+}) in which lone-pair orbitals exhibit a directional bonding and result in net polarization [9]. Similar to $BaTiO_3$, other ferroelectrics like lead titanate ($PbTiO_3$), lead zirconate titanate {$Pb(Zr_xTi_{1-x})O_3$, PZT}, lead lanthanum zirconate titanate (PLZT), and lead magnesium niobate (PMN) are extensively studied and utilized for a variety of technological applications, e.g., non-volatile memories, electro-optic devices, transistors, phonograph pickups, band-pass filters, sonic delay lines, sonar, ultrasonic cleaning, medical ultrasound uses, watches, and accelerometers, etc [9].

Other exciting properties in dielectric materials are viz. piezoelectricity and pyroelectricity. Piezoelectricity is the ability of some crystalline materials to develop an electrical charge for the application of mechanical stress [10]. Only crystals that are anisotropic with a lack of inversion symmetry are piezoelectric (Out of 32 crystal classes, 20 of them are piezoelectric, as shown in Figure 1.2). Polarization occurs in single crystals of piezoelectric materials upon application of stress. One side of the crystal develops a net positive charge, and the opposite side develops a net negative charge. When subjected to an external applied electric field, piezoelectric crystals undergo a reversible piezoelectric effect, and they change shape by a small amount [9]. Pierre and Jacques Curie first discovered the piezoelectric effect in 1880. The Curie brothers spotted the piezoelectricity in many naturally occurring, laboratory-grown crystals, e.g., quartz, zinc blende (sphalerite), sugar, topaz,

tourmaline, and Rochelle salt. Piezoelectric materials are used as transducers in ultrasonic devices, phonograph pickups, microphones, accelerometers, and sonar devices [9].

The other intriguing property of dielectrics is pyroelectricity. Pyroelectrics are subgroups of piezoelectrics, as shown in Figure 1.2. They are polar in nature and exhibit change in polarization with respect to temperature. The polarization of pyroelectric materials cannot be switchable by an electric field which is converse to ferroelectricity which changes polarization direction by changing the direction of an electric field. Hence, all ferroelectrics are pyroelectrics, but the reverse is not true. Example for pyroelectric materials is tourmaline, lead zirconate titanate, wurtzite, and triglycine sulfate, etc. Pyroelectrics can be used in IR detection, imaging, and power generation, etc. The pyroelectric material $LiTaO_3$ is used in scanning microcalorimeter and microenthalpimeter [9].

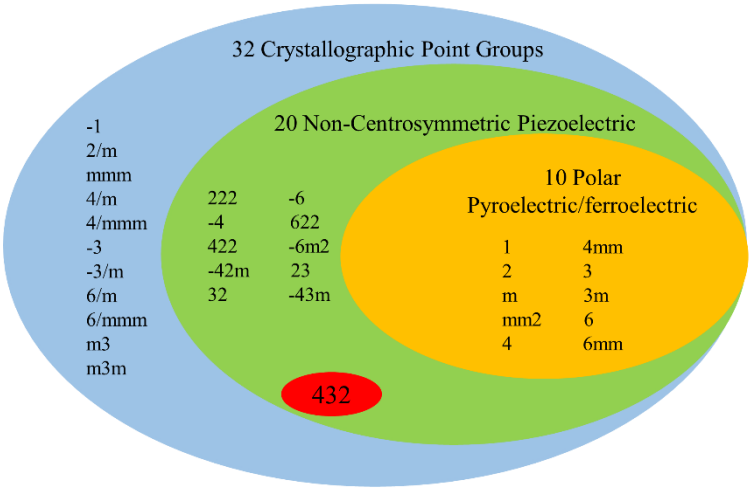

Figure 1.2 Crystallographic point groups (point group 432 is noncentrosymmetric but not piezoelectric)

1.2 Multiferroics

Looking at history, Hans Schmid coined the term multiferroic in 1993, considering the previous classification of ferroic materials by Aizu [11,12]. Multiferroic materials are those materials that exhibit two or more primary orders, such as ferromagnetism, ferroelectricity, ferroelasticity, and ferrotoroidicity [11,13]. A subset of these materials is called magnetoelectric, i.e., these materials exhibit coupling between their magnetic and electric properties. This coupling is an important parameter for modern-day applications, as it allows the control of magnetic order by an electric field and vice versa. The term magnetoelectric

initially specified to a linear coupling between electric polarization (magnetization) and magnetic (electric) field, nowadays this includes all types of coupling phenomena that take place between charge and spin degrees of freedom when discussing magnetoelectric multiferroics [14]. Furthermore, the initial concept of coexisting order parameter has been expanded, which also includes antiferromagnetism.

In the pool of multiferroic materials in the literature, the most intensely investigated present-day multiferroics are $BiFeO_3$, hexagonal $RMnO_3$ (R = Sc, Y, In, Dy-Lu) [15,16], orthorhombic $TbMnO_3$ [17], $TbMn_2O_5$ [18], etc. However, the celebrity of the initial multiferroic materials were boracites. Asher *et al.* reported a hysteric switching of a multiferroic state of $Ni_3B_7O_{13}I$ by either magnetic or electric fields in 1966 [19]. Such experimental findings were accompanied by the development of a theoretical framework that leads to new magnetoelectric multiferroics for future technological applications. Magnetoelectric multiferroic materials consist of many applications for modern-day technologies [20,21]. Among these, the most promising use would be in a magnetoelectric memory device [22]. Multiferroics can be used in devices such as spin wave generators, magnetic field sensors, microwave resonators, phase shifter, domain wall devices, photovoltaic solar cells, thermal energy harvesting, oxide electronics etc [20,22,23].

1.2.1 Symmetry aspects of multiferroics

Symmetries are the most fundamental deciding factors for magnetoelectric effect and multiferroicity [14,20]. As we discussed in the previous section, for ferroelectricity, **spatial inversion symmetry** (I) should be broken. On the other hand, the **time reversal symmetry** (T) should be broken for magnetism. The electric polarization ($\vec{P}$), defined as dipole moment per unit volume, which is a polar vector, the dipole moment is given by $q\vec{r}$, where $\vec{r}$ defines the distance between the charges $\pm q$. Electric polarization ($\vec{P}$) is odd under spatial inversion and even under time reversal as given below [24],

$$\vec{P}_I' = I\vec{P} = -\vec{P}$$

$$\vec{P}_T' = T\vec{P} = \vec{P}$$

As stated by Neumann's principle, "the symmetry of any physical property of a crystal must include the symmetry elements of the point group of the crystal," which implies that any physical property of this crystal would remain invariant with respect to that symmetry element present in the crystal. Thus, the materials to show spontaneous polarization should

break the spatial inversion symmetry. Because of this, ferroelectricity or pyroelectricity results only in the ten noncentrosymmetric (polar) point groups out of total 32 crystallographic point groups (Figure 1.2) [25]. Using Neumann's principle, the direction of the electric polarization can be determined. For example, in the case of orthorhombic point group *mm*2, the allowed polarization is only along the *z* direction. If the polarization is directed along the *x*- or *y*-direction, it would be reversed under the two-fold rotation. Detailed polarization directions for the crystal systems are given in the book [25].

As we know, the magnetization ($\vec{M}$) is an axial vector. Under spatial inversion (*I*) and time reversal (*T*), the magnetization ($\vec{M}$) transforms as,

$$\vec{M}_I' = I\vec{M} = \vec{M}$$

$$\vec{M}_T' = T\vec{M} = -\vec{M}$$

Symmetry operations on magnetization can be understood by considering magnetic moment as a current carrying loop $M \sim \vec{r} \times \vec{j}$, where $\vec{j} = ed\vec{r}/dt$. The magnetization changes its sign under time reversal symmetry and remains invariant under spatial inversion symmetry, as shown in Figure 1.3. Thus, ferromagnetic materials exhibit spontaneous magnetization by breaking time reversal symmetry.

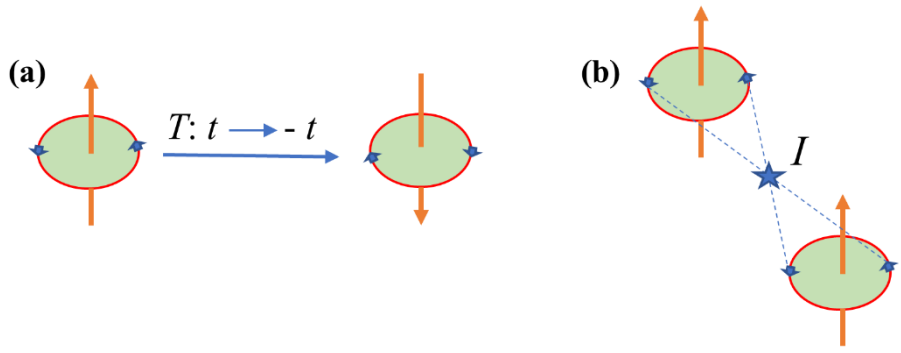

Figure 1.3 (a) Time reversal operation and (b) Inversion operation on the magnetic moment.

Similarly, the antiferromagnetic order parameter is also odd under time reversal symmetry, which is given by $\vec{L} = \vec{S}_i - \vec{S}_j$, changes under time reversal (*T*) as,

$$\vec{L}_T' = T\vec{L} = T\vec{S}_i - T\vec{S}_j = -(\vec{S}_i - \vec{S}_j) = -\vec{L}$$

Therefore, the antiferromagnetic order parameter changes its sign upon time reversal, indicating the antiferromagnetic ordering also breaks the time reversal symmetry.

In the case of multiferroics, with the breaking of time reversal (*T*) and spatial inversion (*I*), the product of time reversal followed by inversion (*TI*) also should be broken, whereas the product (*IT*) is not broken in magnetoelectric. Thus, by checking the symmetries, one can understand whether a material with a corresponding magnetic structure would be multiferroic (polarization is observed without application of magnetic field) or only a magnetoelectric (polarization is observed only under the application of magnetic field).

1.2.2 Combining ferroelectricity and magnetism

For multiferroic property, we need to combine ferroelectricity and magnetism in a single material. According to the classical concept, magnetic and ferroelectric properties cannot coexist in a single-phase material [26,27]. As we know, for magnetism, the material should have *d* or *f* electrons, while an empty *d* orbital is crucial for the observation of ferroelectricity. Most ferroelectrics have an empty *d* orbital which contributes to the formation of a bond between transition metal ions with the oxygen ligand. The interaction between the empty *d* orbital and filled *p* orbital of the oxygen atom leads to the lowering of the energy, as shown in Figure 1.4. This bonding interaction induces the effective displacement of the transition metal cation towards the oxygen. This collective shift of cations and anions over the whole crystal leads to net polarization resulting in ferroelectricity. If the *d* orbital has an electron, the overlap between the *d* orbital of the transition metal and the *p* orbital of the oxygen will not result in a reduction of the energy. The bond formation between the transition metal ion and oxygen ligand will be less energetically favourable because the electron from the *d* orbital would go into the anti-bonding orbital and opposes the energy gain due to the presence of electrons in the bonding site. Therefore, displacement essential for ferroelectricity will not occur. Many different routes have been tried to incorporate magnetic cations in ferroelectric materials to overcome this mutual exclusive requirement. Multiferroics are mainly classified into type-I and type-II multiferroics based on the mechanism of coupling between ferroelectricity and magnetism [24,27].

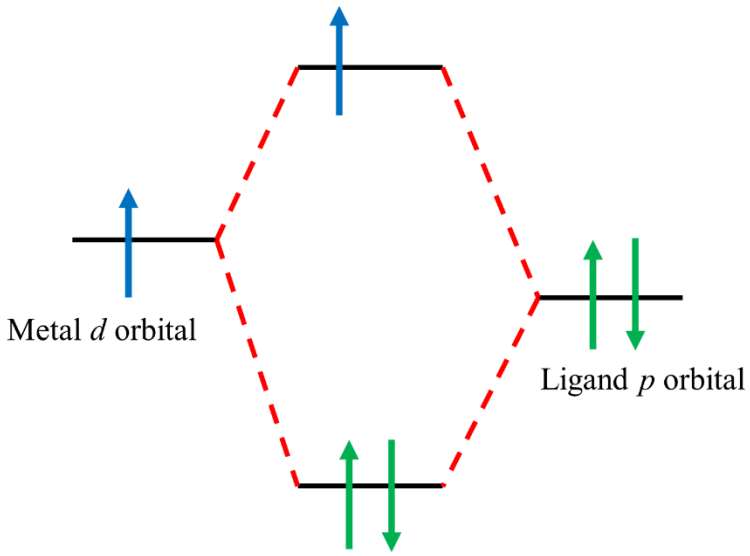

Figure 1.4 The bonding occurs between the empty *d*-orbital of the transition metal cation and the filled *p*-orbital of the oxygen ion. The arrows in green are electrons of oxygen that go into the bonding state. If the *d*-orbital contains an electron (arrow in blue), then the electrons would fill up the anti-bonding orbital and results in weakening the bond between the metal cation and the ligand oxygen.

1.2.3 Type-I: Ferroelectricity and magnetism have independent origins

In type-I multiferroics, ferroelectricity and magnetism occur individually from two different ions at different temperatures, and thus the coupling between ferroelectric and magnetic ordering is very weak [27]. Various ways have been tried to solve the well-known d^0 *vs.* d^n problem by combining ferroelectricity and magnetism independently in a single material. The following mechanisms are discussed below.

1.2.3.1 Ferroelectricity due to lone pair effect

In the perovskite $BiFeO_3$, the lone pair effect of $6s^2$ electrons of Bi^{3+} ion causes the ferroelectricity below 1100 K by breaking the inversion center, and magnetism appears from the ordering of Fe^{3+} ions below 643 K [27,28]. Sometimes these $6s^2$ electrons do not take part in bonding: instead, they form stereochemically active lone pairs. The hybridization occurs between the 6s orbitals of these ions and their own *p* orbitals or the *p* orbitals of the oxygen ligand. After this, 6*s* orbitals are no longer spherical. Instead, they become a lobe-type shape, as shown in Figure 1.5 (a). These lobes are free to rotate and distort the crystal structure. Below a certain temperature, these lobes may break inversion symmetry by aligning in a uniform direction and thus yields a net electric polarization [24,28]. The multiferroicity is

observed with the above-discussed mechanism in the vastly studied $BiFeO_3$ compound [28–30].

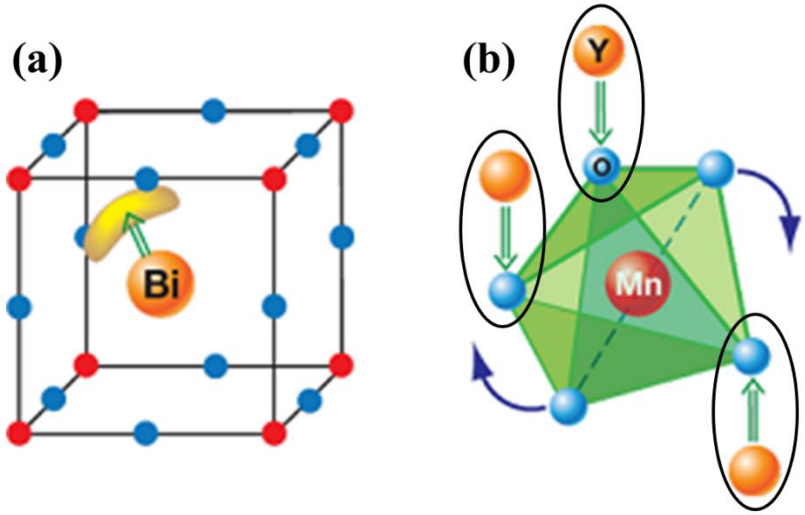

Figure 1.5 Microscopic mechanism for ferroelectricity in $BiFeO_3$ and $YMnO_3$ (adapted from Ref. [31]). (a) The ordering of $6s^2$ lone pairs (yellow lobe) of Bi^{3+} ions contribute to the net polarization. (b) Distortion of a rigid MnO_5 block in $YMnO_3$ resulting in a net polarization.

1.2.3.2 Geometric ferroelectricity

Geometric frustrated ferroelectricity is realized in $AMnO_3$ (A = Ho to Lu and Y) [32]. In this mechanism, geometric frustration leads to a polar distortion in the lattice and is responsible for ferroelectricity. The compound $YMnO_3$ crystallizes in a hexagonal polar $P6_3cm$ under ambient pressure. In the crystal structure of h-$YMnO_3$, the titling of MnO_5 polyhedra below ferroelectric transition temperature (T_C ~ 600 K) leads two downward Y – O dipoles and one upward Y – O dipole (see Figure 1.5 (b)) and thus results in net electric polarization [27,32]. The Mn^{3+} spins order antiferromagnetically below T_N ~ 80 K, and thus this compound is multiferroic below 80 K. Another family, $BaMF_4$ (M = Ni and Co), also undergoes geometric frustration and belong to this class of multiferroics [33–35].

1.2.3.3 Ferroelectricity due to charge ordering

The general mechanism of charge ordering leads to ferroelectricity is illustrated in Figure 1.6. Homogenous crystal represents as a neutral one-dimensional chain is given in Figure 1.6(a). Sometimes site centered charge ordering occurs (Figure 1.6(b)) because of the charge ordering of metal ions which have different valencies. In some cases, bond centered ordering occurs due to the dimerization of homogenous crystals, as shown in Figure 1.6(c).

Here, sites are equivalent, but bonds become different. Site and bond centered ordering do not break inversion symmetry individually because of the presence of mirror planes; therefore, no net dipole moment is observed. Sometimes both types of charge order take place simultaneously, breaks the inversion symmetry, and develop a net polarization, as shown in Figure 1.6(d) [36,37]. The ferroelectricity is reported in $LuFe_2O_4$ because of the charge ordering of Fe^{2+} and Fe^{3+} ions [38]. However, even after a decade of research, the ferroelectricity of this compound is still questioned [39].

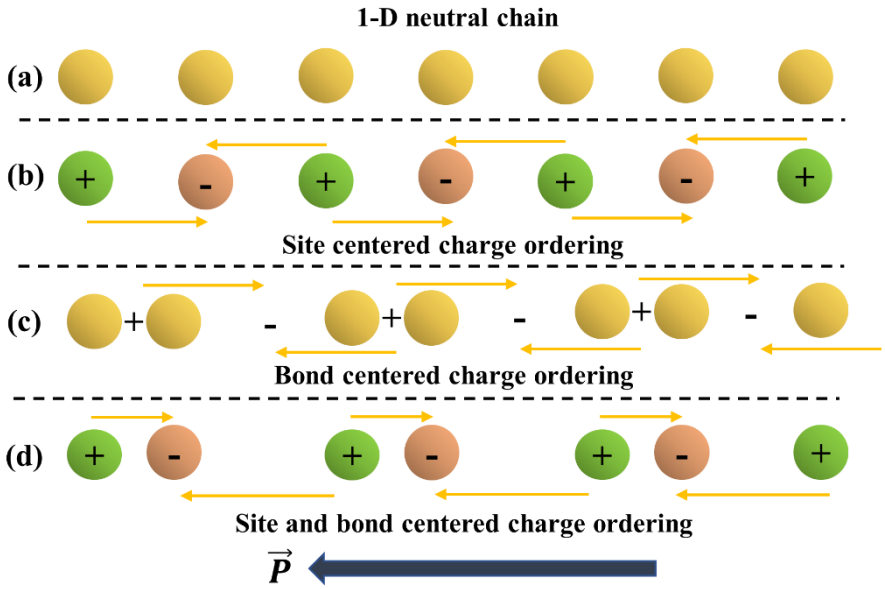

Figure 1.6 Illustration of charge ordering and direction of polarization.

1.2.3.4 Other mechanisms

Many other schemes with the combination of ferroelectricity and magnetism are adopted to achieve multiferroicity. **Ferroelectricity in hybrid organic-inorganic materials, incorporation of magnetic ions in a ferroelectric material, heterostructures.** Recently, extensive work has been carried out on organic-inorganic hybrid materials for multiferroic properties. In these materials, ferroelectricity generally originates from the ordering alignments of the organic moiety. Most of the reported hybrid multiferroics are a series of metal-organic perovskite formates, [ammonium][M(HCCO)$_3$] (M = Cu, Mn, Fe, and Ni) [40–42]. The magnetism of these materials is derived from the [M(HCCO)$_3$]$^-$ framework, while the ferroelectric order is associated with the order-disorder transition of organic components through hydrogen bonding, as shown in Figure 1.7. The material [$(CH_3)_2NH_2$][Mn(HCCO)$_3$]

undergoes a phase transition from noncentrosymmetric structure ($R\bar{3}c$) to polar structure (Cc) at 187 K and shows a magnetic transition at T_N ~ 8.5 K. Since the origin of ferroelectricity and magnetism are different, these materials are classified under type-I multiferroics.

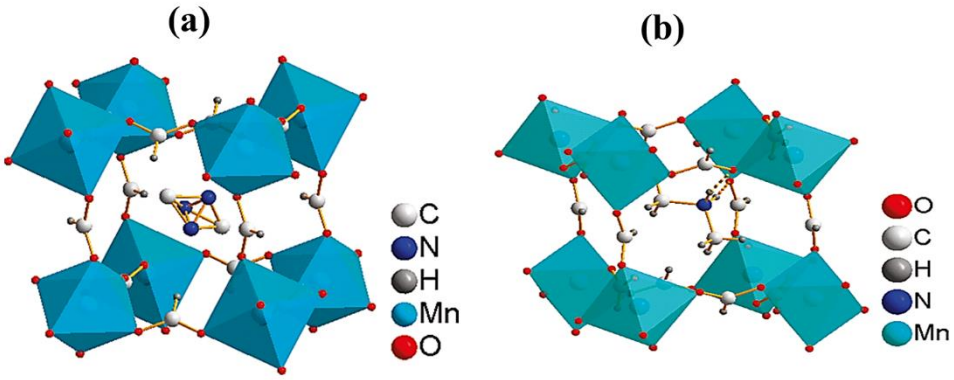

Figure 1.7 (a) Perovskite $[(CH_3)_2NH][Mn(HCOO)_3]$ crystallizes in $R\bar{3}c$, and it is paraelectric at 300 K. (b) Low-temperature structure, where it forms hydrogen bonding (dotted line) between N-atom of the $[(CH_3)_2NH]^+$ cation and the formate oxygen which leads to polar Cc, and it is ferroelectric (adapted from Ref [43]).

The other way towards achieving multiferroic materials is to incorporate magnetic ordering in a ferroelectric material or vice versa. This method is adopted mainly by substituting magnetic ions in a ferroelectric material. For example, in ferroelectric $PbWO_3$, the Co^{2+} ion is substituted for magnetism leads to $Pb_2(CoW)O_6$. Several multiferroic materials have been prepared using this strategy [44,45]. However, the magnetoelectric coupling of these materials is also weak because the origin of ferroelectricity and magnetism is from different atoms. Furthermore, due to the dilution of the magnetic ions, the magnetic interaction strength of these materials is weak thus has low Curie or Néel temperatures.

A large amount of work has been dedicated to making the heterostructures of magnetic and ferroelectric layers for magnetoelectric functioning at the interfaces [46,47]. This strategy is quite promising because it can be used in device applications. Since it is beyond the scope of this thesis, we will be discussing the multiferroic properties of only single-phase materials.

1.2.4 Type-II: Magnetism induced ferroelectricity

Type-II multiferroics are those where both magnetism and ferroelectricity have a common origin [27]. In this type of multiferroics, the particular type of complex magnetic ordering breaks the inversion symmetry [27,28,48–50]. Since ferroelectricity arises below

magnetic ordering temperature, the coupling between them is strong compared to type-I multiferroics. These magnetically induced improper ferroelectric materials are the most demanding in condensed matter physics for technological aspects. So far, three well-known microscopic mechanisms explain the observation of ferroelectricity by magnetism. (i) Spin current or inverse Dzyaloshiniskii-Moriya (DM) interaction mechanism, (ii) Exchange striction mechanism (iii) Spin-dependent $p - d$ hybridization [50,51]. In characterizing these mechanisms, a cluster model is proposed with two neighbouring magnetic ions carrying spins $\vec{S}_i$ and $\vec{S}_j$ and a ligand ion. Ferroelectric polarization in this cluster induced by spin ordering can be represented as [50],

$$\Delta P = P^{sp}\,\vec{e}_{ij} \times \left(\vec{S}_i \times \vec{S}_j\right) + P^{ms}\left(\vec{S}_i.\vec{S}_j\right)\vec{e}_{ij} + P^{orb}\left[\left(\vec{e}_{ij}.\vec{S}_i\right)\vec{S}_i - \left(\vec{e}_{ij}.\vec{S}_j\right)\vec{S}_j\right]$$

Here the unit vector $\vec{e}_{ij}$ connects the magnetic spins $\vec{S}_i$ and $\vec{S}_j$. The first, second and third term gives the ferroelectric polarization due to above-mentioned three mechanisms, respectively.

1.2.4.1 Spin current or inverse DM interaction mechanism

Magnetically induced ferroelectricity is observed in many materials, originates from magnetic frustration. A magnetic compound with moderate frustration tends to reduce the extent of its spin frustration by adopting a noncollinear magnetic structure such as cycloid, which is a noncentrosymmetric magnetic order and responsible for the so-called inverse DM interaction [52,53]. The microscopic mechanism that induces the polarization in noncollinear spiral magnetic structure compounds is explained by the inverse DM interaction mechanism, also called the spin current model. In this interaction, polarization is induced under the effect of spin-orbit interaction (SOI) in particular spiral spin structures. This model was first introduced by Katsura and Nagosa [53]. According to this model, due to the canting of spins in noncollinear magnets, the ligand ion would shift in order to gain the DM interaction energy. In some particular noncollinear magnets, this shift can project onto the crystal lattice and induces a small polar displacement and hence results in macroscopic polarization of form $P \propto \vec{e}_{ij} \times \left(\vec{S}_i \times \vec{S}_j\right)$, as shown in Figure 1.8.

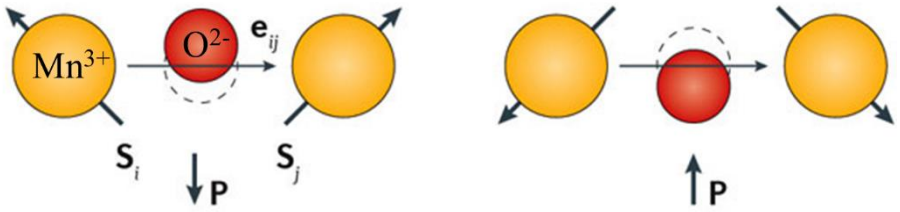

Figure 1.8 The inverse DM interaction can induce a canting of neighboring spins, $\vec{S}_i$ and $\vec{S}_j$, and results in polar displacement (adapted with permission from Ref. [54], © (2016) by the Springer Nature).

The exchange interaction in these multiferroics is weak. Because of this reason, the electric polarization is small relative to classical ferroelectric materials. However, the coupling between order parameters is strong because the polarization direction is linked to the direction of the spins. Because of the frustration, the magnetic system can adopt different types of noncollinear spin structures, as shown in Figure 1.9. Sinusoidal spin density wave (Figure 1.9(a)) is a centrosymmetric magnetic structure that does not induce individual polarization in the material unless the paramagnetic crystal structure is polar. A spin density wave (SDW) state consists of collinear magnetic moments, but their magnitudes vary sinusoidally from one spin site to its adjacent one along the propagation direction. The spin moment of a cycloid rotates in the *xz* plane with the propagation direction $\overrightarrow{\mathbf{Q}}$, and it is moving from one spin site to its adjacent one, as shown in Figure 1.9(b). The cycloidal magnetic structure breaks the inversion symmetry and allows the polarization perpendicular to the propagation vector $\overrightarrow{\mathbf{Q}}$ [27,49]**.** A more discussion on SDW and cycloidal magnetic structure is given in chapter 3. Figure 1.9(c) shows the proper-screw structure where the spins rotate in the *xz* plane perpendicular to $\overrightarrow{\mathbf{Q}}$**.** Although inversion symmetry is broken in this case, it does not allow polarization according to inverse DM interaction, but in some instances, it might [55–57]. The best example for cycloidal magnetic structure-driven ferroelectricity is $TbMnO_3$ [17]. It is the first discovered spin-induced multiferroic. It possesses a centrosymmetric orthorhombic crystal structure with *Pbnm*. At first, $TbMnO_3$ undergoes a sinusoidal magnetic ordering at T_N ~ 41 K, and then it changes to cycloidal magnetic ordering below T_N ~ 28 K, where cycloidal structure breaks the inversion symmetry and induce polarization according to inverse DM interaction. Further, the spin-induced ferroelectricity based on the cycloidal (transverse spiral) spin ordering discovered in many materials such as $MnWO_4$, $LiCuO_4$, $BaYFeO_4$, CuO, $Ni_3V_2O_8$, and $LiCu_2O_2$ [58–62]. Apart

from the cycloidal magnetic structure, the transverse conical spin structure can induce polarization as reported in $CoCr_2O_4$ and ceratin hexaferrite [63].

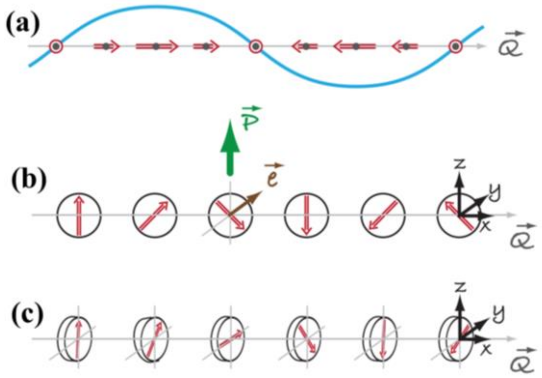

Figure 1.9 Different types of non-collinear magnetic spin structures relevant for type-II multiferroics (adapted from Ref. [31]).
(a) Spin density wave, (b) Cycloidal, and (C) Screw-type magnetic

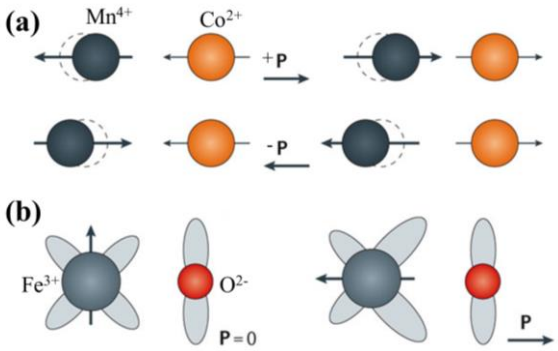

Figure 1.10 (a) Electric polarization can arise due to exchange striction mechanism as in Ca_3CoMnO_6 .
(b) Spin induced polarization by *d-p* hybridization as in $CuFeO_2$.
(adapted with permission from Ref. [54], © (2016) by the Springer Nature).

1.2.4.2 Exchange striction mechanism

The other mechanism of magnetically driven ferroelectrics is those in which collinear magnetic structures induce electric polarization. In this case, all magnetic moments are aligned along a specific axis (commensurate magnetic structure) without the necessary participation of the spin-orbit interaction [64]. In the exchange striction mechanism, the crystal structure deforms because of the change in bond length caused by the magnetic ordering below magnetic ordering temperature and results in net dipole moment. If the magnetic chain contains equivalent valence, the dipoles cancel out, and no net polarization is obtained. When the magnetic chain consists of alternating differently charged ions, electric polarization is induced, as shown in Figure 1.10(a). For example, the collinear up-up-down-down magnetic spin structure induces electric polarization according to the exchange striction mechanism. This particular up-up-down-down spin arrangement in the magnetic chain is observed due to the existence of competing nearest-neighbor ferromagnetic (J_{FM}) and the next nearest neighbor antiferromagnetic (J_{AFM}) interactions. For collinear magnetic structure, the ratio should be $|J_{FM}/J_{AFM}| > 1/2$; if $1/4 < |J_{FM}/J_{AFM}| < 1/2$, a spiral magnetic ground state is preferred [49].

A typical example is Ca_3CoMnO_6 which has a centrosymmetric structure ($R\bar{3}c$) exhibits alternating Co^{2+} and Mn^{4+} ordering and possesses up-up-down-down spin structure below its magnetic ordering temperature (T_N ~ 16.5 K). This spin structure breaks the inversion symmetry and induces electric polarization along the chain axis due to exchange interaction (Figure 1.10(a)) [65]. In Ca_3CoMnO_6, exchange striction results from magnetic transition metal cations with a different valence (Co^{2+} and Mn^{4+}). In some cases, one can expect the same effect even for identical magnetic ions. This kind is observed in high-pressure stabilized orthorhombic RMnO$_3$ (R = Ho-Lu) [51,64]. These materials have the zig-zag fashion of Mn^{3+}-O-Mn^{3+} bonds and spins in the form of up-up-down-down sequence. This magnetic structure is called as *E*-type AFM, which shifts the oxygen ions perpendicular to the Mn-Mn bonds by means of exchange striction and induces the polarization along the same direction. It is shown that in the LnMn$_2$O$_5$ family, where Mn^{3+} and Mn^{4+} spins are ordered in a similar zig-zag fashion, and the observed electric polarization is ruled by the exchange striction mechanism [18,66]. This mechanism is also observed in weak ferromagnetic systems such as LnFeO$_3$ (Ln = Gd and Dy). In these systems, the exchange striction between the Ln^{3+} and Fe^{3+} moments shift the Ln^{3+} ions in such a way that it induces a uniform polar distortion and results in large macroscopic polarization. Since the electric polarization of these materials involves ionic displacements, the observed polarization is larger than that of other spin-induced polarization discussed in the previous section [64].

1.2.4.3 *d-p* hybridization

As discussed in section 1.2.4.1, the inverse DM interaction model does not allow polarization in the compounds having a screw-type magnetic structure. However, the polarization is observed in triangular lattice antiferromagnet delafossite oxides $CuFeO_2$, ACrO$_2$ (A = Ag, Cu) and MI$_2$ (M = Mn, Ni) with CdI_2 structure, which possess a screw-type magnetic structure [24,48,51,67]. Thus, *d-p* hybridization is proposed to describe the proper screw-type magnetic structure induced polarization in these materials [68]. This model was proposed based on spin-orbit coupling as an alternative mechanism for DM interaction [69]. An apparent difference is that this mechanism involves a single magnetic site for a local electric dipole, whereas the DM interaction deals with the two magnetic sites. In the screw-type spin arrangement compounds, where the magnetic ion occupies a low symmetric crystal environment, the *d-p* hybridization between the metal and ligand ions is responsible for electric polarization. For example, $CuFeO_2$ exhibits a proper screw magnetic structure, and *d-p* hybridization is considered to describe the polarization of this compound [22,70]. However,

careful analysis of the crystal symmetry eliminates this mechanism since all the dipoles over the bonds cancel each other and give no net polarization. Furthermore, the *d-p* hybridization may be responsible for the polarization observed in noncentrosymmetric materials $Ba_2CoGe_2O_7$ and $RFe_3(BO_3)_4$ with screw-type spin structure [71,72].

1.3 Polar magnetic oxides: a new class of multiferroics

Here, we discuss a new class of multiferroics based polar magnetic oxides, where the polar distortion driven by the chemical ordering of cations is stabilized right at the formation temperature of these compounds, and they do not seem to undergo nonpolar to polar transition. Consequently, some of these polar materials have been shown to be pyroelectric at all temperatures. These polar magnetic oxides differ from type-I multiferroics, where they undergo ferroelectric (polar) - paraelectric (nonpolar) transition at high temperatures. However, a change in polarization (ΔP) occurs at the magnetic ordering temperatures, which is influenced by the applied magnetic field, but the extent of magnetoelectric coupling depends on the magnetic spin structure and, therefore, the microscopic mechanisms that couple the magnetism with electric polarization. Though this behavior is similar to that of type-II multiferroics, the inversion symmetry in the later is broken only at the magnetic ordering temperature by complex magnetic structures. For these reasons, we can classify the polar pyroelectric magnets as another class of multiferroics. This class of multiferroics is promising because they do not necessarily involve complex magnetic structures arising from spin frustration, and therefore, one can combine appropriate magnetic ions with a polar structure to achieve a magnetoelectric effect at room temperature. Furthermore, because of the pyroelectric nature, these materials may not require the poling electric field to measure electric polarization at the magnetic ordering temperature. In these materials, the microscopic mechanism responsible for the observation of electric polarization below magnetic ordering temperature might be magnetoelastic coupling. Nevertheless, the possibility of symmetric exchange striction or inverse DM interaction cannot be ruled out.

In the following, we will discuss several structural families of materials where the inversion symmetry is broken by chemical ordering and their impact on magnetoelectric multiferroic properties. By chemical ordering, we mean the following arrangements of atoms or ions; (i) Two or more number of atoms or ions with symmetrically independent sites are generated from symmetrically equivalent atomic position, (ii) atoms and ions of the same

charge with different chemical coordination environment, and (iii) charge ordering of the same or different ions.

1.3.1 Inversion symmetry breaking from chemical ordering

The simple and textbook example of inversion symmetry breaking due to chemical ordering is zinc blende (Sphalerite, ZnS). The structure of zinc blende can be related to the highly symmetrical cubic structure of diamond where zinc and sulfur occupy the position of carbon alternatively, and they are bonded to each other in the same way as shown in (Figure 1.11) [73]. Thus, both structures have the same kind of chemical unit cell. However, the symmetry of zinc blende structure ($F\bar{4}3m$) is lower than that of diamond ($Fd\bar{3}m$) because the symmetry equivalent position (8*a*) of carbon atoms in diamond is split into two symmetrically independent atomic sites (4*a* and 4*c*) in zinc blende, where zinc and sulfur are located, respectively. In this symmetry lowering process, the centre of inversion connecting two carbon atoms in diamond is removed, and thus zinc blende becomes noncentrosymmetric but nonpolar.

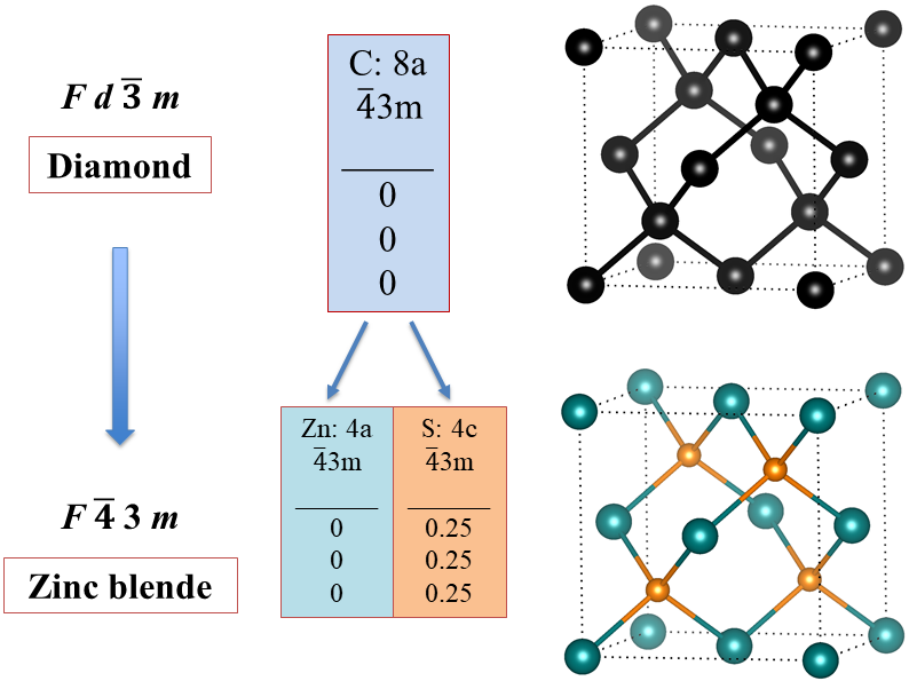

Figure 1.11 The symmetry relation between diamond and zinc blende structures showing inversion symmetry breaking due to chemical ordering (adapted from Ref. [73]).

1.3.2 Literature of polar magnetic oxides

In this section, a detailed discussion on polar magnetic oxides resulting from inversion symmetry breaking by chemical ordering and responsible for multiferroic properties are explained with few examples.

1.3.2.1 Kamiokite

A family of $M_2Mo_3O_8$ (M = 3d transition metal) compounds related to mineral Kamiokite crystallizes in the polar hexagonal structure ($P6_3mc$). In this structure (Figure 1.12(a)), the M^{2+} ions occupy two different crystallographic sites with MO_4 tetrahedra (M_{td}) and MO_6 octahedra (M_{oh}) forming a honeycomb-like layer in the *ab*-plane by sharing their corners. The nonmagnetic trimeric unit of Mo^{4+} ions forms a kagome-like layer. These two layers are stacked along the *c*-axis. In these compounds, a variety of magnetic properties have been reported depending on the nature of transition metal ions at M_{td} and M_{oh} sites [74–76]. A large linear magnetoelectric effect has been reported in the polar magnet $Fe_2Mo_3O_8$ [75,77,78]. Below T_N = 60 K, the compound orders antiferromagnetically with an uncompensated Fe^{2+} moment between Fe_{td} and Fe_{oh} sites, resulting in the ferrimagnetic ground state. A change in electric polarization ($\Delta P \sim 0.3 \mu C/cm^2$) along the *c*-axis at the collinear antiferromagnetic ordering temperature has been reported as shown in Figure 1.12 (b).

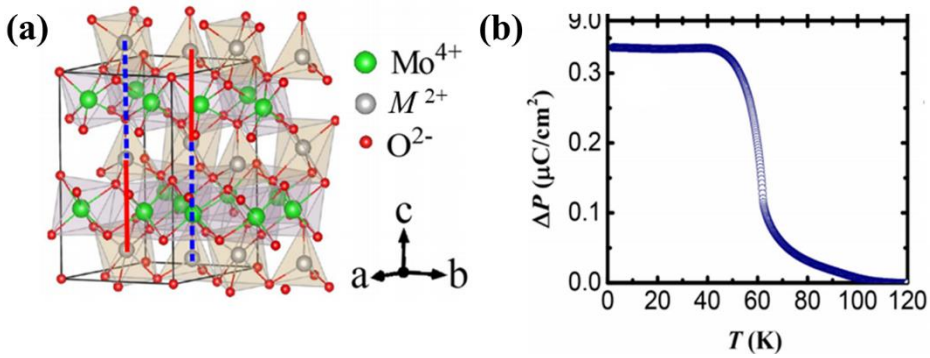

Figure 1.12 (a) Crystal structure of $M_2Mo_3O_8$ exhibiting ordered octahedra (MO_6) and tetrahedra (MO_4) framework. (b) Variation of the electric polarization ΔP with temperature, respectively (adapted with permission from Ref. [75], © (2015) by the Springer Nature).

1.3.2.2 Swedenborgite

Another example could be the pyroelectric ferrimagnet $CaBaCo_4O_7$ crystallizing in the polar orthorhombic structure ($Pbn2_1$), where CoO_4 tetrahedra form alternating layers of

triangular and Kagome lattices with Co^{2+}/Co^{3+} charge ordering in four different crystallographic sites as shown in Figure 1.13(a) [79]. The intrinsic geometric frustration associated with these layers is relieved due to the buckling of CoO_4 tetrahedra, which results in ferrimagnetic ordering at T_C = 64 K [80]. Single-crystal measurements have confirmed that the electric polarization appearing below the magnetic ordering is not switchable by the external electric field [81]. Change in polarization below the T_C of a single-crystal sample is shown in Figure 1.13(b). The exchange striction mechanism has been suggested to be responsible for the enhancement of polarization at the magnetic ordering temperature. A similar magnetoelectric effect has been reported in another polar ferrimagnetic compound, $CaBaFe_4O_7$ [82].

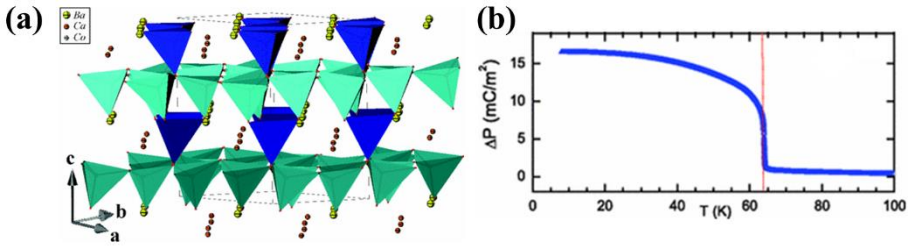

Figure 1.13 (a) Crystal structure of $CaBaCo_4O_7$ consists of alternating layers of triangular and Kagome lattices with Co^{2+}/Co^{3+} charge ordering. (b) Change in polarization with temperature along the *c*-axis after poling with an electric field of E = 1.1 kV/cm (adapted with permission from Ref. [81], © (2013) by the American Physical Society).

1.3.2.3 Aeschynite

Aeschynite is a mineral having the general formula AB_2O_6 where *A* is rare-earth or alkaline earth ions, and *B* is transition metal ions. The representative compound is $CaTa_2O_6$, which crystallizes in a centrosymmetric orthorhombic structure (*Pnma*), where the Ca^{2+} and Ta^{5+} cations are coordinated with oxygen ions in eight- and six-coordination, respectively [83,84]. In this structure, the edge-sharing dimers of TaO_6 octahedra share corners to form a three-dimensional framework with Ca^{2+} ions occupying the channels parallel to the *b*-axis. Upon introducing chemical ordering by replacing the Ta_2-ions with two cations of different charges can result in breaking of inversion symmetry because of the rigidity of the edge-shared octahedra [85–87].

Recently, it has been reported that an alternate ordering of Fe^{3+} and W^{6+} ions in $RFeWO_6$ (*R* = Eu, Tb, Dy, and Y) results in the polar structure with the space group $Pna2_1$, which is a sub-group of the centrosymmetric space group *Pnma* [88]. In $RFeWO_6$, the Fe^{3+}

and W^{6+} ions are ordered alternatively because of the significant difference in size and charge of these ions, which is responsible for stabilizing the polar structure. The ordered aeschynite structure of $DyFeWO_6$ is shown in Figure 1.14(a). The Fe-moments in these compounds undergo antiferromagnetic ordering at T_N^{Fe} ~ 15-18 K. Electric polarization is observed at T_N^{Fe}, as shown in Figure 1.14(b). It is also clear that the electric polarization below the magnetic ordering can be switched by external electric field.

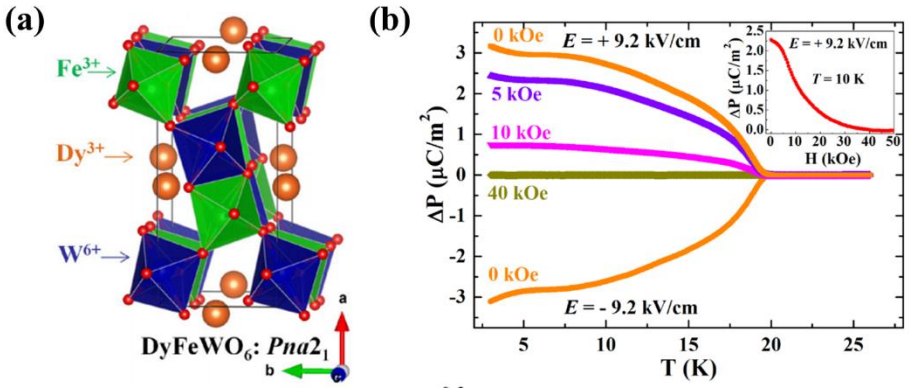

Figure 1.14 (a) Crystal structure of $DyFeWO_6$ showing cation ordering. (b) Temperature evolution of electric polarization ΔP (T) of $DyFeWO_6$ below T_N^{Fe} = 18K (adapted with permission from Ref. [88], © (2017) by the American Physical Society).

1.3.2.4 Corundum oxides and Brownmillerites

A number of polar compounds can be derived from the simple sesquioxide M_2O_3 having the centrosymmetric corundum structure ($R\bar{3}c$). Unlike the simple ABO_3 compounds, the ordered $LiNbO_3$ type (also known as Ni_3TeO_6-type) and ordered ilmenite (Li_2GeTeO_6) form polar structure ($R3$) [89,90]. The ordering pattern is strongly correlated to the charge and size difference of cations involved in chemical ordering. The ordered LNO-type compound Ni_3TeO_6 (NTO) (Figure 1.15(a)) with $R3$ symmetry has been reported to exhibit a spontaneous electric polarization and colossal magnetoelectricity below T_N = 52 K with magnetoelectric switching without hysteresis [91–94]. $AlFeO_3$ adopts a polar orthorhombic structure ($Pna2_1$) where the isovalent cations (Al^{3+} and Fe^{3+}) are ordered in different crystallographic sites with some anti-site disorder. This compound with ferrimagnetic ordering below 250 K has been shown to exhibit magnetoelectric properties [95–97].

The other family of compounds that can be brought under polar oxides is brownmilletrites. Ca_2FeAlO_5 with brownmillerite structure ($Ibm2$) is an antiferromagnet with

a Néel temperature of T_N = 350 K [98,99]. The structure is constituted of an alternate arrangement of (Fe, Al)O_6 octahedra and (Fe, Al)O_4 tetrahedra layers as shown in Figure 1.15(b) [98,100]. In this compound, the magnetic field induced spin-flop transition accompanies anomalies in the electric polarization [51,101]. These results may open a route to realize the magnetoelectric effect in polar oxides.

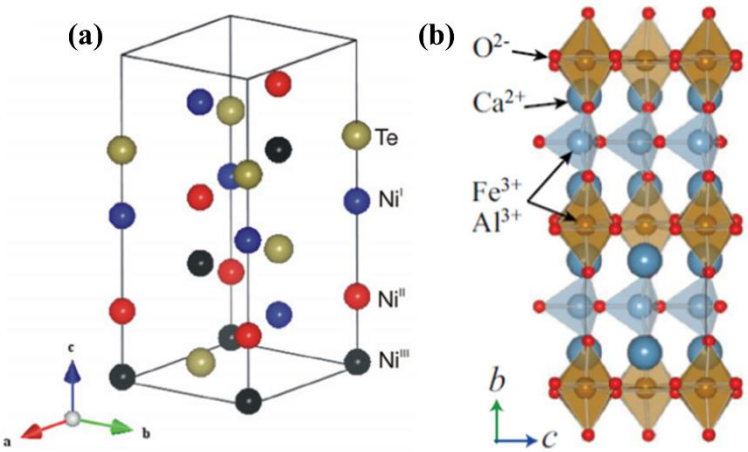

Figure 1.15 (a) Crystal structure of Ni_3TeO_6, where Te and Ni ions stacked along the *c*-axis in an ordered fashion (adapted with permission from Ref. [91], © (2010) by the IOP Publishing, Ltd). (b) Crystal structure of the Brownmillerite Ca_2FeAlO_5 (adapted with permission from Ref. [101], © (2013) by the American Physical Society).

A similar symmetry relationship to diamond-zinc blende exists in the high symmetry ($Fd\bar{3}m$) normal spinel $ZnCr_2O_4$ where the replacement of Zn^{2+} ions by two non-equivalent cations with different oxidation states, Li^+ and Ga^{3+} (In^{3+}, Fe^{3+}), results in a reduction of symmetry to the noncentrosymmetric space group ($F\bar{4}3m$) [102,103]. In the case of trirutile-type fluoride $LiFe_2F_6$ ($P4_2/mnm$), it is reported that the inversion symmetry is broken by charge ordering of Fe^{2+}/Fe^{3+} configuration [104–106]. It is interesting to note that an ordered insertion of oxygen in the centrosymmetric ($P2_1/n$) Ba_2YFeO_5 by the low-temperature topochemical oxidation results in loss of inversion symmetry, leading to the formation of noncentrosymmetric $Ba_2YFeO_{5.5}$ ($Pb2_1m$) [107]. Interestingly, while most of the delafossite oxides $MCrO_2$ (M = Ag and Cu) are centrosymmetric and type-II multiferroic ($R\bar{3}m$) [56,108], the chalcogenide $AgCrS_2$ is polar ($R3m$) and multiferroic [109].

1.3.3 Doubly ordered perovskites

Most of the perovskite oxides are centrosymmetric except those with the second-order Jahn-Teller effect. Recently, an unusual layered ordering of *A*-site cations and rock-salt

ordering of *B*-site cations combined with certain octahedral rotation in perovskite oxides has been reported to stabilize a polar ($P2_1$) structure, and these are called doubly ordered perovskites. These compounds mostly order antiferromagnetically and exhibit a change in polarization below T_N. Therefore, these compounds can be classified under polar magnetic oxides. It is these compounds we have discussed structural and physical properties in the next working chapters. Before that, we present a brief introduction about perovskites, octahedral tilting, different types of ordering in double perovskites, and the background of doubly ordered perovskites.

1.3.3.1 Perovskite and tolerance factor

The perovskite structure is one of the most studied and technologically important in the field of material science. The first known perovskite structure is the mineral $CaTiO_3$. Currently, there are thousands of known examples of materials that adopt perovskite structures. The ideal perovskite structure can be represented as ABX_3, where *A* and *B* are cations, and *X* is the anion. The possibility of substituting almost all the elements in the periodic table at the *A* or *B*-sites increases the ABX_3 perovskite family's compositional space, eventually tailoring the structure and properties. The structure of perovskite can be viewed as a three-dimensional array of corner-sharing BX_6 octahedra where the *A*-site cations present in the 12 coordinate cubooctahedral cavity that is formed between any eight octahedral (BX_6) units, as shown in Figure 1.16.

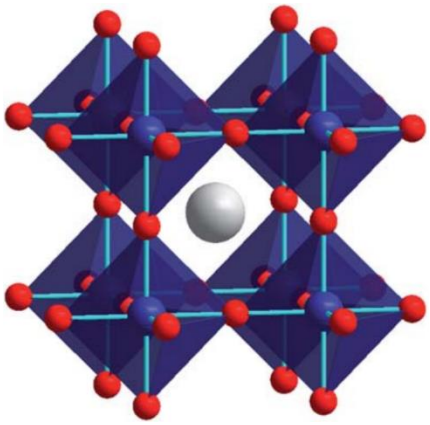

Figure 1.16 The cubic ABX_3 perovskite structure. Gray and blue spheres represent the *A*- and *B*-site cations, respectively (adapted with permission from Ref. [110], © (20103) by the Royal Society of Chemistry).

The ideal perovskite crystallizes in cubic symmetry with space group $Pm\bar{3}m$ when tolerance factor τ = 1. The tolerance factor (τ), a geometric relationship between the length of the unit cell edge, size of the *A*- and *B*-site cations is given by

$$\tau = \left(\frac{R_A + R_X}{\sqrt{2}R_B + R_X}\right)$$

where R_A, R_B, and R_X are the ionic radii of the *A*-, *B*-site cations, and anion, respectively [111]. For more than one ion in the site, the average radii of cations are used.

1.3.3.2 Octahedral distortion or tilting

The majority of perovskites undergo octahedral distortions when the tolerance factor is less than one. This leads to a large number of distorted perovskites in various space groups, but most of them are centrosymmetric. When the size of the *A*-site cation is too small for the cavity formed by the BX_6 octahedral units, these polyhedra will rotate as rigid units. This permits shorter *A*-*X* bonds to form without changing the lengths of the *B*-*X* bonds. Hence, these distortions reduce the coordination number of the *A*-site cation below 12 and reduce the symmetry of the perovskite structure below cubic. In order to maintain the corner sharing connectivity of the BX_6 framework, the rotations of the octahedra must be cooperative. In any given layer of BX_6 octahedra, if the rotation of the one octahedron around the axis is normal to that layer, then all four neighboring octahedra within that layer should rotate in the opposite direction to maintain the connectivity.

There are two types of tilting that occur in the octahedra, in-phase tilting, and out-of-phase tilting, as shown in Figure 1.17. In the case of in-phase tilting, all the octahedra rotate in the same direction going down the axis, while during out-of-phase tilting, the direction of rotation alternates from one to the next layer of octahedra. A convenient shorthand notation developed by Glazer has been used to describe the octahedral rotations in perovskites [112]. In Glazer notation, letters indicate the magnitude of the tilting distortion around each of the crystallographic axes, and a superscript represents whether the octahedra rotations are in-phase (+) or out-of-phase (-) along a particular axis (Figure 1.17). A superscript 0 indicates that there is no tilting around that axis. The notation $a^-a^-c^+$ indicates the equal magnitude of out-of-phase tilting around *a*- and *b*-axes and in-phase tilting around the *c*-axis. The probable space groups which can arise from the different modes of octahedral tilting of aristotype compounds have been determined using group-theoretical analysis [113–115].

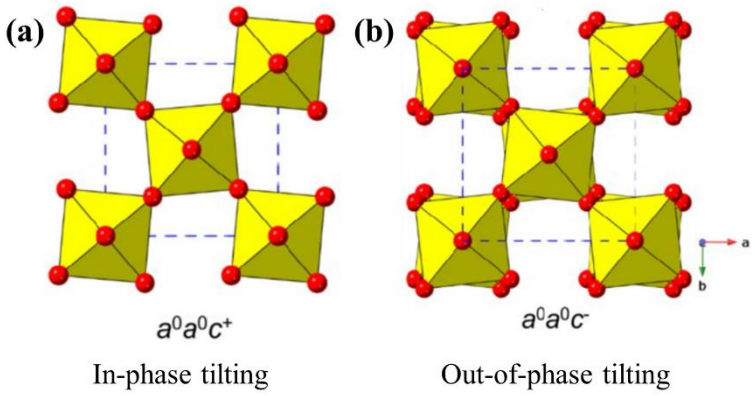

Figure 1.17 The two types of octahedral tilting around a *c*-axis (adapted with permission from Ref. [116], © (2021) by the IUCrJ).

1.3.3.3 Cation ordering in double and doubly ordered perovskites

The substitution of different cations at *A*- and *B*-sites of ABO_3 is known to form a larger number of double perovskites with random or an ordered arrangement at both the site cations. Ordering is favored when there is a sufficient size and charge difference between the two cations. If the size and charge difference between the cations are similar, that will tend to a disordered arrangement. Generally, an ordered arrangement is expected when oxidation state difference of 3 or greater (e.g., Sr_2MgWO_6), while an oxidation state difference of 0 or 1 (e.g., La_2CrFeO_6) mostly leads to a disordered arrangement. In the case of difference of 2, depending on the size difference and bonding preference, fully ordered (e.g., Sr_2YNbO_6), disordered (e.g., Sr_2FeRuO_6), or partly ordered (e.g., Sr_2AlTaO_6) arrangement may result in the different degree of ordering. Substitution of ions at the *A*- and *B*-sites of ABO_3 results in double perovskite structures, i.e., $R_2MM'O_6$ (*R* = lanthanide ions and *M*, *M'* = transition metal ions), R_2CuSnO_6 (*R* = La, Pr, Nd, Sm), La_2CuZrO_6, $CaMnTi_2O_6$, etc., triple perovskites such as $Ba_3Fe_{1.56}Ir_{1.44}O_9$, $Ba_3NiIr_2O_9$, etc., and quadruple perovskites such as $LaMn_3Cr_4O_{12}$ structures, etc., [117–124]. In different types of perovskites, two or more cations of different or same valences are located in the corresponding crystallographic positions, and they might be ordered or disordered. It plays a crucial role in determining the crystal structure and properties of most of these compounds.

Here, we will only discuss ordering in double perovskites. The most commonly observed ordering in double perovskites ($A_2BB'O_6$) is a rock-salt ordering of *B*-site cations. The three simple patterns of ordering that can be seen for either the *A*- or *B*-site cations in

perovskites are rock salt, columnar, and layer ordering, as shown in Figure 1.18. According to the electrostatic point of view, rock salt ordering is most favorable because it keeps the more highly charged cations far apart. Each highly charged *B′* cation has six *B* cations as its nearest neighbors. In comparison, columnar ordering is the next best arrangement as each *B′* cation is surrounded by four *B* and two *B′* nearest neighbors. Layered ordering has the least favorable electrostatic condition because each *B′* cation surrounded by two *B* and four *B′* nearest neighbors.

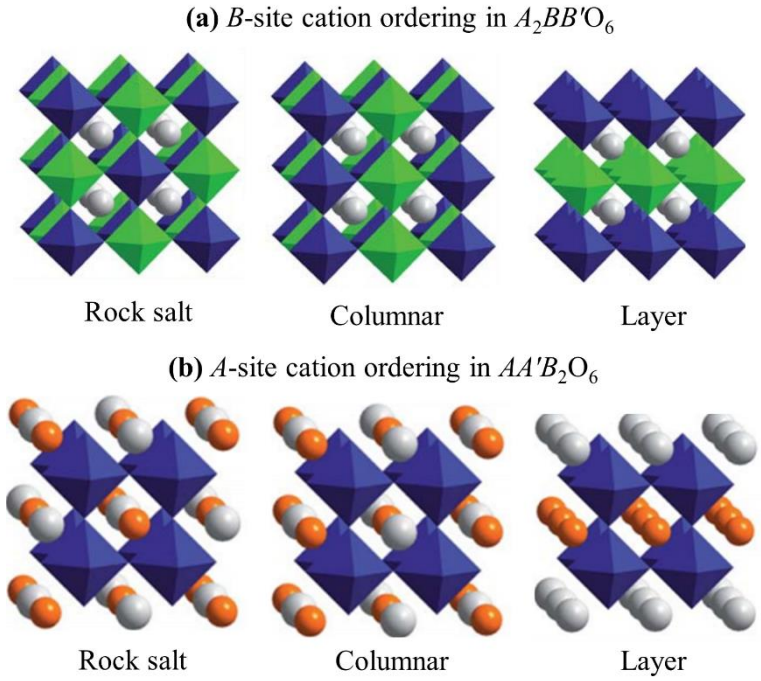

Figure 1.18 (a) Three types of ordering in $A_2BB'O_6$ perovskites where blue and green polyhedra represent *B*-site cations and grey sphere represents *A*-site cations. (b) Three types of ordering in $AA'B_2O_6$ perovskites where orange and grey spheres represent *A*-site cations and blue polyhedra represent *B*-site cations (adapted with permission from Ref. [110], © (20103) by the Royal Society of Chemistry).

Although the combined ordering of both the site cations is rare because of the bonding instabilities and other factors, recently, attention has been turned to class $AA'BB'O_6$ called doubly ordered perovskites. In which *A*-site cations exhibit uncommon layer ordering and *B*-site cations show rock-salt ordering. These compounds with the combinations of combined ordering and octahedral tilting crystalize in polar monoclinic structure. In doubly ordered perovskites, *A*-site cations prefer layer ordering while *B*-site cations prefer most observed rock-salt ordering. Ordering preference of *A*- and *B*-site cations can be understood by considering the bonding aspects.

In the rock-salt ordering of the *B*-site cations, each anion is surrounded by one highly charged *B′* cation and one less charged *B* cation (Figure 1.19(a)), as a consequence, anions can shift toward the *B′* cation and away from the *B* cation to provide ideal bond distance to each and hence to optimize the bonding. In contrast, if *B′* and *B* cations order in a layer arrangement, then three anion environments would be formed, as shown in Figure 1.19(b). One-sixth of the anions are bonded with two of the less charged *B* cation which leads to an under-bonded environment, while another one-sixth of the anions are bonded with highly charged *B′* cation which leads to an over-bonded environment, and only the remaining anions coordinated by one *B′* and one *B* cation could obtain stable environment. The layer arrangement of *B*-site cations violates Paulings's fifth rule, which states that all ions of the same kind should sit in the same environment if possible [110]. This explains the relative rarity of layer ordering of *B*-site cations over rock-salt ordering.

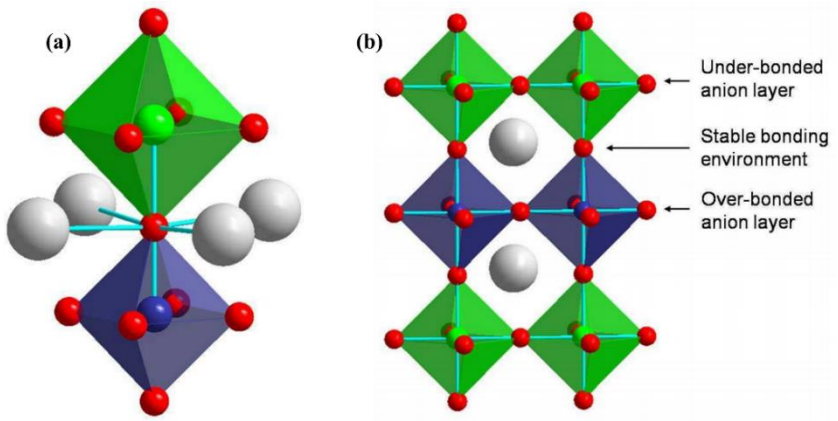

Figure 1.19 (a) A depiction of rock-salt ordering and (b) layer ordering of the *B*/*B′* cations in an $A_2BB'O_6$ perovskite. Blue and green spheres are the *B* and *B′* cations, grey sphere stands for *A*-site cations, and small red spheres are the anions (adapted with permission from Ref. [110], © (20103) by the Royal Society of Chemistry).

In order to understand the *A*-site cation's preference for layered ordering, one needs to analyze the bonding in a similar way. If *A*-site cations exhibit rock-salt ordering, the anion would be at an inversion site coordinated by two *A* cations and two *A′* cations, where it is impossible to move to relieve bond strains resulting from the *A*/*A′* size mismatch (Figure 1.20(a)) [110]. Whereas this problem does not arise in the layered ordering of *A*-site cations because two-thirds of the anions are surrounded by two less charged *A* cations and two highly charged *A′* cations. Now, these anions can shift and obtain an ideal bonding environment. Still, the instability persists because four less charged *A* cations surround one-sixth of the anion, and the other one-sixth anion is surrounded by four highly charged *A′* cations having

under-bonded and over-bonded environment (Figure 1.20(b)). The layer ordering of *A*-site cations is certainly preferred over a rock-salt ordering because, in the former, two-thirds of the anions can obtain a stable bonding environment while none of them can obtain in the later. However, one-thirds of the anions still face a bonding instability, which explains the rarity of the *A*-site cation ordering relative to *B*-site cation ordering.

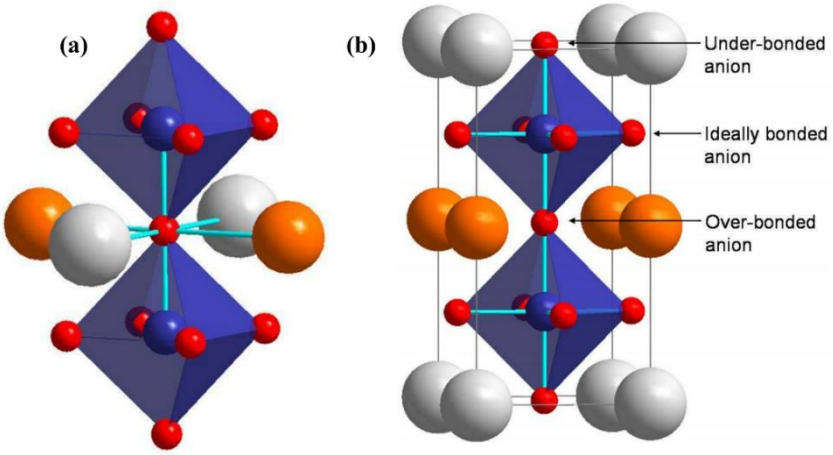

Figure 1.20 (a) A depiction of rock-salt ordering and (b) layer ordering of the *A*/*A′* cations in an $AA'B_2O_6$ perovskite. Grey and orange spheres are the *A* and *A′* cations, blue sphere stands for *B*-site cations, and small red spheres are the anions (adapted with permission from Ref. [110], © (20103) by the Royal Society of Chemistry).

However, the *A*-site layered ordering is observed in the presence of highly charged *B*-site cation (d^0) which stabilizes that by means of second-order Jahn-Teller (SOJT) distortion [125]. When the combined ordering of both site cations occurs in ABO_3, it reduces symmetry from cubic ($Pm\bar{3}m$) to tetragonal ($P4/nmm$). Further, octahedral rotations occur to adopt the size effect of ions and lowers the symmetry, as shown in Figure 1.21. Group theoretical calculations have been carried out by considering combinations of layered ordering (*A*/*A′*), rock-salt ordering (*B*/*B′*), and 12 distinct tilting schemes to predict possible space groups for $AA'BB'O_6$ (Figure 1.21) [125]. Most of these perovskites undergo in-phase titling along *a*- and *b*-axes and out-of-phase tilting along *c*-axis and reduce symmetry to monoclinic ($a^-a^-c^+$) from a parent tetragonal symmetry ($a^0a^0c^0$).

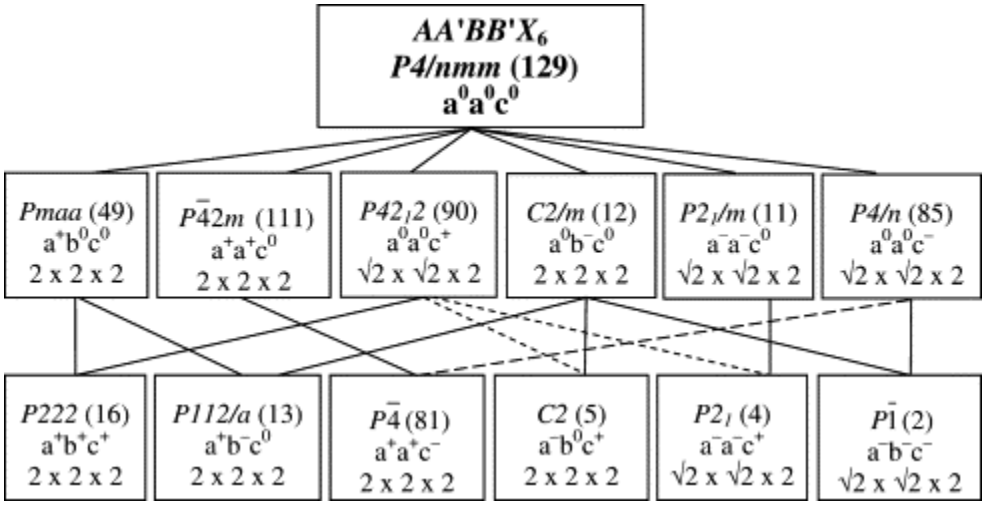

Figure 1.21 A schematic diagram of possible $AA'BB'O_6$ structures predicted by group-theoretical analysis considering the layered ordering of the *A*-site cations, rock-salt ordering of *B*-site cations, and 12 distinct tilting schemes. Each box shows the space group, tilt scheme using Glazer's notation [112], and approximate unit cell dimensions in terms of the cell edge of the undistorted $Pm\bar{3}m$ perovskite. The group-subgroup relationships are denoted by lines, where the solid line indicates possible continuous transition and the dashed lines indicate discontinuous transitions (adapted with permission from Ref. [125], (2006) by the Elsevier Ltd).

1.3.3.4 Background of doubly ordered perovskites

The doubly ordered perovskite structure was first realized in 1984 when $NaLaMgWO_6$ was reported to exhibit rock-salt ordering in *B*-site and a layered ordering in *A*-site. Over the three decades, many such compounds $KLaMgWO_6$, $KLaMnWO_6$, $KLaMgTeO_6$, Na*Ln*$CoWO_6$, Na*Ln*$MnWO_6$, and Na*Ln*$FeWO_6$, etc., were reported to adopt this structure [126–128]. Peculiar superstructures of $NaLaMgWO_6$, $KLaMnWO_6$, and $NaLaCoWO_6$ have been studied through high-resolution TEM studies [129–131]. Further, in these compounds, the stability of ordering of the *A*-site cations was understood by comparing studies on $NaLaMgWO_6$ and $NaLaMgTeO_6$. The long-range order of the Na^+ and La^{3+} was absent when the W^{6+} ion is replaced by the d^{10} Te^{6+} ion [125]. Also, the ordering of cations was found to be synergetic, as *B*-site disordered $NaLaTi_2O_6$ does not show long rage order in *A*-site despite the presence of SOJT cation on the *B*-site [125]. The arrow in Figure 1.22 represents the displacement of the W^{6+} cation towards the Na-layer resulting from SOJT distortion. It allows the under-bonded anions to obtain their ideal valences residing in the Na-layer and stabilizes the overall crystal structure by reducing the distortion caused by layer ordering of *A*-site cations.

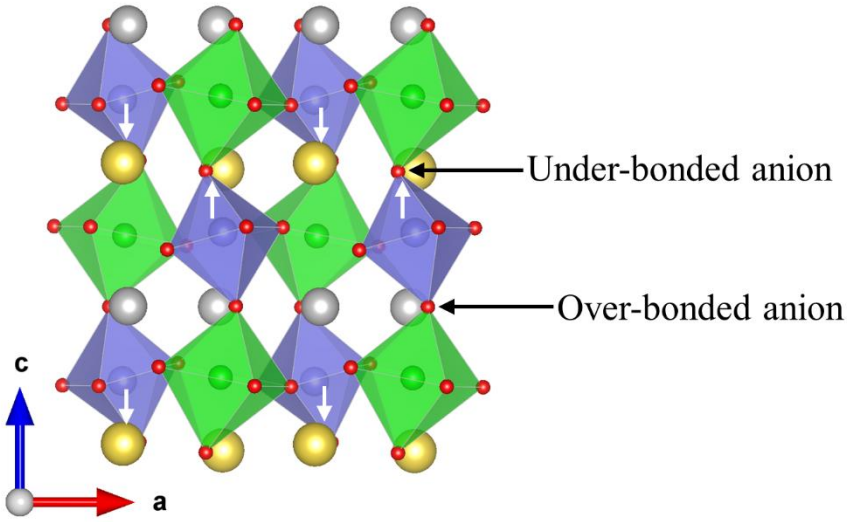

Figure 1.22 Projection of the crystal structure of Na*LnM*WO_6 on the *ac*-plane. Arrows indicate the displacement of the W^{6+} cation from the center of the octahedra towards the under-bonded anion and away from the over-bonded anion. The spheres stand for different ions, Na^+ (yellow), Ln^{3+} (Grey), M^{2+} (blue), W^{6+} (green) and oxygen (red).

Stroppa *et al.* predicted Hybrid Improper ferroelectricity (HIF) in the doubly ordered perovskite $NaLaMnWO_6$ by combining two nonpolar modes of the oxygen octahedra which leads to polar mode [132]. Theoretical studies revealed a high ferroelectric polarization of about 16 $\mu C/cm^2$ in $NaLaMnWO_6$. Further theoretical studies on nine doubly ordered perovskites *AA′*$MnWO_6$ (*A* = Na, K, Rb; *A′* = La, Nd, Y) showed the significance of the size of the rare-earth and alkali ions, where polarization increases with increasing the difference of size of *A*-site cations [133]. Structural, magnetic properties, and magnetic structures of series of compounds Na*Ln*$MgWO_6$, Na*Ln*$MnWO_6$, Na*Ln*$CoWO_6$ (*Ln* = different rare-earth ions), Na*Ln*$FeWO_6$ (*Ln* = La, Nd, Pr, and Sm) were studied [134–138]. Further, experimental investigation on Na*Ln*$MnWO_6$ (*Ln* = La, Nd, and Tb) and Na*Ln*$FeWO_6$ (*Ln* = La, Nd, Pr, and Sm) showed the absence of ferroelectricity at room temperature [137,138]. This could be due to the polycrystalline samples and also difficulties in poling the sintered pellet during measurements. However, the ferroelectricity below magnetic ordering temperature by magnetoelectric coupling was unexplored in many of these series of compounds. It is this motivated us to explore multiferroic properties of series of doubly ordered perovskites.

1.4 Scope of the thesis

As discussed at the beginning of this chapter, the known type-I and type-II multiferroic materials have their limitations because of that not suitable for real applications. In the case of type-I multiferroics, the coupling between ferroelectricity and magnetism is weak because of their different origin. Although type-II multiferroics show strong magnetoelectric coupling, the polarization and magnetic ordering temperature are low. Also, the requirement of complex magnetic structures in type-II limits the number of multiferroic materials. This thesis aims at the magnetic materials which are in polar crystal structure derived from chemical ordering. The advantage of such polar magnets over the type-II multiferroics is that these materials are pyroelectric, and therefore, may not require a poling electric field. Further, they also do not require a complex magnetic structure to break the inversion symmetry. Simple magnetic structures that can couple to the lattice are enough to make these materials magnetoelectric multiferroics. Considering this, we have focused on a completely new series of Ni based doubly ordered perovskites, which are stabilized by a high-pressure synthesis method to investigate the magnetoelectric multiferroic properties. Interestingly, $NaYNiWO_6$ exhibits an unconventional spin density wave (SDW) structure near $T_{N,}$ and with the theoretical collaboration, we understood the formation of SDW through DFT calculations. Subsequently, we have explored doubly ordered perovskites with other transition magnetic cations Co, Fe, and Mn combining with lower size rare-earth cations. Some Co compounds were found to be only pyroelectric where lower size rare-earth cation Ni compounds exhibit switchable change in polarization. In addition, we tried to find many polar oxides, but we could successfully synthesize two polar compounds $LiFeV_2O_7$ and $LiCrAs_2O_7$. The multiferroic property is found in $LiFeV_2O_7$ below magnetic ordering temperature. $LiCrAs_2O_7$ exhibit antiferromagnetic ordering, but no dielectric anomaly is observed at T_N.

References

[1] J. Valasek, Phys. Rev. **17**, 475 (1921).

[2] P. Debye, Phys. Z. **13**, 97 (1912).

[3] B. M. Wul and I. M. Goldman, Compt. Rend. Acad. Sci. URSS **49**, 177 (1945).

[4] S. Miyake and R. Ueda, J. Phys. Soc. Japan **1**, 32 (1946).

[5] L. D. Landau, *I.*, Zh. Eksp. Teor. Fiz. **11**, 19 (1937).

[6] V. L. Ginzburg,J. Phys. USSR **9**, 305 (1945).

[7] H. D. Megaw, *Methuen & Co*, Ltd, London, UK (1957).

[8] M. H. Zhao, D. A. Bonnell, and J. M. Vohs, Surf. Sci. **602**, 2849 (2008).

[9] D. W. Richerson and W. E. Lee, (CRC press, 2018).

[10] D. Segal, (Cambridge University Press, 1991).

[11] H. Schmid, Ferroelectrics **162**, 317 (1994).

[12] K. Aizu, Phys. Rev. B **2**, 754 (1970).

[13] H. Schmid, Ferroelectrics **252**, 41 (2001).

[14] W. Eerenstein, N. D. Mathur, and J. F. Scott, Nature **442**, 759 (2006).

[15] Y. N. Venevtsev, G. S. Zhdanov, S. N. Solov'ev, E. V Bezus, V. V Ivanova, S. A. Fedulov, and A. G. Kapyshev, Kristallografiya **5**, 620 (1960).

[16] S. V Kiselev, Sov. Phys. **7**, 742 (1963).

[17] T. Kimura, T. Goto, H. Shintani, K. Ishizaka, T. Arima, and Y. Tokura, Nature **426**, 55 (2003).

[18] N. Hur, S. Park, P. A. Sharma, J. S. Ahn, S. Guha, and S.-W. Cheong, Nature **429**, 392 (2004).

[19] E. Ascher, H. Rieder, H. Schmid, and H. Stössel, J. Appl. Phys. **37**, 1404 (1966).

[20] M. Fiebig, J. Phys. D. Appl. Phys. **38**, R123 (2005).

[21] J. F. Scott, J. Mater. Chem. **22**, 4567 (2012).

[22] M. M. Vopson, Crit. Rev. Solid State Mater. Sci. **40**, 223 (2015).

[23] V. E. Wood and A. AE, (1974).

[24] D. I. Khomskii, Multiferroic Mater. Prop. Tech. Appl. 1 (2016).

[25] C. Giacovazzo, *Fundamentals of Crystallography* (Oxford University Press, USA, 2000).

[26] B. Wang, *Mechanics of Advanced Functional Materials* (Springer Science & Business Media, 2013).

[27] D. Khomskii, (College. Park. Md). **2**, 20 (2009).

[28] M. Fiebig, T. Lottermoser, D. Meier, and M. Trassin, Nat. Rev. Mater. **1**, 1 (2016).

[29] G. A. Smolenskiĭ and I. E. Chupis, Sov. Phys. Uspekhi **25**, 475 (1982).

[30] J. Wang, J. B. Neaton, H. Zheng, V. Nagarajan, S. B. Ogale, B. Liu, D. Viehland, V. Vaithyanathan, D. G. Schlom, U. V Waghmare, N. A. Spaldin, K. M. Rabe, M. Wuttig, and R. Ramesh, Science (80-.). **299**, 1719 LP (2003).

[31] D. Khomskii, (College. Park. Md). **2**, 20 (2009).

[32] B. B. Van Aken, T. T. M. Palstra, A. Filippetti, and N. A. Spaldin, Nat. Mater. **3**, 164 (2004).

[33] M. Eibschütz, H. J. Guggenheim, S. H. Wemple, I. Camlibel, and M. DiDomenico Jr, Phys. Lett. A **29**, 409 (1969).

[34] C. Ederer and N. A. Spaldin, Phys. Rev. B **74**, 24102 (2006).

[35] J. F. Scott and R. Blinc, J. Phys. Condens. Matter **23**, 113202 (2011).

[36] D. I. Khomskii, J. Magn. Magn. Mater. **306**, 1 (2006).

[37] J. Van Den Brink and D. I. Khomskii, J. Phys. Condens. Matter **20**, 434217 (2008).

[38] N. Ikeda, H. Ohsumi, K. Ohwada, K. Ishii, T. Inami, K. Kakurai, Y. Murakami, K. Yoshii, S. Mori, and Y. Horibe, Nature **436**, 1136 (2005).

[39] A. Ruff, S. Krohns, F. Schrettle, V. Tsurkan, P. Lunkenheimer, and A. Loidl, Eur. Phys. J. B **85**, 1 (2012).

[40] D. Fu, W. Zhang, H. Cai, Y. Zhang, J. Ge, R. Xiong, S. D. Huang, and T. Nakamura, Angew. Chemie Int. Ed. **50**, 11947 (2011).

[41] L. C. Gómez-Aguirre, B. Pato-Doldán, J. Mira, S. Castro-García, M. A. Señarís-Rodríguez, M. Sánchez-Andújar, J. Singleton, and V. S. Zapf, J. Am. Chem. Soc. **138**, 1122 (2016).

[42] G.-C. Xu, W. Zhang, X.-M. Ma, Y.-H. Chen, L. Zhang, H.-L. Cai, Z.-M. Wang, R.-G. Xiong, and S. Gao, J. Am. Chem. Soc. **133**, 14948 (2011).

[43] P. Jain, Theses, Treatises Diss. 3670 (2010).

[44] M. J. Pitcher, P. Mandal, M. S. Dyer, J. Alaria, P. Borisov, H. Niu, J. B. Claridge, and M. J. Rosseinsky, Science (80-.). **347**, 420 (2015).

[45] P. Mandal, M. J. Pitcher, J. Alaria, H. Niu, P. Borisov, P. Stamenov, J. B. Claridge, and M. J. Rosseinsky, Nature **525**, 363 (2015).

[46] T. Nozaki, Y. Shiota, S. Miwa, S. Murakami, F. Bonell, S. Ishibashi, H. Kubota, K. Yakushiji, T. Saruya, and A. Fukushima, Nat. Phys. **8**, 491 (2012).

[47] S. Valencia, A. Crassous, L. Bocher, V. Garcia, X. Moya, R. O. Cherifi, C. Deranlot, K. Bouzehouane, S. Fusil, and A. Zobelli, Nat. Mater. **10**, 753 (2011).

[48] D. Khomskii, *Transition Metal Compounds* (Cambridge University Press, 2014).

[49] S.-W. Cheong and M. Mostovoy, Nat. Mater. **6**, 13 (2007).

[50] T. Kimura, Annu. Rev. Condens. Matter Phys. **3**, 93 (2012).

[51] Y. Tokura, S. Seki, and N. Nagaosa, Reports Prog. Phys. **77**, 76501 (2014).

[52] I. A. Sergienko and E. Dagotto, Phys. Rev. B **73**, 94434 (2006).

[53] H. Katsura, N. Nagaosa, and A. V Balatsky, Phys. Rev. Lett. **95**, 57205 (2005).

[54] M. Fiebig, T. Lottermoser, D. Meier, and M. Trassin, Nat. Rev. Mater. **1**, (2016).

[55] S. Seki, *Magnetoelectric Response in Low-Dimensional Frustrated Spin Systems* (Springer Science & Business Media, 2012).

[56] S. Seki, Y. Onose, and Y. Tokura, Phys. Rev. Lett. **101**, 67204 (2008).

[57] K. Kimura, H. Nakamura, K. Ohgushi, and T. Kimura, Phys. Rev. B **78**, 140401 (2008).

[58] G. Lawes, A. B. Harris, T. Kimura, N. Rogado, R. J. Cava, A. Aharony, O. Entin-Wohlman, T. Yildirim, M. Kenzelmann, and C. Broholm, Phys. Rev. Lett. **95**, 87205 (2005).

[59] S. Park, Y. J. Choi, C. L. Zhang, and S.-W. Cheong, Phys. Rev. Lett. **98**, 57601 (2007).

[60] S. Seki, Y. Yamasaki, M. Soda, M. Matsuura, K. Hirota, and Y. Tokura, Phys. Rev. Lett. **100**, 127201 (2008).

[61] T. Kimura, Y. Sekio, H. Nakamura, T. Siegrist, and A. P. Ramirez, Nat. Mater. **7**, 291 (2008).

[62] K. Taniguchi, N. Abe, T. Takenobu, Y. Iwasa, and T. Arima, Phys. Rev. Lett. **97**, 97203 (2006).

[63] Y. Yamasaki, S. Miyasaka, Y. Kaneko, J.-P. He, T. Arima, and Y. Tokura, Phys. Rev. Lett. **96**, 207204 (2006).

[64] I. A. Sergienko, C. Şen, and E. Dagotto, Phys. Rev. Lett. **97**, 227204 (2006).

[65] Y. J. Choi, H. T. Yi, S. Lee, Q. Huang, V. Kiryukhin, and S.-W. Cheong, Phys. Rev. Lett. **100**, 47601 (2008).

[66] Y. Noda, H. Kimura, M. Fukunaga, S. Kobayashi, I. Kagomiya, and K. Kohn, J. Phys. Condens. Matter **20**, 434206 (2008).

[67] T. Kimura, *Magnetoelectric Hexaferrites*, Annu. Rev. Condens. Matter Phys. **3**, 93 (2012).

[68] T. Kurumaji, S. Seki, S. Ishiwata, H. Murakawa, Y. Tokunaga, Y. Kaneko, and Y. Tokura, Phys. Rev. Lett. **106**, 167206 (2011).

[69] T. Arima, J. Phys. Soc. Japan **76**, 73702 (2007).

[70] M. Gajek, M. Bibes, S. Fusil, K. Bouzehouane, J. Fontcuberta, A. Barthelemy, and A. Fert, Nat. Mater. **6**, 296 (2007).

[71] H. Murakawa, Y. Onose, S. Miyahara, N. Furukawa, and Y. Tokura, Phys. Rev. Lett. **105**, 137202 (2010).

[72] Y. F. Popov, A. P. Pyatakov, A. M. Kadomtseva, G. P. Vorob'ev, A. K. Zvezdin, A. A. Mukhin, V. Y. Ivanov, and I. A. Gudim, J. Exp. Theor. Phys. **111**, 199 (2010).

[73] U. Müller, *Symmetry Relationships between Crystal Structures* (2013).

[74] S. P. McAlister and P. Strobel, J. Magn. Magn. Mater. **30**, 340 (1983).

[75] Y. Wang, G. L. Pascut, B. Gao, T. A. Tyson, K. Haule, V. Kiryukhin, and S.-W. Cheong, Sci. Rep. **5**, 12268 (2015).

[76] J. R. Morey, A. Scheie, J. P. Sheckelton, C. M. Brown, and T. M. McQueen, Phys. Rev. Mater. **3**, 1 (2019).

[77] Y. Li, G. Gao, and K. Yao, Epl **118**, (2017).

[78] T. Kurumaji, Y. Takahashi, J. Fujioka, R. Masuda, H. Shishikura, S. Ishiwata, and Y. Tokura, Phys. Rev. B **95**, 1 (2017).

[79] V. Caignaert, V. Pralong, A. Maignan, and B. Raveau, Solid State Commun. **149**, 453 (2009).

[80] V. Caignaert, V. Pralong, V. Hardy, C. Ritter, and B. Raveau, Phys. Rev. B **81**, 94417 (2010).

[81] V. Caignaert, A. Maignan, K. Singh, C. Simon, V. Pralong, B. Raveau, J. F. Mitchell, H. Zheng, A. Huq, and L. C. Chapon, Phys. Rev. B - Condens. Matter Mater. Phys. **88**, 3 (2013).

[82] V. Kocsis, Y. Tokunaga, S. Bordács, M. Kriener, A. Puri, U. Zeitler, Y. Taguchi, Y. Tokura, and I. Kézsmárki, Phys. Rev. B **93**, 1 (2016).

[83] R. Salmon and J. Grannec, Rev. Chim. Miner. **11**, 71 (1974).

[84] L. Jahnberg, L. S. Hersh, J. M. Toguri, K. Hedberg, and M. Trætteberg, Acta Chemica Scandinavica.

[85] P. Y. and A. Sundaresan, Mater. Res. Express (2019).

[86] S. W. Kim, T. J. Emge, Z. Deng, R. Uppuluri, L. Collins, S. H. Lapidus, C. U. Segre, M. Croft, C. Jin, V. Gopalan, S. V Kalinin, and M. Greenblatt, Chem. Mater. **30**, 1045 (2018).

[87] S. Ghara, F. Fauth, E. Suard, J. Rodriquez-Carvajal, and A. Sundaresan, Inorg. Chem. **57**, 12827 (2018).

[88] S. Ghara, E. Suard, F. Fauth, T. T. Tran, P. S. Halasyamani, A. Iyo, J. Rodríguez-Carvajal, and A. Sundaresan, Phys. Rev. B **95**, 1 (2017).

[89] P. M. Woodward, A. W. Sleight, L.-S. Du, and C. P. Grey, J. Solid State Chem. **147**, 99 (1999).

[90] R. Becker and H. Berger, Acta Crystallogr. Sect. E Struct. Reports Online **62**, 222 (2006).

[91] I. Živković, K. Prša, O. Zaharko, and H. Berger, J. Phys. Condens. Matter **22**, 56002 (2010).

[92] K. Y. Choi, P. Lemmens, E. S. Choi, and H. Berger, J. Phys. Condens. Matter **20**, 505214 (2008).

[93] F. Wu, E. Kan, C. Tian, and M.-H. Whangbo, Inorg. Chem. **49**, 7545 (2010).

[94] L. Zhao, C.-H. Du, and A. C. Komarek, Phys. Status Solidi – Rapid Res. Lett. **11**, 1700073 (2017).

[95] R. Saha, A. Shireen, S. N. Shirodkar, U. V. Waghmare, A. Sundaresan, and C. N. R. Rao, Solid State Commun. **152**, 1964 (2012).

[96] R. Saha, A. Shireen, S. N. Shirodkar, M. S. Singh, U. V Waghmare, A. Sundaresan, and C. N. R. Rao, Inorg. Chem. **50**, 9527 (2011).

[97] P. Kumar, A. Bera, D. V. S. Muthu, S. N. Shirodkar, R. Saha, A. Shireen, A. Sundaresan, U. V Waghmare, A. K. Sood, and C. N. R. Rao, Phys. Rev. B **85**, 134449 (2012).

[98] R. W. Grant, S. Geller, H. Wiedersich, U. Gonser, and L. D. Fullmer, J. Appl. Phys. **39**, 1122 (1968).

[99] A. A. Colville and S. Geller, Acta Crystallogr. Sect. B Struct. Crystallogr. Cryst. Chem. **27**, 2311 (1971).

[100] G. Sharma, D. Kumar, S. Tyagi, V. R. Reddy, R. Rawat, A. K. Sinha, N. P. Lalla, and V. Sathe, J. Alloys Compd. **732**, 358 (2018).

[101] N. Abe, N. D. Khanh, T. Sasaki, and T. Arima, Phys. Rev. B **89**, 54437 (2014).

[102] R. Saha, F. Fauth, M. Avdeev, P. Kayser, B. J. Kennedy, and A. Sundaresan, Phys. Rev. B **94**, 64420 (2016).

[103] R. Saha, R. Dhanya, C. Bellin, K. Béneut, A. Bhattacharyya, A. Shukla, C. Narayana, E. Suard, J. Rodríguez-Carvajal, and A. Sundaresan, Phys. Rev. B **97**, 19905 (2018).

[104] N. N. Greenwood, A. T. Howe, and F. Ménil, J. Chem. Soc. A Inorganic, Phys. Theor. 2218 (1971).

[105] J. L. Fourquet, E. Le Samedi, and Y. Calage, J. Solid State Chem. **77**, 84 (1988).

[106] L. F. Lin, Q. R. Xu, Y. Zhang, J. J. Zhang, Y. P. Liang, and S. Dong, Phys. Rev. Mater. **1**, 2 (2017).

[107] K. Luo, R. D. Johnson, T. T. Tran, P. S. Halasyamani, P. G. Radaelli, and M. A. Hayward, Chem. Mater. **25**, 1800 (2013).

[108] K. Singh, B. Kundys, M. Poienar, and C. Simon, J. Phys. Condens. Matter **22**, 445901 (2010).

[109] K. Singh, A. Maignan, C. Martin, and C. Simon, Chem. Mater. **21**, 5007 (2009).

[110] G. King and P. M. Woodward, J. Mater. Chem. **20**, 5785 (2010).

[111] V. M. Goldschmidt, Naturwissenschaften **14**, 477 (1926).

[112] A. M. Glazer, Acta Crystallogr. Sect. B **28**, 3384 (1972).

[113] C. J. Howard and H. T. Stokes, Acta Crystallogr. Sect. B Struct. Sci. **54**, 782 (1998).

[114] P. M. Woodward, Acta Crystallogr. Sect. B Struct. Sci. **53**, 32 (1997).

[115] M. W. Lufaso and P. M. Woodward, Acta Crystallogr. Sect. B Struct. Sci. **57**, 725 (2001).

[116] J. A. McNulty and P. Lightfoot, IUCrJ **8**, 485 (2021).

[117] D. Choudhury, P. Mandal, R. Mathieu, A. Hazarika, S. Rajan, A. Sundaresan, U. V Waghmare, R. Knut, O. Karis, P. Nordblad, and D. D. Sarma, Phys. Rev. Lett. **108**, 127201 (2012).

[118] M. Azuma, K. Takata, T. Saito, S. Ishiwata, Y. Shimakawa, and M. Takano, J. Am. Chem. Soc. **127**, 8889 (2005).

[119] M. Zhu, Y. Lin, E. W. C. Lo, Q. Wang, Z. Zhao, and W. Xie, Appl. Phys. Lett. **100**, 62406 (2012).

[120] M. Azuma, S. Kaimori, and M. Takano, Chem. Mater. **10**, 3124 (1998).

[121] M. T. Anderson and K. R. Poeppelmeier, Chem. Mater. **3**, 476 (1991).

[122] J. Herrero-Martín, J. Ruiz-Fuertes, T. Bernert, M. Koch-Müller, E. Haussühl, and J. L. García-Muñoz, Phys. Rev. B **97**, 235129 (2018).

[123] T. Ferreira, D. Carone, A. Huon, A. Herklotz, S. A. Stoian, S. M. Heald, G. Morrison, M. D. Smith, and H.-C. zur Loye, Inorg. Chem. **57**, 7362 (2018).

[124] X. Wang, Y. Chai, L. Zhou, H. Cao, C. Cruz, J. Yang, J. Dai, Y. Yin, Z. Yuan, S. Zhang, R. Yu, M. Azuma, and Y. Shimakawa, **087601**, 1 (2015).

[125] M. C. Knapp and P. M. Woodward, J. Solid State Chem. **179**, 1076 (2006).

[126] M. A. Arillo, J. Gomez, M. L. Lopez, C. Pico, and M. L. Veiga, Solid State Ionics **95**, 241 (1997).

[127] M. L. López, M. L. Veiga, and C. Pico, J. Mater. Chem. **4**, 547 (1994).

[128] N. A. Benedek, Inorg. Chem. **53**, 3769 (2014).

[129] S. Garcia-Martin, E. Urones-Garrote, M. C. Knapp, G. King, and P. M. Woodward, J. Am. Chem. Soc. **130**, 15028 (2008).

[130] G. King, S. Garcia-Martin, and P. M. Woodward, Acta Crystallogr. Sect. B Struct. Sci. **65**, 676 (2009).

[131] S. Garcia-Martin, G. King, E. Urones-Garrote, G. Nénert, and P. M. Woodward, Chem. Mater. **23**, 163 (2011).

[132] T. Fukushima, A. Stroppa, S. Picozzi, and J. M. Perez-Mato, Phys. Chem. Chem. Phys. **13**, 12186 (2011).

[133] J. Young, A. Stroppa, S. Picozzi, and J. M. Rondinelli, Dalt. Trans. **44**, 10644 (2015).

[134] P. Zuo, C. V Colin, H. Klein, P. Bordet, E. Suard, E. Elkaim, and C. Darie, Inorg. Chem. **56**, 8478 (2017).

[135] G. King, L. M. Wayman, and P. M. Woodward, J. Solid State Chem. **182**, 1319 (2009).

[136] G. King, A. S. Wills, and P. M. Woodward, Phys. Rev. B - Condens. Matter Mater. Phys. **79**, 1 (2009).

[137] C. De, T. H. Kim, K. H. Kim, and A. Sundaresan, Phys. Chem. Chem. Phys. **16**, 5407 (2014).

[138] J. Blasco, J. A. Rodríguez-Velamazán, G. Subías, J. L. García-Muñoz, J. Stankiewicz, and J. García, Acta Mater. **176**, 53 (2019).

Chapter 2

Experimental techniques

This chapter gives details about sample preparation, characterization, and various experimental techniques used in the present thesis work.

2.1 Sample preparation

2.1.1 High pressure synthesis

In the case of solid-state reaction, to synthesize targeted materials, only a high temperature is not a sufficient condition. The presence of pressure is essential in addition to high temperature to stabilize some of the metastable phases. All the doubly ordered perovskites presented in this thesis were synthesized using cubic anvil type high pressure apparatus with 4.5 GPa pressure and 1000 °C temperature. Trying to synthesize doubly ordered perovskite Na*LnM*WO_6 (*Ln* = Smaller lanthanide ions and *M* = Ni, Co, Mn, and Fe) at high temperature and ambient pressure always generally led to Ln_2WO_6, Na_2WO_4, and *M*O oxides. Because these impurities (Na_2WO_4 and Ln_2WO_6) have more preferences for formation than the expected perovskite phase at ambient pressure. This is related to the requirement of a higher coordination number for alkali and tungsten cations in the perovskite phase compared to the Na_2WO_4 phase, which can be achieved using a high pressure synthesis route. Another factor that leads to impurities at ambient pressure is the small tolerance factor. As the tolerance factor decrease, the larger octahedral distortion that would be required to stabilize the structure is not feasible as it leads to unfavorable shorter O-O distances. But some of these materials with small tolerance factors can be stabilized using high pressure synthesis method. The high pressure apparatus mainly consists of three parts; pressurizing unit, which consists of six identical cubic anvils which are made up of tungsten carbide placed into the die, one temperature controlling unit, and a pressure controlling unit, as shown in Figure 2.1.

To synthesize the targeted materials, at first, we have weighed the stoichiometric amount of ingredients of a total amount of approximately 300-400 mg and grounded thoroughly to make a uniform mixture. The pellet of the grounded mixture was placed in either a cylindrical gold capsule or we can use the BN capsule and sleeve. The sample capsule will then be enclosed with a sleeve and disc, which are made of NaCl (80%) + ZrO_2 (20%). The whole

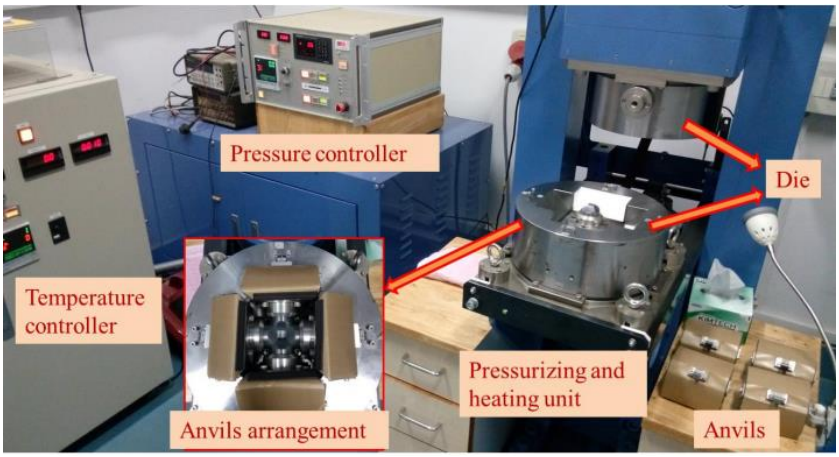

Figure 2.1 High pressure apparatus and its various controlling units, heating and pressurizing unit, and arrangements of anvils between the die.

assembly is inserted into a cylindrical graphite heater and will be kept into the pyrophyllite stone. For the electrical conduction purpose, the molybdenum electrodes are placed on top and bottom along with stainless steel rings. In the present synthesis method, pyrophyllite of dimension 15mm × 15 mm × 15 mm which has a hole of diameter 8mm through one pair of faces, was used. Pyrophyllite stones were preheated at 700 ℃ before using for the synthesis to remove any moisture or water of crystallization. The above-discussed sample assembly is shown in Figure 2.2.

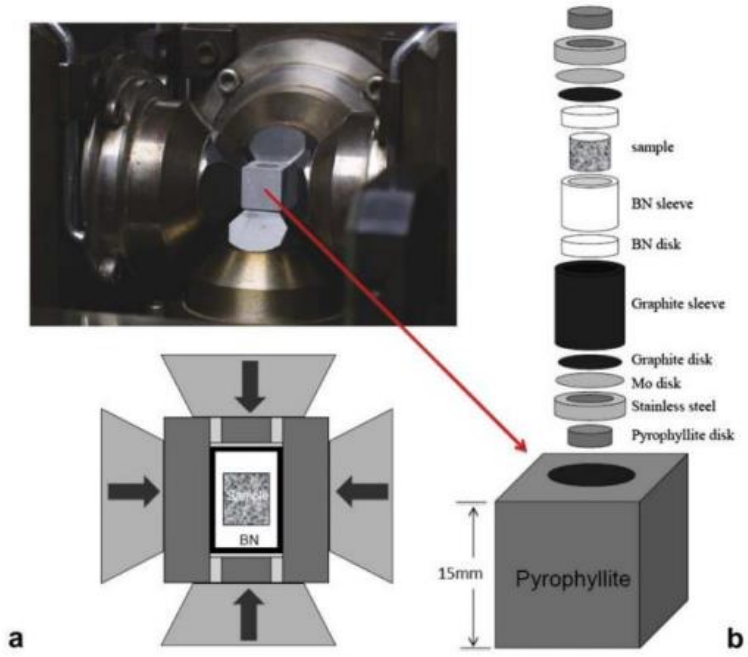

Figure 2.2 (a) Top, view of cubic type anvils between the dies. Bottom, pyrophyllite stone with the anvils (side view). (b) The cell assembly inside pyrophyllite. (adapted from Ref. [1])

The pyrophyllite stone with cell assembly is kept inside the cubic anvils with careful alignment to achieve a uniform compression limit of the pyrophyllite for all six anvils. During the reaction, the required pressure (≤ 4.5 GPa) was reached slowly, and once it is stabilized, the temperature is raised gradually using the temperature control unit up to 1000 ℃. Both the pressure and temperature are maintained during dwelling for the sample reaction. Further, the temperature can be quenched by turning off the heating to stabilize the high pressure metastable phase, or it can be cooled slowly to room temperature. Finally, once the reaction is at room temperature, the pressure is reduced slowly to the atmospheric pressure, and the sample is taken out. Since the reaction rate is higher in the presence of high pressure, we maintained a reaction dwelling time of a maximum of one hour to synthesize all the compounds. The calibration of temperature was carried out by inserting a thermocouple manually, and it is recorded with respect to the heater power provided from the temperature controller unit. The calibration curve was used to decide the required power for any reaction temperature. Similarly, calibration of pressure was carried out using Bi-metal resistance measurement with pressure. The calculated resistance against load was applied to indicate the pressure-induced structural transition of Bi at 2.5 GPa.

2.1.2 High temperature solid state synthesis

We have used high temperature solid state reaction method to synthesize the materials in the last chapter of the thesis. In this method, the stoichiometric mixtures of starting materials are ground thoroughly for a long time. The powder mixture (or pellet) is heated at high temperatures for several hours with intermittent grindings. The high temperature gives the necessary energy for the diffusion of ions during the reaction [2]. The important factor in the reaction mechanism is the diffusion coefficient (D), which is in Fick's law [3], $J = -D \frac{d\varphi}{dx}$, where J is the flux of diffusing elements and $\frac{d\varphi}{dx}$ is the concentration gradient. The diffusion coefficient (D) depends on the temperature of the reaction. In the case of high temperature solid-state synthesis, the diffusion coefficient should be greater than 10^{-12} cm^2/s. The temperature required for the proper solid-state reaction should be at least 2/3 of the melting point of one or more precursor materials, as suggested by Tamman's rule [4]. However, this rule cannot be followed, particularly if the materials are volatile in nature. Usually, the reaction mixtures are kept at temperatures as high as 500 ℃ to 1500 ℃ in order to maximize the diffusion length and also to occur a reaction at an appreciable rate.

2.2 Structural analysis

The structural characterization was carried out by the Rietveld refinement of powder X-ray and neutron diffraction data.

2.2.1 Powder X-ray and neutron diffraction

X-ray diffraction is the primary and extensively used technique in structural analysis. Powder X-ray diffraction experiments are carried out on materials with a laboratory Rigaku SmartLab diffractometer and PANalytical Empyrean alpha 1 diffractometer (monochromatic CuKα1). Mainly, a laboratory powder X-ray diffractometer consists of an X-ray tube, a sample platform, and a detector. When X-rays are incident on the polycrystalline sample, which consists of grains oriented randomly in all possible directions, some of the X-rays will be scattered by the atoms of the first layer or plane (Figure 2.3), and the remaining X-rays will pass through the first layer and will be scattered by the succeeding layers.

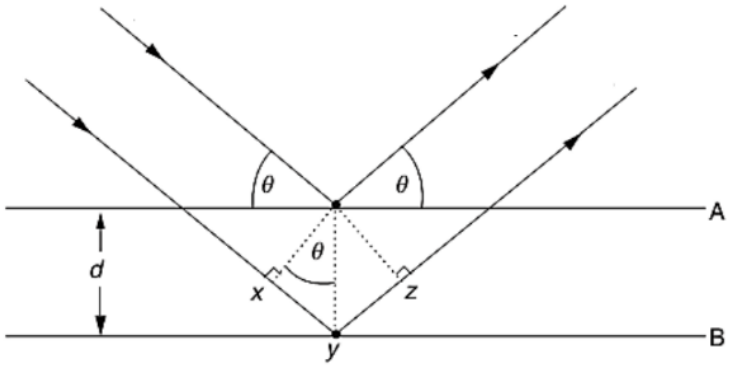

Figure 2.3 Schematic of X-ray diffraction – Bragg's law (Adapted from Ref. [2]).

Scattering of X-rays occurs because the spacing between the atomic layers or crystallographic planes is in the order of the wavelength of incident X-ray radiation. When the scattered X-rays are coming out from the two different planes with the same phase, constructive interference occurs, resulting in an X-ray diffraction peak. Meanwhile, if the two scattered X-rays are out of phase, no such peak will appear in the X-ray diffraction pattern. Interaction of X-rays with the samples causes constructive interference only when Bragg's law is satisfied [2,5].

$$2d\ sin\theta = \lambda$$

where 'd' is the spacing between the consecutive planes, 'λ' is the wavelength of X-rays used, and 'θ' is the incident angle of the X-ray, as shown in Figure 2.3. Thus, when Bragg's law is satisfied by some particular sets of planes, the X-ray diffraction pattern appears, which consists

of many peaks at different 2θ positions, and which is unique for individual materials. Thus, the diffraction peaks with respect to the distance between the planes (d) give information about the phase, unit cell dimension, and the purity of the sample. The different information can get by treating X-ray diffraction data accordingly. The phase purity of a known compound can be checked by matching its X-ray diffraction data with the pattern available in many databases such as Inorganic Crystal Structure Database (ICSD). Similar way, the phase of the impurity present in some compounds can be identified.

In some compounds, due to the overlap of two or more close peaks of laboratory X-ray diffraction patterns, it may be difficult to index the peaks using this technique. In that case, the synchrotron X-ray diffraction experiments are suitable to resolve this issue, which has the ability to tune the wavelength. Because of the higher intensity of the synchrotron X-ray beams can provide high intense peaks with a very good resolution and improved signal to noise ratio. Therefore, synchrotron X-ray diffraction experiments are really helpful to determine complex structures with accurate structural parameters. Sometimes neutron diffraction is necessary for the crystal structure characterization when the compounds have light elements such as oxygen, carbon, lithium, hydrogen, etc. Since the X-ray interaction takes place by the electron cloud only it has a limitation of detecting light elements in the crystal structure. Neutron diffraction is a powerful technique in which neutrons interact with the nucleus of the atom, and hence it helps to determine the position of the light atoms more accurately. Since neutron intrinsic magnetic moment can interact with the moment of a magnetic atom, it can be used to determine the magnetic structure of the compound in addition to its crystal structure. Neutron diffraction experiments are carried out in a WISH diffractometer at RAL, Didcot, UK [6]. This neutron beamline has a high flux and resolution. This diffractometer is very much essential in our case because of the less quantity of the sample from high pressure synthesis.

2.2.2 Rietveld refinement

Rietveld refinement is the most useful method for the analysis of X-ray and neutron diffraction data to obtain complete structural parameters of the materials [7]. In this technique, an X-ray or neutron diffraction pattern is compared with a calculated pattern by considering a certain number of parameters. While during refinement, the intensity at each point of the experimental data (y_{io}) is compared with the corresponding calculated point (y_{ic}) in the model, which is done by minimizing a residual function S through the least square process. The residual function S is given by [5,7],

$$S = \sum_i w_i \, |y_{io} - y_{ic}|^2$$

Where w_i is a weight factor, which depends on the standard deviation in the peak intensity and background intensity. The calculated intensity at a point can be given by [5],

$$y_{ic} = s \sum_k m_k \, L_k |F_k|^2 G(\Delta\theta_{ik}) + y_{ib}$$

Where s is a scale factor, m_k is the multiplicity factor, L_k is the Lorentz polarization factor for reflection k, F_k is the structure factor, $G(\Delta\theta_{ik})$ is the reflection profile function where $\Delta\theta_{ik} = 2\theta_i - 2\theta_k$ and $2\theta_k$ is the calculated position of the Bragg peak, y_{ib} is the background intensity.

The two important factors mentioned above are the structure factors (F_k) and the reflection profile function $G(\Delta\theta_{ik})$.

The structure factor F_{hkl} (= F_k for k^{th} reflection) is given by,

$$F_{hkl} = \sum_{j=1}^{m} N_j f_j \, e^{2\pi(hx_j + ky_j + lz_j)}$$

$$|f|^2 = e^{\frac{-B\sin^2\theta}{\lambda^2}}$$

Where f is the atomic form factor and B is the Debye-Waller temperature factor.

The peak shape (reflection profile function) depends on several parameters such as the radiation source, detector, wavelength distribution, etc. Various functions can be used for the peak shape function. Among them, the pseudo-Voigt (pV) function is widely used since it is a combination of Lorentzian and Gaussian parts, which gives a good fitting.

$$pV = \eta L + (1 - \eta)G; \text{ with } 0 \leq \eta \leq 1$$

where L is the Lorentzian function and G is the Gaussian function, which is given by,

$$L = \frac{C_1^{\frac{1}{2}}}{\pi H_k} \left\{ 1 + C_1 \left(\frac{\Delta\theta_{ik}}{H_k} \right)^2 \right\}^{-1}$$

$$G = \frac{C_0^{\frac{1}{2}}}{\sqrt{\pi} H_k} e^{-C_0 \left(\frac{\Delta\theta_{ik}}{H_k} \right)^2}$$

Where C_0 and C_1 are constants and H_k is the full width at half maxima (FWHM) of the k^{th} reflection.

The FWHM (H_k) for Gaussian and Lorentzain peak function are given by [5],

$$(H_k)_G = (U \tan^2\theta + V \tan\theta - W)^{1/2}$$

$$(H_k)_L = X \tan\theta + \frac{Y}{Cos\,\theta}$$

The parameters *U, V, W,* and *X, Y,* can be refined during pattern matching of the diffraction data.

In the refinement process, the background can be selected manually or as a polynomial function of 2θ [5], as

$$y_{ib} = \sum_n a_n (2\theta_i)^n$$

This background can be refined while pattern matching by refining the coefficient a_n.

The refinement quality can be decided by the values of some following parameters (*R*-factors) [5,7]. These are,

$$R_p(\text{profile}) = \frac{\sum |y_{io} - y_{ic}|}{\sum y_{io}}$$

$$R_{wp}\ (\text{Weighted profile}) = \left(\frac{Wi\,(y_{io} - y_{ic})^2}{\sum w_i y_{io}^2}\right)^{1/2}$$

$$R_{pE}\ (\text{expected}) = \left\{\frac{N-P}{\sum w_i y_{io}^2}\right\}^{1/2}$$

The overall quality of the fitting can be judged by the χ^2 parameter, which should approach 1 as refinement progresses.

$$\chi^2\ (\text{Goodness of fit}) = \left(\frac{R_{wp}}{R_E}\right)^2 = \frac{\sum w_i (y_{io} - y_{ic})^2}{(N-P)}$$

Where N is the number of profile points, and P is the number of refined parameters.

From a technical point of view, the Rietveld refinement is carried out in three steps. Initially, the pattern matching is performed in which the lattice parameters and shape (FWHM) parameters (*U, V, W,* and/or *X, Y,* and asymmetry parameters) are refined. Background points are refined after completing pattern matching. In the next step, a probable structural model contains atomic position should be added in order to fit the experimental data. At the final stage, the bond lengths and bond angles are obtained using bond valence sum calculation. The structural refinement was performed using the 'Full-Prof' software package [8] and in some

cases for magnetic structure determination through Time-Of-Flight data where 'JANA 2006' software has been utilized [9]. The crystal structures were drawn using Vesta software [10].

2.3 Physical property measurements

2.3.1 DC magnetization

The basic principle of magnetization measurement is based on Faraday's law of induction. This law states that the induced voltage in a closed circuit is equal to the rate of change of magnetic flux enclosed by the circuit. The law is given by the following equation:

$$V = -n\frac{d\phi}{dt} = -nA\frac{dB}{dt}$$

Where V is the induced voltage, ϕ is the magnetic flux through a coil of n turns with area A, B is the magnetic field.

The magnetic measurements of all the compounds are carried out with a Magnetic Property Measurement System (MPMS3-SQUID), Quantum Design, USA. The schematic diagram of different parts of the MPMS3 is shown in Figure 2.4(a) [11]. The important fundamental unit of the MPMS3 is a Superconducting Quantum Interference Device (SQUID), which has high sensitivity to measure the sample's magnetic moment. SQUID contains thin insulating layers sandwiched between two superconducting layers from two parallel Josephson junctions, which is an integral part of a dc-SQUID, as shown in Figure 2.4(b). During magnetization measurement, the sample is made to move through the superconducting detection coil, which induces a change in flux passing through it. Such a change in magnetic flux generates a change in the persistent current in the detection coil. Since SQUID is an extremely sensitive linear current to voltage converter, the change in current in the detection coil causes the corresponding change in output voltage, which is proportional to the magnetic moment of the sample. Thus the sample magnetic moment is measured. Two possible different modes are available for the magnetization measurements: Vibrating sample magnetometer (VSM) mode and dc scan mode. In VSM mode, the sample vibrates sinusoidally up and down with very high frequency, while in dc scan mode, the sample is moved up and down uniformly instead of oscillating. Therefore, dc scan mode is always preferred for more reliable data. Both sample and the superconducting magnet is contained in Dewar and cooled with liquid Helium. The helium cryostat is used to control the sample temperature in the system. The sample is mounted on a quartz sample holder with the help of a stand, which has a mirror for centering

the sample position. Then the quartz sample holder is attached to the sample probe and inserted into the sample chamber of the SQUID.

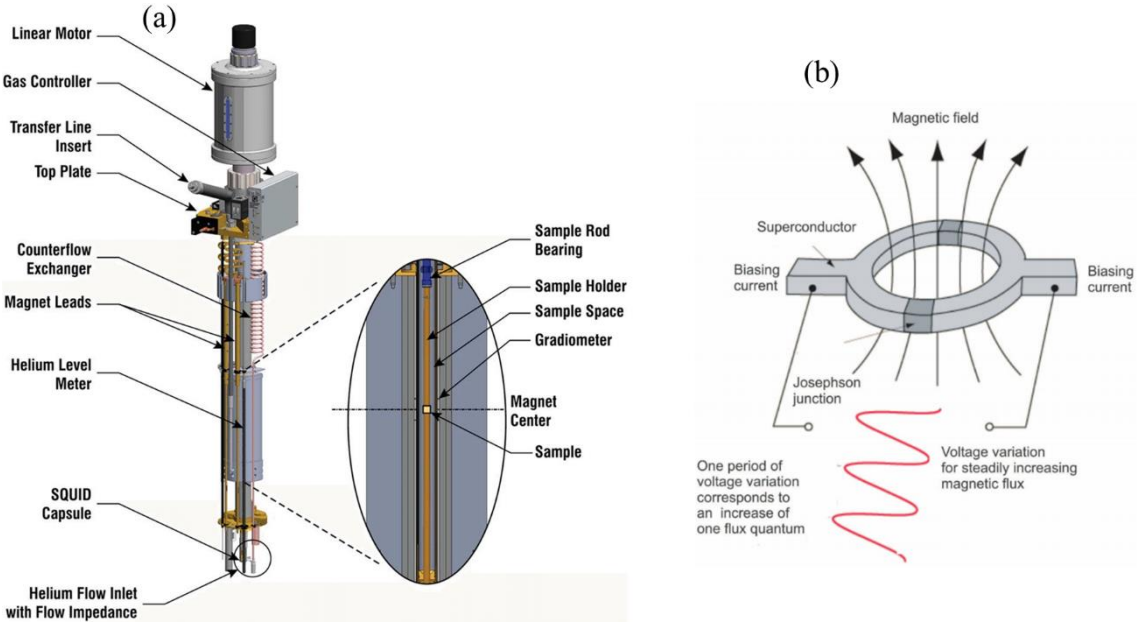

Figure 2.4 (a) Different parts of MPMS3 system (adapted from Ref. [11]). (b) Principle of SQUID magnetometer.

The magnetic measurements of samples are usually done in two ways, i.e., fixed field temperature-dependent measurement and fixed temperature field sweep measurements. Temperature-dependent measurements are carried out in two methods, e.g., Zero Field Cooled (ZFC) and Field Cooled (FC). In Zero Field Cooled (ZFC) measurement, the sample is cooled in the absence of field, and data is recorded in the presence of a constant field with warming. For Field Cooled (FC) measurement, a sample is cooled down in the presence of a constant magnetic field, and the moment is recorded during warming in the presence of the field. For a fixed temperature field sweep measurement, a constant temperature is maintained, and a sample magnetic moment is recorded with an oscillating external magnetic field. The magnetization measurements can be carried out within the temperature range: 1.8 K – 400 K with the application of a magnetic field varying from 0 T to 7 T.

2.3.2 Heat Capacity

Specific heat measurements are performed by heat capacity option in Physical Property Measurement System (PPMS), Quantum Design. A schematic of the specific heat option is

shown in Figure 2.5. Specific heat of a sample at a particular temperature is determined by relaxation technique. The sample chamber should be maintained in a high vacuum (10^{-6} torr using cryopump) so that the heat cannot dissipate. During heat capacity measurements, a cycle of consecutive heating and cooling of the sample is carried out. Initially, a known amount of heat is provided to the sample for a constant time, and then the sample is allowed to cool for the same time. The temperature response is recorded during both the heating and cooling cycle, and the program available in MultiVu software fits the temperature response for the full cycle with a model and finally provides the heat capacity of the sample [12]. Before the sample heat capacity measurement, only addenda measurement is carried out. For that, a small amount of Apiezon grease is applied to the puck sample platform. After the addenda measurement, the sample (small pellet with approximate geometry ~2.5 mm × 2.5 mm × 0.5 mm) is placed on the addenda, which holds the sample and makes a good thermal contact of the sample to the calorimeter puck. The total heat capacity measured includes the sample, grease, and sample platform. Then the sample heat capacity is obtained by subtracting the heat capacity of the addenda from the total heat capacity automatically by the MultiVu software of PPMS.

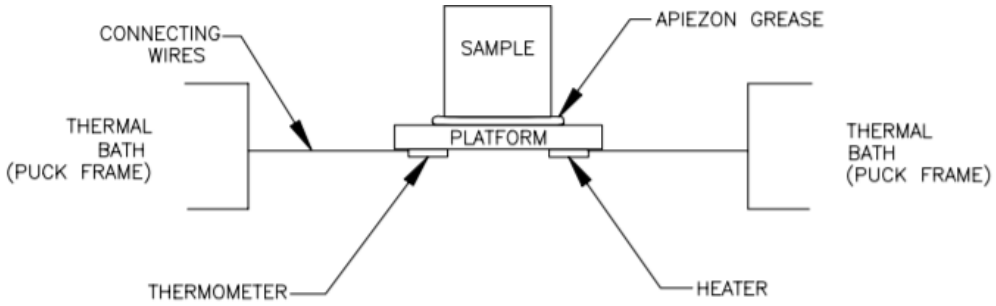

Figure 2.5 Sample platform in PPMS heat capacity option (adapted from Ref. [12]).

Generally, the heat capacity data shows a peak at the long-range magnetic ordering temperature or corresponding to structural transition where a change of entropy happens at the phase transitions. The change in magnetic entropy associated with the long-range magnetic ordering can be calculated by subtracting lattice contribution from total heat capacity. The lattice contribution can be obtained by measuring the heat capacity of an isostructural nonmagnetic sample or by using a Debye-Einstein model. Heat capacity measurement is a very important measurement for some cases to observe the magnetic ordering transition where the overall magnetization is much larger because of the large contribution from the paramagnetic moment, which will be discussed in some of the compounds in the thesis chapters.

2.3.3 Dielectric properties

To determine the dielectric constant, the sample is made into parallel plate shapes. Electrical contacts are given using copper wire and silver paste on both flat surfaces of the sample. We have used PELCO high-performance silver paste for electrical data collection. Dielectric properties are measured with an Agilent LCR meter (model no. E4980A). The dielectric constant is a complex quantity,

$$\varepsilon_r = \varepsilon_r' - \varepsilon_r''$$

$$\text{loss} = \tan(\delta) = \frac{\varepsilon_r''}{\varepsilon_r'}$$

ε_r' and ε_r'' are the real and imaginary parts of the dielectric constant, respectively. The real part of the dielectric constant (ε_r') specifies the charge storing capacity of the dielectric media. Whereas the imaginary part (ε_r'') specifies the dielectric loss, which is usually high in the less insulating materials.

The real dielectric constant is given by,

$$\varepsilon_r' = \frac{d}{\varepsilon_0 A} C$$

where, ε_0 is the permittivity of free space (8.854×10^{-12} Fm^{-1}), A is the area, and d is the distance of the parallel plate capacitor. The dielectric constant is obtained by measuring impedance Z of the material under an electric field ($E_0 \sin wt$), the capacitance C (complex) is determined by [13],

$$C = \frac{1}{iwZ}$$

Here, the impedance of the material is measured in the Agilent LCR meter by the auto-balancing bridge method (Figure 2.6(a)) [13]. The voltage (V_x) across the terminal High and ground and the voltage V_r across the range resistor R_r and ground are measured and maintaining the Low terminal at zero volts. The impedance of the material (DUT) is calculated by [13],

$$\frac{V_x}{Z_x} = I_x = I_r = \frac{V_r}{R_r}$$

$$Z_x = \frac{V_x}{I_x} = R_r = \frac{V_x}{V_r}$$

Temperature and magnetic field dependent dielectric constant measured in PPMS with the help of a multifunctional probe (shown in Figure 2.6(b)) supplied by Quantum Design, USA.

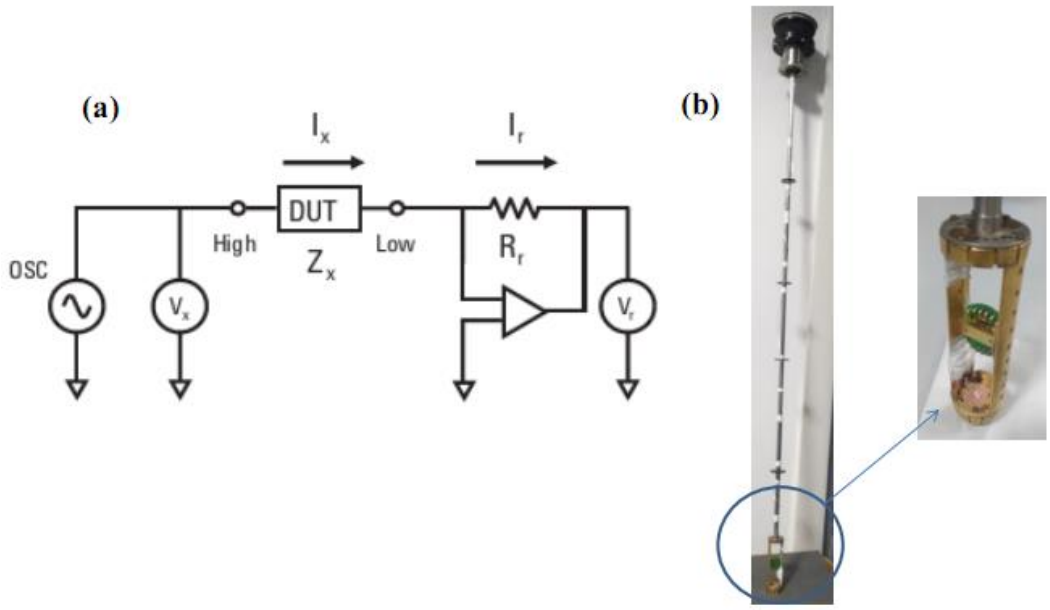

Figure 2.6 (a) An auto-balancing bridge method used for impedance measurements. Adapted from [13]. DUT (device under test) represents the sample. (b) Multifunctional probe for dielectric and pyroelectric current measurements in PPMS.

2.3.4 Pyroelectric current measurements

The electric polarization of ferroelectric materials can be obtained by measuring pyroelectric current across the ferroelectric ordering temperature. The pyroelectric current exhibits an asymmetric peak at the ferroelectric transition. During pyroelectric current measurements, the sample is cooled in the presence of an electric field across the transition temperature. Afterward, the electric field is removed, and the electrodes are kept short for a sufficiently long time in order to remove stray charges. With the help of an electrometer, the current is recorded while warming the sample. The value of the electric polarization is small in the case of magnetoelectric multiferroic materials compared to conventional ferroelectrics. In some cases, pyrocurrent peak remains below the background noise level. In that case, in order to detect a very small polarization, a high heating rate is required during pyroelectric current measurement. The amplitude of the pyroelectric current peak depends on the warming rate. The electric polarization $P(T)$ is obtained by integrating the pyroelectric current $I(T)$ data against the measurement duration,

$$P(T) = \frac{1}{A}\int Idt$$

Since the sample is poled across the ferroelectric transition, the small electric field is sufficient to polarize the material, and a small polarization can be detected, which may not be possible in conventional P-E loop measurement. Because of comparatively less polarization in the case of multiferroic materials, percurrent measurement is a standard protocol for polarization measurement. The switching polarization of ferroelectric materials can be measured by reversing the poling electric field. Determining the electric polarization from pyroelectric current measurements may mislead in polycrystalline materials [14]. A ferroelectric material exhibit a sharp asymmetric peak in the pyroelectric data. But, sometimes pyroelectric measurement shows broad and symmetric peaks which is due to thermally stimulated depolarization current (TSDC) from free or trapped charges of the samples [15,16]. Such peaks should not be ascribed to the intrinsic polarization (ferroelectric transition). The peaks from TSDC can be distinguished from ferroelectric transition by measuring them under different warming rates. The peak due to TSDC shifts to higher temperature with increasing warming rates, while if the peaks are from ferroelectric transition, it doesn't shift with increasing warming rate [16].

In this thesis, ferroelectricity of materials below magnetic ordering temperature is probed by two methods above discussed conventional pyroelectric current measurement and dc-biased current measurement. The second method clearly distinguishes the peak from ferroelectricity and TSDC [17]. During dc-biased current measurement, the sample is cooled below transition temperature without applying an electric field. Current is then measured while warming the sample in the presence of an electric field. In the case of true pyroelectric current peak (intrinsic ferroelectric transition), the dc-biased current shows two peaks – one upward peak related to the polarization of the ferroelectric dipoles and a subsequent downward peak arises from the depolarization of these polarized dipoles. However, this double peak structure is not observed in the case of extrinsic TSDC peaks. Dc-biased current measurement is very much helpful to distinguish extrinsic origin, particularly in polycrystalline samples. Pyroelectric current and dc-biased current measurements are carried out in PPMS with a Keithley 6517A electrometer.

2.3.5 *P*(*E*) hysteresis loop measurement

For a ferroelectric material, the electric polarization is measured conventionally by a polarization (*P*) versus electric field (*E*). The *P*(*E*) loop measurement is carried out using a Radiant Technology precision workstation, which is based on the Sawyer-Tower circuit, which

is shown in Figure 2.7(a). In *P*(*E*) loop measurement, a triangular voltage pulse with a given frequency is applied to the sample. Since the sample is connected in series with a known capacitor (sense capacitor) of capacitance C_1, the same charge (Q) will be accumulated in the sample and in the sense capacitor, which can be determined by measuring the voltage over the known capacitor. The electric polarization (P) in the sample (with area A) can be obtained as,

$$C = \frac{Q}{V}$$

$$P = \frac{Q}{A} = \frac{C_1 V_1}{A}$$

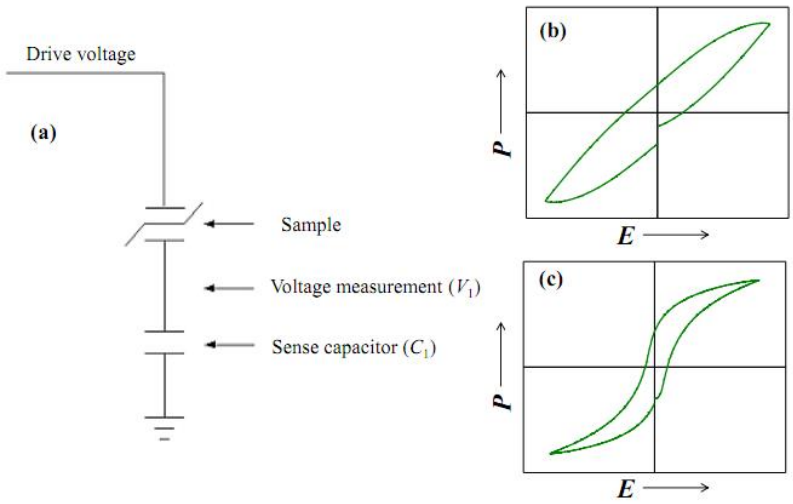

Figure 2.7 (a) A basic Sawyer-Tower circuit, (b) a leaky *P*(*E*) hysteresis loop, (c) a proper ferroelectric *P*(*E*) hysteresis loop measured in $BaTiO_3$.

It is very important to know that sometimes the observed hysteresis loop, as shown in Figure 2.7(b), may not be intrinsic [18]. The hysteresis may appear due to the sample's resistive and capacitive character, which often shows a lossy banana loop which can occasionally be misinterpreted as a ferroelectric loop. Also, if the ferroelectric material is itself not highly insulating, the material will not take enough voltage; therefore, it is difficult to measure the conventional *P*(*E*) loop. The proper ferroelectric loop is shown in Figure 2.7(c), where saturation of polarization is observed. To measure intrinsic ferroelectric polarization and to avoid the leakage contribution, an alternative *P*(*E*) loop measurement is introduced, which is called a Double Wave method (DWM) or positive-up-negative-down (PUND) method [19].

References

[1] P. M. Shirage, K. Miyazawa, M. Ishikado, K. Kihou, C. H. Lee, N. Takeshita, H. Matsuhata, R. Kumai, Y. Tomioka, T. Ito, H. Kito, H. Eisaki, S. Shamoto, and A. Iyo, Phys. C Supercond. **469**, 355 (2009).

[2] A. R. West, *Solid State Chemistry and Its Applications*, 2nd ed. (John Wiley & Sons, 2014).

[3] R. C. Ropp, Solid *State Chemistry* (Elsevier, 2003*)*.

[4] N. K. C. Muniraju, *Crystal and Spin Structure and Their Relation to Physical Properties in Some Geometrical and Spin Spiral Multiferroics*, Vol. 44 (Forschungszentrum Jülich, 2012).

[5] C. Giacovazzo, *Fundamentals of Crystallography* (Oxford University Press, USA, 2000).

[6] L. C. Chapon, P. Manuel, P. G. Radaelli, C. Benson, L. Perrott, S. Ansell, N. J. Rhodes, D. Raspino, D. Duxbury, E. Spill, and J. Norris, Neutron News **22**, 22 (2011).

[7] H. M. Rietveld, J. Appl. Crystallogr. **2**, 65 (1969).

[8] J. Rodriguez-Carvajal, in *Satellite Meeting on Powder Diffraction of the XV Congress of the IUCr*, Vol. 127 (Toulouse, France:[sn], 1990).

[9] *Crystallographic Computing System JANA2006: General Features* , Zeitschrift für Kristallographie - Crystalline Materials .

[10] K. Momma and F. Izumi, J. Appl. Crystallogr. **41**, 653 (2008).

[11] *Magnetic Property Measurement System - MPMS 3 User's Manual (Quantum Design)*.

[12] *Physical Property Measurement System - Heat Capacity Option - User's Manual (Quantum Design)*.

[13] M. Honda, *The Impedance Measurement Handbook: A Guide to Measurement Technology and Techniques. Hauptw* (Hewlett-Packard Company, 1990).

[14] M. Maglione and M. A. Subramanian, Appl. Phys. Lett. **93**, 32902 (2008).

[15] S. W. S. McKeever and D. M. Hughes, J. Phys. D. Appl. Phys. **8**, 1520 (1975).

[16] Y. Kohara, Y. Yamasaki, Y. Onose, and Y. Tokura, Phys. Rev. B **82**, 104419 (2010).

[17] C. De, S. Ghara, and A. Sundaresan, Solid State Commun. **205**, 61 (2015).

[18] J. F. Scott, J. Phys. Condens. Matter **20**, 21001 (2007).

[19] M. Fukunaga and Y. Noda, J. Phys. Soc. Japan **77**, 64706 (2008).

Chapter 3

Structural, magnetic, multiferroic properties of Na*Ln*NiWO$_6$ (*Ln* = Y, Dy-Lu) and unconventional spin density wave (SDW) structure of NaYNiWO$_6$*

Summary

The multiferroic properties of a doubly ordered perovskites Na*Ln*NiWO$_6$ (*Ln* = Y, and Dy-Lu) are demonstrated. Using X-ray and neutron diffraction studies (Y), we have shown that these compounds crystallize in a polar monoclinic ($P2_1$) structure, where they exhibit an unusual combination of the layered *A*-site cation ordering and *B*-site rock-salt ordering. Long-range antiferromagnetic ordering of Ni^{2+} spins at T_N ~ 18 – 23 K accompanied with a dielectric anomaly. The change in electric polarization (ΔP) is observed below magnetic ordering temperature. Analysis of neutron diffraction data for NaYNiWO$_6$ at 20 K reveals an unconventional spin density wave structure with the propagation vector, $\mathbf{k_i}$ = (0.471(2), 0, 0.491(4)) and a commensurate collinear spin structure with $\mathbf{k_c}$ = (0.5, 0, 0.5) below 18 K. Further, we probed the formation of unconventional spin density waves (SDWs) by evaluating the spin-exchanges of NaYNiWO$_6$ based on DFT calculations and analyzing the nature of the spin frustration in NaYNiWO$_6$. A double-peak structure in the heat capacity data of Na*Ln*NiWO$_6$ (*Ln* = Dy-Lu) suggested the presence of an incommensurate and commensurate magnetic phase transition similar to NaYNiWO$_6$. The observed polarization at T_N could be due to the possible enhancement of high temperature polarization expected from the magnetoelastic coupling.

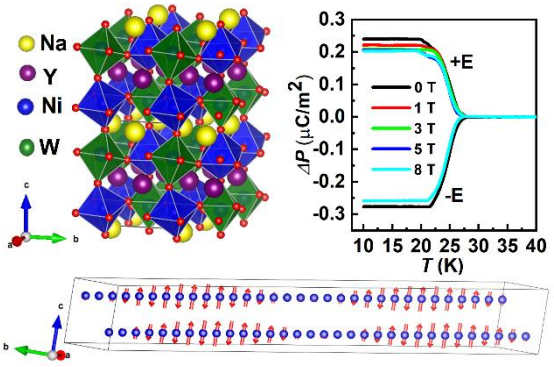

….

*Paper based on this work is published in Chem. Mater, **32**, 5641 (2020), Inorg. Chem. **59**, 17856 (2020) © 2020 by the American Chemical Society, and J. Magn. Magn. Mater. **540**, 168412 (2021) © 2021 by the Elsevier Ltd.

3.1 Introduction

Similar to simple perovskites, most of the double perovskites crystallize in centrosymmetric structure except few polar double perovskites, such as Pb_2MnWO_6, Bi_2NiMnO_6, and $Bi_2Mn_{4/3}Ni_{2/3}O_6$ [1–4], where the presence of stereochemical active cation at the *A*-site drive the system to polar structure, and the *B*-site cations provide magnetism as discussed in chapter 1. Thus, these double perovskites belong to type-I multiferroics. Recently, an unusual combination of the layered ordering of *A*-site cations and rock-salt ordering of *B*-site cations in $NaLaMnWO_6$ has been shown to exhibit polar $P2_1$ structure [5]. Such an unusual ordering of the *A*-site cations is primarily stabilized by highly charged second-order Jahn-Teller (SOJT) distortion of the $W^{6+}(d^0)$ cation. Theoretical studies on $NaLaMnWO_6$ revealed that the stability and amplitudes of the two non-polar rotation modes and induced polar mode cause the spontaneous ferroelectric polarization, which is predicted to be as large as 16 $\mu C/cm^2$ [6]. Further investigation shows that the size of the *A*-site cation plays a crucial role in terms of electrical polarization, with a large increase of the latter with the difference in the ionic size of the *A*-site cations [6,7]. Several compounds belonging to this family of oxides have been reported and can be classified under polar magnetic oxides [5,8–12]. However, there is no experimental report on the existence of ferroelectricity in the paramagnetic state of these compounds. In this chapter, we synthesized and characterized the new series of polar ($P2_1$) compounds, Na*Ln*$NiWO_6$ (*Ln* = Y, Dy-Lu) containing Ni^{2+} ions, and show that these compounds exhibit multiferroic properties below the antiferromagnetic ordering of Ni^{2+} ions. The magnetic spin structure of $NaYNiWO_6$ is a spin density wave just below T_N with $\mathbf{k_i}$ = (0.471(2), 0, 0.491(4)), and changes to a simple collinear magnetic structure with $\mathbf{k_c}$ = (0.5, 0, 0.5), below 18 K. Further, with the help of DFT calculation we understood the formation of the unconventional spin density wave structure of $NaYNiWO_6$.

3.2 Experimental section

3.2.1 Synthesis

The Na*Ln*$NiWO_6$ compounds with *Ln* = Y, Dy-Lu were prepared by high pressure and high temperature synthesis using, $Na_2WO_4{\cdot}2H_2O$ (preheated at 150 °C), Ln_2O_3 (preheated at 950 °C), NiO, and WO_3 as starting materials. Stoichiometric amounts of the starting materials were ground and pressed into a cylindrical pellet and wrapped in a thin gold foil and kept in an enclosure prepared from NaCl and ZrO_2 mixture which was covered with a graphite heater.

Molybdenum disc and stainless-steel ring were placed on both sides of the heater, and the whole assembly was inserted into the pyrophyllite cube used as a pressure transmitting medium. The pressure was first increased to 4.5 GPa and heated to 1000 ^{0}C. After one hour, the sample was quenched directly to room temperature, and then the pressure was released slowly.

3.2.2 Characterization

Powder X-ray diffraction was carried out with a PANalytical Empyrean alpha-1 diffractometer using monochromatized Cu Kα_1 radiation, and the data were acquired in the 2θ range 10-120^o for Rietveld refinement, which was performed using FullProf suite program [13,14]. The neutron powder diffraction measurements were carried out on the WISH diffractometer located at the ISIS pulsed neutron and muon facility of the Rutherford Appleton Laboratory (UK) [15]. The data were collected in the temperature range of 1.5-100 K using an Oxford instrument cryostat. Rietveld refinement of neutron diffraction data was performed using the JANA2006 program [16]. Group theoretical calculations were performed with the help of the ISOTROPY and ISODISTORT software [17]. Second-harmonic generation (SHG) measurements were done on Na*Ln*NiWO$_6$ (*Ln* = Y, Dy, Ho) samples at room temperature using a modified Kurtz-nonlinear optical system with a pulsed Nd:YAG laser (λ = 1064 nm). The technicalities of apparatus and procedure have already been reported in the literature [18,19].

DC magnetization measurements were carried out with a Magnetic Property Measurement System (MPMS3-SQUID), Quantum Design, USA. Heat capacity data were recorded with a Physical Property Measurement System (PPMS, Quantum Design). Temperature dependent dielectric and pyroelectric measurements were carried out with an Agilent E4980A LCR and Keithley 6517A electrometer, respectively. For all electrical measurements, PELCO silver paste was used to make electrodes. During pyroelectric measurements, the samples were poled with an electric field (± E), and to remove any stray charges, the electrodes were shorted for 15 min. The current was recorded while warming with a rate of 15 K/min because of the small value of the polarization. During these measurements, temperature and magnetic were controlled through PPMS. DC-biased current was measured after cooling the sample to the lowest temperature without any poling field and recording the current during warming the sample at the rate of 10 K/min under an applied electric field using Keithley 6517A electrometer.

3.3 Results and discussion

3.3.1 Experimental results on $NaYNiWO_6$

3.3.1.1 Crystal structure

Room temperature X-ray powder diffraction pattern could be best fitted with the polar $P2_1$ space group, which is derived from the undistorted doubly ordered structure $P4/nmm$, and characterized by the octahedral tilt system $a^-a^-c^+$ in Glazer notation [20]. The refined XRD pattern at room temperature and the structural parameters are given in Figure A-1.3.1 and Table A-1.3.1. To further confirm the non-centrosymmetric nature of $NaYNiWO_6$, we have performed SHG studies at room temperature, which is found to be SHG active under a 1064 nm laser. The laser intensity is around 0.53 times of alpha-SiO_2 for $NaYNiWO_6$, confirming the polar nature of this compound. Since oxygen positions cannot be determined accurately by X-ray diffraction, we have analyzed the neutron data collected at 100 K by Rietveld refinement using the program JANA2006, and the refined pattern is given in Figure 3.1. The corresponding structural details are given in Table 3.1. A small amount of Y_2WO_6 and NiO were present as impurity phases, which were included in the refinement. However, we could not index the peak at 3.3 Å with any known impurity phase.

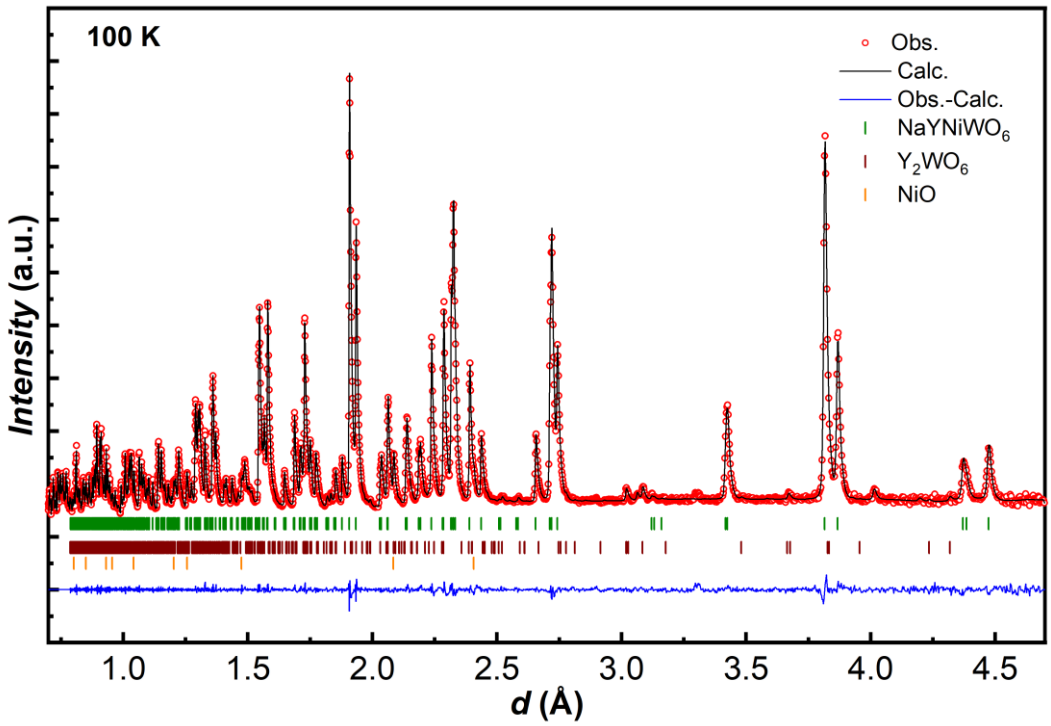

Figure 3.1 Rietveld refined neutron data of $NaYNiWO_6$ collected at 100 K from the high-resolution WISH bank with an average $2\theta = 152.8^{o}$.

Table 3.1 Structural parameters of $NaYNiWO_6$ at 100 K from the refinement of NPD data.

Atom	Wyckoff position	*x*	*y*	*z*	U_{iso}(Å^2)	Occ.
Na	2*a*	0.2545(4)	0.1992(5)	0.0159(3)	0.0015(4)	1.0
Y	2*a*	0.2682(2)	0.3044(3)	0.5033(1)	0.0222(2)	1.0
Ni	2*a*	0.7409(2)	0.2672(2)	0.2488(1)	0.0128(1)	1.0
W	2*a*	0.7461(4)	0.2500	0.7627(2)	0.0021(1)	1.0
O(1)	2*a*	0.5637(3)	0.5293(3)	0.6840(2)	0.0074(2)	1.0
O(2)	2*a*	0.5246(2)	0.5545(3)	0.3026(2)	0.0115(3)	1.0
O(3)	2*a*	-0.0578(3)	-0.0669(4)	0.2112(2)	0.0044(2)	1.0
O(4)	2*a*	-0.0706(3)	-0.0544(3)	0.7901(2)	0.0055(3)	1.0
O(5)	2*a*	0.8456(3)	0.2165(3)	0.5076(2)	0.0151(3)	1.0
O(6)	2*a*	0.6617(3)	0.2833(4)	-0.0132(2)	0.0069(2)	1.0

Space group: $P2_1$; a = 5.31362(5) Å, b = 5.48659(5) Å, c = 7.73727(6) Å, β = 90.202(9)º. Vol.: 225.55 Å^3; GOF = 1.52, R_p = 1.37 (%), R_{wp}= 1.75 (%).

The crystal structure obtained from the structural data for $NaYNiWO_6$ is shown in Figure 3.2, in which each NiO_6 octahedron shares all its corners with other WO_6 units in an ordered arrangement typical of rock-salt ordering, while Na and Y cations are arranged in layers alternatively between the layers of *B*-site octahedra, along the *c*-axis.

Selected bond lengths and bond angles obtained from the refinement of the crystal structure are given in Table 3.2. Careful inspection of Ni-O and W-O bond lengths suggest that the WO_6 octahedra are highly distorted, with the W-O(6) bond shorter (1.829(1) Å) than the W-O(5) one (2.074(1) Å), indicating the displacement of W^{6+} cations from the center of the octahedra towards the layer with the monovalent Na^+ cations. The displacement of W^{6+} ions are due to SOJT, and it is usually observed for highly charged d^0 cations in octahedral coordination as it has been reported in other W compounds, e.g., WO_3 and Pb_2MnWO_6 [1,2,21,22]. SOJT is favored when the energy gap between the highest occupied molecular orbital (HOMO; ligand 2p-nonbonding orbitals) and the lowest unoccupied molecular orbital (LUMO; metal t_{2g} orbitals) is small, and the mixing of these orbitals are symmetry forbidden in the undistorted phase. In this case, a shift of the metal atom from the center of the octahedron allows the mixing of these orbitals with a concomitant energy gain. The shift of the metal atom from the center of the octahedra results in a lowering of the filled HOMO energy while the energy of empty LUMO increases, and therefore, it lowers the overall energy of the structure [23]. All the Ni-O bond distances are approximately equal to 2 Å with almost undistorted octahedra.

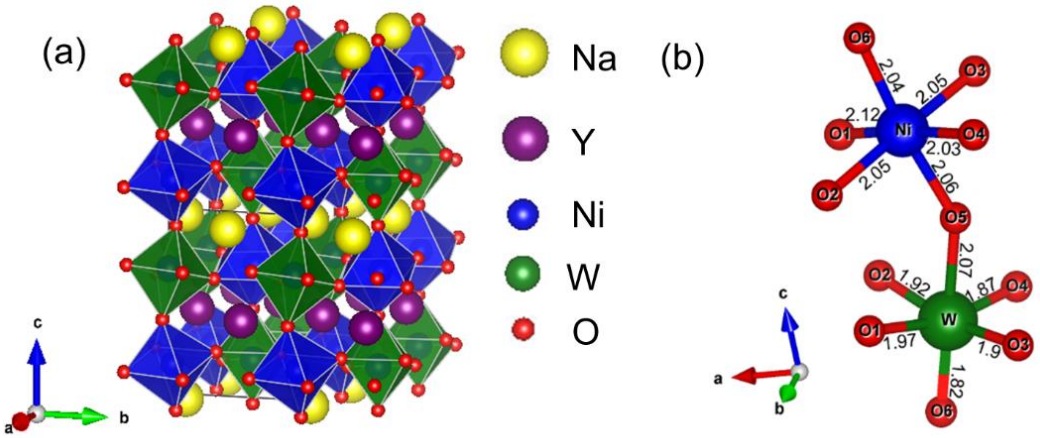

Figure 3.2 (a) Crystal structure of $NaYNiWO_6$, where *A*-site cations (Na and Y) exhibit layered ordering and *B*-site cations (Ni and W) exhibit rock-salt ordering with distorted NiO_6 and WO_6 octahedra. (b) Octahedral coordination of Ni^{2+} and W^{6+} cations surrounded by oxygen with different Ni-O and W-O bond lengths.

The calculated octahedral distortion parameter Δd of both the octahedra ($\Delta d \times 10^{-3}$ = 3.733 for W^{6+} cation and 0.537 for Ni^{2+} cation) indicates that WO_6 octahedra are highly distorted by the effect of SOJT compared to NiO_6 octahedra. The monoclinic structure with space group $P2_1$ results from the antiphase rotation of the octahedra with respect to both *a*- and *b*-axes and in-phase rotation with respect to *c*-axis according to tilt scheme $a^-a^-c^+$ in Glazer's notation, which results in all Ni-O-W bond angles being smaller than 180º, as shown in Table 3.2. The calculated bond valance sums (BVS) show expected oxidation states for the cations and anions [24]. Also, BVS calculations reveal the underbonding of O(6) ions and overbonding of O(5) ions, which is consistent with WO_6 octahedral distortion.

Table 3.2. Selected bond lengths, angles, and bond valence sums (BVS) for $NaYNiWO_6$ at 100 K.

Bond lengths (Å)			Bond angles (deg)		Bond valence sums	
Ni	O(1)	2.126(1)	Ni-O(1)-W	139.85(4)	Na	1.26(3)
	O(2)	2.059(1)	Ni-O(2)-W	143.94(5)	Y	2.73(5)
	O(3)	2.077(1)	Ni-O(3)-W	150.59(5)	Ni	2.15(4)
	O(4)	2.044(1)	Ni-O(4)-W	149.67(5)	W	5.8(1)
	O(5)	2.063(9)	Ni-O(5)-W	147.18(4)	O(1)	1.84(6)
	O(6)	2.049(8)	Ni-O(6)-W	153.00(4)	O(2)	1.98(5)
W	O(1)	1.970(1)			O(3)	1.91(5)
	O(2)	1.926(1)			O(4)	2.05(7)
	O(3)	1.901(1)			O(5)	1.86(4)
	O(4)	1.870(1)			O(6)	2.10(4)
	O(5)	2.074(1)				
	O(6)	1.829(1)				

3.3.1.2 Magnetic properties

Temperature dependence of magnetization data *M(T)* measured under zero-field-cooled (FC) and field-cooled (FC) conditions with an applied magnetic field of 1000 Oe for $NaYNiWO_6$ is shown in Figure 3.3(a). The heat capacity data $C_p(T)$ measured under the zero applied field is given in the right axis of Figure 3.3(a). Both *M(T)* and $C_p(T)$ data indicate a long-range antiferromagnetic transition of Ni^{2+} ions at T_N = 21.5 K. In addition to the peak at T_N in $C_p(T)$ data, and there is a small shoulder around 18 K. We show later that these two peaks correspond to incommensurate and collinear magnetic transitions, respectively. Isothermal magnetization curves of $NaYNiWO_6$ measured at 3 and 30 K as a function of the magnetic field are shown in Figure 3.3(b). These results are consistent with the antiferromagnetic and paramagnetic nature of the sample, respectively.

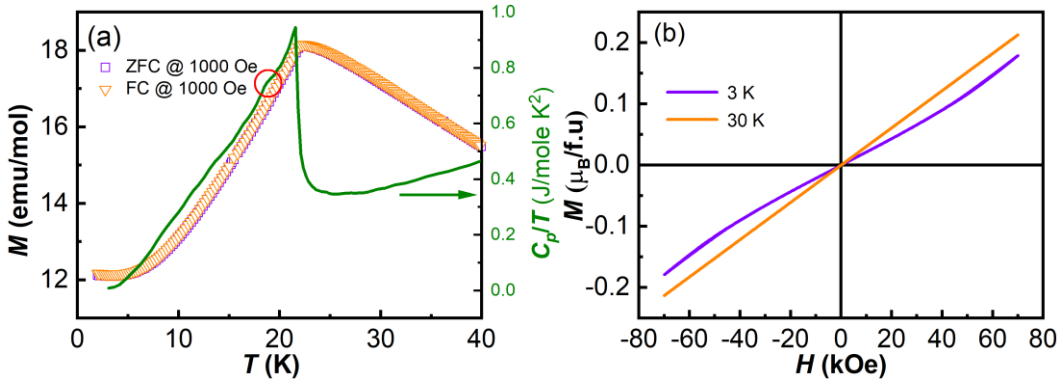

Figure 3.3 (a) Zero-field-cooled (FC) and field-cooled (FC) magnetization data of $NaYNiWO_6$ as a function of temperature measured under a magnetic field of 1000 Oe and heat capacity divided by temperature on the right axis of the Figure at 0 T. (b) Magnetic field dependent magnetization *M*(*H*) at 3 K and 30 K.

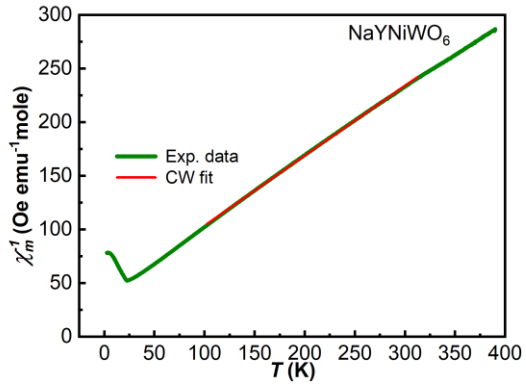

Figure 3.4 Inverse susceptibility ($1/\chi_{mol}$) as a function of temperature.

Temperature dependent inverse susceptibility ($1/\chi_m$) in the high temperature paramagnetic region follows a Curie-Weiss behavior as shown in Figure 3.4. The obtained effective magnetic moment (μ_{eff}) is 3.36 μ_B/Ni, corresponding to the calculated spin only contribution of Ni^{2+} ions. The negative value of Curie-Weiss temperature (-49.76 K) is consistent with the antiferromagnetic ordering.

3.3.1.3 Magnetic structure

The compound $NaYNiWO_6$ was chosen for the neutron diffraction experiment because it does not contain any neutron-absorbing element and the only magnetic element present in the compound is Ni^{2+}. Long scans were collected at 100 K, 30 K to determine the crystal structure in the paramagnetic state and at 1.5 K to determine the magnetic ground state. Several short collection scans were carried out between 4 K and 20 K with a step size of 2 K. The NPD at 100 K and 30 K are well fitted with the $P2_1$ space group. On cooling, two small magnetic diffraction peaks appeared just below T_N, around 8.8 Å, which on further cooling became a single prominent peak at ~ 18 K, as marked in Figure 3.5.

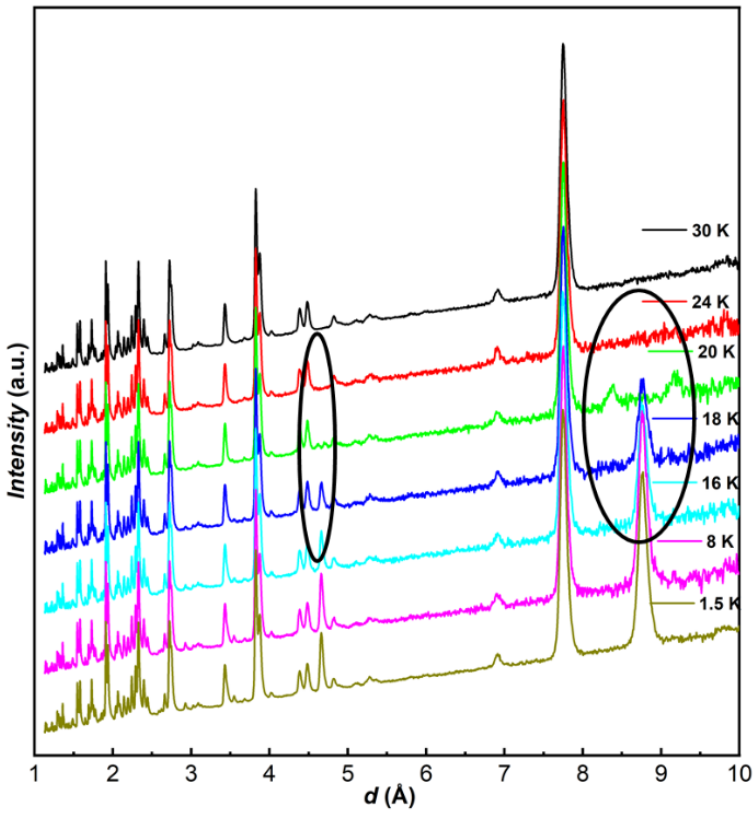

Figure 3.5 Neutron powder diffraction patterns of $NaYNiWO_6$ for selected temperatures.

This suggests a change in the magnetic structure at ~ 18 K, as indicated by the double peak in heat capacity data. At 20 K, the magnetic satellites were indexed by the incommensurate **k**-vector (0.471(2), 0, 0.491(4)) and at lower temperatures (1.5 K ≤ T ≤ 18 K), the magnetic peaks can be indexed by the commensurate **k**-vector (0.5, 0, 0.5).

ISODISTORT was used to perform group theoretical calculations to determine the possible magnetic space groups of the ordered phases. Starting from the magnetic ground state at 1.5 K, the collected diffraction data can be well modeled with the $B[a]2_1$ magnetic space group corresponding to the mA2 irreducible representation. The Rietveld plot is shown in Figure 3.6, which shows a good agreement between the observed and calculated data. The best fit is achieved when refining the magnetic moments along both *a*- and *c*- directions. The magnitude of the *b*-component was negligible compared to the other two, and the removal of the latter did not degrade the refinement. The collinear refined magnetic structure at 1.5 K is presented in Figure 3.7(a). This magnetic structure has moment components of M_x = 0.25(2) μ_B and M_z = 1.88(1) μ_B with the total magnetic moment of 1.89(2) μ_B close to the theoretical value of 2 μ_B for Ni^{2+} ion. The evolution of the magnetic moment of Ni^{2+} as a function of temperature (Figure 3.7(b)) follows a mean-field power-law behavior, $m(T) = m_0(1 - T/T_N)^{\beta}$ with a critical exponent β = 0.17(1) [25].

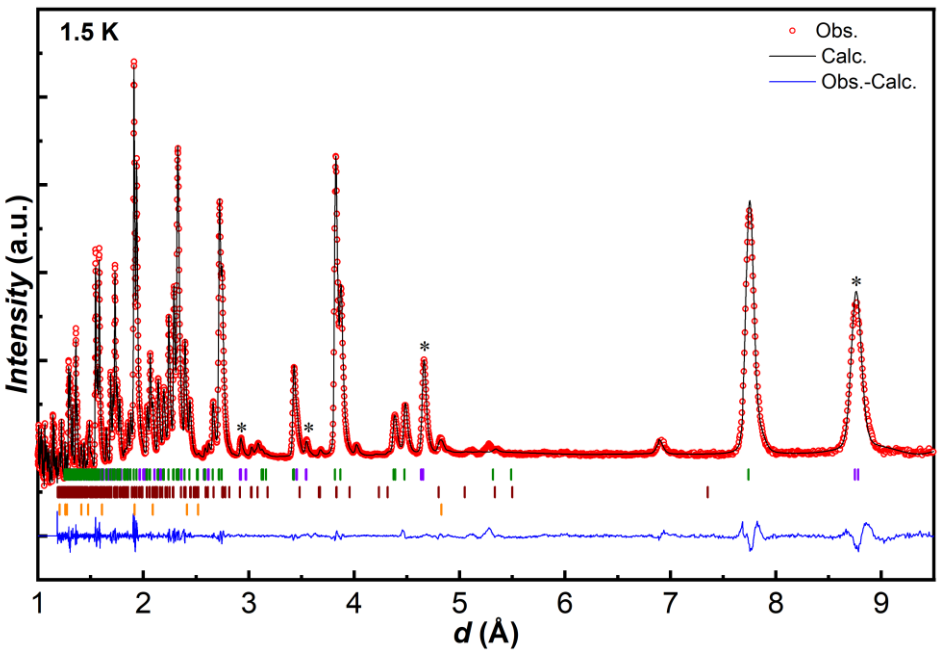

Figure 3.6 Rietveld refinement fit for the WISH neutron powder diffraction data collected at average 2θ = 58.3º at 1.5 K of $NaYNiWO_6$ compound. Olive green and violet tick marks indicate the Bragg reflections for nuclear and magnetic structures of $NaYNiWO_6$. Intense magnetic reflections are indicated by an asterisk. Wine and orange tick marks indicate the Bragg reflections for Y_2WO_6 and NiO impurity phases.

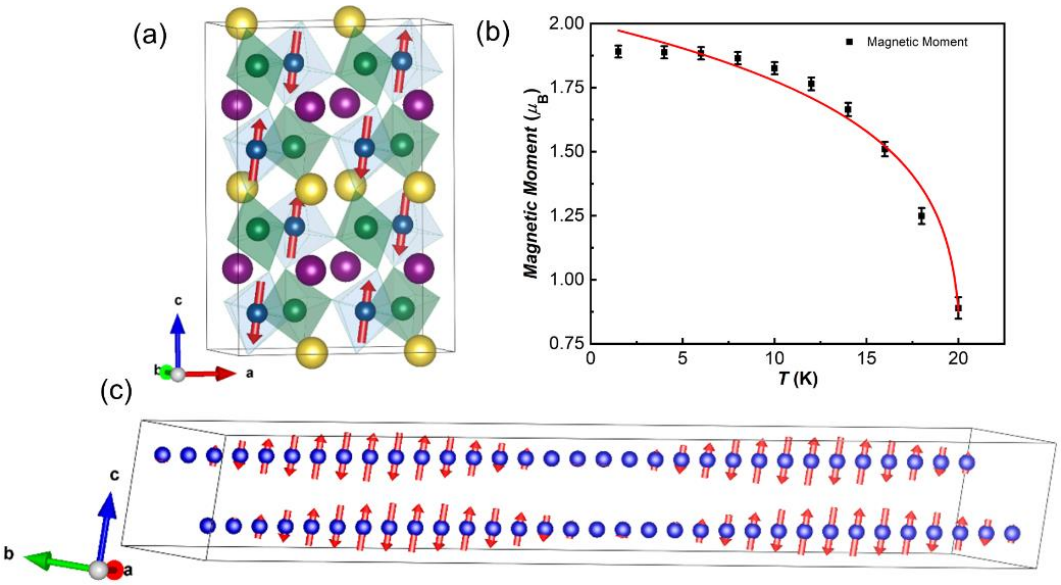

Figure 3.7 (a) Representation of the magnetic structure of $NaYNiWO_6$ with the magnetic moments plotted on the Ni atoms at 1.5 K and (b) the evolution of Ni^{2+} magnetic moment as a function of temperature, showing the power-law fit as discussed in the text and (c) the incommensurate sinusoidal structure at 20 K.

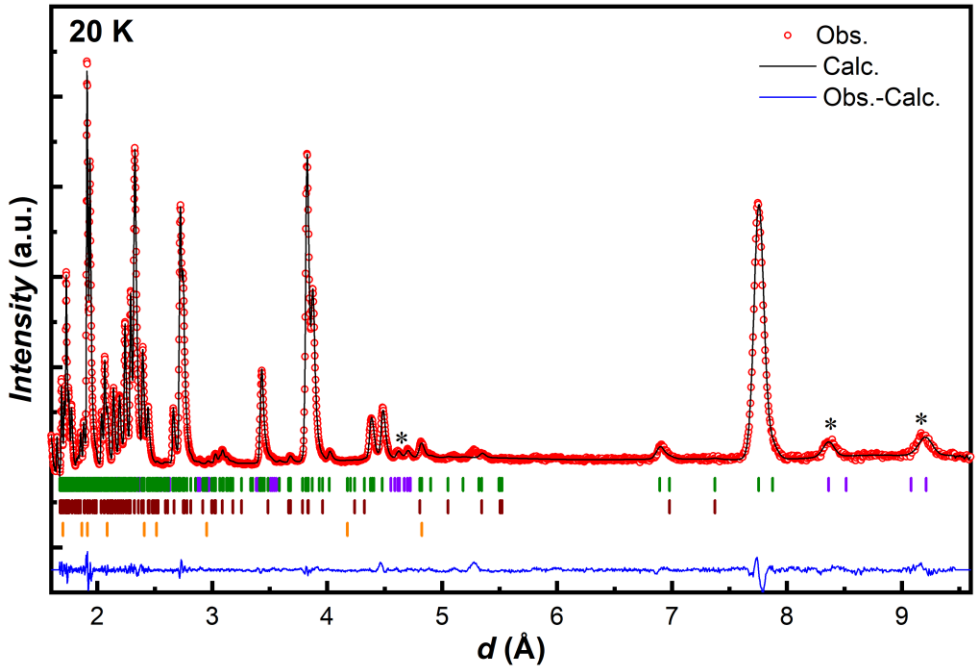

Figure 3.8 Rietveld refinement fit for the WISH neutron powder diffraction data collected at average 2θ = 58.3º at 20 K of $NaYNiWO_6$ compound. Olive green and violet tick marks indicate the Bragg reflections for nuclear and magnetic structures of $NaYNiWO_6$. Intense magnetic reflections are indicated by asterisk. Wine and orange tick marks indicate the Bragg reflections for Y_2WO_6 and NiO impurity phases.

At 20 K the magnetic reflections can be indexed with the incommensurate propagation vector $\mathbf{k_i}$ = (0.471(2), 0, 0.49(4)). The data can be modeled with the $P2_11'(a0g)0s$ magnetic superspace group corresponding to the mF1 irreducible representation. The obtained magnetic model is a spin density wave (SDW) with an amplitude of 0.89(4) μ_B with the moment oriented along the *c*-direction, as shown in Figure 3.7(c). The Rietveld plot of NPD data at 20 K is shown in Figure 3.8 and shows a good agreement between the observed and calculated data.

3.3.1.4 Dielectric, pyroelectric, and DC-bias measurements

To explore the dielectric properties and the magnetoelectric coupling near the magnetic ordering temperature, we have carried out electrical measurements on this compound. The temperature dependence of dielectric constant, $\varepsilon_r(T)$, under different magnetic fields at 50 kHz, shows a clear anomaly at the magnetic ordering temperature (T_N = 21 K) as shown in Figure 3.9(a). Temperature dependence of the dielectric constant $\varepsilon_r(T)$ with different frequencies is shown for a wide temperature range in Figure 3.9(b). The dielectric peak at T_N does not shift with an increasing frequency indicating the absence of relaxation phenomena. However, it shows broad maxima around 50 K, corresponding to dipolar relaxation (DR), as shown in the loss data in the inset of Figure 3.9(b). To investigate whether the dielectric anomaly at the magnetic ordering temperature is related to ferroelectric transition, we have recorded pyroelectric current against temperature with a poling electric field of E = ± 18.9 kV/cm. The observed pyroelectric current was integrated against time and presented as temperature dependent electric polarization, as shown in Figure 3.9(c). Considering the polar nature of this compound, one can expect a nonzero electric polarization above Néel temperature, but we did not find ferroelectric polarization indicating that this doubly ordered perovskite is pyroelectric in the paramagnetic phase. However, the magnetic ordering induces a change in polarization (ΔP) that is switchable by changing the direction of the applied electric field. It should be noted that the ΔP starts appearing slightly higher than T_N because of the higher warming rate (15 K/min) followed in the pyrocurrent measurement, which is essential because of the low value of ΔP. It is also worth mentioning that both commensurate and incommensurate magnetic structures themselves are non-polar, but the point group of the paramagnetic structure is polar. Therefore, the change in polarization at T_N is due to a renormalization of the latter caused by the magnetic phase transitions. This is usually related to a magnetoelastic coupling which is well known in literature [26–29]. No anomalies were detected in the evolution of the cell parameters across T_N in our data, probably because of the small value of ΔP. The related structural changes are likely below the resolution of the present diffraction experiment.

To distinguish between polarization due to ferroelectric dipoles and thermally stimulated free charges, the dc-bias current measurement was performed. In this measurement, the current is recorded around T_N with increasing temperature by applying the dc electric field without pre-poling the sample [30]. Temperature dependent dc-biased current measured under an applied electric field E = + 15.7 kV/cm is shown in Figure 3.9(d). It shows a broad positive peak associated with the polarization of the dipoles, followed by a sharp negative current peak indicating the depolarization of the polarized diploes, hence confirming the intrinsic polarization of $NaYNiWO_6$. The *P-E* loop measurement at 77 K exhibits a linear curve, which does not represent ferroelectricity. However, the appearance of electric polarization at T_N and switchability of the polarization direction by changing the direction of the applied poling electric field suggests the multiferroic properties of $NaYNiWO_6$.

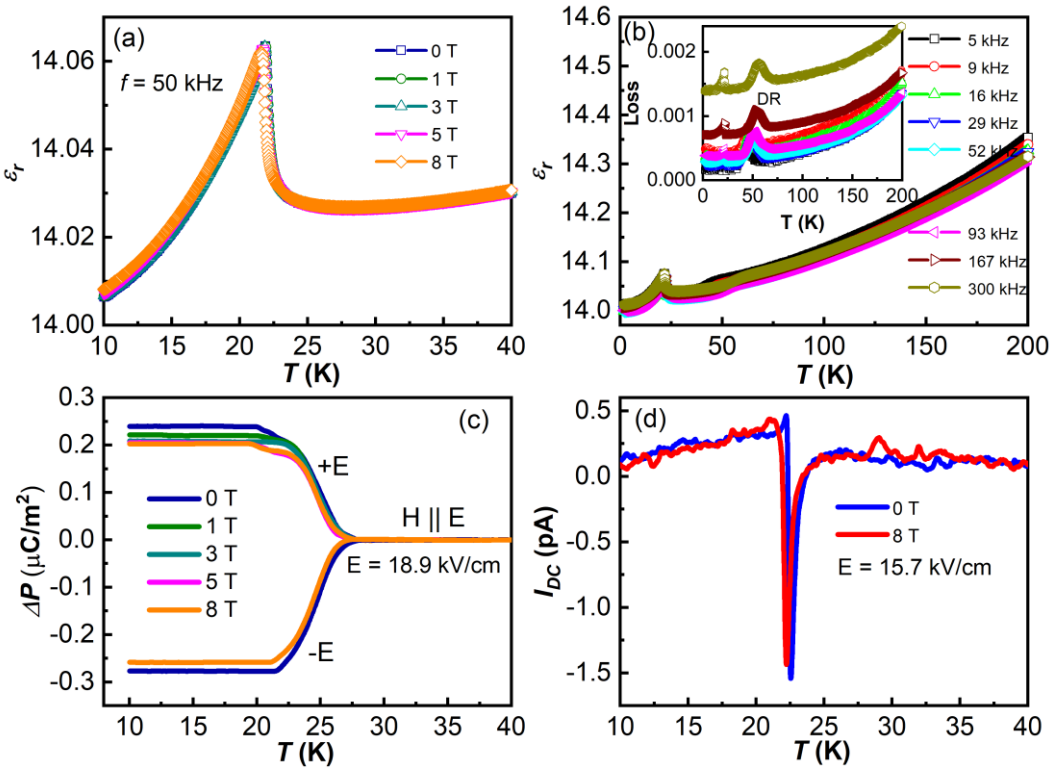

Figure 3.9 (a and b) Temperature dependent dielectric constant $\varepsilon_r(T)$ of $NaYNiWO_6$ measured at different magnetic fields and various frequencies, respectively, and loss data is shown in inset Figure (b). (c and d) Change in electric polarization $\Delta P(T)$ with the temperature at different magnetic fields obtained from integration of pyroelectric current peak and dc-biased current measured against temperature with an electric field of E_{dc} = + 15.7 kV/cm and magnetic fields of 0 and 8 T.

3.3.2 Theoretical results on $NaYNiWO_6$

In this section, we discussed the difference between conventional SDW and unconventional SDW and the formation of unconventional SDW of $NaYNiWO_6$ by evaluating the spin-exchanges and analyzing the nature of the spin frustration through DFT calculations.

3.3.2.1 Conventional spin density wave

The spin arrangement of a magnetic solid tends to be collinear because the energy of a spin arrangement is described as the sum of spin-exchanges, and each spin-exchange is minimum in energy when the two spins involved are collinear (either antiferromagnetic (AFM) or ferromagnetic (FM)). When a magnetic solid is weakly spin-frustrated (namely, when not all spin-exchanges can be made collinear), it adopts a noncollinear magnetic superstructure such as a cycloid or a helix [31–36]. For a cycloid formed in a chain of magnetic ions (Figure 3.10(a,b), and (d,e)), each successive spin rotates in one direction by a certain angle so that the moments of the ions differ in orientation but are identical in magnitude. There are two opposite ways of rotating the successive spins, so the resulting two cycloids are opposite in chirality but identical in energy [37]. When the temperature is lowered below the onset temperature of a spin density wave T_{SDW}, the two cycloids of opposite chirality occur with equal probability, resulting in their superposition (Figure 3.10(c) and (f)), a state identified as a SDW [37].

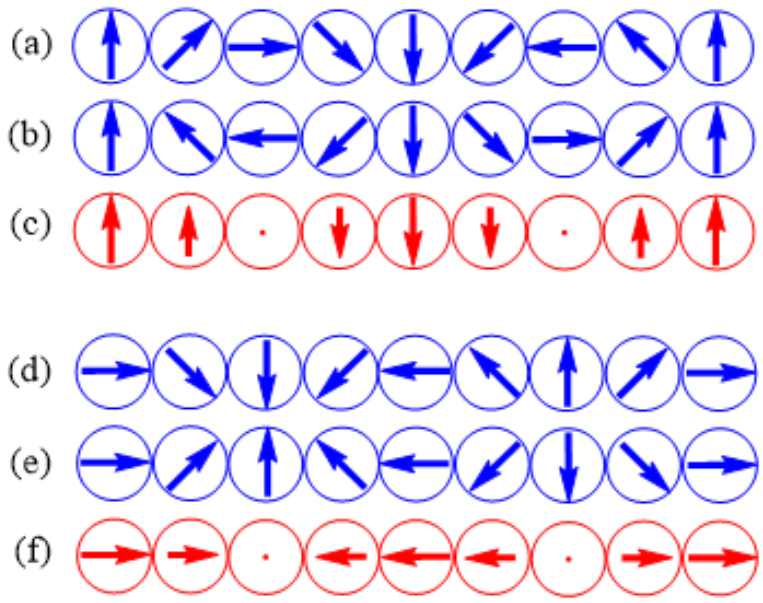

Figure 3.10 (a and b) Two chiral cycloids are leading to a transverse SDW shown in part (c). (d and e) Two chiral cycloids are leading to a longitudinal SDW shown in part (f). For simplicity, the angle of the spin rotation was taken to be 45°.

A SDW is transverse (Figure 3.10(c)) if the preferred spin orientation at each magnetic ion is perpendicular to the SDW propagation direction but is longitudinal if the spin orientation prefers the SDW propagation direction [37]. As the temperature is lowered further below T_{SDW}, the electronic structure of the spin-lattice relaxes to energetically favor one of the two chiral cycloids so that one often observes a cycloid state at a temperature slightly below T_{SDW} [37–43]. Either a SDW or a cycloid phase is typically incommensurate. A SDW might undergo a phase transition to a commensurate AFM phase upon further lowering of the temperature below T_N [37,43,44].

3.3.2.2 Unconventional spin density wave

From experimental studies, as we discussed previously, an unconventional kind of SDW was observed in the $NaYNiWO_6$ compound. At 20 K, this compound exhibits an incommensurate magnetic structure of propagation vector $\mathbf{k} = (k_a, k_b, k_c) = (0.47, 0, 0.49)$, which is followed by a commensurate AFM structure of propagation vector (0.5, 0, 0.5) at 18 K, showing a very narrow temperature region favorable for the existence of the incommensurate phase. Note that the **k**-space supercell (0.5, 0, 0.5) corresponds to the real-space supercell (2*a*, *b*, 2*c*). When the propagation of the incommensurate magnetic structure along the [100]-direction is approximated by SDWs using a 32*a* supercell, each half-wave is found to consist of alternating up and down spins [45], as illustrated in Figure 3.11. This feature is in sharp contrast to conventional SDWs, in which each half-wave consists of identical spins (e.g., Figure 3.10(c,f)) [37]. To distinguish the two types of SDWs, we used the term "a ferro-

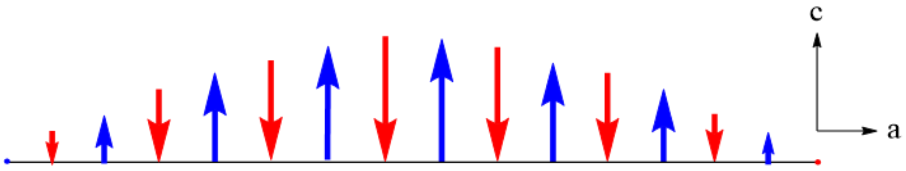

Figure 3.11 Alternating up- and down-spins (indicated by blue and red arrows, respectively) in each half-wave of the SDW propagating along the [100] direction in $NaYNiWO_6$. Only one chain of Ni^{2+} ions along the *a*-direction is shown using a 32*a* supercell.

SDW (f-SDW)" for a SDW composed of half-waves containing identical spins, and the term "an antiferro-SDW (af-SDW)" for a SDW whose half-waves have alternating up and down spins. Here, we probe the origin of the af-SDWs observed along the [100]-direction of $NaYNiWO_6$ and considered its implications. For this objective, we evaluate the spin-exchange interactions of $NaYNiWO_6$ and analyze the nature of spin frustration present in the spin-lattice

of $NaYNiWO_6$, to find that the af-SDWs along the[100]-direction give rise to f-SDWs along the [101]-direction.

3.3.2.3 Spin-exchange paths and spin frustration

$NaYNiWO_6$ is made up of NiO_6 octahedra containing magnetic ions Ni^{2+} (d^8, S = 1) and WO_6 octahedra containing nonmagnetic ions W^{6+} (d^0, S = 0). It has a double-perovskite structure so that the corner-sharing NiO_6 and WO_6 octahedra alternate along each of the *a*-, *b*- and *c*-directions. Thus, all spin-exchanges between adjacent Ni^{2+} ions are of the Ni-O···O-Ni type, in which the O···O contact is bridged by a W^{6+} ion to form a O···W^{6+}···O bridge [31,46,47]. There are nine nearest-neighbor (NN) spin-exchanges to consider: J_a, J_b, and J_c along the *a*-, *b*- and *c*-directions, respectively, and two diagonal exchanges J_{ab} and J_{ab}' in each layer of Ni^{2+} ions parallel to the *ab*-plane (Figure 3.12(a,b)).

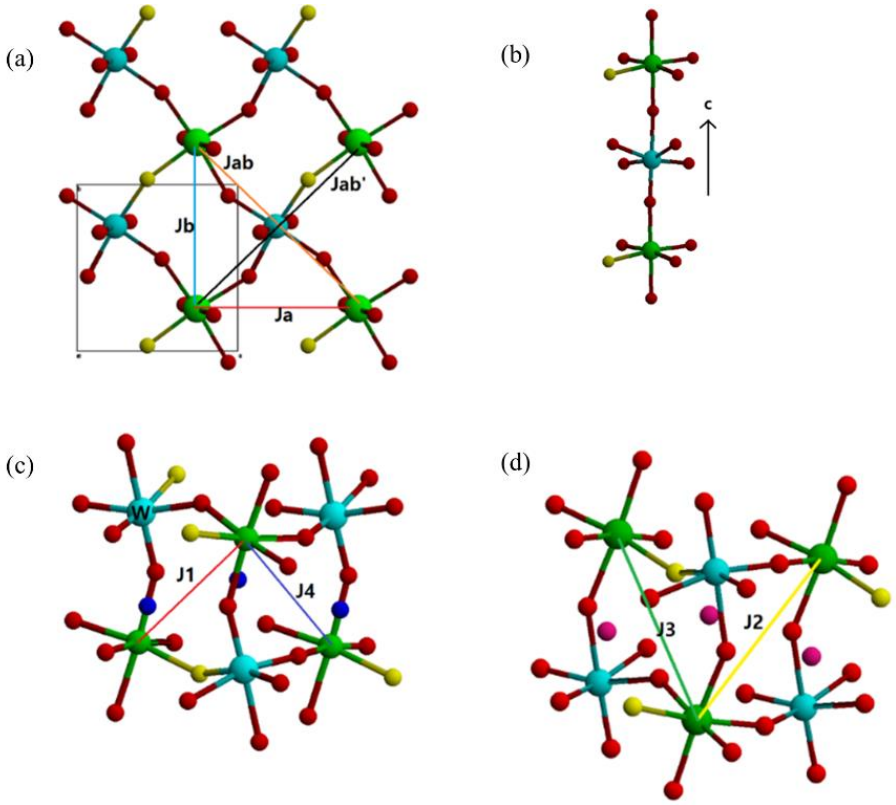

Figure 3.12 (a) Spin-exchange paths J_a, J_b, J_{ab}, and J_{ab}' in a layer of Ni^{2+} ions parallel to the *ab*-plane. (At z = 0.25). (b) Spin-exchange path J_c along the *c*-direction. (c,d) Spin-exchange paths J_1, J_2, J_3, and J_4 between two layers of Ni^{2+} ions parallel to the *ab*-plane. The Ni^{2+} ions are represented by green spheres and the W^{6+} ions by cyan spheres.

The oxygen atom of the longest Ni-O bond of each NiO_6 octahedron is represented by a yellow sphere and the rest oxygen atoms by red spheres. The J_{ab}' path includes a yellow O atom in the O···W^{6+}···O bridge, but the J_{ab} path does not. In every two adjacent layers of Ni^{2+}

ions parallel to the *ab*-plane, the Ni^{2+} ions form Ni_4 tetrahedra, so there are four spin-exchanges along the four edges of each Ni_4 tetrahedron (J_1, J_2, J_3, and J_4) connecting the two layers (Figure 3.12(c,d)). The three-dimensional (3D) arrangement of these exchange paths is shown in Figure 3.13 (a). The geometrical parameters associated with the nine spin-exchange paths based on the crystal structure determined by neutron diffraction refinement at 100 K are summarized in Table A-1.3.2. For evaluation of the spin-exchanges, an experimentally determined crystal structure was employed for DFT+U calculations [48–51] using U_{eff} = 3, 4, and 5 eV as discussed in the details of the calculation (Appendix-1).

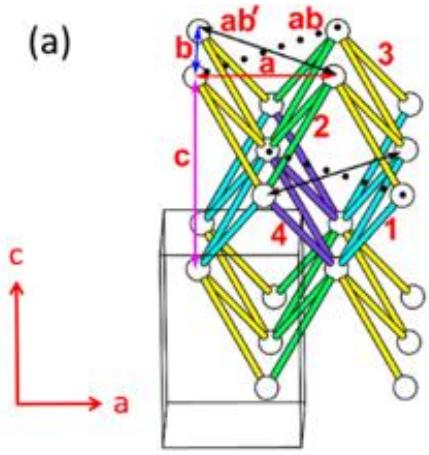

(b)

J_a	-3.8
J_b	-5.3
J_c	-14.5
J_{ab}	-9.3
J_{ab}'	-9.4
J_1	-6.8
J_2	+0.7
J_3	+0.5
J_4	-1.1

Figure 3.13 (a) Arrangement of the nine spin-exchange paths in $NaYNiWO_6$. The labels a, b, c, ab, ab′, 1, 2, 3, and 4 refer to J_a, J_b, J_c, J_{ab}, J_{ab}', J_1, J_2, J_3, and J_4, respectively. (b) Values of the spin-exchanges in K from DFT+U calculations with U_{eff} = 4 eV.

For the spin orientation of the Ni^{2+} spins, DFT+U+SOC calculations [52] show that the *c*-direction is more stable than the *a*- and *b*-directions (by 0.70 and 0.52 meV per Ni^{2+}, respectively), in agreement with the experiment. To determine the values of the nine spin-exchanges, we perform DFT+U calculations for 11 ordered spin states, depicted in Figure A-1.3.2. The relative energies obtained for these states are summarized in Table 3.3. In terms of the spin Hamiltonian,

$$H = -\sum_{i>j} J_{ij}\,\vec{S_i}\cdot\vec{S_j}$$

the energies of the 11 ordered spin states are expressed in terms of the spin-exchange parameters, as summarized in Table A-1.3.3. Thus, by equating the nine relative energies from the DFT+U calculations to the corresponding relative energies expressed in terms of spin-exchange interactions, [31,46,47] we obtain the values of the nine spin-exchanges summarized

in Table A-1.3.4. The spin-exchanges determined using U_{eff} = 3, 4, and 5 eV show similar trends. For simplicity, only those obtained with U_{eff} = 4 eV are listed in Figure 3.13(b). With the spin Hamiltonian defined above, a negative spin-exchange ($J_{ij} < 0$) signifies an AFM interaction and a positive spin-exchange ($J_{ij} > 0$), a FM interaction.

In the commensurate magnetic structure (0.5, 0, 0.5) of $NaYNiWO_6$, the spins of the Ni^{2+} ions are antiferromagnetically coupled along with the *a*- and *c*-directions, but ferromagnetically along the *b*-direction. Figure 3.13(b) shows that J_b/J_c is greater than J_a/J_c (i.e., 0.36 vs. 0.26 with U_{eff} = 4 eV), so one would have expected an AFM coupling along the *b*-direction rather than along *a*-direction, leading to the (0, 0.5, 0.5) supercell. This apparent puzzle is associated with the spin frustration arising largely from the spin-exchanges J_a, J_b, J_c, J_{ab}, J_{ab}', J_1 and J_3 (Figure 3.14). The arrangement of six exchange paths J_a, J_b, J_c, J_{ab}', J_1 and J_3 of $NaYNiWO_6$ are presented in Figure 3.14(a).

Table 3.3 Relative energies (in meV per formula unit) of the 11 states of $NaYNiWO_6$ obtained from DFT+U calculations.

	U_{eff} = 3 eV	U_{eff} =4 eV	U_{eff} = 5 eV
EFM	9.39	7.29	5.62
EAF1	4.38	3.40	2.62
EAF2	3.05	2.37	1.83
EAF3	4.32	3.36	2.58
EAF4	7.94	6.15	4.72
EAF5	3.35	2.62	2.03
EAF6	3.47	2.68	2.05
EAF7	0.14	0.12	0.10
EAF8	0	0	0
EAF9	6.49	5.03	3.87
EAF10	5.58	4.33	3.33

The spin arrangements in the (0.5, 0, 0.5) and (0, 0.5, 0.5) structures are depicted in Figures 3.14(b) and (c), respectively. In the two structures, spin frustration occurs in each of the spin-exchange triangles (J_a, J_b, J_{ab}), (J_a, J_b, J_{ab}'), (J_1, J_1, J_b), and (J_3, J_3, J_b). The two structures differ in how the spin frustration takes place.

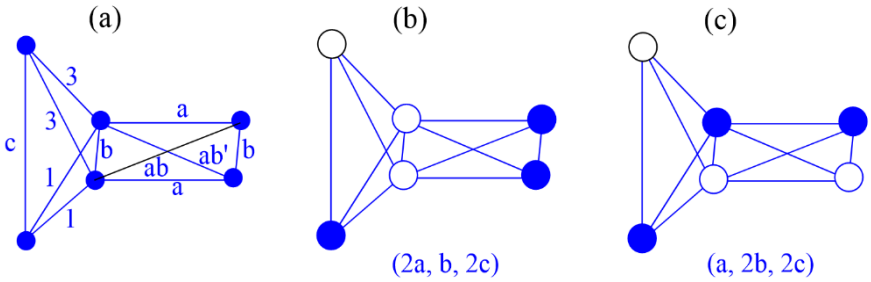

Figure 3.14 (a) Arrangement of six exchange paths J_a, J_b, J_c, J_{ab}', J_1 and J_3. (b) (2a, b, 2c) arrangement of spins. (c) (a, 2b, 2c) arrangement of spins. The shaded and unshaded circles in (b, c) refer to up- and down-spins, respectively.

DFT+U calculations show that the (0.5, 0, 0.5) spin arrangement (the AF8 state) is more stable than the (0. 0.5, 0.5) spin arrangement (the AF7 state) very slightly (i.e., by 1.6, 1.4 and 1.2 K per formula unit with U_{eff} = 3, 4 and 5 eV, respectively; Table 3.3).

It is of interest to consider a commensurate supercell approximation for the incommensurate structure (0.47, 0, 0.49) observed at 20 K. The 32*a* supercell representation in Figure 3.11 corresponds to $\mathbf{k}_a = 1/32 \cong 0.031$. To find the real space supercell corresponding to the (0.47, 0, 0.49) structure, we note that $1/\mathbf{k}_a = 1/0.47 \cong 2.13$. In an integer representation, the latter corresponds to 213*a* supercell in real space, which very closely amounts to seven 30*a* supercells in terms of the commensurate-cell approximation. Similarly, $1/\mathbf{k}_c = 1/0.49 \cong 2.04$, which corresponds to 204*c* supercell, or equivalently, to three 68*c* supercells. Thus, the (0.47, 0, 0.49) structure can be approximated by the (30*a*, *b*, 68*c*) supercell. Note that $1/30 \cong 0.033$ and $0.5 - 0.033 \cong 0.467$, which is close to the observed $\mathbf{k}_a \cong 0.47$, and $1/68 \cong 0.015$ and $0.5 - 0.015 \cong 0.485$, which is close to the observed $\mathbf{k}_c \cong 0.49$. The nature of spin frustration in $NaYNiWO_6$ was analyzed in terms of the calculated spin-exchanges. To account for the occurrence of the af-SDW along the [100] direction, we probe the spin frustration in each chain of Ni^{2+} ions along the *a*-direction. The 3D spin-lattice of $NaYNiWO_6$ can be described by starting with a two-dimensional (2D) rectangular lattice made up of J_b and J_c (Figure 3.15(a)). This 2D lattice repeats along the *a*-direction to form a set of 2D rectangular lattices (Figure 3.15(b)). The 3D spin-lattice consists of two such sets of 2D rectangular lattices, which are indicated by blue and red sets in Figure 3.15(c). For clarity, only one vertex of each red rectangle, located at the center between every two adjacent blue rectangles, is shown in Figure 3.15(c).

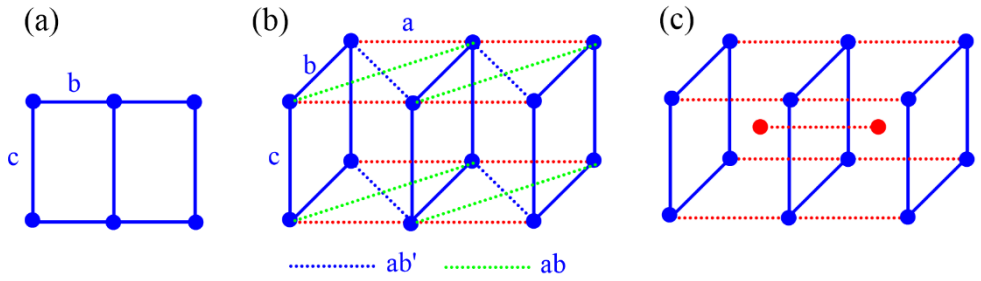

Figure 3.15 Illustration of the spin frustration in $NaYNiWO_6$. (a) 2D rectangular spin-lattice made up of J_b and J_c. (b) A set of 2D rectangular spin lattices, which are spin-frustrated by (J_a, J_b, J_{ab}) and (J_a, J_b, J_{ab}') triangles. In (a, b), the symbols a, b, ab, and ab′ refer to J_a, J_b, J_{ab} and J_{ab}', respectively. (c) Two sets of 2D rectangular spin lattices, represented by blue and red sets. For clarity, only one lattice point is shown for each red rectangle at the center between every two adjacent blue rectangles.

As discussed above, the spins in the chains of Ni^{2+} ions along the *a*-direction tend to have an AFM coupling, but this tendency is spin-frustrated due to the (J_a, J_b, J_{ab}) and (J_a, J_b, J_{ab}') triangles because all three spin-exchanges are AFM. Besides, slight spin frustration also exists between the two sets of 2D rectangular spin lattices, as discussed previously.

As noted above, there are two sets of 3D sublattices (i.e., the set of blue 2D sheets and that of red 2D sheets), which interpenetrate each other. As shown in Figure 3.16, each red 2D sheet was represented by a red line, each red dot at the center of each blue box, and each blue dot at the center of each red box. For example, the 2D AFM lattices 1, and 2 of the blue set have spin frustration with the 2D rectangular lattice 1′ of the red set due to the spin-exchanges J_1, J_2, J_3, and J_4. As shown in Figure 3.17, spin frustration exists in the (J_c, J_3, J_4, J_a) quadrangle, in the (J_1, J_4, J_a) and (J_2, J_4, J_c) triangles.

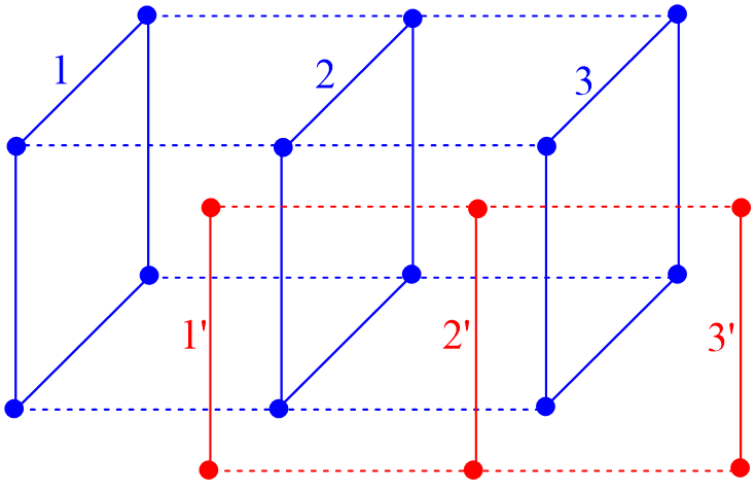

Figure 3.16 Two sets of 2D rectangular spin lattices in $NaYNiWO_6$.

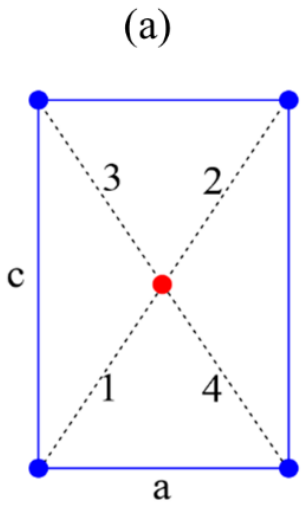

(b)

J_a	-3.77
J_b	-5.33
J_c	-14.48
J_{ab}	-9.26
J_{ab}'	-9.38
J_1	-6.78
J_3	0.50
J_4	-1.06
J_2	0.72

Figure 3.17 (a) Arrangement of two adjacent blue and red 2D rectangular spin lattices. (b) Values of the nine spin-exchanges (in K) were obtained with U_{eff} = 4 eV.

To probe the condition for the formation of an af-SDW, we imagine that an AFM chain (Figure 3.18(a)) is spin-frustrated by intrachain and/or interchain interactions, and the extent of its spin frustration is reduced when the AFM chain adopts a cycloid in which the successive spins rotate by an angle θ. (Because a SDW is the superposition of two cycloids of opposite chirality, the formation condition for a SDW is the same as that for the formation of a cycloid from a spin-frustrated AFM chain.) Then, there are two equally probable cycloids of opposite chirality (Figure 3.18(b)), the superposition of which leads to an af-SDW (Figure 3.18(c)). With the NN spin-exchange as J_a (< 0), the spin rotation by θ raises the spin-exchange energy by $J_a(-1 + \cos\theta)$ per spin site. Given the energy lowering from the reduction in spin frustration as $-\Delta$ per spin site ($\Delta > 0$), the formation of a cycloid in the AFM chain requires that $-\Delta + J_a(-1 + \cos\theta) < 0$, namely, $\cos\theta > 1 - \Delta/|J_a|$.

A long SDW such as a 30a-supercell af-SDW (equivalently, a 30a-supercell cycloid) is explained by $\theta = 360°/30$ (i.e., $\cos\theta \cong 1/45$). Thus, for such a long SDW to occur, $\Delta \geq 0.98|J_a|$, i.e., Δ should be nearly equal to, or greater than, $|J_a|$.

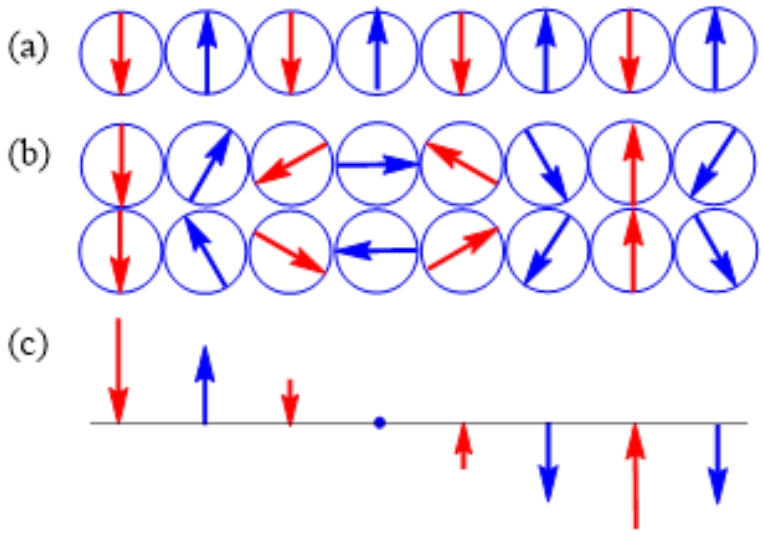

Figure 3.18 Formation of an af-SDW: (a) an AFM chain; (b) two cycloids of opposite chirality generated by rotating each successive spin of the AFM chain by $\pm\theta$ °; (c) af-SDW resulting from the superposition of the two cycloids in part (b). For this illustration, we choose $\theta = 30°$.

3.3.2.4 Antiferromagnetic SDW and ferromagnetic SDW

Let us now consider other SDWs associated with the (0.47, 0, 0.49) superstructure of $NaYNiWO_6$. If the $\mathbf{k}_c$ value of (0.47, 0, 0.49) is approximated by 0.5, the af-SDWs along the [100]-direction are antiferromagnetically coupled along the *c*-direction in $NaYNiWO_6$, as depicted in Figure 3.19. The latter shows that longitudinal af-SDWs running along the [001]-direction are antiferromagnetically coupled along the [100] direction (Note that the af-SDWs appear as AFM chains because the $\mathbf{k}_c$ value of 0.49 was approximated by 0.5). Figure 3.19 also shows that f-SDWs running along the [101]-direction are antiferromagnetically coupled along the $[10\bar{1}]$-direction. Each f-SDW along the [101]-direction is neither transverse nor longitudinal because the spin orientation at each Ni^{2+} site is along the [001]-direction.

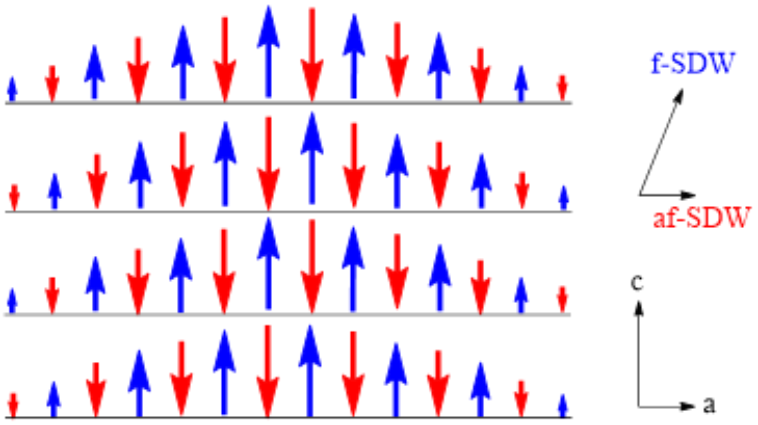

Figure 3.19 AFM coupling of the af-SDWs in the *ac* plane of $NaYNiWO_6$, giving rise to f-SDWs.

For the transverse SDW to propagate along the *a*-direction, the two cycloids of opposite chirality must be contained in the *ac*-plane. This is explained by two factors. (1) The preferred spin direction is along the *c*-axis. (2) There are more spin-frustrated triangles involving J_a than those involving J_b, namely, (J_a, J_1, J_4), (J_a, J_b, J_{ab}) and (J_a, J_b, J_{ab}') vs. (J_b, J_1, J_1). Consequently, the extent of spin frustration is more efficiently reduced if the noncollinear spins occur along the *a*-direction rather than along the *b*-direction. Thus, the spin rotation in the *ac*-plane is energetically more favorable than that in the *bc*-plane.

An incommensurate SDW state may undergo a phase transition to either a commensurate AFM state or an incommensurate cycloid or helix. A SDW undergoes a phase transition to a commensurate AFM state in two ways; one involves a cycloid state between the SDW and AFM [38–44], and the other does not [53,54]. We note that a magnetic insulator exhibiting an af-SDW may not adopt a commensurate AFM ground state but a cycloid or spiral ground state [55–57]. In conclusion, an af-SDW arises from a spin-frustrated AFM chain of magnetic ions to lower the extent of spin frustration. In general, incommensurate SDWs are likely to arise from all AFM compounds with moderate spin frustration.

3.3.3 Results on Na*Ln*NiWO$_6$ (*Ln* = Dy-Lu)

3.3.3.1 Structural analysis

The structure and macroscopic properties of all these compounds are similar to NaYNiWO$_6$. The powder X-ray diffraction data of compounds at room temperature are refined with the $P2_1$ space group. We have performed SHG studies for NaDyNiWO$_6$ and NaHoNiWO$_6$ at room temperature, which is found to be SHG active under 1064 nm laser. The laser intensity is around 0.67 and 0.53 times of alpha-SiO_2 for Dy and Ho, respectively, confirming the polar nature. Structural parameters for all the compounds are given in appendix-1 (Figure A-1.3.3 and Table A-1.3.5 to A-1.3.10). All the compounds contain a small amount of Ln_2WO_6, NiO, and $Na_2WO_4{\cdot}2H_2O$ impurities that are included in the refinement, and the weight% of the main and impurity phases are given in the appendix (Table A-1.3.11). The lattice parameters of all compounds are listed in Table 3.4. The bond angle Ni-O-W decreases with decreasing size of rare-earth cation as given in Table 3.5 due to the higher degree of Ni/W octahedral tilting. As a consequence, compounds with smaller rare-earth cations exhibit larger distortions which should lead to large electric polarization [6,7].

Table 3.4 Lattice parameters obtained from Rietveld refinement of PXRD data of Na*Ln*NiWO$_6$ at RT. (*Ln* = Y, Dy-Lu).

Compound	*a* (Å)	*b* (Å)	*c* (Å)	*β* (°)	*V* (Å^3)
NaYNiWO$_6$	5.3226(2)	5.4894(2)	7.7499(2)	90.202(9)	225.55(1)
NaDyNiWO$_6$	5.3379(3)	5.4874(3)	7.7578(5)	90.246(4)	227.234(2)
NaHoNiWO$_6$	5.3271(3)	5.4912(4)	7.7499(2)	90.239(2)	226.853(3)
NaErNiWO$_6$	5.3089(2)	5.4858(2)	7.7429(2)	90.215(2)	225.50(1)
NaTmNiWO$_6$	5.2951(2)	5.4797(2)	7.7345(2)	90.221(2)	224.42(3)
NaYbNiWO$_6$	5.2834(5)	5.4792(5)	7.7284(8)	90.209(7)	223.728(4)
NaLuNiWO$_6$	5.271(1)	5.4777(2)	7.725(1)	90.192(1)	223.06(5)

Table 3.5 Selected Bond lengths (Å) and angles (°) from PXRD refinement at room temperature.

Ln	Y	Dy	Ho	Er	Tm	Yb	Lu
Ni-O(1)	2.07(2)	2.04(3)	2.04(2)	1.98(2)	1.84(2)	2.01(2)	2.10(2)
Ni-O(2)	1.95(2)	1.89(3)	1.86(2)	2.01(2)	1.81(2)	1.80(2)	1.98(2)
Ni-O(3)	2.07(2)	2.09(3)	1.99(2)	2.07(2)	2.01(2)	2.08(2)	2.03(2)
Ni-O(4)	2.09(2)	1.92(3)	2.04(2)	2.07(2)	2.07(2)	2.14(2)	2.18(2)
Ni-O(5)	2.02(1)	1.78(2)	1.80(1)	2.02(1)	2.01(1)	1.94(2)	2.02(1)
Ni-O(6)	2.03(1)	2.08(2)	2.03(1)	2.03(1)	1.96(1)	2.1(1)	2.10(1)
W-O(1)	2.02(2)	1.96(2)	1.81(2)	2.04(2)	2.18(2)	2.17(2)	1.96(2)
W-O(2)	2.02(2)	2.11(2)	2.20(2)	1.95(2)	2.16(2)	2.23(2)	1.94(2)
W-O(3)	1.90(0)	1.85(2)	2.01(2)	1.90(2)	1.95(2)	1.9(0)	1.95(2)
W-O(4)	1.81(2)	1.99(2)	2.09(2)	1.91(2)	1.96(2)	2.16(2)	1.79(2)
W-O(5)	2.13(1)	2.42(2)	2.41(1)	2.16(1)	2.19(1)	2.35(2)	2.08(1)
W-O(6)	1.81(1)	1.86(2)	1.83(1)	1.80(1)	1.87(1)	1.88(2)	1.74(1)
Ni-O(1)-W	149.3(10)	151.9(1)	158.8(10)	154.7(8)	151.0(8)	136.5(9)	149.8(7)
Ni-O(2)-W	145.5(10)	150.2(1)	155.1(9)	146.9(9)	143.1(8)	144.7(9)	149.0(8)
Ni-O(3)-W	153.8(10)	149.5(1)	134.6(9)	150.8(8)	152.9(8)	143.8(9)	148.6(8)
Ni-O(4)-W	144.2(11)	149.1(1)	138.8(9)	137.8(8)	136.1(8)	120.7(9)	136.6(8)
Ni-O(5)-W	150.8(8)	144.2(8)	146.3(6)	147.4(6)	146.3(6)	140.7(8)	153.8(5)
Ni-O(6)-W	153.5(8)	145.6(9)	148.8(7)	153.6(6)	151.8(6)	136.9(8)	153.0(6)

3.3.3.2 Magnetic properties

The dc magnetization measured between the temperature range of 2-40 K under a field of 100 Oe in zero-field-cooled (ZFC) and field-cooled (FC) conditions for Na*Ln*NiWO$_6$ (*Ln* = Dy, Ho, Er, Tm, Yb, and Lu) are shown in Figure 3.20(a-f). The absence of magnetic anomaly in *M*(*T*) data for the ordering of Ni^{2+} ions in all magnetic rare-earth cation compounds is due to the large paramagnetic contribution of the magnetic rare-earth cations over the Ni^{2+}

moments. Therefore, the magnetic ordering temperature of the Ni^{2+}-ion is determined by heat capacity measurement, as shown in the right axis of Figure 3.20 (a-f). These compounds exhibit antiferromagnetic transition around 23 K for Dy, 22 K for Ho, 21 K for Er, 20 K for Tm, Yb, and 18 K for Lu compounds. The small peak in the heat capacity data of the Ho compound at low temperature ~ 2.3 K and peak in heat capacity data around 4.5 K for the Tm compound indicates the magnetic ordering of Ho^{3+} and Tm^{3+} ions. The marked broad peaks below T_N in the heat capacity data $C_p(T)/T$ vs. T of Er, Tm, Yb, Lu, and probably a shoulder-like feature in Dy sample below T_N compounds may suggest the change in the magnetic structure of Ni^{2+} spins.

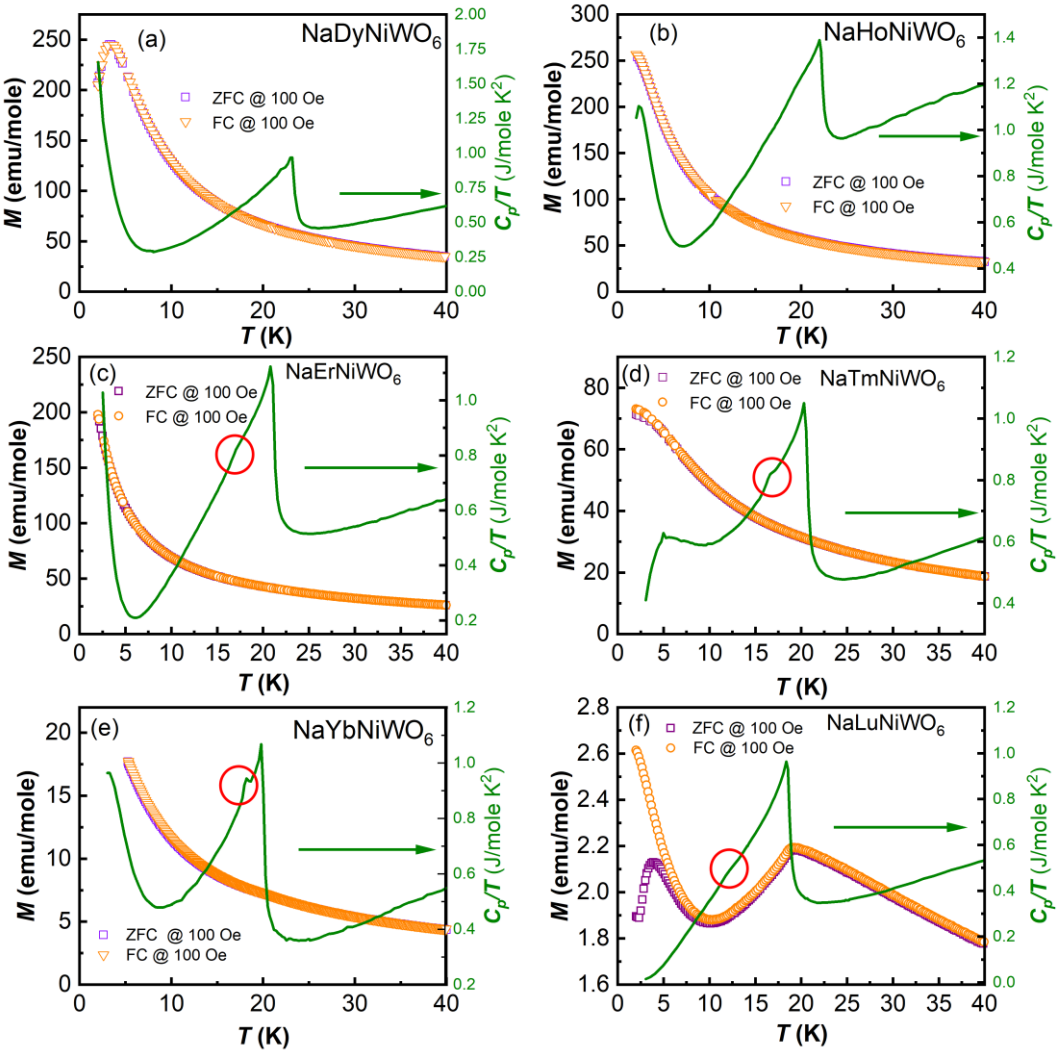

Figure 3.20 (a-f) Temperature dependent dc magnetization data in zero-field-cooled (ZFC) and filed-cooled (FC) sequence measured under a magnetic field of 100 and C_P/T (heat capacity divided by temperature) data on the right axis of Figures.

This double peak structure indicates the change in the magnetic structure in a similar way to $NaYNiWO_6$, which has an incommensurate magnetic structure at 20 K and collinear magnetic structure below 18 K. The low-temperature behavior of the Lu compound (Figure 3.20(f)) below 10 K may be due to the NiO impurity phase [33].

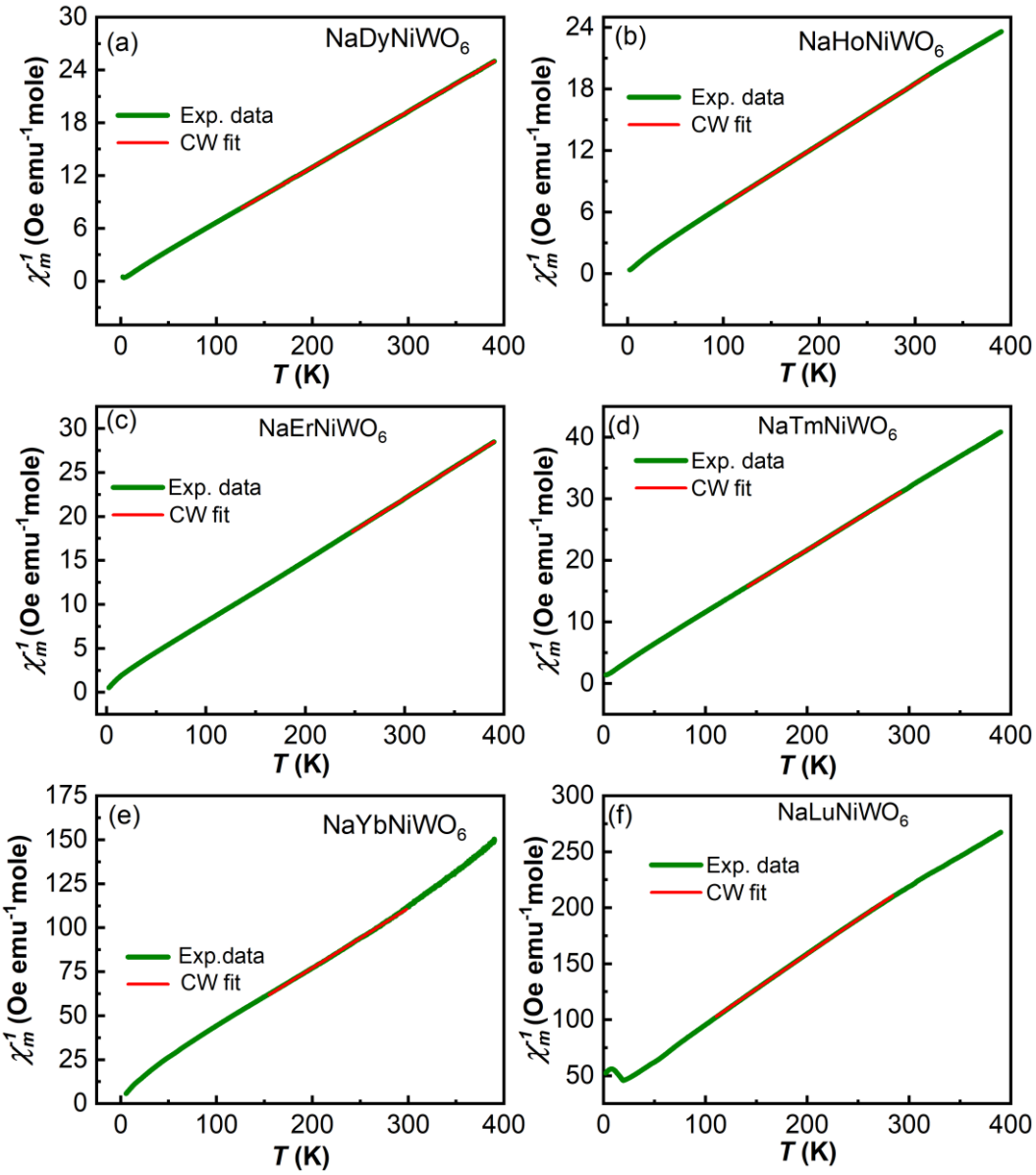

Figure 3.21 (a-f) Inverse susceptibility ($1/\chi_{mol}$) as a function of temperature.

The temperature dependent $1/\chi$ data (Figure 3.21(a-f)) were fitted to the Curie-Weiss law, $\chi = C/(T-\theta)$ in the paramagnetic region, where C and θ are the Curie and Weiss constants, respectively. The obtained effective magnetic moments from the Curie-Weiss fits are shown in Figure 3.21(a-f), which are close to the calculated moment. The effective magnetic moment is

calculated by the formula $\mu_{eff} = g(S(S+1))^{1/2}$, μ_{eff} is 2.83 for Ni^{2+}, where g = 2.0023 and S = 1. In the case of magnetic rare-earth cation compounds, the relation $(\mu_{total})^2 = (\mu_{Ln})^2 + (\mu_{Ni})^2$ was used to obtain contribution from magnetic rare-earth cation and Ni^{2+} ion. The obtained negative Curie-Weiss temperatures are consistent with antiferromagnetic ordering through various superexchange pathways, Ni^{2+}-O^{2-}-W^{6+}-O^{2-}-Ni^{2+}, as reported earlier [25]. The obtained μ_{eff} and Curie-Weiss temperatures (θ_{cw}) from the Curie-Weiss fit for all the compounds are given in Table 3.6, which are in good agreement with the reference value.

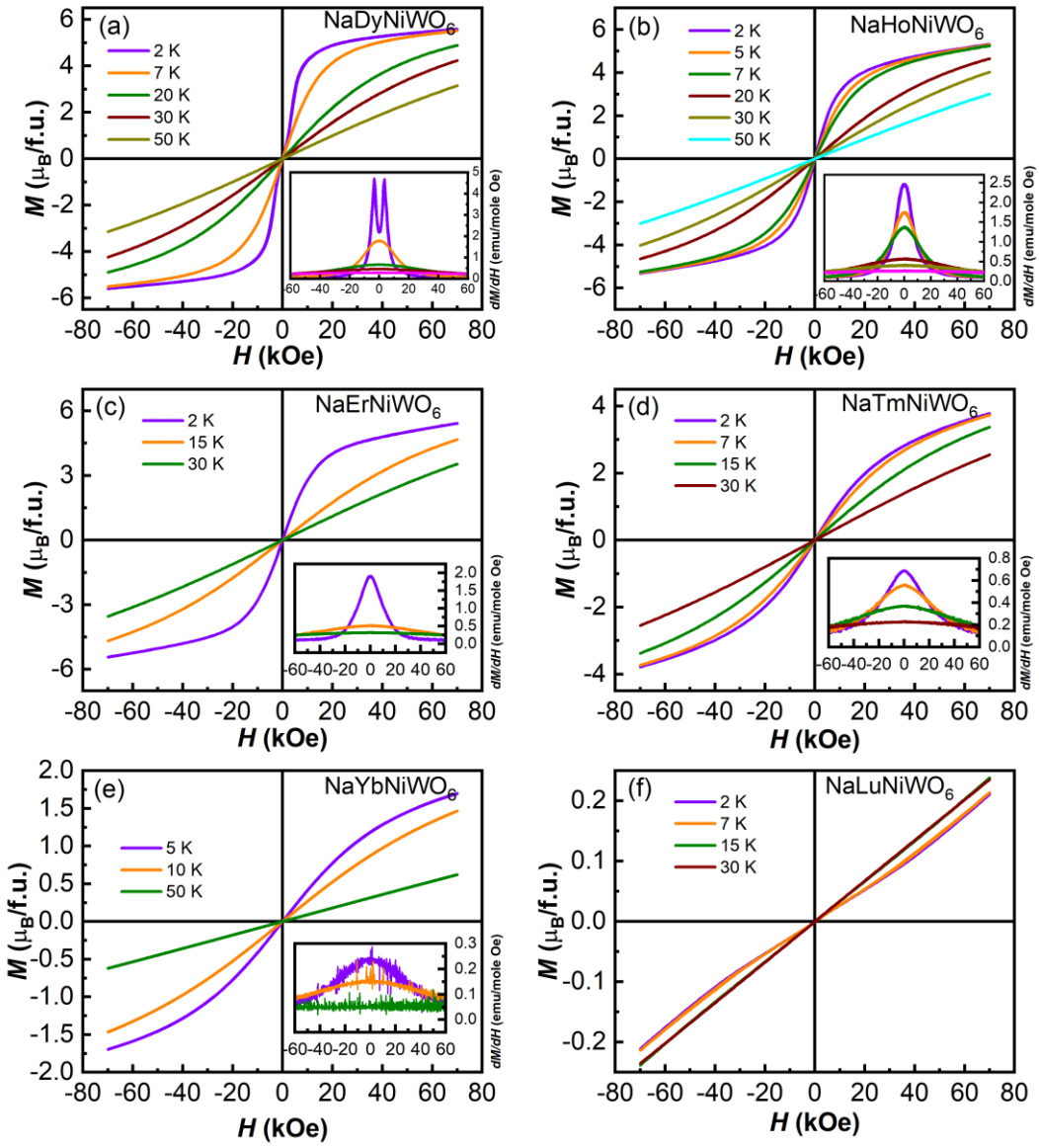

Figure 3.22 (a-f) Magnetic field dependent magnetization *M*(*H*) at different temperatures and *dM/dH* in the inset of Figures (a-e).

Table 3.6 Curie-Weiss constant, μ_{eff} (experimental), and μ_{eff} (theory/reference value) derived from the magnetization data measured under FC condition, T_N (K) for Ni^{2+} ion determined from heat capacity data.

Compound name	θ (K)	μ_{eff} (μ_B)	μ_{eff} (μ_B) theory/ref	T_N (K)
$NaYNiWO_6$	-49.7	3.3	2.83	21
$NaDyNiWO_6$	-4.8	11.2	11.01	23
$NaHoNiWO_6$	-13.6	11.6	10.97	22
$NaErNiWO_6$	-8.2	10.5	9.98	21
$NaTmNiWO_6$	-13.7	8.8	8.1	20
$NaYbNiWO_6$	-2.2	4.8	5.34	20
$NaLuNiWO_6$	-54.9	3.5	2.8	18

Magnetic field dependent isothermal magnetizations $M(H)$ of these compounds at different temperatures are shown in Figure 3.22(a-f). The non-linear behavior in M vs. H curves at low temperatures suggests a metamagnetic transition due to the field-induced effect on the magnetic Ln^{3+} ions ordering, as seen in the dM/dH curves in the inset of Figures 3.22 (a-e). The slight nonlinearity in the M vs. H curve of the Lu compound at lower temperatures (Figure 3.22(f)) is probably due to some degree of spin reorientation at higher fields. Above T_N, the $M(H)$ curves of all these compounds resemble paramagnetic behavior.

3.3.3.3 Dielectric and ferroelectric properties

In Figure 3.23(a-f) dielectric constant (ε_r) measured in the temperature range, 2 - 40 K with 50 kHz under different applied magnetic fields is shown. An apparent anomaly is observed for all three compounds at the magnetic ordering temperature. In the case of $NaHoNiWO_6$ and $NaTmNiWO_6$ at low temperature, a broad anomaly corresponding to the short-range ordering of Ho^{3+} and Tm^{3+} ions is observed. The anomaly varies slightly with applied fields in $\varepsilon_r(T)$ data. Therefore, we have measured magnetocapacitance at different temperatures between 2-30 K and observed a sizeable magnetodielectric effect below 10 K, as shown in Figure 3.24. The frequency-dependent dielectric data $\varepsilon_r(T)$ are shown in Figure 3.25(a-f). The dielectric anomaly observed at the antiferromagnetic ordering temperature (T_N) is independent of applied frequencies, indicating that these anomalies are not related to any relaxation phenomenon. Also, the value of dielectric loss is very low indicating that these compounds are highly insulating around the magnetic ordering temperature.

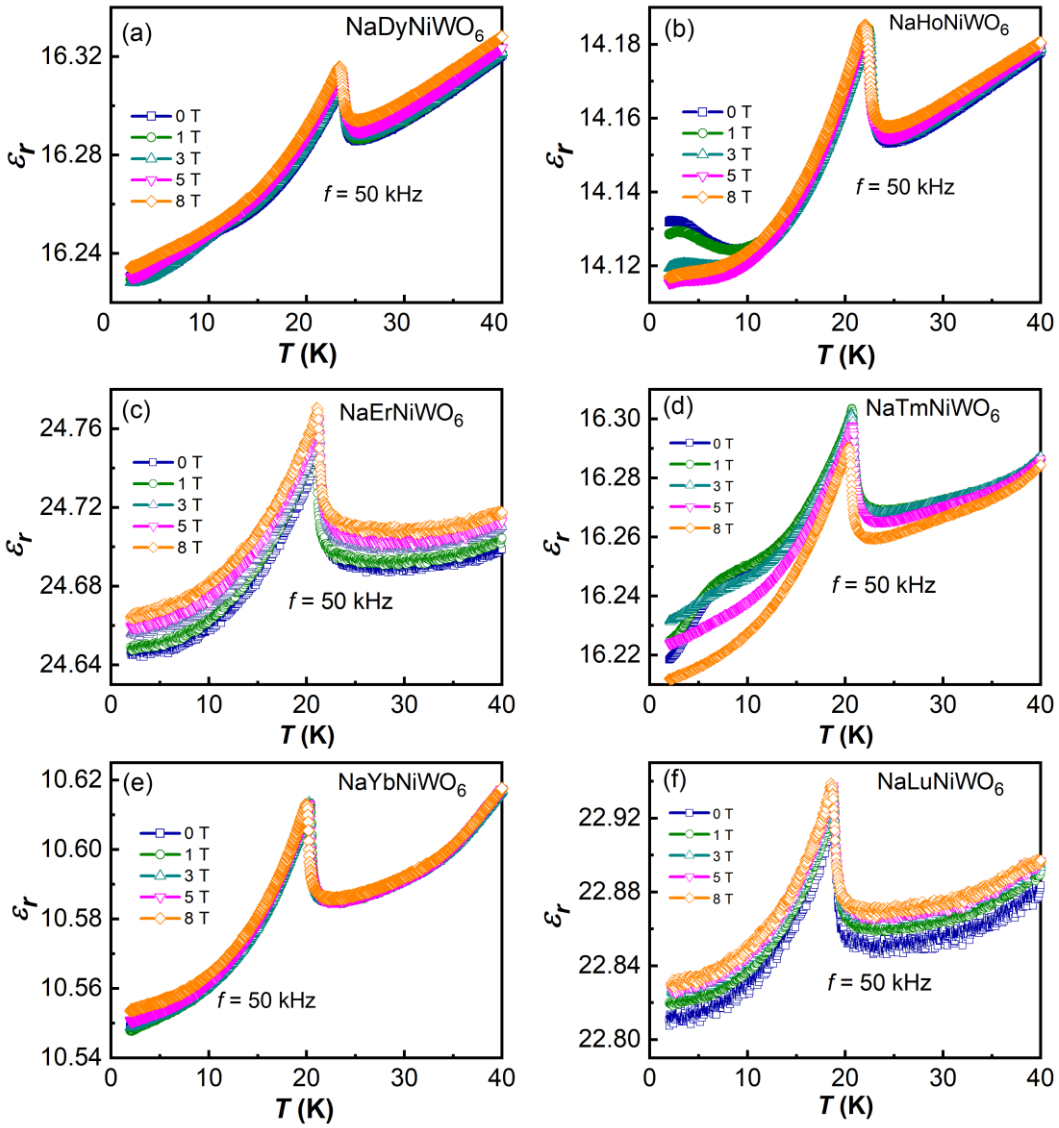

Figure 3.23 (a-f) Temperature variation of dielectric constant $\varepsilon_r(T)$ of Na*Ln*NiWO$_6$ (*Ln* = Dy-Lu) compounds measured at 0-8 T with 50 kHz frequency.

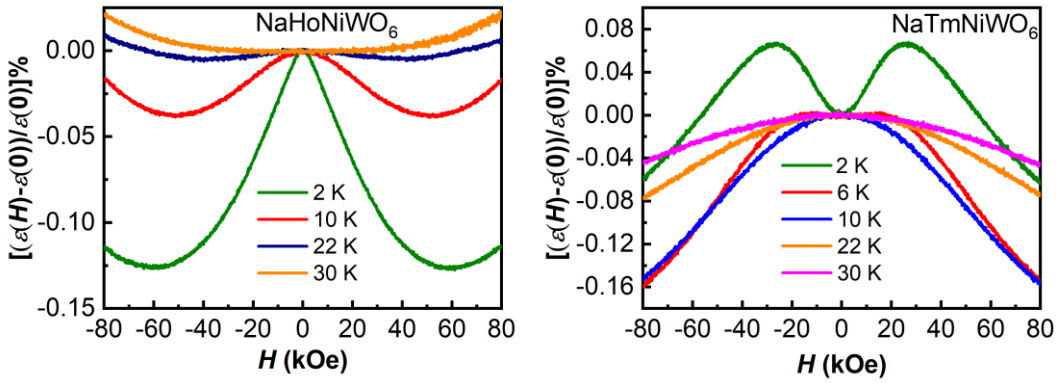

Figure 3.24 Magnetodielectric effect measured at different temperatures for NaHoNiWO$_6$ and NaTmNiWO$_6$.

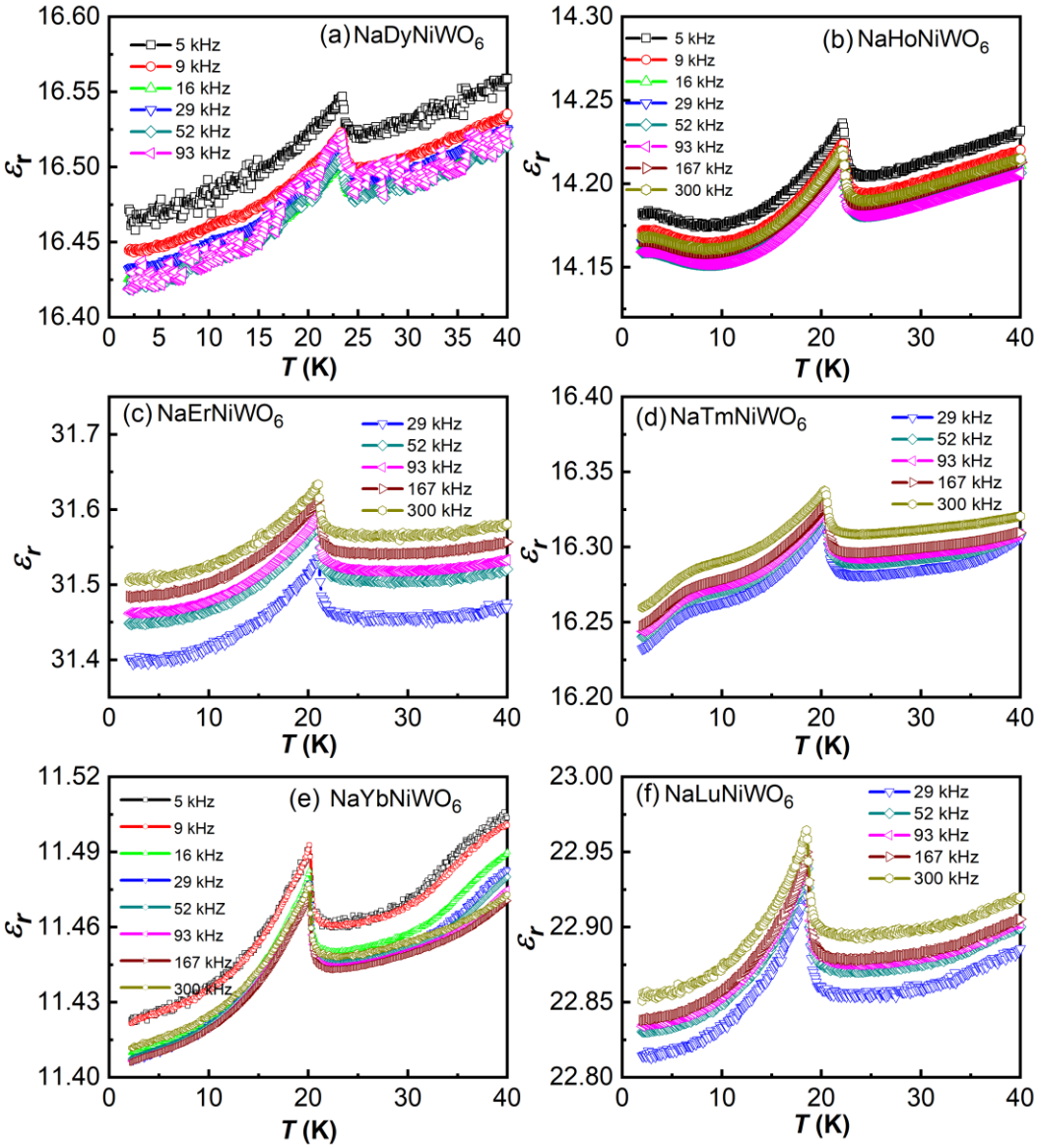

Figure 3.25 (a-f) Dielectric constant (ε_r) as a function of temperature with various frequencies.

The observed dielectric anomaly at T_N confirmed the magnetodielectric behavior of these compounds. In $NaTmNiWO_6$, another dielectric anomaly occurs at the Tm^{3+} ordering as observed in field dependent dielectric data.

Temperature dependent polarization and dc-bias data for $NaDyNiWO_6$ are shown in Figure 3.26(a,b). Temperature dependent dc-bias current measurement, measured with an applied electric field of E = +12.9 kV/cm, shows a small positive peak followed by a sharp negative depolarization current peak, which confirmed the ferroelectric nature of this compound at magnetic ordering temperature. Also, we have measured the dc-bias current by applying the electric field of E = -12.9 kV/cm to get the reverse dc-bias signal. By removing a

small positive polarization peak in the dc-bias signal, we have integrated depolarization peak to obtain spontaneous polarization.

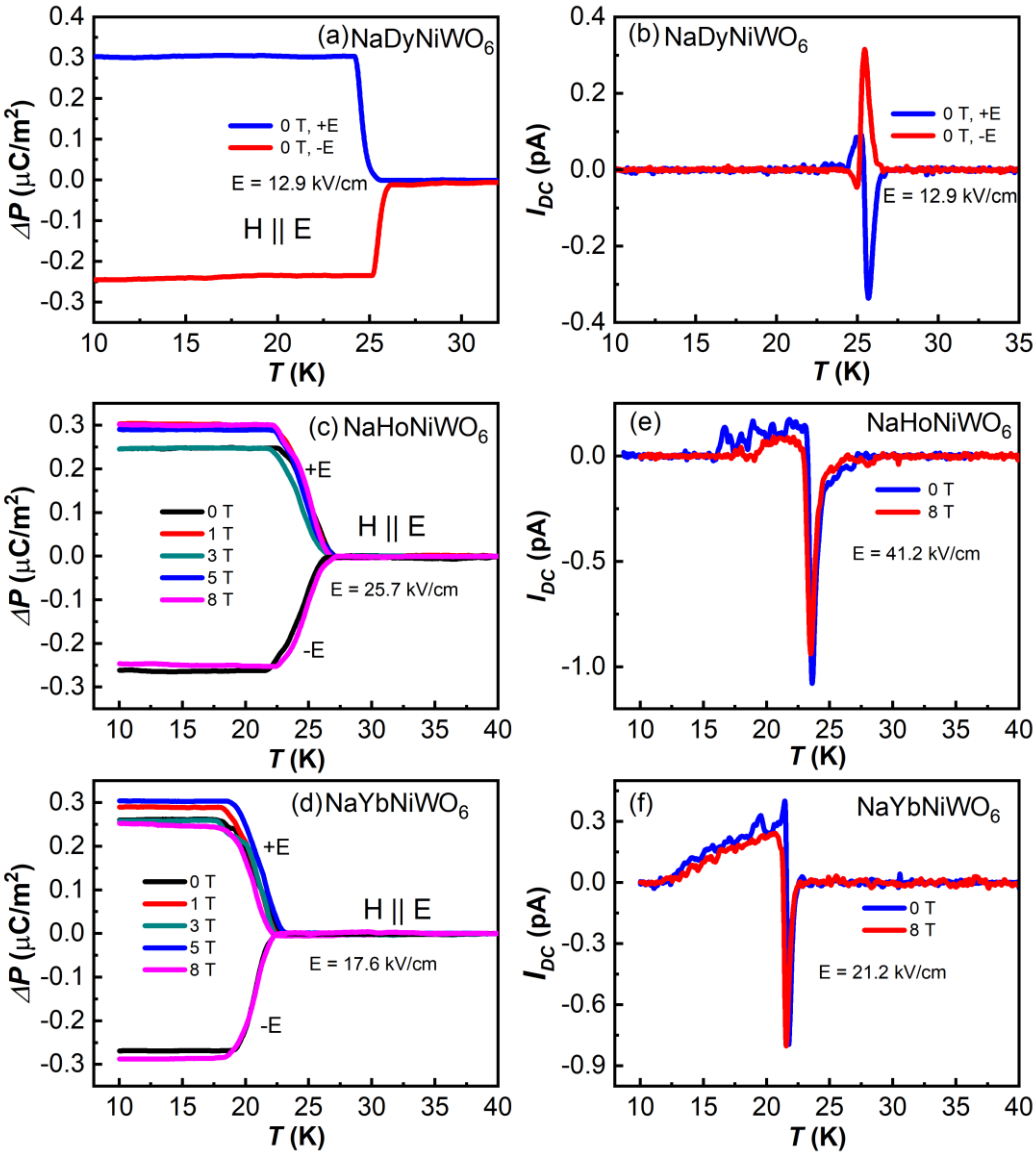

Figure 3.26 (a) Temperature dependent electric polarization $\Delta P(T)$ obtained from the integration of negative depolarization peak in dc-bias current measurement data of $NaDyNiWO_6$. (c,d) Change in electric polarization $\Delta P(T)$ against temperature under different magnetic fields obtained from the integration of pyroelectric current peak for Ho, Yb compounds. (b, e, and f) dc-bias current as a function of temperature measured with an electric field as mentioned in Figure and under magnetic fields 0 and 8 T.

The observed dc-bias signal at the magnetic ordering temperature confirmed the coupling between ferroelectricity and magnetism in this compound. We could not measure the pyroelectric current at T_N for $NaDyNiWO_6$, likely because the change in pyro current signal is too low to be detected. Temperature dependent electric polarization $\Delta P(T)$ and dc-bias current

measurement for the other two compounds $NaHoNiWO_6$ and $NaYbNiWO_6$ are shown in Figure 3.26, which confirmed the magnetoelectric coupling of these compounds below magnetic ordering temperature.

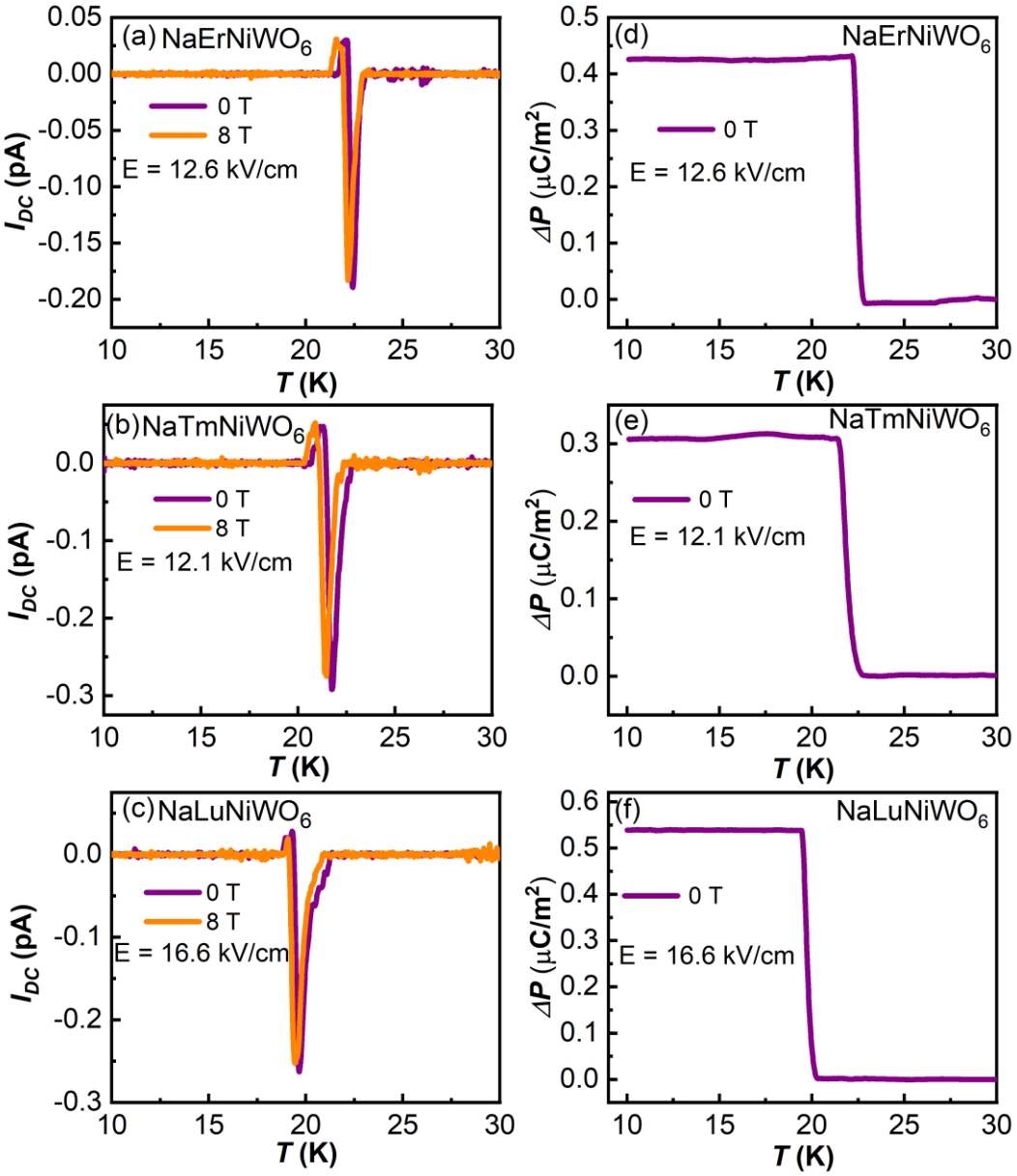

Figure 3.27 (a-c) Temperature dependent dc-bias current measured while warming the sample from 10 - 30 K in the presence of electric field (E). (d-f) Change in electric polarization (ΔP) against temperature obtained from the integration of the negative depolarization peak in dc-bias current data at 0 T.

We have not observed the significant pyroelectric anomaly for $NaErNiWO_6$, $NaTmNiWO_6$, and $NaLuNiWO_6$ compounds. The observed pyroelectric current was an order of magnitude smaller and close to the resolution limit of the measurement, which could be due

to the small value of change in electric polarization $\Delta P(T)$ of these compounds. However, the dc-bias current measurements of all these compounds (Figure 3.27(a-c)) show successive positive polarization and negative depolarization peaks near T_N. The observed positive peak is associated with ferroelectric polarization and subsequent sharp negative current peak related to depolarization of the ordered electric dipoles. The dc-biased current measurement is a well-known method that differentiates the sample's intrinsic pyroelectric peak from the extrinsic origin, which might appear due to the thermally stimulated free charge carriers (TSFC) [29]. To obtain the change in polarization below the magnetic ordering temperature, we integrated the depolarization peak of the dc-bias signal against time and presented it in Figure 3.27(d-f). The electric polarization obtained from the dc-bias signal at the magnetic ordering temperature confirmed the multiferroic properties of these compounds.

Although we have not performed neutron diffraction measurement in the other compounds, the observed double peak in the heat capacity data and appearance of ferroelectric polarization at magnetic ordering temperature of Ni^{2+} ions suggest that all other compounds should also have a similar incommensurate and commensurate magnetic structure of the Ni^{2+} moments. In all the compounds, the observed polarization at T_N could be due to possible enhancement of high temperature polarization expected from the magnetoelastic coupling, which was observed in the other class of compounds as well [9, 36–38]. The observation of multiferroic properties in these doubly ordered perovskites implies that the polar compounds constitute a very important family of compounds for magnetoelectric coupling without the requirement of a complex magnetic structure as reported in several type-II multiferroics.

3.4 Conclusion

We have synthesized a new family of doubly ordered perovskites Na*Ln*$NiWO_6$ (*Ln* = Y, Dy-Lu) under high pressure and high temperature conditions. These compounds crystallize in the polar $P2_1$ structure with the layered *A*-site and rock-salt *B*-site cation ordering. SHG studies were performed on $NaYNiWO_6$, $NaDyNiWO_6$, and $NaHoNiWO_6$ confirmed the non-centrosymmetric nature of these compounds. Magnetic and heat capacity measurements show that these compounds order antiferromagnetically between the temperature range of 18-23 K. Neutron diffraction studies revealed that at 20 K, the $NaYNiWO_6$ compound has an AFM spin density wave structure, and it changes to a commensurate collinear structure below 18 K. Theoretical studies show that the AFM chain of $NaYNiWO_6$ adopted unconventional AFM-SDW structure to reduce the spin frustration. A double-peak structure in the heat capacity data

of Na*Ln*NiWO$_6$ (*Ln* = Dy-Lu) suggests the presence of an incommensurate and commensurate magnetic phase transition in these compounds as well. Particularly, NaHoNiWO$_6$ and NaTmNiWO$_6$ compounds showed an additional dielectric anomaly below T_N corresponding to the short-range ordering of magnetic rare-earth cations and thus exhibited a magnetodielectric effect. The dielectric anomaly, switchability of the polarization change ($\Delta P(T)$), and dc-bias current signal at T_N suggest the multiferroic properties of these compounds. Experimental results of multiferroicity in doubly ordered perovskites open an avenue to design and predict new polar magnetic materials for interesting properties.

References

[1] F. Orlandi, L. Righi, R. Cabassi, D. Delmonte, C. Pernechele, F. Bolzoni, F. Mezzadri, M. Solzi, M. Merlini, and G. Calestani, Inorg. Chem. **53**, 10283 (2014).

[2] S. A. Ivanov, A. A. Bush, A. I. Stash, K. E. Kamentsev, V. Y. Shkuratov, Y. O. Kvashnin, C. Autieri, I. Di Marco, B. Sanyal, O. Eriksson, P. Nordblad, and R. Mathieu, Inorg. Chem. **55**, 2791 (2016).

[3] H. Hughes, M. M. B. Allix, C. A. Bridges, J. B. Claridge, X. Kuang, H. Niu, S. Taylor, W. Song, and M. J. Rosseinsky, J. Am. Chem. Soc. **127**, 13790 (2005).

[4] M. Azuma, K. Takata, T. Saito, S. Ishiwata, Y. Shimakawa, and M. Takano, J. Am. Chem. Soc. **127**, 8889 (2005).

[5] G. King, S. Thimmaiah, A. Dwivedi, and P. M. Woodward, Chem. Mater. **19**, 6451 (2007).

[6] T. Fukushima, A. Stroppa, S. Picozzi, and J. M. Perez-Mato, Phys. Chem. Chem. Phys. **13**, 12186 (2011).

[7] J. Young, A. Stroppa, S. Picozzi, and J. M. Rondinelli, Dalt. Trans. **44**, 10644 (2015).

[8] M. A. Arillo, J. Gómez, M. L. López, C. Pico, and M. Luisa Veiga, J. Mater. Chem. **7**, 801 (1997).

[9] C. De, T. H. Kim, K. H. Kim, and A. Sundaresan, Phys. Chem. Chem. Phys. **16**, 5407 (2014).

[10] P. Zuo, C. V Colin, H. Klein, P. Bordet, E. Suard, E. Elkaim, and C. Darie, Inorg. Chem. **56**, 8478 (2017).

[11] M. Retuerto, M. R. Li, A. Ignatov, M. Croft, K. V Ramanujachary, S. Chi, J. P. Hodges, W. Dachraoui, J. Hadermann, T. T. Tran, P. S. Halasyamani, C. P. Grams, J. Hemberger, and M. Greenblatt, Inorg. Chem. **52**, 12482 (2013).

[12] C. De and A. Sundaresan, Phys. Rev. B **97**, 214418 (2018).

[13] J. Rodriguez-Carvajal, in *Satellite Meeting on Powder Diffraction of the XV Congress of the IUCr*, Vol. 127 (Toulouse, France:[sn], 1990).

[14] H. M. Rietveld, J. Appl. Crystallogr. **2**, 65 (1969).

[15] L. C. Chapon, P. Manuel, P. G. Radaelli, C. Benson, L. Perrott, S. Ansell, N. J. Rhodes, D. Raspino, D. Duxbury, E. Spill, and J. Norris, Neutron News **22**, 22 (2011).

[16] V. Petříček, M. Dušek, and L. Palatinus, Zeitschrift Für Krist. Cryst. Mater. **229**, 345 (2014).

[17] B. J. Campbell, H. T. Stokes, D. E. Tanner, and D. M. Hatch, J. Appl. Crystallogr. **39**, 607 (2006).

[18] S. K. Kurtz and T. T. Perry, J. Appl. Phys. **39**, 3798 (1968).

[19] K. M. Ok, E. O. Chi, and P. S. Halasyamani, Chem. Soc. Rev. **35**, 710 (2006).

[20] A. M. Glazer, Acta Crystallogr. Sect. B **28**, 3384 (1972).

[21] T. Vogt, P. M. Woodward, and B. A. Hunter, J. Solid State Chem. **144**, 209 (1999).

[22] F. Orlandi, L. Righi, F. Mezzadri, P. Manuel, D. D. Khalyavin, D. Delmonte, C. Pernechele, R. Cabassi, F. Bolzoni, M. Solzi, and G. Calestani, Inorg. Chem. **55**, 4381 (2016).

[23] M. C. Knapp and P. M. Woodward, J. Solid State Chem. **179**, 1076 (2006).

[24] N. E. Brese and M. O'keeffe, Acta Crystallogr. Sect. B Struct. Sci. **47**, 192 (1991).

[25] H. Ikeda, I. Hatta, and M. Tanaka, J. Phys. Soc. Japan **40**, 334 (1976).

[26] M. R. Li, E. E. McCabe, P. W. Stephens, M. Croft, L. Collins, S. V. Kalinin, Z. Deng, M. Retuerto, A. Sen Gupta, H. Padmanabhan, V. Gopalan, C. P. Grams, J. Hemberger, F. Orlandi, P. Manuel, W. M. Li, C. Q. Jin, D. Walker, and M. Greenblatt, Nat. Commun. **8**, 2037 (2017).

[27] Y. S. Tang, S. M. Wang, L. Lin, C. Li, S. H. Zheng, C. F. Li, J. H. Zhang, Z. B. Yan, X. P. Jiang, and J. Liu, Phys. Rev. B **100**, 134112 (2019).

[28] A. Gauzzi, F. P. Milton, V. Pascotto Gastaldo, M. Verseils, A. J. Gualdi, D. Von Dreifus, Y. Klein, D. Garcia, A. J. A. De Oliveira, P. Bordet, and E. Gilioli, Appl. Phys. Lett. **115**, 152902 (2019).

[29] M. Chandra, S. Yadav, R. J. Choudary, R. Rawat, A. K. Sinha, M.-B. Leptit, K. singh, Phys. Rev. B **98**, 104427 (2018).

[30] C. De, S. Ghara, and A. Sundaresan, Solid State Commun. **205**, 61 (2015).

[31] H. Xiang, C. Lee, H.-J. Koo, X. Gong, and M.-H. Whangbo, Dalt. Trans. **42**, 823 (2013).

[32] H. J. Xiang, S.-H. Wei, M.-H. Whangbo, and J. L. F. Da Silva, Phys. Rev. Lett. **101**, 37209 (2008).

[33] E. J. Kan, H. J. Xiang, Y. Zhang, C. Lee, and M.-H. Whangbo, Phys. Rev. B **80**, 104417 (2009).

[34] C. Lee, E. Kan, H. Xiang, and M.-H. Whangbo, Chem. Mater. **22**, 5290 (2010).

[35] X. Z. Lu, M.-H. Whangbo, S. Dong, X. G. Gong, and H. J. Xiang, Phys. Rev. Lett. **108**, 187204 (2012).

[36] J. H. Yang, Z. L. Li, X. Z. Lu, M.-H. Whangbo, S.-H. Wei, X. G. Gong, and H. J. Xiang, Phys. Rev. Lett. **109**, 107203 (2012).

[37] E. E. Gordon, S. Derakhshan, C. M. Thompson, and M.-H. Whangbo, Inorg. Chem. **57**, 9782 (2018).

[38] C. M. Thompson, J. E. Greedan, V. O. Garlea, R. Flacau, M. Tan, P.-H. T. Nguyen, F. Wrobel, and S. Derakhshan, Inorg. Chem. **53**, 1122 (2014).

[39] D. Senff, P. Link, K. Hradil, A. Hiess, L. P. Regnault, Y. Sidis, N. Aliouane, D. N. Argyriou, and M. Braden, Phys. Rev. Lett. **98**, 137206 (2007).

[40] D. Senff, N. Aliouane, D. N. Argyriou, A. Hiess, L. P. Regnault, P. Link, K. Hradil, Y. Sidis, and M. Braden, J. Phys. Condens. Matter **20**, 434212 (2008).

[41] O. Prokhnenko, R. Feyerherm, E. Dudzik, S. Landsgesell, N. Aliouane, L. C. Chapon,

and D. N. Argyriou, Phys. Rev. Lett. **98**, 57206 (2007).

[42] A. Sobolev, V. Rusakov, A. Moskvin, A. Gapochka, A. Belik, I. Glazkova, A. Akulenko, G. Demazeau, and I. Presniakov, J. Phys. Condens. Matter **29**, 275803 (2017).

[43] N. Terada, D. D. Khalyavin, P. Manuel, Y. Tsujimoto, K. Knight, P. G. Radaelli, H. S. Suzuki, and H. Kitazawa, Phys. Rev. Lett. **109**, 97203 (2012).

[44] I. Urcelay-Olabarria, J. M. Perez-Mato, J. L. Ribeiro, J. L. García-Muñoz, E. Ressouche, V. Skumryev, and A. A. Mukhin, Phys. Rev. B **87**, 14419 (2013).

[45] R. Shankar P N, F. Orlandi, P. Manuel, W. Zhang, P. S. Halasyamani, and A. Sundaresan, Chem. Mater. **32**, 5641 (2020).

[46] M.-H. Whangbo, H.-J. Koo, and D. Dai, J. Solid State Chem. **176**, 417 (2003).

[47] M.-H. Whangbo and H. Xiang, 285 (2017).

[48] G. Kresse and J. Furthmüller, Comput. Mater. Sci. **6**, 15 (1996).

[49] G. Kresse and D. Joubert, Phys. Rev. B **59**, 1758 (1999).

[50] J. P. Perdew, K. Burke, and M. Ernzerhof, Phys. Rev. Lett. **77**, 3865 (1996).

[51] S. L. Dudarev, G. A. Botton, S. Y. Savrasov, C. J. Humphreys, and A. P. Sutton, Phys. Rev. B **57**, 1505 (1998).

[52] J. Kuneš, P. Novák, R. Schmid, P. Blaha, and K. Schwarz, Phys. Rev. B **64**, 153102 (2001).

[53] P. Manuel, L. C. Chapon, I. S. Todorov, D. Y. Chung, J.-P. Castellan, S. Rosenkranz, R. Osborn, P. Toledano, and M. G. Kanatzidis, Phys. Rev. B **81**, 184402 (2010).

[54] F. Orlandi, L. Righi, C. Ritter, C. Pernechele, M. Solzi, R. Cabassi, F. Bolzoni, and G. Calestani, J. Mater. Chem. C **2**, 9215 (2014).

[55] A. Muñoz, J. A. Alonso, M. T. Casais, M. J. Martínez-Lope, J. L. Martínez, and M. T. Fernández-Díaz, J. Phys. Condens. Matter **14**, 3285 (2002).

[56] C. De, R. Bag, S. Singh, F. Orlandi, P. Manuel, S. Langridge, M. K. Sanyal, C. N. R. Rao, M. Mostovoy, and A. Sundaresan, Phys. Rev. Mater. **3**, 44401 (2019).

[57] C. V Colin, L. Ding, E. Ressouche, J. Robert, N. Terada, F. Gay, P. Lejay, V. Simonet, C. Darie, P. Bordet, and S. Petit, Phys. Rev. B **101**, 235109 (2020).

Chapter 4

Structural, magnetic and electrical properties of Na*Ln*NiWO$_6$ (*Ln* = La, Pr, Nd, Sm, Eu, Gd, and Tb)*

Summary

The crystal structure and physical properties of series of compounds Na*Ln*NiWO$_6$ (*Ln* = La, Pr, Nd, Sm, Eu, Gd, and Tb) with higher size rare-earth cations are investigated in this work. Using neutron (*Ln* = La), X-ray diffraction, and second-harmonic generation (SHG) studies, these compounds are found to be crystallized in the monoclinic structure with the polar space group $P2_1$. These materials exhibit a combined layered ordering of *A*-site cations and rock-salt ordering of *B*-site cations with octahedral tilting, which breaks the inversion symmetry similar to NaYNiWO$_6$. These compounds undergo a long-range antiferromagnetic ordering in the temperature range of 23 – 30 K, depending on the *Ln*-ion. NaLaNiWO$_6$ has a simple collinear magnetic structure with the propagation vector, **k** = (½, 0, ½). In contrast to the compounds with smaller lanthanide ions (*Ln* = Y, Dy-Lu), these compounds do not exhibit measurable electric polarization at T_N but show a dielectric anomaly.

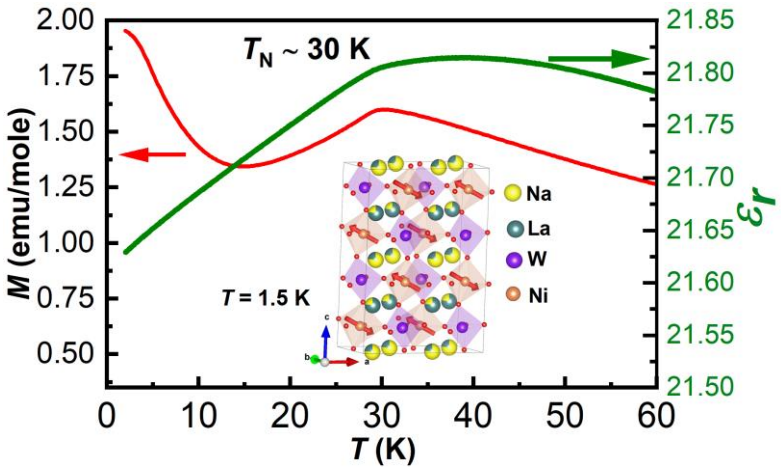

……

*Paper based on this work is published in *J. Phys. Chem. C*, **125**, 6749 (2021), © 2021 by the American Chemical Society.

4.1 Introduction

By substituting suitable aliovalent cations at both the sites in $AA'BB'O_6$ perovskites, it is possible to expand the doubly ordered perovskites family further. The compounds NaLa*M*WO_6 (*M* = Co, Ni), $KLaMnWO_6$, Na*Ln*$MnWO_6$, Na*Ln*$MgWO_6$, Na*Ln*$CoWO_6$ (*Ln* = different rare-earth ions), and Na*Ln*$FeWO_6$ (*Ln* = La, Nd, Pr, and Sm) are reported, but their electrical properties are unexplored [1–5], except for Na*Ln*$MnWO_6$ (*Ln* = La, Nd, and Tb) and Na*Ln*$FeWO_6$ (*Ln* = La, Nd, Sm, and Pr), where they showed the absence of polarization despite the polar crystal structure ($P2_1$) [3,5]. Further, it has been reported that doubly ordered perovskites possess different magnetic structures depending on the different rare-earth cations and magnetic M^{2+} ions. The magnetic structure of $NaLaMnWO_6$ is collinear with a propagation vector of **k** = (½, 0, ½) [6]. In the case of $NaNdMnWO_6$, the Nd and Mn moments order with incommensurate **k**-vector = (0, 0.48, ½) and magnitude of moment size vary sinusoidally along the *b*-direction [6]. Further, Na*Ln*$FeWO_6$ (*Ln* = Nd, Pr) shows a commensurate propagation vector k = (½, 0, ½) and a collinear magnetic structure with both the magnetic ion moments along the *b*-axis [5]. The magnetic structure of $NaTbMnWO_6$, determined at 11 K, shows two propagation vectors $\mathbf{k}_1$ = (½, 0, ½) and $\mathbf{k}_2$ = (0, 0.427, ½), which became a single **k** structure at lower temperature with the $\mathbf{k}_1$ propagation vector [6].

In the previous chapter, a series of compounds, Na*Ln*$NiWO_6$ (*Ln* = Y, Dy-Lu), was shown to exhibit multiferroic properties below the antiferromagnetic order of Ni^{2+} ions (T_N ~ 18 to 23 K) [7]. Given the multiferroic properties shown by the doubly ordered perovskites, we have extended the studies on doubly ordered perovskites with larger size rare-earth cations Na*Ln*$NiWO_6$ (*Ln* = La, Pr, Nd, Sm, Eu, Gd, and Tb). Neutron powder diffraction (NPD) data on $NaLaNiWO_6$ and powder X-ray diffraction (PXRD) data on all other compounds viz. (Pr, Nd, Sm, Eu, Gd, and Tb) are fitted with the monoclinic $P2_1$ space group. The non-centrosymmetric nature of Na*Ln*$NiWO_6$ (*Ln* = La, Sm, Eu, Gd, and Tb) is confirmed by second harmonic generation studies. All these compounds exhibit antiferromagnetic ordering of Ni^{2+} ions between 23-30 K. The magnetic structure of $NaLaNiWO_6$ is collinear with a propagation vector of **k** = (½, 0, ½). Na*Ln*$NiWO_6$ (*Ln* = La, Pr, and Nd) show a small change in dielectric value. In contrast, other compounds exhibited a sharp dielectric anomaly at the magnetic ordering temperature but without measurable change in electric polarization. This could be due to very small polarization that cannot be measured within the instrument's resolution limit.

4.2 Experimental section

All the compounds Na*Ln*NiWO$_6$ (*Ln* = La, Pr, Nd, Sm, Eu, Gd, and Tb) were synthesized at 4.5 GPa and 1000 ºC using a cubic-anvil type high pressure apparatus as depicted in the previous chapter. The starting materials Ln_2O_3 (preheated at 950 °C), $Na_2WO_4{\cdot}2H_2O$ (preheated at 150 ºC), NiO, and WO_3 were used to synthesize the required compounds. Pr_6O_{11} and Tb_4O_7 were reduced by 5% H_2/95% Ar flux at 1000 ºC for 12 h to obtain Pr_2O_3 and Tb_2O_3. Powder X-ray diffraction data were collected using a monochromatic PANalytical Empyrean alpha-1 diffractometer, and Rietveld refinements were carried out using the FullProf suite program for all the compounds [8]. Time-of-flight neutron diffraction data were collected in the temperature range of 1.5 - 100 K for NaLaNiWO$_6$ using the high-resolution WISH diffractometer at the ISIS pulsed neutron and muon facility (Rutherford Appleton Laboratory UK) [9]. Rietveld refinement of neutron data was carried out using the JANA2006 program [10]. Online-based ISOTROPY and ISODISTORT software were used to perform group-theoretical analysis. Similar physical property characterization was performed on these compounds, as mentioned in the previous chapter.

4.3 Results and discussion

4.3.1 Structural analysis

Powder X-ray diffraction was performed to characterize the crystal structure of these compounds. Various superstructural peaks, indexed for the simple cubic perovskite (with $a_p \approx$ 3.8 Å), appear in the diffraction pattern. The reflections (0 0 ½), (1 0 ½) indicate the layered ordering of *A*-site cations, whereas the strong reflections (½ ½ ½) and (1 ½ ½) indicate the rock-salt ordering of the *B*-site cations. When both the *A*-site and *B*-site cations exhibit combined layer and rock-salt ordering, symmetry reduces from cubic ($Pm\bar{3}m$) to tetragonal ($P4/nmm$) with the unit cell parameters $\sqrt{2}a_p{*}\sqrt{2}a_p{*}2a_p$. The $P4/nmm$ space group accounts for most of the superstructural peaks observed in the X-ray diffraction data, but some reflections remain unindexed and relate to octahedral tilting distortions.

Knapp *et al*. have predicted all possible lower symmetry space groups by considering the layered ordering of *A*-site and rock-salt ordering of *B*-site cations accompanied by the $BO_6/B'O_6$ octahedral tiltings [11]. Space groups $P2_1/m$ and $P2_1$ are deduced via the out-of-phase octahedral tilting along the *a*- and *b*-direction represented as $a^-a^-c^0$ in Glazer notation and by the in-phase tilting ($a^-a^-c^+$) along the *c*-axis [12]. Additional in-phase rotation of the

octahedra along the *c*-axis breaks the inversion center and allows the symmetry to lower to the $P2_1$ space group. Since only La compound is characterized by neutron diffraction, SHG measurements are performed to verify whether the compounds are centrosymmetric or not. The compounds La, Sm, Eu, and Gd showed SHG activity with laser intensities, 0.52, 0.65, 0.58, and 0.48 times of α-SiO_2, supporting the polar space group $P2_1$.

However, we have analyzed the PXRD pattern of these compounds using both $P2_1/m$ and $P2_1$ space groups. Because of the same extinction conditions of $P2_1$ and $P2_1/m$, these can only be differentiated by considering the peak intensities. PXRD patterns showed a higher degree of peak splitting with increasing octahedral distortion, which is in accordance with the decreasing tolerance factor with respect to the lanthanide contraction. Diffraction peak intensities of the Pr, Nd, Sm, Eu, Gd, and Tb compounds were better fitted with a $P2_1$ space group. Rietveld refinement revealed a slight disorder of *A*-site cations and complete ordering of *B*-site cations owing to the large difference in cationic charges (differing by four) at the *B*-site, whereas at the *A*-site is differing by two. This difference in the valence states favors the cation ordering due to the minimization of the electrostatic energy. In particular, rock-salt ordering of the *B*-site cations keeps the highly charged cations far apart and thereby helps for the complete ordering in $AA'BB'O_6$ perovskite. A plot of unit cell parameters as a function of the radius of eight coordinated Ln^{3+} ions [13] is shown in Figure 4.1, where the *a* and *c* parameters decrease while the *b* parameter almost remains unchanged and the volume decreases steadily with the decreasing size of the Ln^{3+} cations.

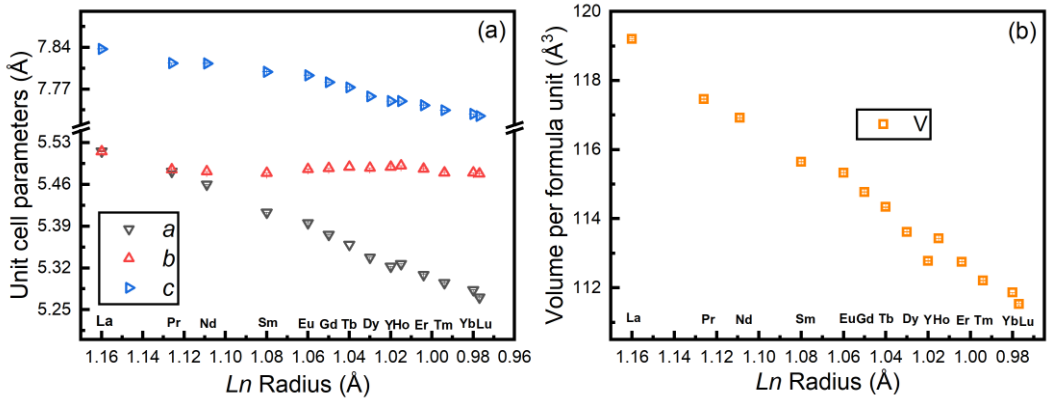

Figure 4.1 Unit cell parameters and volume per formula unit of Na*Ln*$NiWO_6$ plotted as a function of the radius of eight coordinated Ln^{3+} ions.

4.3.2 Results on $NaLaNiWO_6$

4.3.2.1 Crystal structure

$NaLaNiWO_6$ was first reported by Arillo *et al*. by a sol-gel synthesis procedure. Although we could synthesize at ambient pressure, the impurities were relatively high. The observed impurities were La_2WO_6, and Na_2WO_4 which have more preferences for formation than the expected perovskite phase at ambient pressure. This is related to the requirement of a higher coordination number for alkali and tungsten cations in the perovskite phase compared to the Na_2WO_4 phase, which can be achieved using a high pressure synthesis route. Rietveld refinement of room temperature PXRD data with the $P2_1$ space group is shown in Figure A-2.4.1, and the structural parameters are listed in Table A-2.4.1. A minute amount of impurity phases viz. La_2WO_6 (~0.5%), NiO (~1%), and $Na_2WO_4{\cdot}2H_2O$ (~1%) were identified, and their corresponding weight percentages were derived from Rietveld refinement analysis [14].

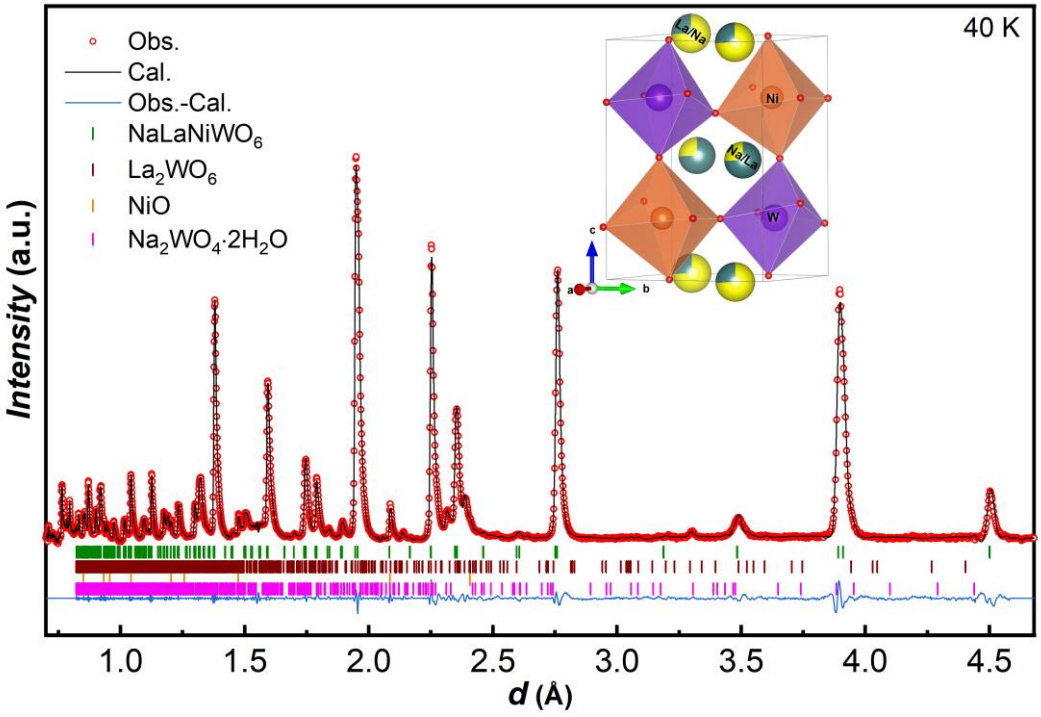

Figure 4.2 Rietveld fit of neutron diffraction data at 40 K, from the high-resolution WISH bank with an average 2θ = 152.8º, and the inset shows the crystal structure of $NaLaNiWO_6$.

The refined NPD pattern of $NaLaNiWO_6$ at 40 K with the $P2_1$ space group is shown in Figure 4.2, and the corresponding structural parameters are tabulated in Table 4.1. The crystal structure of $NaLaNiWO_6$, showing rock-salt ordering on the *B*-site and layered ordering on the

A-site, is shown in the inset of Figure 4.2. The various bond lengths in Ni(W)O_6 octahedra obtained from the refinements are given in Table 4.2. The octahedra tilting is out-of-phase along the *a*- and *b*-axes and in-phase along the *c*-axis resulting in all Ni-O-W bond angles less than 180º as listed in Table 4.2.

Table 4.1 Crystallographic parameters of $NaLaNiWO_6$ from the refinement of NPD data collected at 40 K.

Atom	Wyckoff position	*x*	*y*	*z*	U_{iso}(Å^2)	Occ.
Na1	2*a*	0.2264(5)	0.2256	0.0126(8)	0.0241(1)	0.7938(4)
La2	2*a*	0.2264(5)	0.2256	0.0126(8)	0.0241(1)	0.2062(4)
La1	2*a*	0.2522(9)	0.2643(2)	0.4948(2)	0.0148(1)	0.7938(4)
Na2	2*a*	0.2522(9)	0.2643(2)	0.4948(2)	0.0148(1)	0.2062(4)
Ni	2*a*	0.7567(2)	0.24961	0.2418(3)	0.0158(1)	1.0
W	2*a*	0.7735(6)	0.24824	0.7569(8)	0.0042(1)	1.0
O1	2*a*	0.5460(2)	0.5073(5)	0.7194(2)	0.0106(2)	1.0
O2	2*a*	0.5390(3)	0.5371(6)	0.2583(3)	0.0367(1)	1.0
O3	2*a*	0.0572(3)	0.0232(8)	0.2149(3)	0.0061(2)	1.0
O4	2*a*	0.0460(4)	0.0494(6)	0.7367(4)	0.0432(1)	1.0
O5	2*a*	0.8190(3)	0.2714(6)	0.5149(4)	0.0215(2)	1.0
O6	2*a*	0.6688(3)	0.2502(7)	-0.0169(3)	0.0405(1)	1.0

Space group: $P2_1$; a = 5.5054(2) Å, b = 5.5076(2) Å, c = 7.8275(1) Å, β = 90.094(5)°. Vol.: 237.35(1) Å^3; GOF = 2.47, R_p = 1.21 (%), R_{wp} = 1.58 (%).

Table 4.2 Selected bond lengths and angles for $NaLaNiWO_6$ at 40 K.

Atom	O1	O2	O3	O4	O5	O6
Ni (Å)	2.083(3)	2.058(2)	2.091(4)	2.006(3)	2.036(4)	2.152(3)
W (Å)	2.076(3)	2.060(3)	1.826(5)	1.822(3)	1.795(5)	2.050(5)
Ni-O-W (deg)	153.4(2)	157.2(1)	147.7(2)	156.9(1)	162.3(1)	149.6(9)

4.3.2.2 Magnetic measurements

Temperature-dependent dc magnetic susceptibility measured under zero-field-cooled (ZFC) and field-cooled (FC) conditions with an applied magnetic field of 100 Oe and heat capacity data (C_p) reveal antiferromagnetic ordering around 30 K, as depicted in Figure 4.3(a). At low temperatures, ZFC and FC curves diverged around 5 K, wherein the ZFC curve exhibits a peak. The observed peak in the ZFC curve at 5 K and the irreversibility between ZFC and FC curves may be due to the presence of NiO particles as an impurity phase [15]. Isothermal magnetization curves *vs*. the magnetic field at various temperatures exhibit linear behavior, as shown in Figure 4.3(b), consistent with antiferromagnetic order.

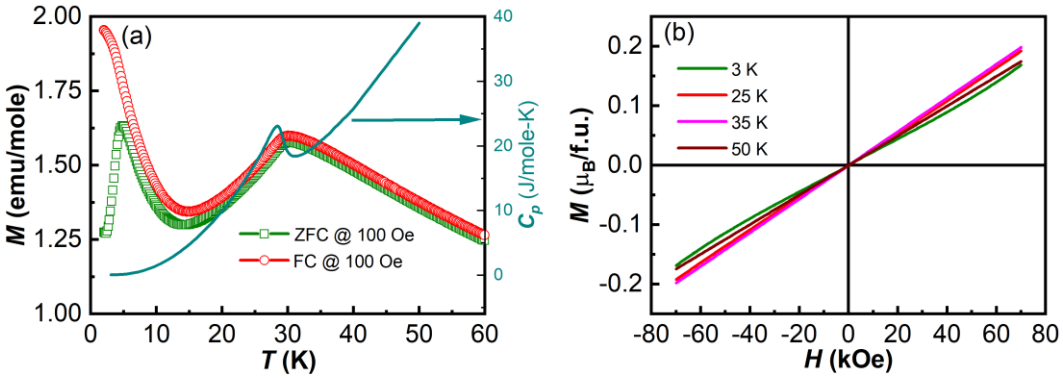

Figure 4.3 (a) Temperature-dependent magnetization of $NaLaNiWO_6$ measured with a magnetic field of 100 Oe and C_P data as a function of temperature. (b) Magnetic-field dependent magnetization $M(H)$ at different isothermal temperatures.

The linear fitting of inverse molar susceptibility ($1/\chi_m$) *vs.* temperature at high temperature follows the Curie-Weiss law as depicted in Figure 4.4. The obtained value of effective magnetic moment (μ_{eff} = 3.43 μ_B/f.u) of Ni^{2+} is slightly higher than the free-ion value (2.83 μ_B) but comparable to the generally observed magnetic moment for Ni^{2+} ion (3.2 μ_B) in other compounds [16]. Also, the Curie-Weiss fitting was performed by subtracting the experimental NiO magnetization considering the 1% NiO impurity phase obtained during Rietveld refinement of $NaLaNiWO_6$, but the effective magnetic moment is almost the same. Hence, the higher value of the experimental magnetic moment may indicate an orbital contribution. The Curie-Weiss temperature was found to be -40 K, which is consistent with the antiferromagnetic interaction of Ni^{2+} ions.

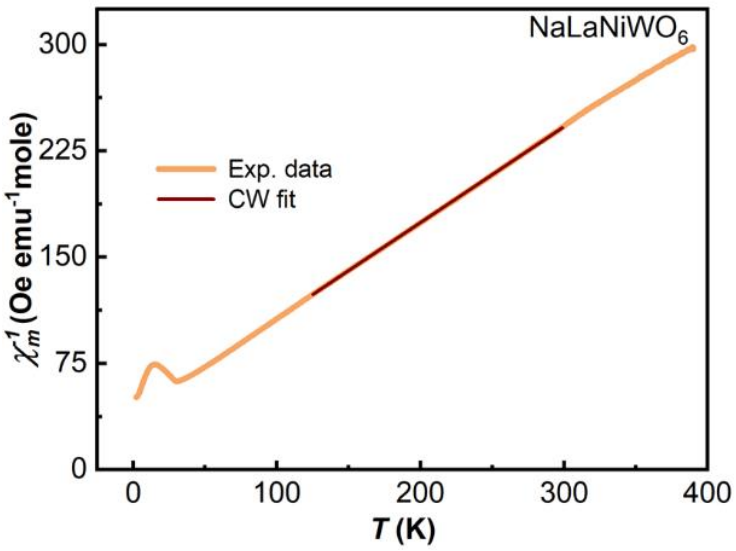

Figure 4.4 Linear Curie-Weiss fit was performed on the inverse susceptibility ($1/\chi_m$) *vs.* temperature (T) plot.

4.3.2.3 Magnetic structure

The NPD data were collected to determine the magnetic structure of $NaLaNiWO_6$, considering that the neutron absorption cross-section of La^{3+} is relatively small compared to other rare-earth cations. Long scan data were collected at 40 and 1.5 K to determine the paramagnetic structure and magnetic ground state. The new magnetic satellites observed below T_N, as in Figure 4.5, can be indexed with the propagation vector (½ 0 ½). The Rietveld fit of NPD data at 1.5 K using the JANA2006 program is depicted in Figure 4.5. The magnetic space group was determined by performing group-theoretical calculations with the help of the ISODISTORT program [17]. The magnetic space group $B[a]2_1$ described in the unit cell ($2a$ b $2c$) obtained by the action of the mA2 irreducible representation is in excellent agreement with the observed data. Various combinations of magnetic moments have been tried, but the better fit was achieved when we refined the moment values along the a- and c-axes.

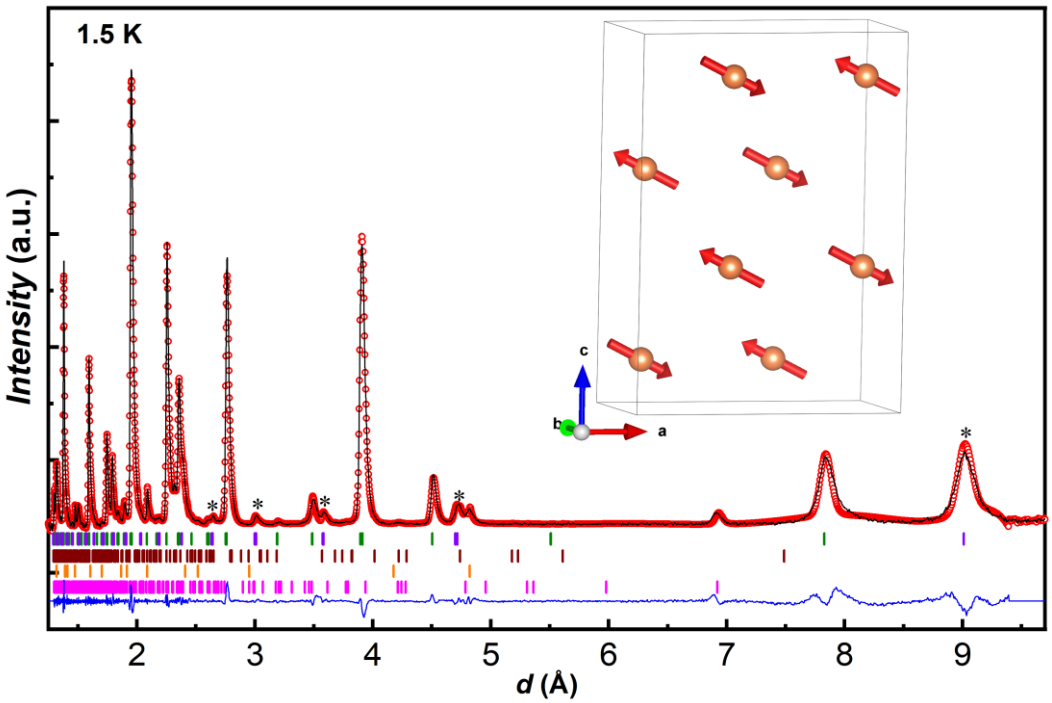

Figure 4.5 Rietveld refinement pattern of $NaLaNiWO_6$ for neutron powder diffraction data collected on WISH at 2θ = 58.3º and 1.5 K. The experimental data, fit, and difference are presented in red, black, and blue color. Olive green and violet tick marks indicate the Bragg reflections for nuclear and magnetic structures of $NaLaNiWO_6$. Intense magnetic reflections are indicated by the asterisks. Wine, orange, and magenta tick marks indicate the Bragg reflections for La_2WO_6, NiO, and $Na_2WO_4{\cdot}2H_2O$ impurity phases. Inset: magnetic structure of $NaLaNiWO_6$ with the magnetic moments plotted on the Ni atom.

The magnetic spin structure at 1.5 K exhibits a collinear structure, as shown in the inset of Figure 4.5. The magnetic structure has moment components of M_x = 1.29(1) μ_B and M_z = -0.5(1) μ_B, with a total magnetic moment of 1.38(2) μ_B at 1.5 K.

4.3.2.4 Dielectric studies

The temperature dependence of the dielectric constant is measured to examine possible magnetoelectric coupling around the magnetic ordering temperature. Dielectric data at 50 kHz under applied fields in the range 0 - 8 T for $NaLaNiWO_6$ are given in Figure 4.6(a) and at different frequencies and zero field, in the temperature range 2 - 60 K, are shown in Figure 4.6(b). A small change in dielectric value around the magnetic ordering temperature is seen in Figure 4.6. Although the structure is polar, pyroelectric, and dc-bias current measurements did not show an anomaly indicating the absence of spin-induced change in polarization or the induced polarization is too small to be detected within the limit of our measurement. Our attempt to measure the *P-E* loop above the magnetic ordering temperature did not indicate ferroelectricity, although the paramagnetic structure is polar, indicating that this compound may remain pyroelectric.

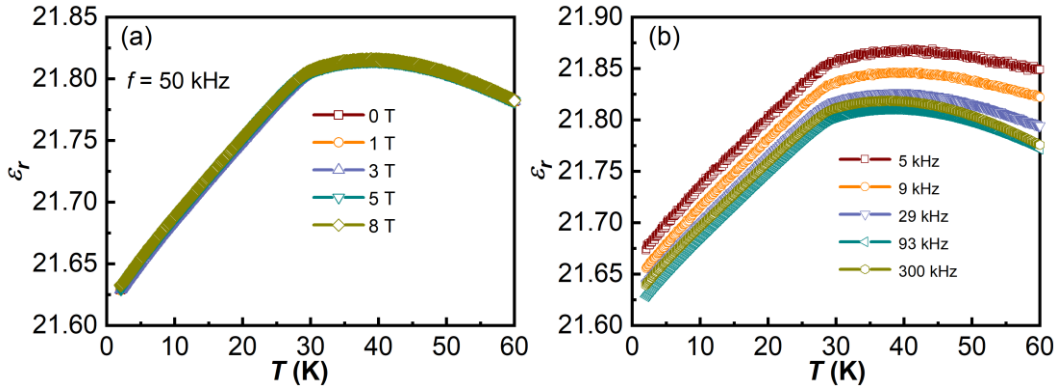

Figure 4.6 (a) Temperature and field-dependent dielectric constant $\varepsilon_r(T)$ at 50 kHz. (b) Temperature- frequency-dependent dielectric constant.

4.3.3 Results on Na*Ln*NiWO$_6$ (*Ln* = Pr, Nd, Sm, Eu, Gd, and Tb)

4.3.3.1 Crystal structure

All these compounds were characterized using powder x-ray diffraction at room temperature (RT), and they are well fitted with the $P2_1$ space group. The intensity of reflections

(0 0 ½) and (1 0 ½), corresponding to the *A*-site layer ordering, were fitted better if we consider a certain degree of disorder in the *A*-site for all compounds. Results of Rietveld refinement and the corresponding structural details are given in appendix-2 (Figure A-2.4.2 to A-2.4.7 and Table A-2.4.2 to A-2.4.7).

Table 4.3 Lattice parameters obtained from Rietveld refinement of PXRD data of Na*Ln*$NiWO_6$ (*Ln* = La, Pr, Nd, Sm, Eu, Gd, and Tb) at room temperature.

Compound	*a* (Å)	*b* (Å)	*c* (Å)	*β* (°)	*V* (Å^3)
$NaLaNiWO_6$	5.5158(8)	5.5151(8)	7.8372(2)	90.12(1)	238.41(5)
$NaPrNiWO_6$	5.4818(4)	5.4849(4)	7.8134(2)	90.110(3)	234.92(2)
$NaNdNiWO_6$	5.4599(1)	5.4814(1)	7.8131(1)	90.164(2)	233.83(2)
$NaSmNiWO_6$	5.4131(1)	5.4788(1)	7.7990(2)	90.25(1)	231.29(1)
$NaEuNiWO_6$	5.3957(1)	5.4855(1)	7.7931(1)	90.261(2)	230.66(1)
$NaGdNiWO_6$	5.3761(1)	5.4868(1)	7.7815(1)	90.248(2)	229.54(1)
$NaTbNiWO_6$	5.3596(0)	5.4892(0)	7.7729(1)	90.258(2)	228.67(3)

Table 4.4 Selected bond lengths (Angstroms) and bond angles (Degrees) obtained from Rietveld refinement of PXRD data of Na*Ln*$NiWO_6$ (*Ln* = La, Pr, Nd, Sm, Eu, Gd, and Tb).

	La	**Pr**	**Nd**	**Sm**	**Eu**	**Gd**	**Tb**
Ni-O(1)	2.1(1)	2.03(6)	1.86(4)	1.85(6)	1.80(3)	1.85(4)	1.94(3)
Ni-O(2)	2.1(2)	2.04(7)	1.85(4)	1.78(5)	1.92(3)	1.92(4)	1.95(3)
Ni-O(3)	2.0(1)	2.00(8)	1.88(4)	2.26(3)	1.99(2)	1.89(3)	1.95(3)
Ni-O(4)	1.68(8)	1.71(4)	1.94(4)	1.85(4)	1.98(2)	2.03(3)	1.99(3)
Ni-O(5)	1.85(3)	1.99(2)	1.99(2)	2.01(2)	2.0(2)	1.87(2)	2.01(2)
Ni-O(6)	1.96(3)	1.92(2)	1.83(2)	1.89(2)	1.94(2)	2.02(2)	1.95(2)
W-O(1)	1.8(1)	2.06(6)	2.10(4)	2.07(6)	2.16(3)	2.14(4)	2.10(2)
W-O(2)	1.8(2)	1.84(7)	2.08(4)	2.10(5)	2.04(3)	2.01(4)	2.08(2)
W-O(3)	2.0(1)	1.89(7)	1.99(4)	1.77(3)	1.87(2)	1.98(3)	1.95(2)
W-O(4)	2.25(8)	2.42(3)	2.27(3)	2.18(4)	1.95(2)	1.83(3)	1.98(2)
W-O(5)	2.20(2)	2.22(2)	2.21(2)	2.18(2)	2.20(2)	2.33(2)	2.21(2)
W-O(6)	1.90(3)	1.83(2)	2.00(2)	1.90(2)	1.88(2)	2.04(2)	1.87(2)
Ni-O(1)-W	163(7)	143(2)	157(3)	160(6)	155(3)	152(4)	149(1)
Ni-O(2)-W	156(8)	173(3)	162(3)	168(6)	155(3)	161(4)	148(1)
Ni-O(3)-W	155(5)	173(3)	171(3)	145(2)	165(1)	159(2)	155(1)
Ni-O(4)-W	170(4)	140(2)	133(2)	144(3)	153(2)	161(3)	146(2)
Ni-O(5)-W	168(3)	155(4)	154(2)	155(1)	156(1)	155(1)	149(1)
Ni-O(6)-W	160(4)	163(4)	152(2)	156(2)	150(1)	130(1)	152(1)

Rietveld refinements were carried out using laboratory XRD data, and the obtained B_{iso} values are high for Na but comparable to that obtained for $NaLaNiWO_6$ using neutron diffraction data. The refinement of occupancies also resulted in reasonable values. However, better thermal

parameters and occupancies require neutron diffraction data. Impurities present in each sample have been included in the Rietveld refinement, and the corresponding weight percentage is obtained by refining the scale factor of each phase (Table A-2.4.8). A decrease in unit cell parameters with the decreasing size of rare-earth cations is observed, as tabulated in Table 4.3. The selected bond lengths and bond angles are listed in Table 4.4. Bond angles of Ni-O-W are found to be less than 180º, indicating tilted octahedra. Further, bond angles decreased with the decreasing size of rare-earth cations suggesting a higher degree of octahedral tilting than La-compound.

4.3.3.2 Magnetic measurements

Temperature-dependent dc magnetization measured under ZFC and FC conditions with 100 Oe for Na*Ln*NiWO$_6$ (*Ln* = Pr, Nd, Sm, Eu, Gd, and Tb) compounds are shown in Figure 4.7. These compounds exhibit antiferromagnetic transition around T_N = 30 K for Pr and Nd, 27 for Sm, 26 for Eu, 24 for Gd, and 23 K for Tb as determined from heat capacity data as shown in Figures 4.7(a-f). The inset of Figures 4.7(a and b), for the Pr and Nd compounds, shows the *dM/dT* at 100 Oe underlying the magnetic transition around 30 K. The anomaly in the heat capacity of the Pr and Nd compounds confirmed the magnetic transition. A broad peak around 6 K in the ZFC curve of Sm-compound may be due to the NiO impurity phase [15]. In the case of Eu-compound, the ZFC and FC curves exhibit ascending behavior because of the paramagnetic contribution of Eu^{3+} ion. Since magnetization is inductive measurement and because of the larger paramagnetic contributions of Gd^{3+} and Tb^{3+} over Ni^{2+} moments, the magnetization of the compounds containing Gd and Tb ions did not display any signature of magnetic ordering for Ni^{2+} cation, whereas the anomaly in the heat capacity corresponds to the change in magnetic entropy associated with the long-range magnetic ordering. Thus, the T_N of Ni^{2+} cation was determined by the maximum slope on the heat capacity curves, as shown in Figures 4.7(e and f). An anomaly observed in Figure 4.7(f) for NaTbNiWO$_6$ in both the magnetic and heat capacity data at a lower temperature can be ascribed to the ordering of Tb^{3+} cations. The Tb^{3+} sublattice might have ordered partially below T_N^{Ni} because of the polarizing effect of the ordered Ni^{2+} sublattice as in NaTbMnWO$_6$, but further neutron studies are required to confirm [6].

The linear fit to the temperature-dependent inverse molar susceptibility ($1/\chi_m$) data for Pr, Nd, Gd, and Tb compounds are shown in Figure 4.8(a-d). The effective Bohr magnetons obtained for Pr, Gd, and Tb samples are 5.01, 8.52, and 10.63 μ_B/f.u., respectively, which are

in good agreement with the calculated magnetic moments 4.56, 8.43, and 10.12 μ_B/f.u. The experimentally obtained magnetic moment for the Nd compound is 6.1 μ_B/f.u., which is higher than the calculated value of 4.6 μ_B/f.u. This may be due to the unidentified magnetic impurity present in the compound.

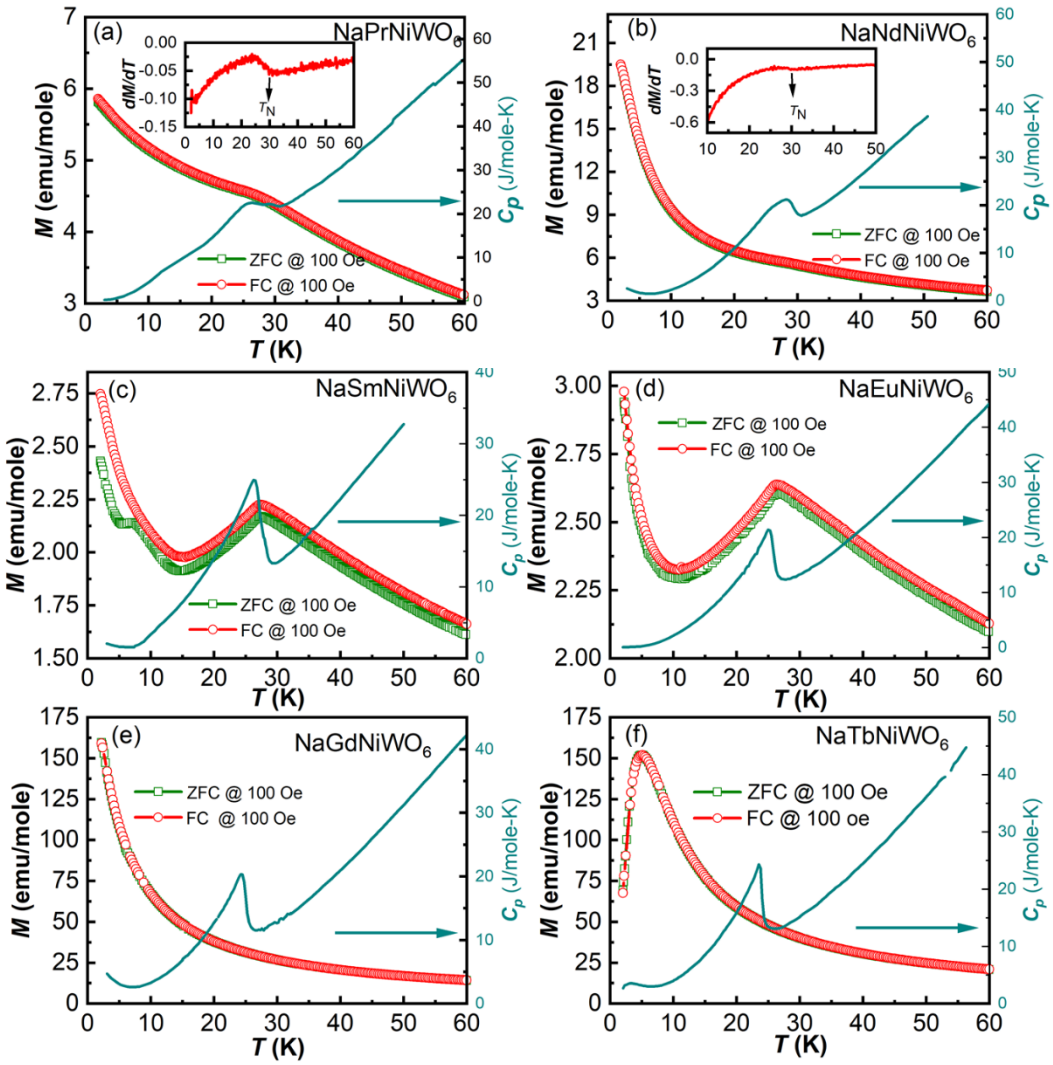

Figure 4.7 (a-f) ZFC and FC of Na(Pr, Nd, Sm, Eu, Gd, and Tb)$NiWO_6$ compounds as a function of temperature measured with a magnetic field of 100 Oe, C_P data as a function of temperature, and *dM/dT* in the inset of Figures (a and b).

The negative sign of the Curie-Weiss temperature indicates the antiferromagnetic interaction of Ni^{2+} ions, as tabulated in Table 4.5. A linear fit was not performed for $NaSmNiWO_6$ and $NaEuNiWO_6$ compounds, as these compounds do not follow Curie-Weiss behavior [18,19]. These compounds show Van Vleck paramagnetic behavior. In the case of Sm^{3+} and Eu^{3+} ions, the ground state's energy gap and first excited states are almost equal to

the thermal energy at room temperature. This causes the low-lying excited states to be populated at room temperature. The Sm^{3+} ion ground state has a moment of about 0.84 μ_B, but generally, it has a moment of 1.5 μ_B at room temperature because of the thermal population of the first excited state. Although the ground state of the Eu^{3+} cation is nonmagnetic, it is found to possess a magnetic moment of 3.4 μ_B due to the thermal population of the first two excited states at room temperature [20,21].

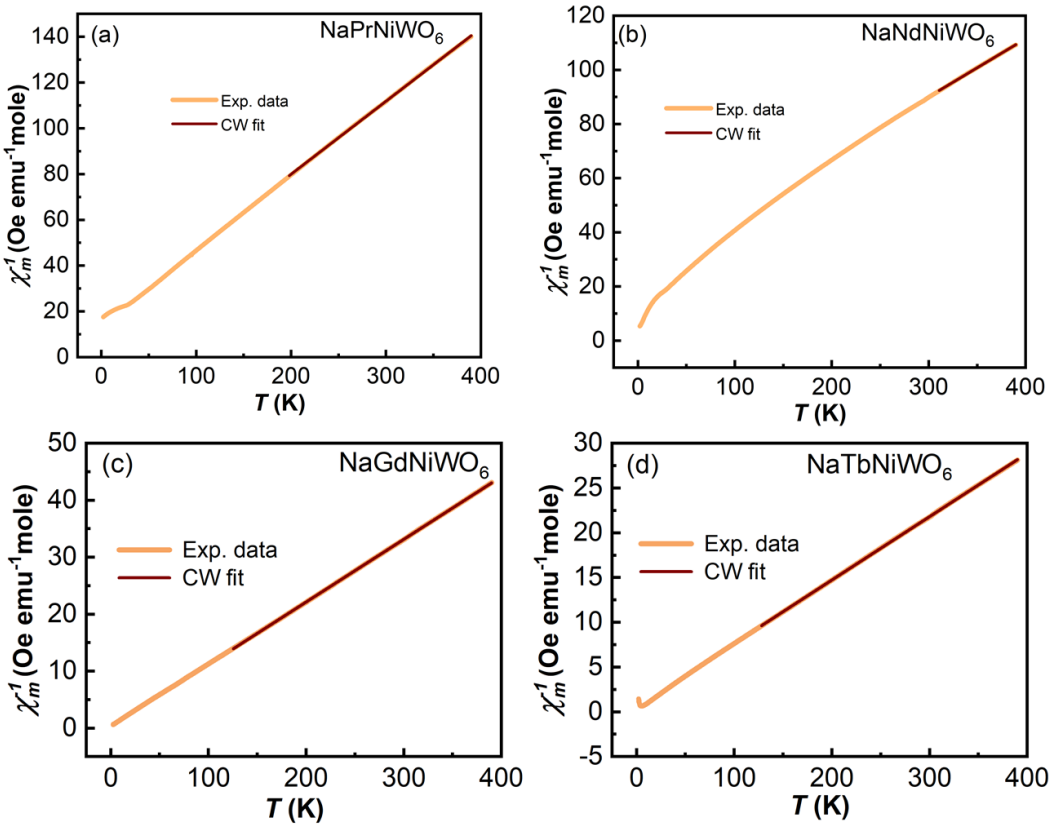

Figure 4.8 Linear Curie-Weiss fits were performed on the inverse susceptibility ($1/\chi_m$) *vs.* temperature (T) plots.

Table 4.5 Weiss constant, μ_{eff} (experimental), and μ_{eff} (calculated/reference value) derived from the magnetization data measured under FC condition, T_N (K) for Ni^{2+} ion determined from heat capacity data (C_p).

Compound name	θ (K)	μ_{eff} (μ_B)	μ_{eff} (μ_B) ref	T_N (K)
$NaLaNiWO_6$	-40	3.4	2.83	30
$NaPrNiWO_6$	-50.7	5.01	4.56	30
$NaSmNiWO_6$				26
$NaEuNiWO_6$				24
$NaNdNiWO_6$	-119.9	6.1	4.6	30
$NaGdNiWO_6$	-1.3	8.52	8.43	24
$NaTbNiWO_6$	-8.3	10.63	10.12	23

The isothermal magnetization curves measured at different temperatures are shown in Figure 4.9. In Na(Pr, Sm, Eu)$NiWO_6$, the linear behavior of *M vs. H* is observed, which is expected for antiferromagnetic order. Whereas in Na(Nd, Gd, Tb)$NiWO_6$, a non-linear behavior was observed at lower temperatures because of the ordering of the rare-earth magnetic ions with the applied fields. The *M* vs. *H* curves at low temperatures exhibit metamagnetic transition associated with the Nd^{3+}, Gd^{3+}, and Tb^{3+} ions as depicted in the inset of Figures 4.9 (b, e, and f).

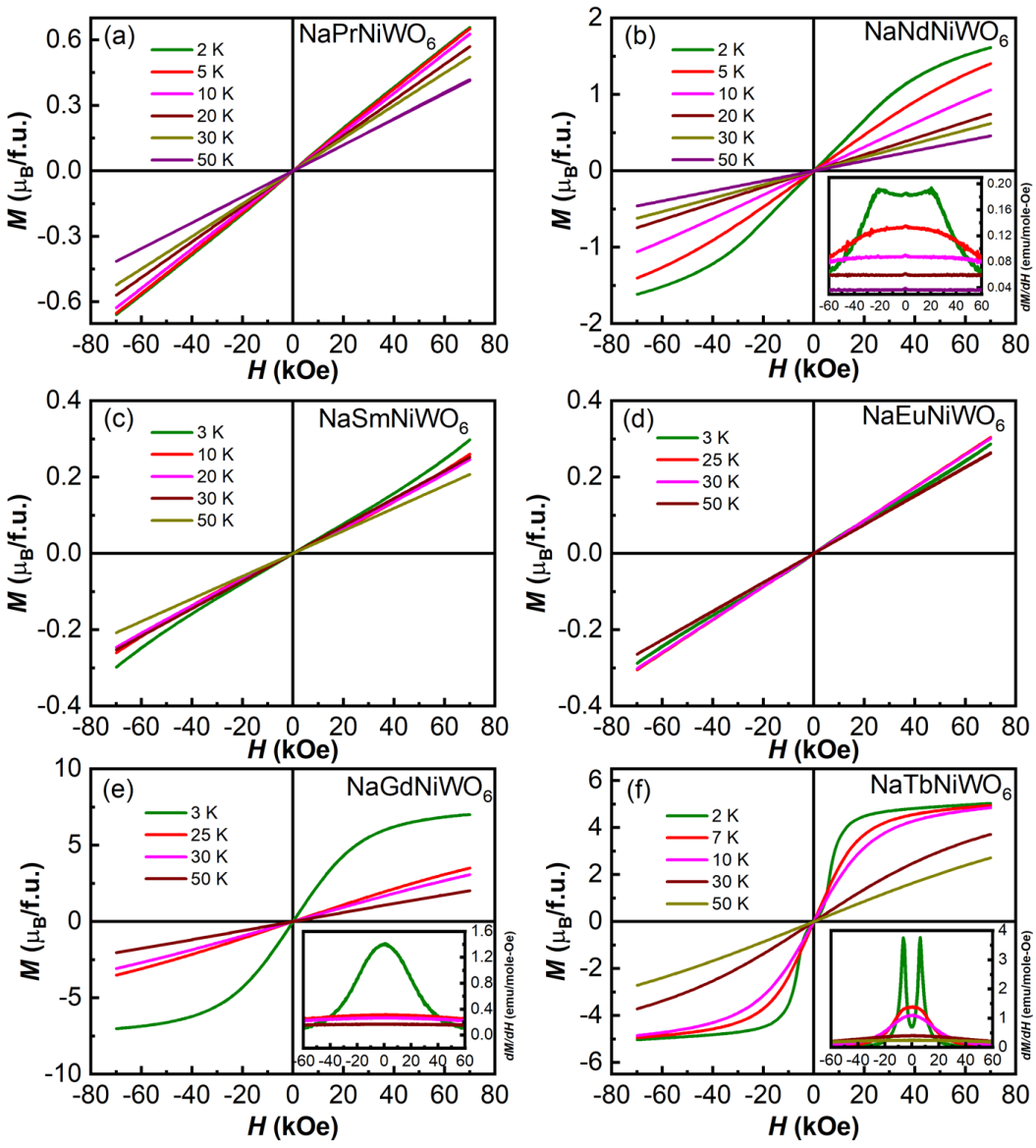

Figure 4.9 (a-f) Magnetic field-dependent magnetization at different temperatures and *dM/dH* in the inset of Figures (b, e, and f).

4.3.3.3 Dielectric studies

Temperature-dependent dielectric studies were carried out to validate the possibility of magnetoelectric coupling of these compounds around T_N. The compounds Na(Pr, Nd)$NiWO_6$ show a small change in dielectric value, and other compounds exhibit sharp anomaly around magnetic ordering temperature measured at different fields under 50 kHz, as shown in Figure 4.10. In $NaGdNiWO_6$, observation of little variation in dielectric value at lower temperatures corresponding to the short-range ordering of Gd^{3+} ions. The temperature-dependent dielectric constant values exhibit anomaly and slight variations under different frequencies around T_N, as shown in Figure 4.11. The appearance of the dielectric peak at magnetic ordering temperature has confirmed the magnetodielectric coupling of these compounds.

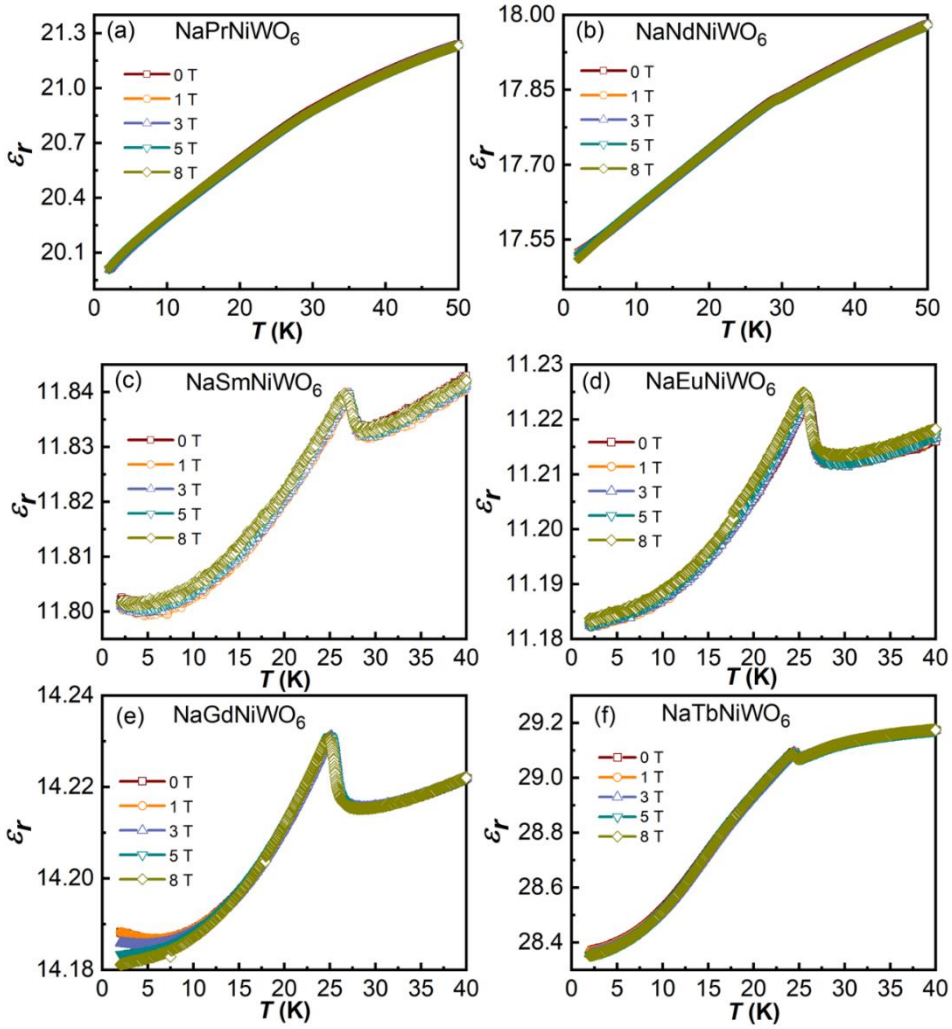

Figure 4.10 (a-f) Temperature-dependent dielectric constant was measured at different magnetic fields under 50 kHz.

Further, pyroelectric current and dc-bias measurements have been carried out to investigate the ferroelectric properties of these compounds. However, no anomaly in the temperature dependent pyroelectric current and dc-bias current measurements was observed. Experimental investigation on other compounds, Na*Ln*MnWO$_6$ (*Ln* = La, Nd, and Tb) and Na*Ln*FeWO$_6$ (*Ln* = La, Nd), showed the absence of ferroelectricity [3,5]. The compounds with smaller-sized rare-earth cations have larger distortions compared to that of compounds with higher-sized rare-earth cations, exhibit an appreciable change in polarization at magnetic ordering temperature. Despite having a polar structure, the change in polarization was not observed in the case of higher-sized rare-earth compounds. Hence, the octahedral distortions play a crucial role in electric polarization. Further studies are required to understand the importance of the size of rare-earth cations in these compounds.

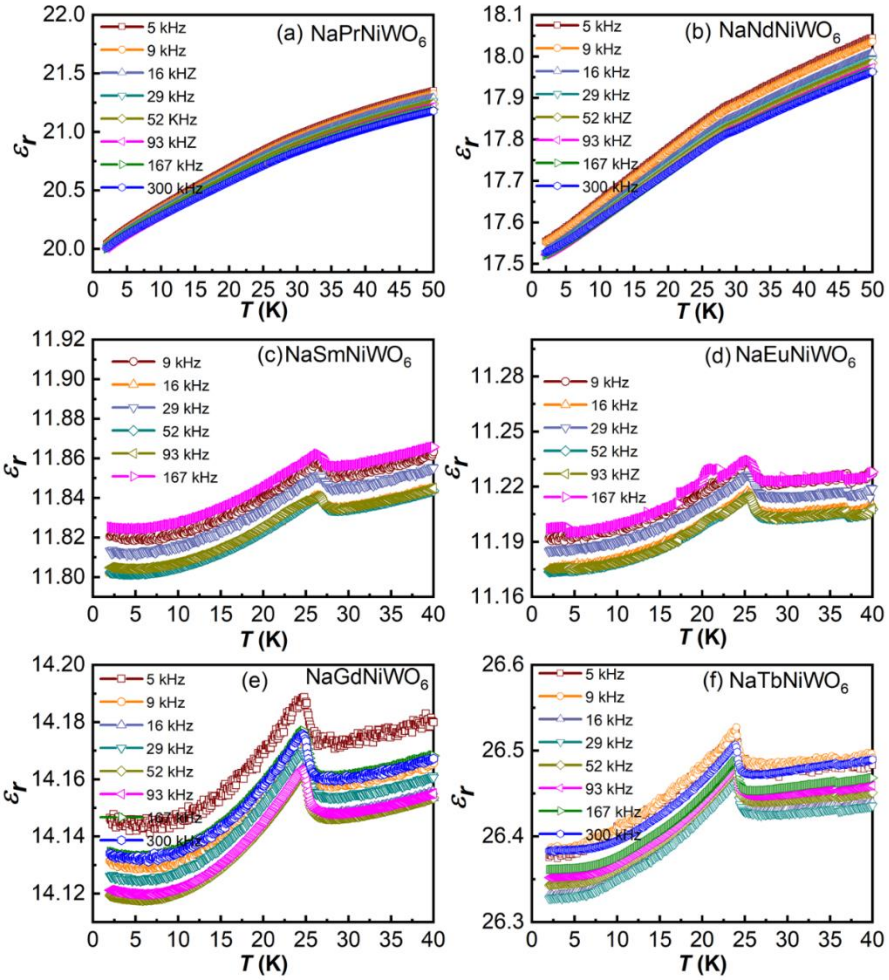

Figure 4.11 Dielectric constant ($\mathcal{E}_r$) *vs.* temperature (T) data measured at different frequencies.

However, we have estimated the polarization from structural details using the equation, $P = \Sigma_i q_i \delta z_i / V$, where q_i is the nominal charge of each ion, δz_i is the atomic displacement along

the *y*-axis, and *V* is the unit cell volume [22]. The polarization obtained is the contribution of all the ions in the unit cell. The polarization estimated from the neutron data for $NaLaNiWO_6$ is ~ 23 $\mu C/cm^2$. This value is in good agreement with the earlier calculated ferroelectric polarization for doubly ordered perovskites $NaLaMnWO_6$, $NaPrFeWO_6$, and $NaSmFeWO_6$ [23,24]. Since the polarization calculation involves atomic displacements, it is better to use structural details from neutron data. We have calculated the polarization from PXRD structural details for the other compounds (Pr, Nd, Sm, and Eu-Tb). The obtained polarization values are around 30 $\mu C/cm^2$, which is slightly high compared to the values determined from NPD data. Polarization values for each compound calculated from PXRD data are given in Table 4.6.

Table 4.6 Spontaneous polarization estimated from room temperature PXRD data.

Compound	Polarization ($\mu C/cm^2$)
$NaPrNiWO_6$	28
$NaNdNiWO_6$	31
$NaSmNiWO_6$	32
$NaEuNiWO_6$	32
$NaGdNiWO_6$	29
$NaTbNiWO_6$	30

4.4 Conclusion

High pressure and high temperature synthesis conditions were used to stabilize the structure of doubly ordered perovskites Na*Ln*$NiWO_6$ (*Ln* = La, Pr, Nd, Sm, Eu, Gd, and Tb). These compounds crystallize in a polar perovskite structure with space group $P2_1$ and exhibit combined layered ordering of *A*-cations and rock-salt ordering of *B*-cations. SHG studies confirmed the non-centrosymmetric behavior of Na*Ln*$NiWO_6$. These compounds order antiferromagnetically in the temperature range 21 – 30 K and exhibit magnetodielectric behavior. $NaLaNiWO_6$ shows a collinear spin arrangement at 1.5 K with the propagation vector **k** = (½, 0, ½). The ferroelectric polarization estimated from the neutron data for $NaLaNiWO_6$ is P ~ 23 $\mu C/cm^2$, which is comparable with earlier reported values for similar compounds. Unlike the smaller rare-earth compounds, Na*R*$NiWO_6$ (*R*= Y, Dy-Lu), these compounds do not show any change in polarization at the magnetic ordering temperature despite the presence of a dielectric anomaly. The absence of polarization change may be due to a smaller octahedral distortion than the compounds with smaller size rare-earth cations.

References

[1] M. A. Arillo, J. Gómez, M. L. López, C. Pico, and M. Luisa Veiga, J. Mater. Chem. **7**, 801 (1997).

[2] G. King, S. Thimmaiah, A. Dwivedi, and P. M. Woodward, Chem. Mater. **19**, 6451 (2007).

[3] C. De, T. H. Kim, K. H. Kim, and A. Sundaresan, Phys. Chem. Chem. Phys. **16**, 5407 (2014).

[4] P. Zuo, C. V Colin, H. Klein, P. Bordet, E. Suard, E. Elkaim, and C. Darie, Inorg. Chem. **56**, 8478 (2017).

[5] M. Retuerto, M. R. Li, A. Ignatov, M. Croft, K. V Ramanujachary, S. Chi, J. P. Hodges, W. Dachraoui, J. Hadermann, T. T. Tran, P. S. Halasyamani, C. P. Grams, J. Hemberger, and M. Greenblatt, Inorg. Chem. **52**, 12482 (2013).

[6] G. King, A. S. Wills, and P. M. Woodward, Phys. Rev. B - Condens. Matter Mater. Phys. **79**, 1 (2009).

[7] R. Shankar P N, F. Orlandi, P. Manuel, W. Zhang, P. S. Halasyamani, and A. Sundaresan, Chem. Mater. **6**, (2020).

[8] H. M. Rietveld, J. Appl. Crystallogr. **2**, 65 (1969).

[9] L. C. Chapon, P. Manuel, P. G. Radaelli, C. Benson, L. Perrott, S. Ansell, N. J. Rhodes, D. Raspino, D. Duxbury, E. Spill, and J. Norris, Neutron News **22**, 22 (2011).

[10] M. Poupon and M. Henriques, (2018).

[11] M. C. Knapp and P. M. Woodward, J. Solid State Chem. **179**, 1076 (2006).

[12] A. M. Glazer, Acta Crystallogr. Sect. B **28**, 3384 (1972).

[13] R. D. Shannon, Acta Crystallogr. Sect. A **32**, 751 (1976).

[14] R. J. Hill and C. J. Howard, J. Appl. Crystallogr. **20**, 467 (1987).

[15] M. Tadic, D. Nikolic, M. Panjan, and G. R. Blake, J. Alloys Compd. **647**, 1061 (2015).

[16] S. A. Ivanov, R. Mathieu, P. Nordblad, R. Tellgren, C. Ritter, E. Politova, G. Kaleva, A. Mosunov, S. Stefanovich, and M. Weil, Chem. Mater. **25**, 935 (2013).

[17] B. J. Campbell, H. T. Stokes, D. E. Tanner, and D. M. Hatch, J. Appl. Crystallogr. **39**, 607 (2006).

[18] K. Koteswara Rao, M. Vithal, and D. Ravinder, J. Magn. Magn. Mater. **253**, 65 (2002).

[19] S. J. Mugavero, M. D. Smith, and H.-C. zur Loye, J. Solid State Chem. **178**, 200 (2005).

[20] L. Thompson, J. Legendziewicz, J. Cybinska, L. Pan, and W. Brennessel, J. Alloys Compd. **341**, 312 (2002).

[21] T. Aitasalo, J. Hölsä, M. Lastusaari, J. Legendziewicz, L. Lehto, J. Lindén, and M. Maryško, J. Alloys Compd. **380**, 296 (2004).

[22] Y. Inaguma, M. Yoshida, and T. Katsumata, J. Am. Chem. Soc. **130**, 6704 (2008).

[23] T. Fukushima, A. Stroppa, S. Picozzi, and J. M. Perez-Mato, Phys. Chem. Chem. Phys. **13**, 12186 (2011).

[24] J. Blasco, J. A. Rodríguez-Velamazán, G. Subías, J. L. García-Muñoz, J. Stankiewicz, and J. García, Acta Mater. **176**, 53 (2019).

Chapter 5

Switchable, nonswitchable polarization in Na*Ln*CoWO$_6$ (*Ln* = Y, Er, Tm, Yb, and Lu), NaLuMnWO$_6$, and magnetodielectric properties of Na*Ln*FeWO$_6$ (*Ln* = Y, Ho)*

Summary

This chapter deals with the structural, magnetic and multiferroic properties of Na*Ln*CoWO$_6$ (*Ln* = Y, Er, Tm, Yb, and Lu), NaLuMnWO$_6$, as well as magnetic and dielectric properties of Na*Ln*FeWO$_6$ (*Ln* = Y, Ho). These compounds are isostructural to Ni compounds. A clear long-range antiferromagnetic ordering (T_N ~ 6-8 K) is observed for Na*Ln*CoWO$_6$ (*Ln* = Y, Er, Tm, Yb, and Lu) and NaLuMnWO$_6$, which is accompanied by the dielectric anomaly. A nonswitchable polarization is realized below T_N for Na*Ln*CoWO$_6$ (*Ln* = Y, Er, Tm, and Yb) and NaLuMnWO$_6$. In contrast, the polarization is switchable in NaLuCoWO$_6$ by changing the direction of the electric field (*E*), indicating the ferroelectric nature of this compound. Neutron powder diffraction studies revealed a collinear antiferromagnetic structure for NaYCoWO$_6$ with the propagation vector **k** = (½, 0, ½). All these compounds exhibit magnetoelectric coupling below magnetic ordering temperature (T_N). Magnetic, heat capacity and dielectric measurements of NaYFeWO$_6$ and NaHoFeWO$_6$ signified antiferromagnetic ordering (T_N) is coupled with the dielectric peak. Miserably, the pyroelectric current anomalies for NaYFeWO$_6$ and NaHoFeWO$_6$ are overshadowed by leakage currents.

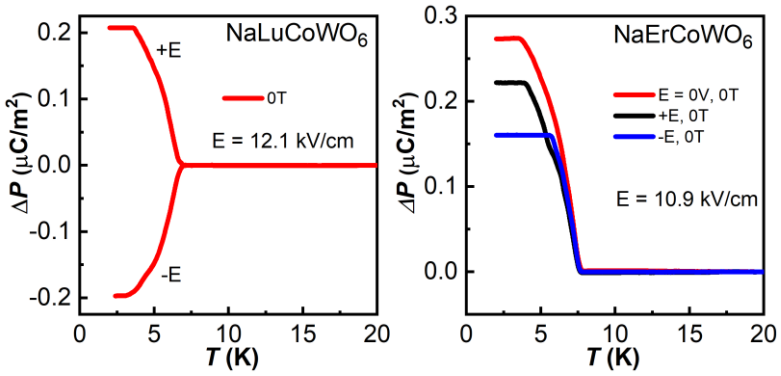

……

*Results on Na*Ln*CoWO$_6$ (*Ln* = Er-Lu) published in *J. Phys. Chem. C*, **125**, 10803 (2021), ©2021 by the American Chemical Society. *Manuscript based on Na*Ln*FeWO$_6$ (*Ln* = Y, Ho) is under preparation.

5.1 Introduction

The magnetoelectric coupling is realized below the magnetic ordering temperature of polar oxides $M_2Mo_3O_8$ (*M* = Mn, Fe, Co, and Ni), $CaBaCo_4O_7$, $GaFeO_3$, Ni_3TeO_6, $DyFeWO_6$ [1–7]. In these materials, the inversion symmetry is absent at all temperatures, and the presence of magnetic cation often undergoes long-range magnetic ordering. Thus, fulfilling the imperative conditions of the simultaneous breaking of spatial inversion and time-reversal symmetry for multiferroicity. Consequently, polar oxides usually show magnetoelectric coupling below the magnetic ordering temperature. Generally, in some of the polar oxides, the monodomain formation eliminates the need for electric field poling. Hence, exploring more polar oxides for the multiferroic property is promising for technological applications. In the previous chapter, a series of compounds, Na*Ln*$NiWO_6$ (*Ln* = Y, Dy-Lu), was shown to exhibit switchable polarization below the antiferromagnetic order of Ni^{2+} ions (T_N ~ 18 to 23 K) [8]. Further studies on Na*Ln*$NiWO_6$ (*Ln* = La, Pr, Nd, Sm-Tb) with larger size rare-earth cations indicate that these compounds are only magnetodielectric.

In this chapter, we have extended the studies on doubly ordered perovskites with other transition metal cations (Co, Mn, and Fe) and smaller size rare-earth cations. We have studied the magnetic and electrical properties of Na*Ln*$CoWO_6$ (*Ln* = Y, Er, Tm, Yb, and Lu) and $NaLuMnWO_6$. Amidst these, the structural and magnetic properties of Na*Ln*$CoWO_6$ (Ln = Y, Er, and Yb) are already reported, but the electrical properties are unknown [9,10]. These compounds are prepared under high pressure (4.5 GPa) and high temperature (1000 ºC). Room temperature powder X-ray diffraction (PXRD) studies confirmed that all the aforementioned compounds crystallize in a polar structure ($P2_1$). Temperature dependent dc magnetization and heat capacity measurements confirmed the existence of long-range antiferromagnetic ordering in the temperature range of 6-8 K for Co^{2+} and Mn^{2+} ions. The polarization was observed below the T_N without applying a poling electric field in the case of Na*Ln*$CoWO_6$ (*Ln* = Y, Er, Tm, and Yb), and it was not switchable when the polarity of the electric field (*E*) was reversed. Interestingly, the observed polarization under electric field (*E*) for $NaLuCoWO_6$ was switchable and required a poling electric field.

Further, we have measured the polarization of $NaLuMnWO_6$ to understand the influence of the size of rare-earth cations for switching polarization. The observed polarization was similar to other cobalt compounds. These results demonstrate a magnetoelectric coupling of doubly ordered perovskites below magnetic ordering temperature. Neutron powder

diffraction (NPD) has been carried out to determine the magnetic structure of $NaYCoWO_6$. It is observed that the magnetic structure of $NaYCoWO_6$ is collinear with **k** = (½, 0, ½). In addition, we have studied Na*Ln*$FeWO_6$ (*Ln* = Y, Ho) doubly ordered perovskites. Antiferromagnetic transition is observed around 13 K for Y and 15 K for Ho compounds corresponding to the ordering of Fe^{3+} ions. Dielectric anomaly exhibits at magnetic ordering temperature (T_N) confirmed the magnetodielectric behavior of these compounds. Further, the pyroelectric current anomaly is dominated by the leakage currents; because of that, we could not probe the ferroelectricity of $NaYFeWO_6$ and $NaHoFeWO_6$ compounds.

5.2 Experimental details

The polycrystalline Na*Ln*$CoWO_6$ (*Ln* = Y, Er, Tm, Yb, and Lu), $NaLuMnWO_6$, Na*Ln*$FeWO_6$ (*Ln* = Y, Ho) samples were synthesized by applying 4.5 GPa pressure and at 1000 ºC using a cubic anvil press as mentioned in chapter 3. Stochiometric amounts of Ln_2O_3 (preheated at 950 ºC), $Na_2WO_4{\cdot}2H_2O$ (preheated at 150ºC), *M*O (*M* = Co, Mn), Fe powder, and WO_3 were used to synthesize the targeted samples. $KClO_3$ was used to provide stoichiometric oxygens for Fe compounds. Structural, magnetic, and electrical characterizations were carried out as mentioned in the previous chapters.

5.3 Results and discussion

5.3.1 Results on $NaYCoWO_6$

5.3.1.1 Crystal structure

Crystallographic characterization of $NaYCoWO_6$ is carried out by using the powder neutron diffraction (PND) data collected at 15 K. The pattern is successfully indexed based on $P2_1$ unit cell $\sqrt{2}a_0*\sqrt{2}a_0*2a_0$ (a_p = 3.8 Å, for ideal cubic perovskite) and the Rietveld fit for NPD data is shown in Figure 5.1. Since room temperature structure is already reported, here we have given details from neutron data at 15 K (Table 5.1). The SOJT distortion of the W^{6+} cation is clear by checking the different W-O bond lengths. Where, W^{6+} cation tends to move towards the Na-layer by having a shorter W-O(6) bond length compared to W-O(5) (see Table 5.2). The different bond lengths of WO_6 octahedra helps to release the strain and hence, stabilize the double-double ordering of the cations in these compounds. Further, the examination of the *M*-O-W bond angles (Table 5.2) indicates the octahedra are tilted.

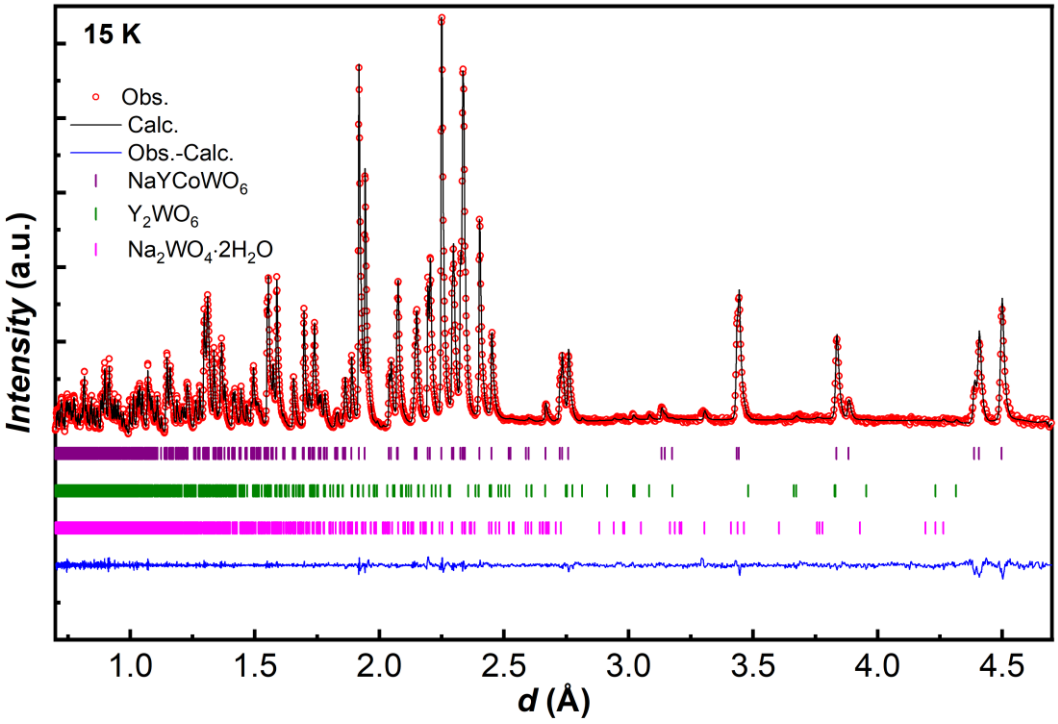

Figure 5.1 Rietveld refined NPD data of $NaYCoWO_6$ recorded on WISH at 2θ = 152.8º and 15 K.

Table 5.1 Crystallographic parameters of $NaYCoWO_6$ from the refinement of NPD data collected at 15 K.

Atom	Wyckoff position	*x*	*y*	*z*	U_{iso}(Å^2)	Occ.
Na	2*a*	0.2543(1)	0.216	0.0073(1)	0.023(2)	1.0
Y	2*a*	0.2671(6)	0.3156(7)	0.5016(6)	0.0109(8)	1.0
Co	2*a*	0.753(2)	0.274(3)	0.2500(2)	0.005(2)	1.0
W	2*a*	0.7683(1)	0.250	0.7617(9)	0.0055(1)	1.0
O1	2*a*	0.5603(1)	0.5358(1)	0.6882(7)	0.0084(2)	1.0
O2	2*a*	0.5353(1)	0.5608(1)	0.3155(7)	0.0154(2)	1.0
O3	2*a*	-0.0556(9)	-0.0680(1)	0.2182(7)	0.0071(1)	1.0
O4	2*a*	-0.0796(1)	-0.0460(1)	0.7868(7)	0.0095(2)	1.0
O5	2*a*	0.8561(7)	0.2200(1)	0.5073(5)	0.0066(1)	1.0
O6	2*a*	0.6681(6)	0.2868(1)	-0.0068	0.0113(1)	1.0

Space group: $P2_1$; a = 5.3371(1) Å, b = 5.5197(1) Å, c = 7.7702(1) Å, β = 90.265(1)°. Vol.: 228.9(1)Å^3; GOF = 2.21, R_p = 1.65 (%), R_{wp} = 2.01 (%).

Table 5.2 Selected bond lengths and angles for $NaYCoWO_6$ at 15 K.

Atom	O1	O2	O3	O4	O5	O6
Co (Å)	2.182(2)	2.030(1)	2.161(2)	1.999(1)	2.092(1)	2.028(7)
W (Å)	1.989(6)	1.973(6)	1.882(6)	1.866(7)	2.031(7)	1.875(7)
Co-O-W (deg)	145.63(4)	141.61(4)	149.86(4)	143.06(5)	147.06(4)	150.80(4)

5.3.1.2 Magnetic and electrical studies

Figure 5.2 (a) shows the temperature dependence of the magnetization collected under a field of 1000 Oe in zero-field-cooled (ZFC) and field-cooled (FC) conditions for $NaYCoWO_6$, which orders antiferromagnetically around 7 K [10]. Isothermal magnetization as a function of the magnetic field for $NaYCoWO_6$ showed slight non-linearity at a lower temperature (2 K) which could be because of the spin reorientation with the field (Figure 5.2 (b)).

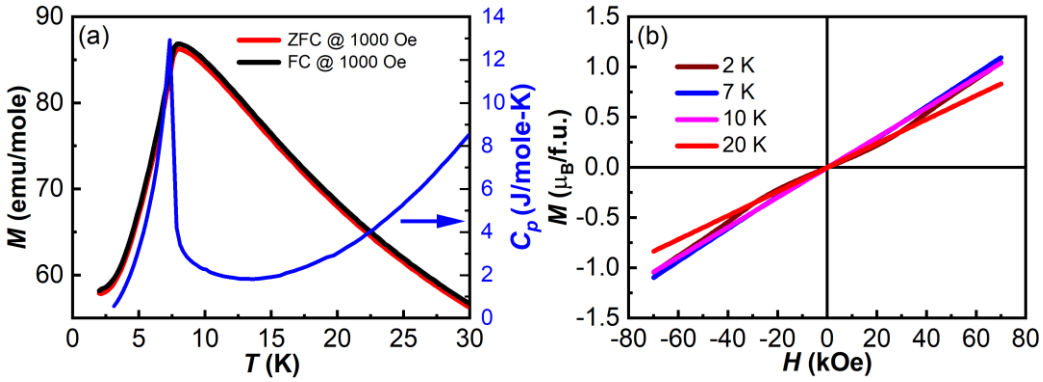

Figure 5.2 (a) Temperature dependent ZFC/FC magnetization, heat capacity plotted as C_p *vs.* T (right axis). (b) Field dependent isothermal magnetization of $NaYCoWO_6$.

Temperature dependent dielectric measurements of $NaYCoWO_6$ at 50 kHz under different magnetic fields and with different frequencies in the temperature range of 2-30 K are shown in Figures 5.3(a) and (b), respectively. Dielectric anomalies observed at magnetic ordering temperature shifted to lower temperature with increasing field and are frequency-independent, as seen in Figure 5.3(b). Since this compound is polar, we have measured the pyroelectric current over the magnetic ordering temperature. Knowing the nature of this compound, first, the pyroelectric current was measured without poling and further with electric field (± 9.4 kV/cm) poling, as shown in Figure 5.3(c). The pyroelectric peak was shifted to a lower temperature with field 8 T in agreement with dielectric data. Further, the change in electric polarization (ΔP) is obtained by integrating the pyrocurrent against time as presented in Figure 5.3(d), and the polarization (ΔP) decreases with increasing the magnetic field. The polarization observed below the magnetic ordering temperature (T_N) without an electric field poling infers the presence of preferred domain orientation or monodomain orientation in $NaYCoWO_6$ owing to its polar nature. The sign of change in electric polarization remains the same as that of the zero ΔP after changing the poling electric field (± 9.4 kV/cm).

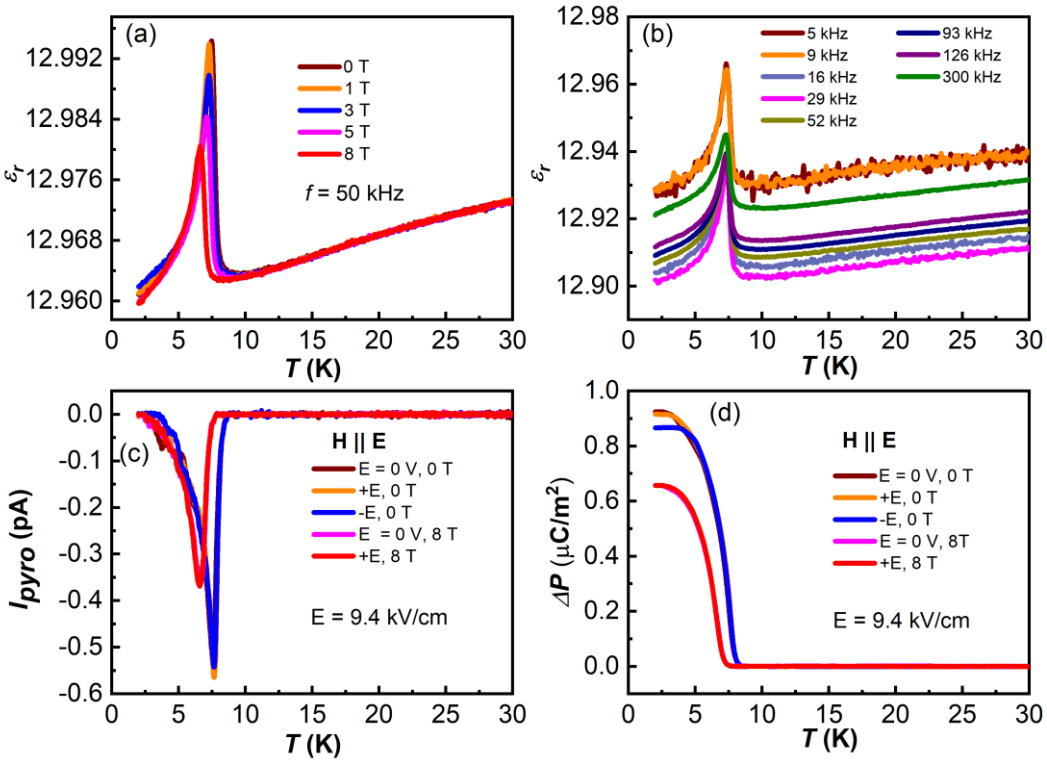

Figure 5.3 Temperature dependence of (a) dielectric constant with 50 kHz frequency in the presence of various fields and (b) dielectric constant with different frequencies. (c) Temperature variation of pyroelectric current I_{pyro} without and with an electric field (± 9.4 kV/cm) under 0 and 8 T and (d) time-integrated change in polarization (ΔP) without and with an electric field (± 9.4 kV/cm) under 0 and 8T.

5.3.1.3 Magnetic structure

The neutron powder diffraction studies have been carried out to understand the role of the magnetic spin structure of $NaYCoWO_6$ in the observation of polarization at magnetic ordering temperature. The observed series of new reflections in NPD data of $NaYCoWO_6$ below T_N were indexed with a **k**-vector = (½, 0, ½). The propagation vector was determined by indexing magnetic peaks using the "k-search program," which is available in the FullProf Suite [11]. Group theoretical computation, done with the ISOTROPY software, suggests two irreducible representations (Irreps): mA1 and mA2. Both the models were checked, where mA2 was better fitted to the experimental data and correspond to the magnetic space group $B[a]2_1$. The Rietveld refinement of NPD data of $NaYCoWO_6$ at 1.5 K was performed using JANA 2006 is shown in Figure 5.4. After checking several combinations of magnetic moment directions, the best fit is achieved when moments were refined along *a*- and *c*-axis. The collinear magnetic structure of $NaYCoWO_6$ is presented in the inset of Figure 5.4(a). The

refined magnetic structure contains moment components of M_x = -0.29(2) μ_B and M_z = 2.24(1) μ_B with the total magnetic moment of 2.26(2) μ_B for Co^{2+} ions at 1.5 K. The temperature dependent magnetic moment of Co^{2+} ion (inset Figure 5.4(b)) is fitted with the mean-field power law, $m(T) = m_0(1 - T/T_N)^{\beta}$ with a critical exponent β = 0.13(1) [12]. Since the magnetic structure of $NaYCoWO_6$ does not induce any additional individual polarization, the observed ΔP is attributed to magnetoelastic coupling.

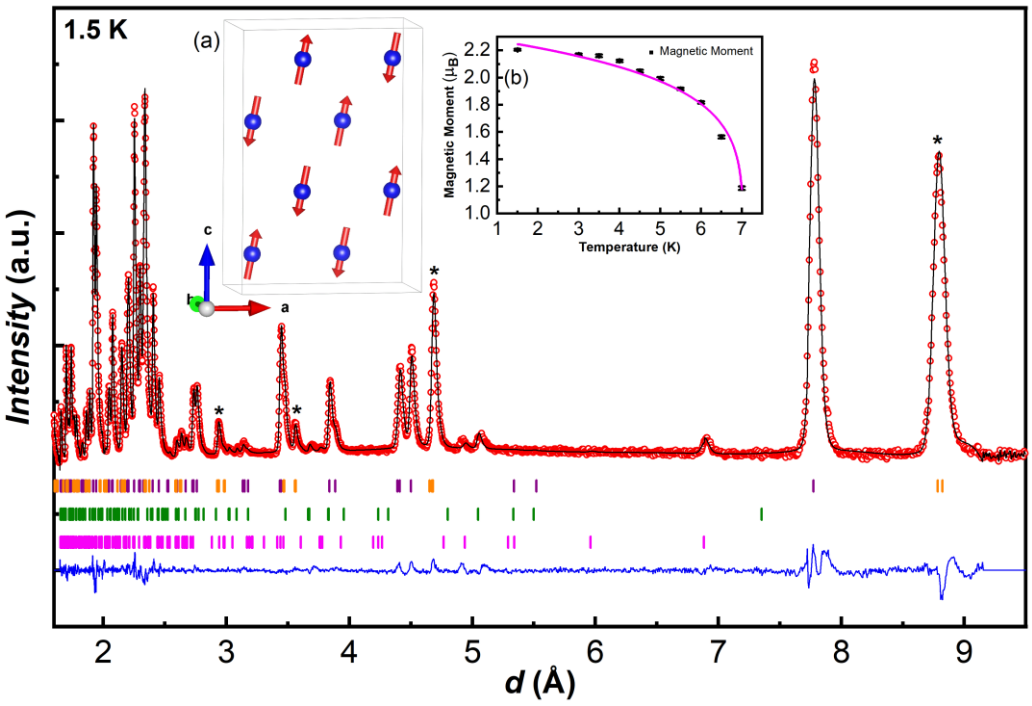

Figure 5.4 Rietveld refined NPD data recorded on WISH at 2θ = 58.3° and 1.5 K. The first-row tick marks indicate the nuclear Bragg reflections (purple) and magnetic Bragg reflections (orange). The second-row and third-row tick marks indicate the Bragg reflections for Y_2WO_6 (olive green) and $Na_2WO_4{\cdot}2H_2O$ (magenta) impurity phases, respectively. Inset Figure (a) shows the magnetic structure of $NaYCoWO_6$ in the magnetic unit cell with the magnetic moments plotted on the Co atom. Inset Figure (b) shows the temperature dependent evolution of Co^{2+} magnetic moment and power-law fit as discussed in the text.

5.3.2 Results on Na*Ln*CoWO$_6$ (*Ln* = Er, Tm, Yb, and Lu) and NaLuMnWO$_6$

5.3.2.1 Crystal structure

Crystal structure studies were carried out by analyzing the PXRD data. The PXRD patterns are indexed to monoclinic $P2_1$ structure similar to previous compounds. It displays a typical pattern of perovskite structure with (001) and (111) reflections for layer and rock-salt ordering of these compounds. The Rietveld refinement patterns of $NaTmCoWO_6$, $NaLuCoWO_6$, and $NaLuMnWO_6$ are shown in Figure 5.5. Since the structural characterization

of $NaErCoWO_6$ and $NaYbCoWO_6$ are already reported using synchrotron X-ray diffraction studies, here the data of these compounds are given in the appendix (Figure A-3.5.1 and A-3.5.2) [9].

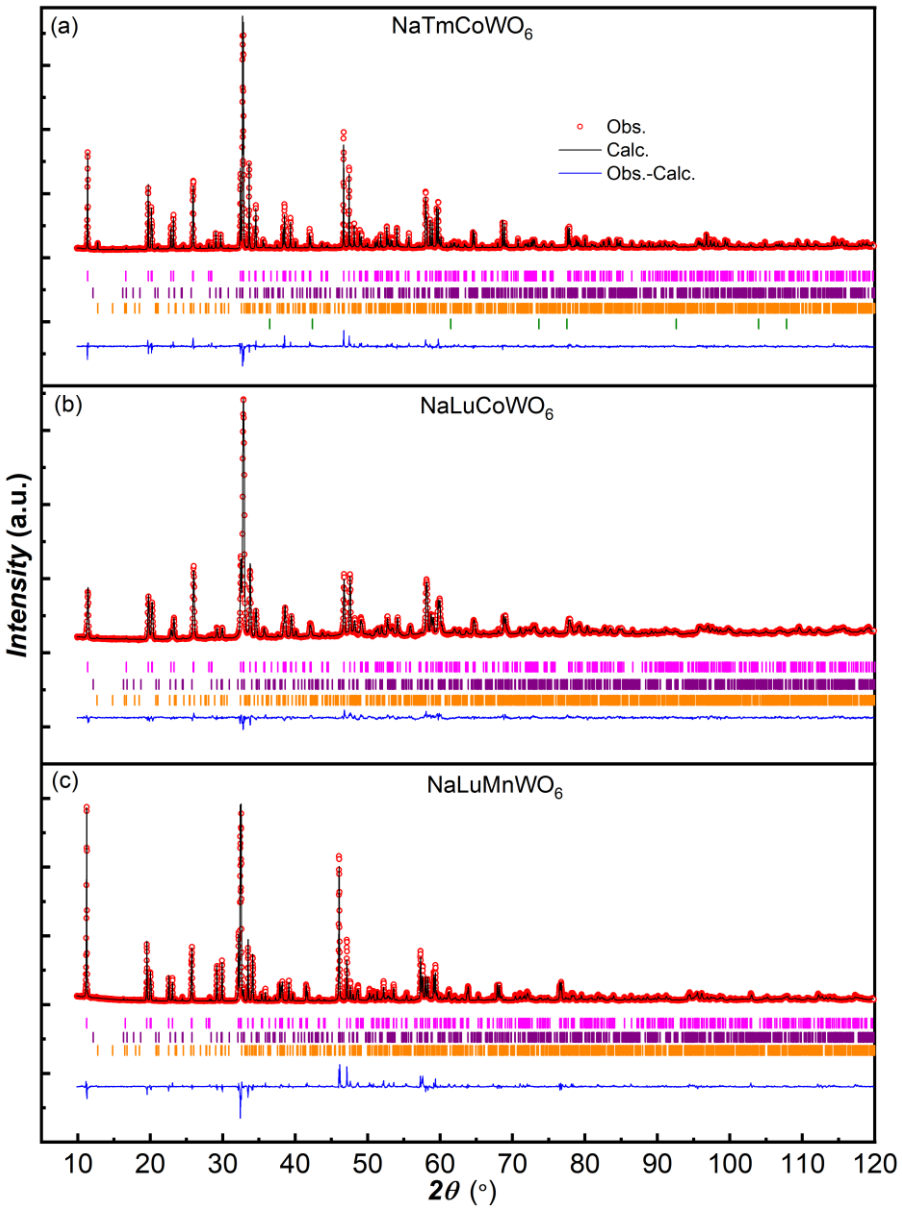

Figure 5.5 Rietveld refined powder X-ray diffraction data collected at room temperature. Magenta tick marks indicate the Bragg reflections of the main phase. Purple, orange, olive green tick marks indicate the Bragg reflections for Ln_2WO_6 (*Ln* = Tm, Lu), $Na_2WO_4{\cdot}2H_2O$, and CoO, respectively.

The preferred orientation along [001] is observed, which was taken care of by grinding the samples for more time for PXRD and refining the preferred orientation parameter during the Rietveld refinement. The fit of PXRD data was improved after including a slight disorder

at *A*-site cations. The structural parameters of these compounds are given in the appendix (Table A-3.5.1 to A-3.5.5). The usual impurities Ln_2WO_6, $Na_2WO_4{\cdot}2H_2O$, and CoO were present along with the main phase, and their corresponding weight percentage is given in Table A-3.5.6. The lattice parameters of all compounds are listed in Table 5.3. The bond lengths are provided in Table 5.4 indicate highly distorted $W(O)_6$ octahedra, where W-O(6) bond length is shorter than W-O(5), confirming displacement of W^{6+} cation towards Na-layer. The bond angles *M*-O-W are less than 180°, as given in Table 5.4.

Table 5.3 Lattice parameters obtained from Rietveld refinement of PXRD data of Na*Ln*$CoWO_6$ (*Ln* = Er, Tm, Yb, and Lu) and $NaLuMnWO_6$ at RT.

Compound	*a* (Å)	*b* (Å)	*c* (Å)	*β* (°)	*V* (Å^3)
$NaErCoWO_6$	5.3341(2)	5.5196(2)	7.8326(2)	90.268(2)	229.13(3)
$NaTmCoWO_6$	5.3217(1)	5.5137(1)	7.7753(1)	90.272(1)	228.14(2)
$NaYbCoWO_6$	5.311(2)	5.512(3)	7.771(3)	90.279(3)	227.44(3)
$NaLuCoWO_6$	5.3022(2)	5.5063(2)	7.768(3)	90.263(4)	226.78(1)
$NaLuMnWO_6$	5.3456(2)	5.5576(3)	7.8744(3)	90.285(3)	233.93(2)

Table 5.4 Selected bond lengths (Angstroms) and angles (Degrees) obtained by Rietveld refinement of PXRD data of Na*Ln*$CoWO_6$ (*Ln* = Er, Tm, Yb, and Lu) and $NaLuMnWO_6$

M = Co, Mn	$NaErCoWO_6$	$NaTmCoWO_6$	$NaYbCoWO_6$	$NaLuCoWO_6$	$NaLuMnWO_6$
M-O(1)	1.99(2)	1.91(3)	1.93(3)	1.84(3)	1.87(2)
M-O(2)	1.93(2)	1.99(3)	2.01(3)	1.88(3)	1.81(2)
M-O(3)	2.05(2)	1.94(3)	1.943(8)	1.93(2)	1.84(3)
M-O(4)	2.11(2)	2.07(3)	1.90(1)	2.06(3)	2.23(3)
M-O(5)	2.10(2)	2.09(2)	2.03(3)	2.02(3)	2.18(3)
M-O(6)	2.03(2)	1.97(2)	1.95(3)	1.99(2)	1.91(3)
W-O(1)	2.09(2)	2.11(2)	2.08(2)	2.32(3)	2.00(2)
W-O(2)	1.99(2)	2.03(2)	2.21(3)	2.17(3)	2.06(3)
W-O(3)	1.97(2)	2.06(3)	1.967(4)	2.02(3)	2.02(3)
W-O(4)	1.82(2)	1.96(2)	1.994(4)	1.90(2)	2.00(2)
W-O(5)	2.15(2)	2.15(2)	2.09(3)	2.20(3)	2.05(3)
W-O(6)	1.79(1)	1.82(2)	1.89(2)	1.85(2)	1.99(3)
M-O(1)-W	154(1)	155(2)	150(1)	138(1)	157(1)
M-O(2)-W	155.1(10)	150(2)	135(1)	146(1)	156(1)
M-O(3)-W	147.0(9)	141(2)	148.3(7)	144(1)	143(1)
M-O(4)-W	140.4(9)	136(2)	152.1(8)	142(1)	135(2)
M-O(5)-W	145.6(6)	147.4(7)	158(1)	148(1)	150(1)
M-O(6)-W	155.1(7)	154.9(8)	154(1)	149(1)	154(1)

5.3.2.2 Magnetic studies

Temperature variation of dc magnetization $M(T)$ measured under zero-field-cooled (ZFC), and field-cooled (FC) conditions with a field of 100 Oe is shown in Figure 5.6(a-e). The compounds $NaLuCoWO_6$ and $NaLuMnWO_6$ exhibit magnetic anomaly around 7 K and 8 K, respectively, corresponding to the long-range antiferromagnetic ordering of the Co^{2+} and Mn^{2+} spins. The absence of magnetic anomaly (for Co^{2+} ion) in the compounds containing rare-earth magnetic cations $NaErCoWO_6$, $NaTmCoWO_6$, and $NaYbCoWO_6$ is because of the larger moment of Er^{3+}, Tm^{3+}, and Yb^{3+} over Co^{2+} ions [8,10]. However, the long-range magnetic ordering temperatures of Co^{2+} ions for all the compounds are determined from the heat capacity ($C_p(T)$) as depicted in the right axis of Figure 5.6(a-e). Since magnetization is the inductive measurement, we do not observe prominent magnetic anomaly for Co^{2+} ion in the compounds with rare-earth magnetic cations (Er^{3+}, Tm^{3+}, and Yb^{3+}), whereas in the case of heat capacity, the observed anomaly corresponds to a change in entropy of Co^{2+} spins indicating long-range magnetic ordering. Magnetic ordering temperature (T_N) decreased to a lower temperature at 7 T, as seen in $C_p(T)$ data. The low-temperature transition below T_N in both $M(T)$ and $C_p(T)$ of $NaErCoWO_6$ corresponds to the ordering of Er^{3+} ions. The low-temperature irreversibility between ZFC and FC magnetization in $NaTmCoWO_6$ and $NaLuCoWO_6$ may be due to a trace amount of impurity (CoO) present in the sample [13]. The presence of the CoO impurity phase (~0.5%) in $NaTmCoWO_6$ is evident from the PXRD pattern shown in Figure 5.5(a). In the case of $NaLuCoWO_6$, we do not see any evidence in the PXRD pattern; probably amount of CoO is below the detection limit. The other possibility of sample inhomogeneities having regions with short-range magnetic order cannot be ruled out.

Parts (f-j) of Figure 5.6 represent the magnetic field dependence of isothermal magnetization $M(H)$ at different temperatures. The non-linear behavior observed at 2 K indicates the metamagnetic behavior due to the field-induced changes related to magnetic rare-earth cations Er, Tm, and Yb and can be seen clearly from dM/dH *vs.* H plots in the inset of respective Figures. The compounds $NaLuCoWO_6$ and $NaLuMnWO_6$ showed a slight non-linearity in M *vs.* H curves at 2 K could be due to field-induced transition (Figures 5.6(i, j)). Temperature variation of the inverse susceptibility ($1/\chi_m$) is fitted to Curie-Weiss law at the paramagnetic region, as given in Figure 5.7(a-e). The obtained Curie-Weiss temperature (θ_{CW}) and the effective magnetic moment are found to be -25.4 K, 11.2 μ_B/f.u. for $NaErCoWO_6$,

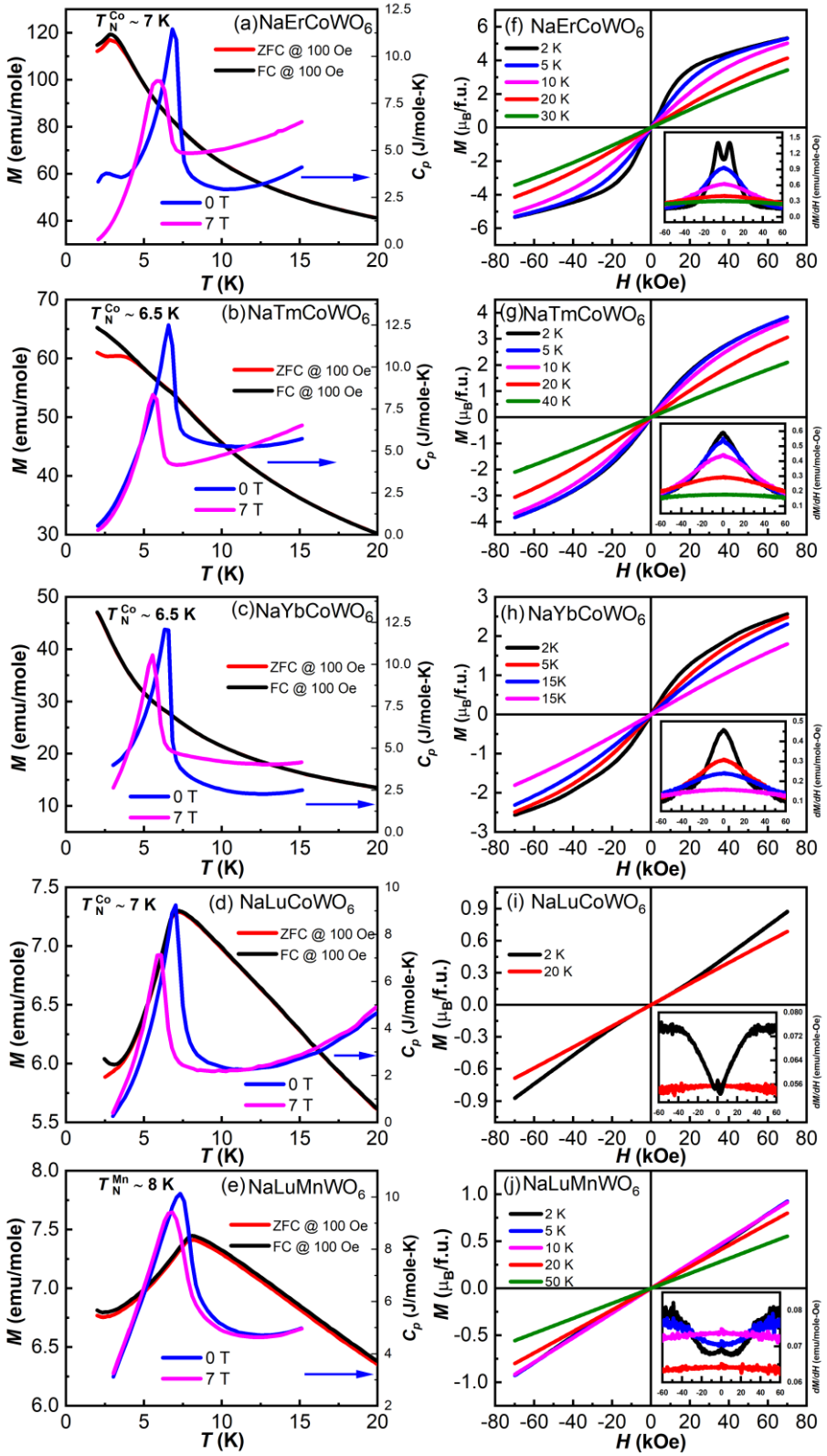

Figure 5.6 (a-e) Temperature variation of dc magnetization measured under ZFC and FC conditions with a field of 100 Oe and heat capacity (C_p) data as a function of temperature measured at 0 and 7 T. (f-j) Isothermal magnetization as a function of the magnetic field at different temperatures and inset figures show the *dM/dH*.

-34.8 K, 9.6 μ_B/f.u. for $NaTmCoWO_6$, -42.9 K, 7.2 μ_B/f.u. for $NaYbCoWO_6$, -32.3 K, 5.2 μ_B/f.u. for $NaLuCoWO_6$, and -61.5 K, 6.2 μ_B/f.u. for $NaLuMnWO_6$. The negative sign of θ_{CW} is consistent with the antiferromagnetic order. The obtained magnetic moments are being close to the reference moment, which are obtained from measurements of paramagnetic salts having the relevant ions [14].

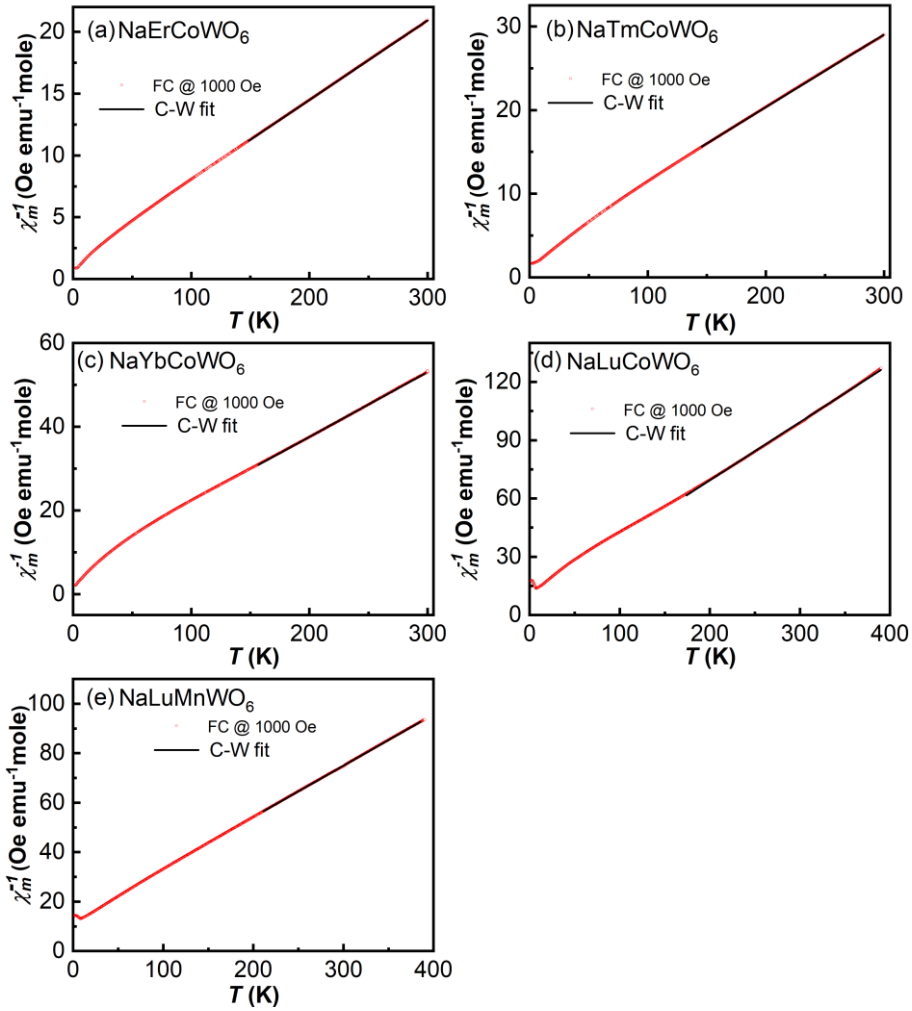

Figure 5.7 (a-e) Linear Curie-Weiss fits were done on the temperature dependent inverse susceptibility data in the paramagnetic region.

5.3.2.3 Dielectric, pyroelectric, and multiferroic studies

To explore the possible magnetoelectric coupling, we have measured the dielectric constant as a function of temperature. The dielectric constants (ε_r) in the temperature range of 2-20 K, at a fixed frequency of 50 kHz under magnetic fields of 0-8 T and at several frequencies, are shown in Figure 5.8(a-j). A dielectric anomaly was observed at $T \sim T_N$, suggesting the coupling of structural and magnetic transitions. It can be seen that the dielectric

anomaly at T_N showed a strong magnetic field dependence and further shifted to lower temperature with an increasing field for Na*Ln*CoWO$_6$ (*Ln* = Er, Tm, Yb, and Lu) compounds, as shown in Figure 5.8(a-d). This is seen in the heat capacity ($C_p(T)$), where T_N has decreased with the field. The dielectric data showed the anomaly around magnetic ordering temperature (T_N ~ 8 K) for NaLuMnWO$_6$ (Figure 5.8(e)), and the field dependence of an anomaly showed in the inset of Figure 5.8(e). The observed dielectric anomaly of these compounds around the magnetic ordering temperature is frequency independent, indicating these anomalies are related to spin-induced transition instead of any relaxation. In the case of NaErCoWO$_6$, another anomaly was observed in dielectric data below T_N corresponding to the ordering of Er^{3+} ions, similar to magnetic and heat capacity data. Isothermal magnetocapacitance was measured at various temperatures 2, 5, 7, and 12 K. The calculated normalized magnetodielectric value, $((\Delta\varepsilon)\% = \frac{\varepsilon_r(H) - \varepsilon_r(0)}{\varepsilon_r(H)} \times 100\%)$ is shown in Figure 5.9. The magnetodielectric effect is observed all over the temperature below T_N, and the maximum value (~ -0.25% for Er, -0.15% for Tm and Yb) is obtained near T_N. The presence of dielectric anomaly and their field dependence around the magnetic ordering temperature confirmed the magnetodielectric behavior of these compounds.

Given the crystal structure of these compounds is polar, it is more significant to examine the electric polarization of these compounds. Therefore, we have measured the temperature dependent pyroelectric current without and with an electric field (*E*) poling. The observed pyroelectric current against temperature was integrated with measurement duration and presented as a change in polarization (ΔP), as shown in Figure 5.10(a-d). The field dependent nature of polarization similar to dielectric properties is observed. It is intriguing to note that the polarization was observed without the poling electric field in Na*Ln*CoWO$_6$ (*Ln* = Er, Tm, and Yb) and NaLuMnWO$_6$. It could be because of the preferred domain orientation or monodomain formation owing to the polar structure of these materials. The observed zero electric field polarization was not switchable by changing the direction of the electric field (±E), similar to NaYCoWO$_6$. The magnetic structure of NaYCoWO$_6$ is collinear with a **k**-vector = (½, 0, ½). Although we have not done neutron studies on Na*Ln*CoWO$_6$ (*Ln* = Er, Tm, and Yb) and NaLuMnWO$_6$, from known magnetic structures of other doubly ordered perovskites, it is suggested that the change in polarization in these compounds could be due to magnetoelastic coupling [8,15–19]. The observed change in polarization is magnetically enhanced since the structure of these materials is already polar in the paramagnetic state.

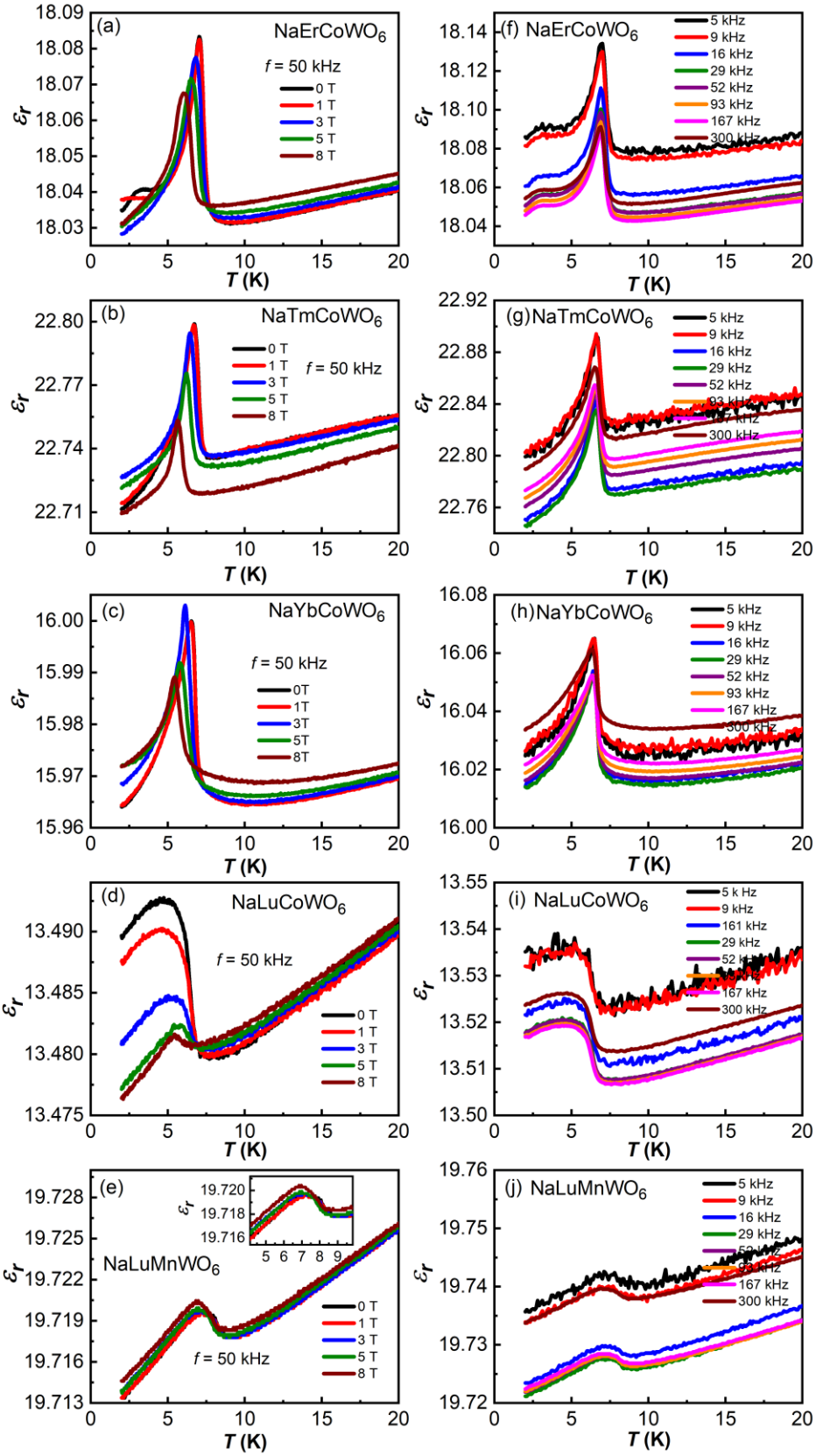

Figure 5.8 (a-e) Temperature dependent dielectric permittivity measured under 0-8 T fields with 50 kHz frequency. (f-j) Temperature and frequency variation of dielectric constant.

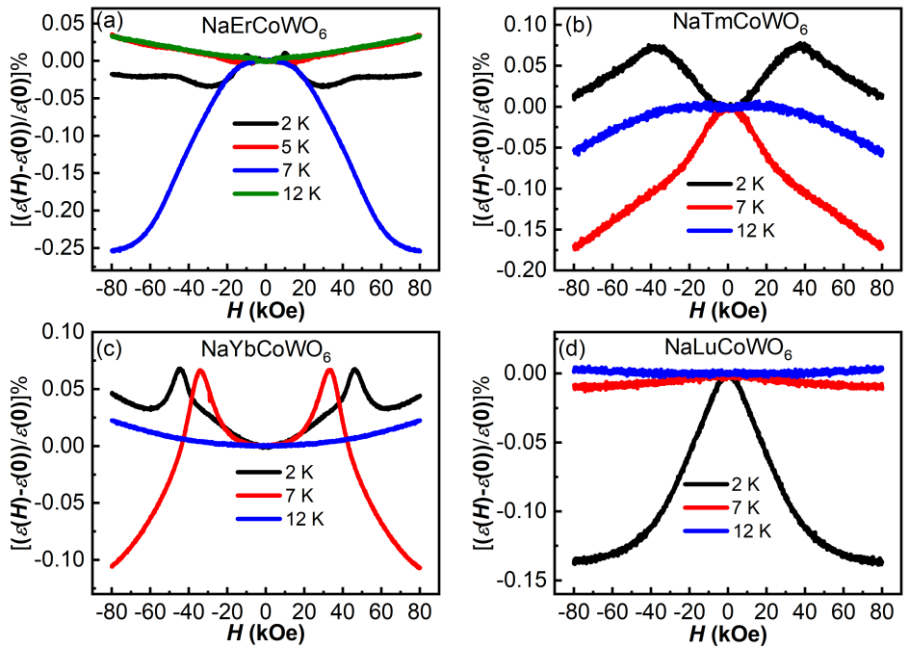

Figure 5.9 Field dependent magnetodielectric effect measured at different temperatures.

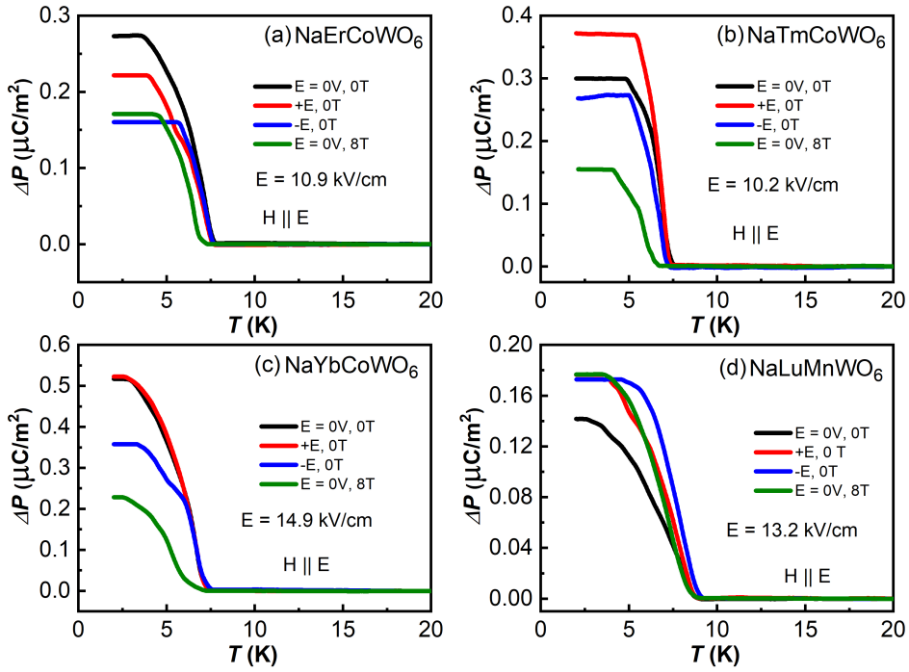

Figure 5.10 (a-d) Temperature dependent change in polarization (ΔP) obtained by integrating pyroelectric current against measurement duration.

Also, the nonswitchable polarization below magnetic ordering temperature reveals that the polarization contribution from magnetic ordering could be in the same direction as that of the paramagnetic state. A relatively large energy barrier between the two polar states of these

pyroelectric materials Na*Ln*CoWO$_6$ (*Ln* = Er, Tm, and Yb) and NaLuMnWO$_6$ may be the reason for the nonswitchable polarization. Further neutron studies are required to determine the magnetic structure of these compounds.

In the NaLuCoWO$_6$ compound, a pyrocurrent signal was not observed without applying an electric field as observed in previously discussed compounds. The pyrocurrent was measured upon poling the sample from temperature 15 to 2 K with the electric field of E = 12.1 kV/cm at 0 and 1T. Although the observed pyrocurrent signal is low, it showed clear switching of signal with changing the direction of the electric field (E = -12.1 kV/cm). The observed pyrocurrent signal was greatly suppressed with an applied field. The measured pyrocurrent with ±E was integrated with time at 0 and 1T and presented as temperature dependent change in polarization (ΔP) as shown in Figure 5.11.

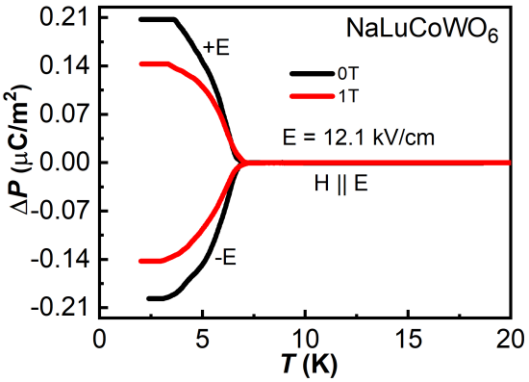

Figure 5.11 Temperature dependent change in electric polarization (ΔP) measured with electric field (±E) poling at 0 and 1T.

The observed switchable polarization in NaLuCoWO$_6$ could be due to magnetoelastic coupling, as discussed in NaYNiWO$_6$. The magnetic structure of NaLuCoWO$_6$ might be different from other cobalt compounds in their series, but further neutron studies are required to confirm. However, the observed change in polarization below magnetic ordering temperature confirmed the magnetoelectric coupling of all these compounds. The dc-bias measurement was carried out to verify the intrinsic polarization. The dc-bias signal below the magnetic ordering temperature confirmed the intrinsic polarization in all these compounds, as shown in Figure 5.12. The suppression of the dc-bias current at 8 T is similar to the dielectric anomaly.

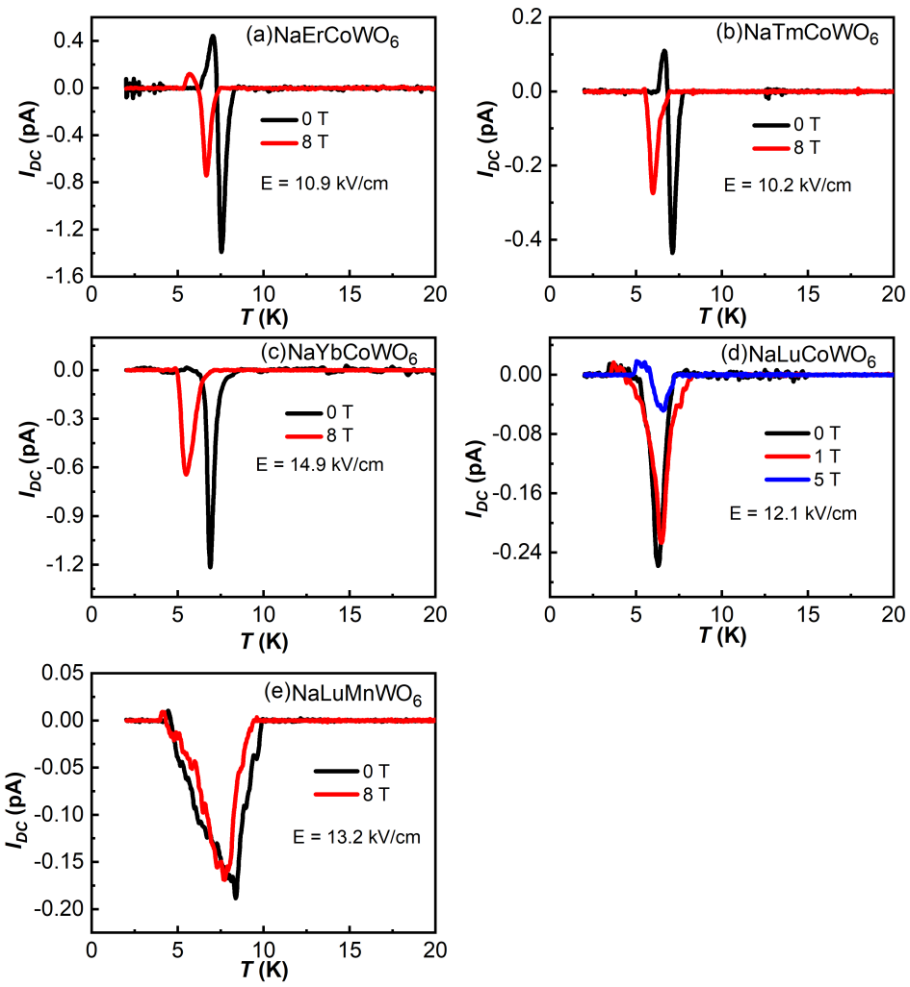

Figure 5.12 Temperature variation of dc bias current measured with an electric field (E) and under magnetic fields.

The attempt to probe ferroelectric polarization in $NaLuCoWO_6$ by polarization *vs.* electric field (P-E) measurements showed a linear *P-E* curve that does not represent ferroelectricity (Figure 5.13). It may be because of the polycrystalline nature of the samples, which has difficulties in poling. The spontaneous polarization was estimated from point charge model with nominal charges (Na = +1, *Ln* = +3, Co and Mn = +2, W = +6, and O = -2), by considering only ionic contribution. The estimated polarizations are ~28 $\mu C/cm^2$ for $NaErCoWO_6$, ~27 $\mu C/cm^2$ for $NaTmCoWO_6$, ~26 $\mu C/cm^2$ for $NaYbCoWO_6$, ~23 $\mu C/cm^2$ for $NaLuMnWO_6$, and 26 $\mu C/cm^2$ for $NaLuCoWO_6$. The obtained polarization values are in the same order of magnitude as that of similar doubly ordered perovskite values [9,16,20].

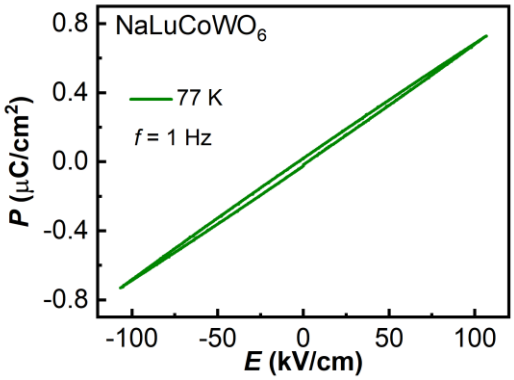

Figure 5.13 Polarization (*P*) *vs*. electric field (*E*) loop measured at 77 K.

5.3.3 Results on $NaYFeWO_6$ and $NaHoFeWO_6$

5.3.3.1 Crystal structure

Figure 5.14 shows the results of Rietveld refined pattern of X-ray diffraction data collected at room temperature for both samples. The structural parameters are given in Table

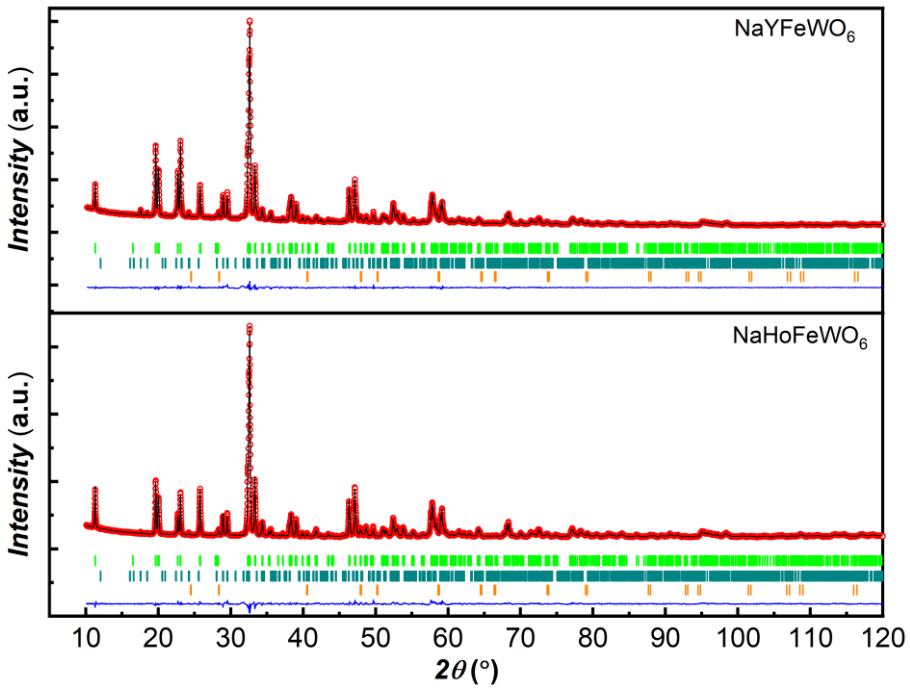

Figure 5.14 Rietveld refined powder x-ray diffraction data of $NaYFeWO_6$ and $NaHoFeWO_6$. The first tick marks (green) are the Bragg reflections of the main phase. The second tick marks (dark cyan) are the Bragg reflections of Ln_2WO_6 (*Ln* = Y and Ho) impurity. The third tick marks (orange) are the Bragg reflections of KCl.

A-3.5.7 and A-3.5.8. The impurities Ln_2WO_6 (*Ln* = Y, Ho) and KCl were present along with the main phase, and their corresponding weight percentage is given in Table A-3.5.9. Lattice and selected bond parameters are shown in Table 5.5 and Table 5.6, respectively. Bond lengths and bond angles have similar values as previously discussed doubly ordered perovskites.

Table 5.5 Lattice parameters obtained from Rietveld refinement of PXRD data of $NYFeWO_6$ and $NaHoFeWO_6$ at RT.

Compound	*a* (Å)	*b* (Å)	*c* (Å)	*β* (°)	*V* (Å^3)
$NaYFeWO_6$	5.3711(1)	5.5296(1)	7.8275(2)	90.248(2)	232.48(3)
$NaHoFeWO_6$	5.3731(2)	5.5304(2)	7.8324(2)	90.231(3)	232.74(1)

Table 5.6 Selected bond lengths (Angstroms) and angles (Degrees) obtained by the Rietveld refinement of PXRD data of $NaYFeWO_6$ and $NaHoFeWO_6$.

Compound	Fe-O(1)	Fe-O(2)	Fe-O(3)	Fe-O(4)	Fe-O(5)	Fe-O(6)
$NaYFeWO_6$	1.77(2)	2.01(2)	2.07(2)	2.17(2)	2.06(1)	1.95(1)
$NaHoFeWO_6$	1.84(2)	1.93(2)	1.97(2)	2.07(2)	2.08(2)	1.88(2)
	W-O(1)	W-O(2)	W-O(3)	W-O(4)	W-O(5)	W-O(6)
$NaYFeWO_6$	2.33(2)	2.08(1)	1.84(2)	1.79(1)	2.24(1)	1.87(1)
$NaHoFeWO_6$	2.18(2)	2.09(2)	1.99(2)	1.97(2)	2.26(2)	1.93(2)
	Fe-O(1)-W	Fe-O(2)-W	Fe-O(3)-W	Fe-O(4)-W	Fe-O(5)-W	Fe-O(6)-W
$NaYFeWO_6$	149(1)	143(1)	158(1)	144(1)	141.2(5)	151.5(6)
$NaHoFeWO_6$	151.5(9)	151.7(8)	149.4(7)	141.8(8)	141.1(7)	159.3(7)

5.3.3.2 Magnetic studies

Temperature dependent magnetization under a field of 1000 Oe in field-cooled (FC) condition for $NaYFeWO_6$ and $NaHoFeWO_6$ is shown in Figures 5.15(a, b). The observed magnetization curves indicate antiferromagnetic transition for these compounds. From the maximum slope in C_p/T *vs*. *T* data, the antiferromagnetic ordering temperature (T_N) of Fe^{2+} ions were determined for $NaYFeWO_6$ (~ 13 K), and $NaHoFeWO_6$ (~ 15 K) at 0 T and T_N decreased to a lower temperature at 8 T. The broad peak below T_N in magnetization and heat capacity data of $NaHoFeWO_6$ corresponds to Ho^{3+} cation ordering. We have shown only FC magnetization because ZFC and FC curves deviate from higher temperatures and exhibit a peak around 120 K, corresponding to magnetic impurity (Fe_3O_4) present in these samples. Magnetic field dependent isothermal magnetization curves below and above T_N are shown in Figure

5.15(c, d). The non-linear *M vs*. *H* curves are observed for $NaHoFeWO_6$, which is attributed to the field induced transition of the Ho^{3+} cation.

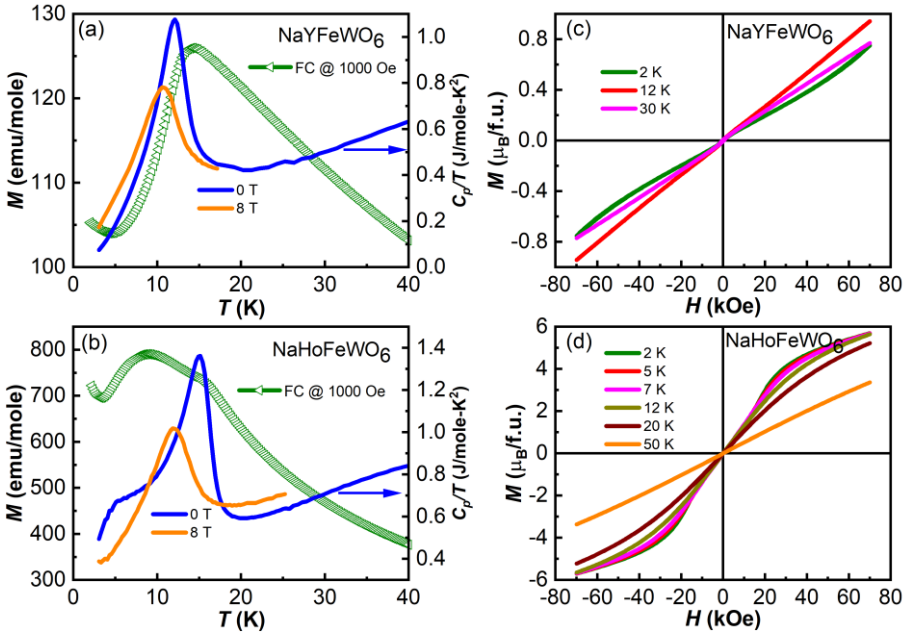

Figure 5.15 (a, b) Temperature dependent FC magnetization and heat capacity plotted as C_p/T *vs*. *T* (right axis). (c, d) Field dependent isothermal magnetization of $NaYFeWO_6$ and $NaHoFeWO_6$.

5.3.3.3 Electrical properties

Dielectric measurements of $NaYFeWO_6$ and $NaHoFeWO_6$ were carried out to investigate the probable magnetoelectric coupling across the magnetic ordering temperature. Figures 5.16(a, c) show the temperature dependence of the dielectric constant with 50 kHz frequency under different fields. The dielectric peaks at the magnetic ordering temperature and the shifting of peaks towards lower temperature with increasing magnetic field demonstrate the magnetodielectric coupling of these compounds. The dielectric peak at T_N was not seen in the case of doubly ordered compounds Na*Ln*$FeWO_6$ (*Ln* = La, Nd, Pr, and Sm) [16,21]. Dielectric peaks of $NaYFeWO_6$ and $NaHoFeWO_6$ at different frequencies across the magnetic ordering temperature are shown in Figures 5.16(b, d). At lower temperatures 2-30 K, the dielectric constant value is in the range of 17-19 and 11-12 for $NaYFeWO_6$ and $NaHoFeWO_6$, respectively. Magnitudes of these values are in the same order as that observed in other compounds in this family. The dielectric constant value increases to very high with increasing temperature, where the value is greatly raised at lower frequencies while the rise in value with higher frequencies is significantly smaller.

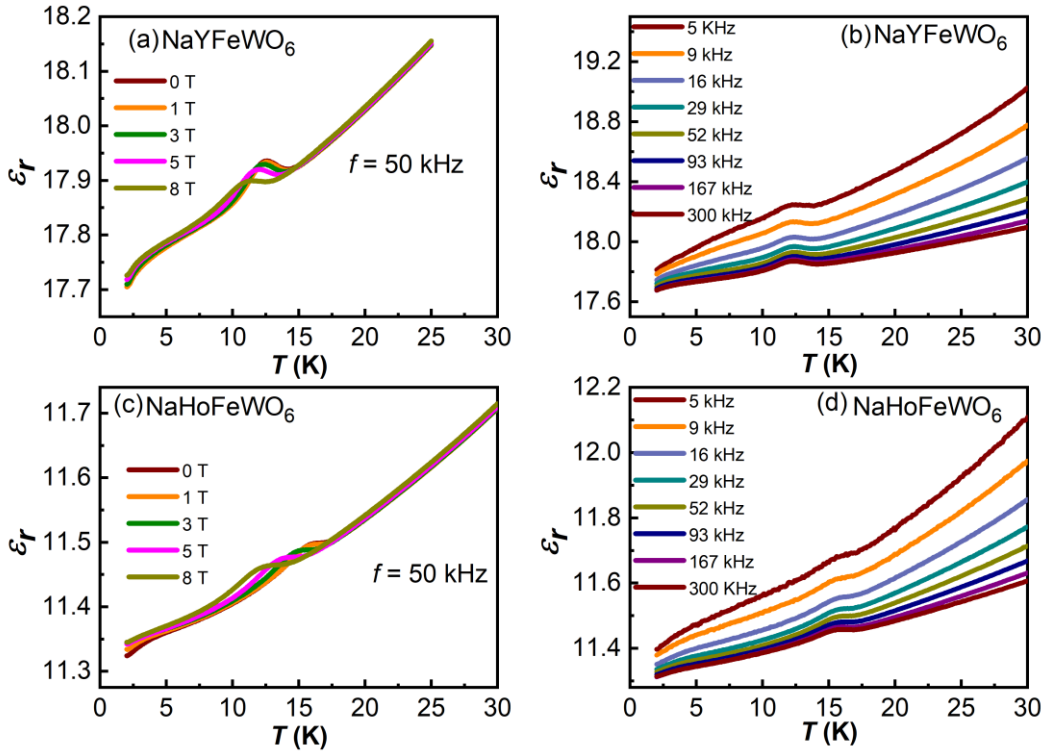

Figure 5.16 (a, c) Temperature dependence of dielectric constant with 50 kHz frequency in presence of various fields. (b, d) Dielectric constant as a function of temperature with different frequencies.

The observation of the dielectric anomaly around the magnetic ordering temperature trigger to perform the pyroelectric and dc-bias current measurement across T_N. Unfortunately, because of the leakage current in both samples, the pyroelectric current peaks are broad. In Figure 5.17(a-d), the observed broad pyroelectric current anomalies around magnetic ordering temperature are shown, which seems to be magnetic field dependent similar to dielectric data. Similar behavior was observed with opposite peaks after changing the direction of the poling electric field (-E). It is known that extrinsic pyrocurrent peaks from thermally stimulated charge carriers (TSFC) are also switchable with the negative electric field [22]. Figure 5.17(e, f) shows the dc-biased current measurement with E ~ 12.5 kV/cm from 2 – 30 K, where the current was increasing with temperature, but little variation was observed around magnetic ordering temperature. The magnetic field dependence of pyrocurrent and dc-bias anomalies may indicate the magnetoelectric coupling of these compounds, but overall peaks are dominated by the contribution of leakage currents. Further need to design synthesis method which apparently helps to avoid leakage contribution in these materials. Also, neutron-diffraction measurements are required to determine the magnetic structure of $NaYFeWO_6$ and $NaHoFeWO_6$ compounds.

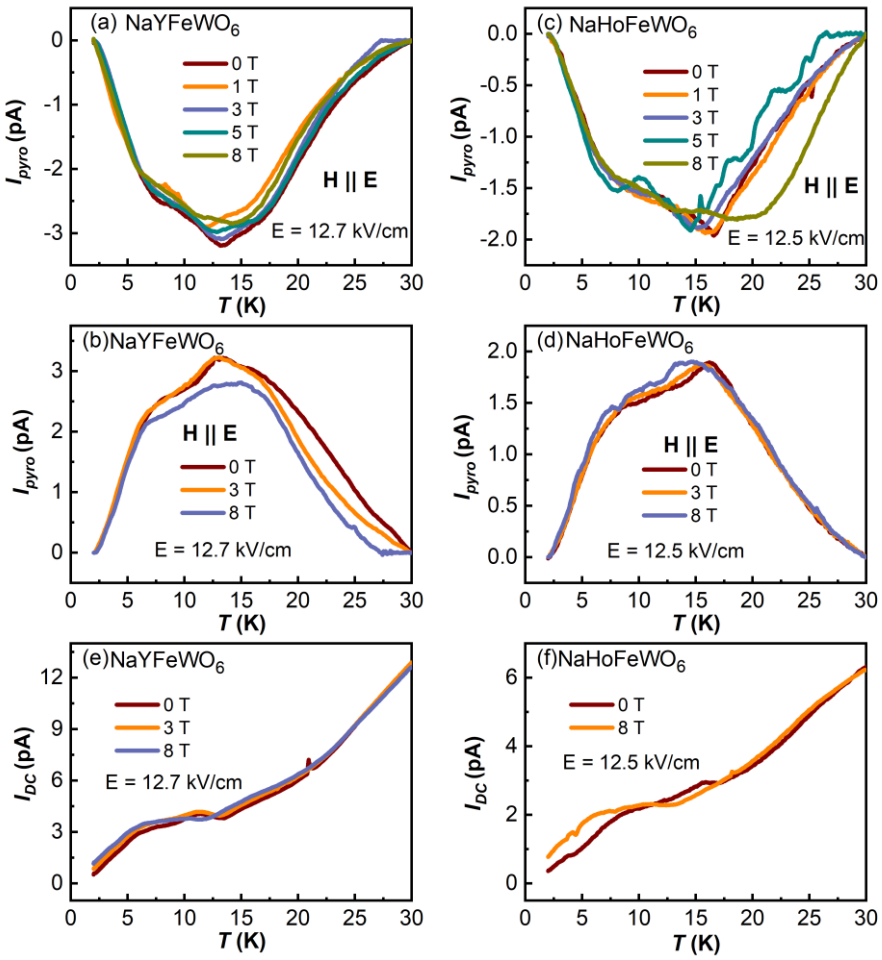

Figure 5.17 Temperature dependent pyroelectric and dc bias current measured with an electric field (E) and under magnetic fields.

5.4 Conclusion

We have studied the structural and physical properties of doubly ordered perovskites with different transition metal cations. The combined cation ordering at both *A*- and *B*-sites as well as the octahedral tilting, are the key factors of these perovskites to crystallize in polar $P2_1$ structure. They exhibit long-range antiferromagnetic ordering along with dielectric anomaly in the temperature range of 6-8 K. Polarization was observed without poling electric field, and it is not switchable because of the large energy barrier between the two polar states of this pyroelectric Na*Ln*$CoWO_6$ (*Ln* = Y, Er, Tm, and Yb) and $NaLuMnWO_6$ compounds. The magnetic structure of $NaYCoWO_6$ is collinear and indicates that the observed change in polarization in this compound could be due to spin-lattice coupling. Interestingly, the polarization of $NaLuCoWO_6$ was switchable with changing the direction of the poling electric field. Further, a neutron diffraction study is required to determine the magnetic structure of

$NaLuCoWO_6$ and other compounds to understand the disparity in the results of polarization property below magnetic ordering temperature. On the other hand, the magnetic and dielectric anomalies confirmed the magnetodielectric behavior of $NaYFeWO_6$ and $NaHoFeWO_6$ compounds. The leakage current was dominated in the case of pyro and dc-bias current measurements because of the conductive nature of these samples.

References

[1] R. S. P. N, S. Mishra, and S. Athinarayanan, **8**, 040906, (2020).

[2] Y. Li, G. Gao, and K. Yao, Epl **118**, (2017).

[3] Y. S. Tang, S. M. Wang, L. Lin, C. Li, S. H. Zheng, C. F. Li, J. H. Zhang, Z. B. Yan, X. P. Jiang, and J. M. Liu, Phys. Rev. B **100**, 1 (2019).

[4] T. Kurumaji, S. Ishiwata, and Y. Tokura, Phys. Rev. B **95**, 1 (2017).

[5] V. Caignaert, A. Maignan, K. Singh, C. Simon, V. Pralong, B. Raveau, J. F. Mitchell, H. Zheng, A. Huq, and L. C. Chapon, Phys. Rev. B - Condens. Matter Mater. Phys. **88**, 3 (2013).

[6] Y. S. Oh, S. Artyukhin, J. J. Yang, V. Zapf, J. W. Kim, D. Vanderbilt, and S. W. Cheong, Nat. Commun. **5**, 1 (2014).

[7] S. Ghara, E. Suard, F. Fauth, T. T. Tran, P. S. Halasyamani, A. Iyo, J. Rodríguez-Carvajal, and A. Sundaresan, Phys. Rev. B **95**, 224416 (2017).

[8] R. Shankar P N, F. Orlandi, P. Manuel, W. Zhang, P. S. Halasyamani, and A. Sundaresan, Chem. Mater. **32,** 5641, (2020).

[9] P. Zuo, C. V Colin, H. Klein, P. Bordet, E. Suard, E. Elkaim, and C. Darie, Inorg. Chem. **56**, 8478 (2017).

[10] P. Zuo, H. Klein, C. Darie, and C. V Colin, J. Magn. Magn. Mater. **458**, 48 (2018).

[11] A. Wills, J. Phys. IV JP **11**, (2001).

[12] H. Ikeda, I. Hatta, and M. Tanaka, J. Phys. Soc. Japan **40**, 334 (1976).

[13] M. Ghosh, E. V. Sampathkumaran, and C. N. R. Rao, Chem. Mater. **17**, 2348 (2005).

[14] S. Blundell, Oxford University Press: 2001.

[15] G. King, A. S. Wills, and P. M. Woodward, Phys. Rev. B - Condens. Matter Mater. Phys. **79**, 1 (2009).

[16] J. Blasco, J. A. Rodríguez-Velamazán, G. Subías, J. L. García-Muñoz, J. Stankiewicz, and J. García, Acta Mater. **176**, 53 (2019).

[17] M. R. Li, E. E. McCabe, P. W. Stephens, M. Croft, L. Collins, S. V. Kalinin, Z. Deng, M. Retuerto, A. Sen Gupta, H. Padmanabhan, V. Gopalan, C. P. Grams, J. Hemberger, F. Orlandi, P. Manuel, W. M. Li, C. Q. Jin, D. Walker, and M. Greenblatt, Nat. Commun. **8**, 2037 (2017).

[18] A. Gauzzi, F. P. Milton, V. Pascotto Gastaldo, M. Verseils, A. J. Gualdi, D. Von Dreifus, Y. Klein, D. Garcia, A. J. A. De Oliveira, P. Bordet, and E. Gilioli, Appl. Phys. Lett. **115**, (2019).

[19] M. Chandra, S. Yadav, R. J. Choudhary, R. Rawat, A. K. Sinha, M.-B. Lepetit, and K. Singh, Phys. Rev. B **98**, 104427 (2018).

[20] T. Fukushima, A. Stroppa, S. Picozzi, and J. M. Perez-Mato, Phys. Chem. Chem. Phys. **13**, 12186 (2011).

[21] M. Retuerto, M. R. Li, A. Ignatov, M. Croft, K. V Ramanujachary, S. Chi, J. P. Hodges, W. Dachraoui, J. Hadermann, T. T. Tran, P. S. Halasyamani, C. P. Grams, J. Hemberger, and M. Greenblatt, Inorg. Chem. **52**, 12482 (2013).

[22] C. De, S. Ghara, and A. Sundaresan, Solid State Commun. **205**, 61 (2015).

Chapter 6

Magnetization plateau, magnetocaloric and multiferroic properties of $LiFeV_2O_7$ and magnetic properties of $LiCrAs_2O_7$*

Summary

We have investigated the emergence of magnetization plateau, magnetocaloric effect and multiferroicity in the frustrated antiferromagnet $LiFeV_2O_7$ and the structural and magnetic properties of polar $LiCrAs_2O_7$. $LiFeV_2O_7$ is crystallized in a polar monoclinic *Cc* structure, and the Fe^{3+} ions in octahedral coordination (FeO_6) occupy three independent crystallographic sites and render this compound magnetically frustrated. Temperature dependent magnetic and heat capacity measurements reveal long-range antiferromagnetic ordering of Fe^{3+}-moments around 5 K, which is suppressed by applied magnetic fields. At 2 K, the magnetization curve exhibits a magnetization plateau with one-third of the saturation moment at 4.3 T. A significant magnetocaloric effect is observed around T_N with a maximum magnetic entropy change ($-\Delta S$ ~ 9 J/kg.K) at 7 T. Analysis of neutron diffraction data at 2 K confirms that the magnetic structure is collinear (**k** = (0, 1, 0)) with different ordered moments associated with each Fe-sites. Dielectric and dc-bias experiments on $LiFeV_2O_7$ confirm the magnetic order induced electric polarization, which disappears in the magnetization plateau region. $LiCrAs_2O_7$ crystallize in the monoclinic *C*2 structure supported by second harmonic generation studies. Temperature dependent magnetic and heat capacity measurements reveal antiferromagnetic long-range ordering of $LiCrAs_2O_7$ around 5 K . We have not observed the dielectric anomaly in the case of $LiCrAs_2O_7$ despite having long-range magnetic ordering and a polar crystal structure.

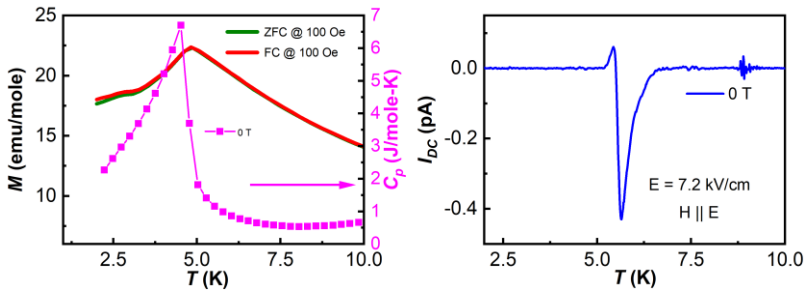

……..

*Manuscript based on this work is under preparation.

6.1 Introduction

The materials $LiFeP_2O_7$, $LiFeV_2O_7$, $LiFeAs_2O_7$, $LiVP_2O_7$, etc., have been studied because of their intriguing crystal chemistry and, more recently, electrochemical properties [1–5]. These compounds are used as a cathode material for lithium-ion batteries because they may undergo reversible electrochemical Li^+ insertion correlated with the Fe^{3+}/Fe^{2+} redox couple. Here, our interest is in the polar crystal structure and the presence of transition magnetic metal cations in these compounds. The pentavalent cations (A = P, As, V) mainly occupies tetrahedra (AO_4) in the structural network, whereas magnetic cations (Fe, Cr, and V) are present in an octahedral environment. These compounds may exhibit long-range magnetic ordering through super-super-exchange (SSE) interactions. Weak ferromagnetism and magnetoelectric effect have been reported in polar ($P2_1$) $LiFeP_2O_7$ [6]. Single crystals of isostructural compound $LiCrP_2O_7$ and its physical properties were reported, but the magnetoelectric effect was not observed [7]. The compound $LiFeAs_2O_7$ with monoclinic polar space group $C2$ exhibited antiferromagnetic ordering at 35 K and was suggested to be a potential multiferroic. The magnetic structure of $LiFeAs_2O_7$ is complex, intermediate between a pure helical and pure cycloidal, whereas the magnetic structure of analog compound $LiFeP_2O_7$ is simple with collinear magnetic moments arrangement [8,9].

In this chapter, we have studied the interaction of the magnetic order with electric polarization in the polar $LiFeV_2O_7$, crystallizing in the monoclinic space group Cc supported by second harmonic generation (SHG) studies. Dielectric anomaly and dc-bias current at the magnetic ordering temperature (T_N = 5 K) confirmed that the compound $LiFeV_2O_7$ is multiferroic. It also exhibits a sizable magnetocaloric effect (MCE) around the magnetic ordering temperature. The magnetic structure is collinear with $\mathbf{k}$ = (0, 1, 0). This compound also exhibits a magnetization plateau with one-third of the saturation magnetization. Further, we have investigated the other polar compound $LiCrAs_2O_7$. The non-centrosymmetric structure of this compound is confirmed by SHG studies. This compound orders antiferromagnetically around 5 K. Electrical measurements show no dielectric anomaly corresponding to magnetic ordering temperature, indicating the absence of magnetoelectric coupling in this compound. Also, we have investigated the multiferroic properties of $LiFeAs_2O_7$ considering its previous studies on structural, magnetic, and incommensurate magnetic structure, but the electrical measurements failed to detect any electrical anomaly to confirm the ferroelectricity below magnetic ordering temperature [8].

6.2 Experimental section

Polycrystalline $LiFeV_2O_7$ was prepared by the solid-state method in air. The stoichiometric mixture of precursors Li_2CO_3, Fe_2O_3, and V_2O_5 was manually ground in an agate mortar. The grounded mixture was heated in the air in an alumina crucible to 580 ℃ with a 5 ℃/min heating rate for 5-6 days. The purity of the obtained sample was confirmed by X-ray diffraction. Polycrystalline $LiCrAs_2O_7$ was prepared using the wet method. The stoichiometric mixture of precursors $Li(CH_3COO)\cdot 2H_2O$, $NH_4H_2AsO_4$, and $Cr(NO_3)_3\cdot 9H_2O$ were dissolved in demineralized water, and the acidic pH (~ 5) was maintained to avoid any precipitance of precursors that prevent the formation of targeted pure compound. The aqueous solutions of precursors were heated around 150 ℃ to evaporate the solvent. Further, the submicronic powders were annealed at 600 ℃ to obtain particles with higher crystallinity.

The samples crystallographic structures were characterized by powder X-ray diffraction (Rigaku SmartLab diffractometer) with non-monochromatized Cu $K\alpha_1$ (1.5406 Å) and Cu $K\alpha_2$ (1.5446 Å). The Rietveld refinement of powder X-ray diffraction (PXRD) data was performed by the FullProf suite program [10]. Time-of-flight (TOF) neutron powder diffraction (NPD) data were collected in the temperature range of 2-10 K for $LiFeV_2O_7$ using the GEM diffractometer at the ISIS pulsed spallation source (Rutherford Appleton Laboratory, U.K.). The Rietveld refinement of NPD data was carried out with the TOPAS V.5.0 using the banks 1-6 of the TOF neutron powder diffractometer [11]. Group theoretical calculations to determine the magnetic space group were performed with the help of online-based ISOTROPY and ISODISTORT software [12]. Physical property characterization was performed on these compounds, as mentioned in the previous chapters.

6.3 Results and discussion

6.3.1 Results on $LiFeV_2O_7$

6.3.1.1 Structural analysis

The powder X-ray diffraction (PXRD) data of $LiFeV_2O_7$ indicate that the sample is crystallized with a polar *Cc* space group, as shown in Figure 6.1, and the corresponding crystallographic parameters are given in appendix Table A-4.6.1. The neutron powder diffraction (NPD) data collected at 10 K and the patterns (bank 1 to 6) are well fitted with the room temperature monoclinic structure (*Cc*), as shown in Figure 6.2.

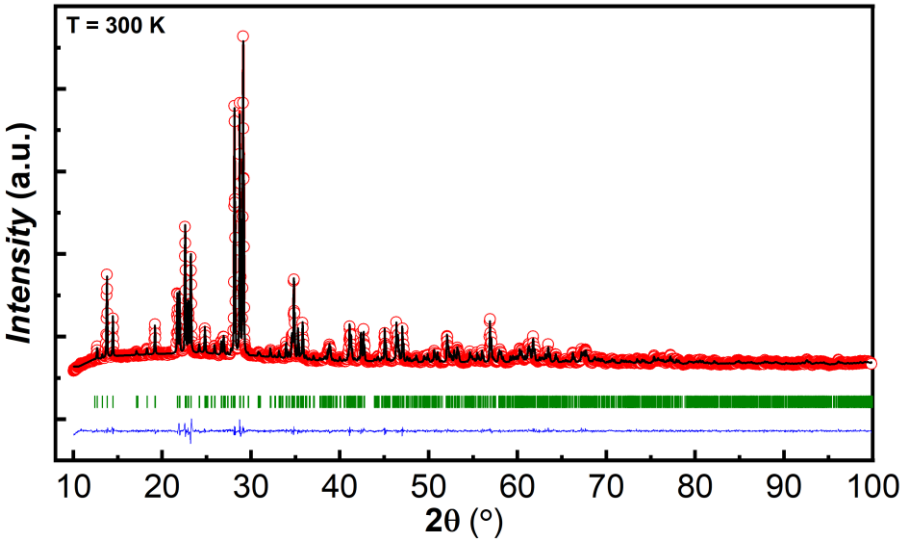

Figure 6.1 Rietveld refined fit of $LiFeV_2O_7$ where calculated and experimental intensities are plotted as a continuous black line and red circles, respectively. The olive-green tick marks correspond to Bragg positions of space group *Cc* and the difference in intensities is shown in the blue line.

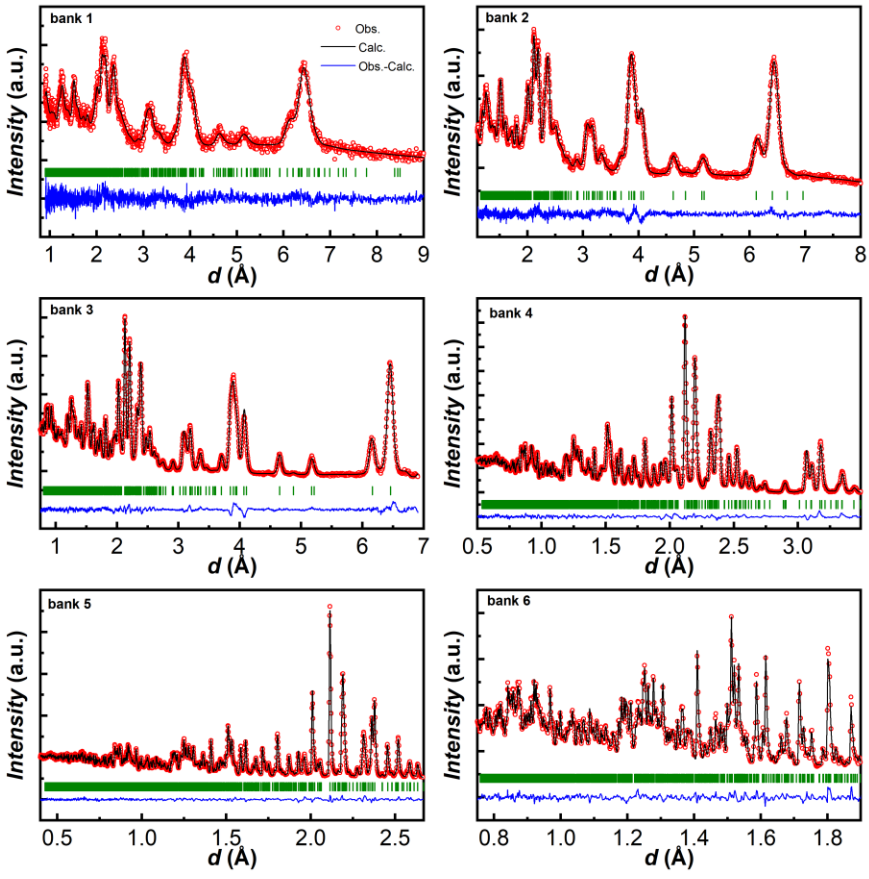

Figure 6.2 Rietveld analysis of GEM bank 1-6 neutron powder diffraction data measured at 10 K. The olive-green tick marks correspond to Bragg positions of space group *Cc* and the difference in intensities is shown in the blue line.

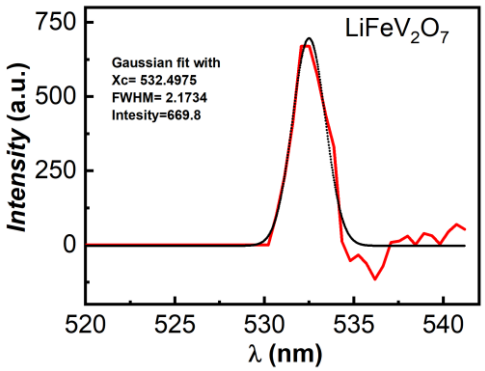

Figure 6.3 The SHG signal from spectrometer data, which is processed by baseline subtraction and five-point average to get clear SHG data. The data is fitted with a Gaussian curve to see the mean value with full width half maxima.

The refinement of the nuclear structure from neutron diffraction data confirmed the room temperature structural model in addition to the precise determination of lithium positions in the crystal structure. The crystallographic parameters and reliability factors of the refinement from time-of-flight NPD data at 10 K are given in Table 6.1. Further, the non-centrosymmetric space group is confirmed by SHG measurements where the signal was observed around half the wavelength of 1064 nm, as shown in Figure 6.3. The crystal structure of $LiFeV_2O_7$ is given in Figure 6.4(a).

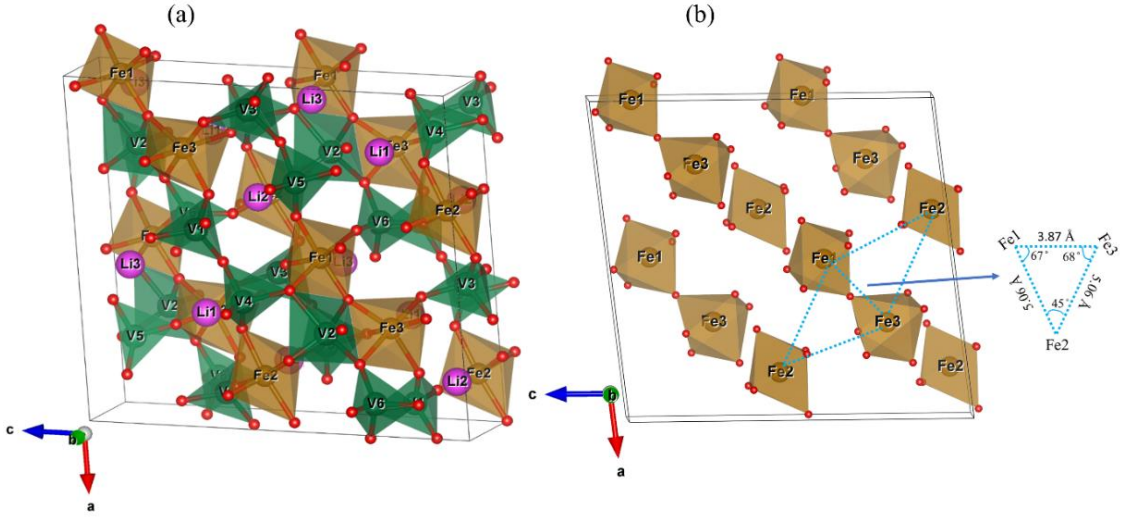

Figure. 6.4 (a) Crystal structure of $LiFeV_2O_7$ viewed along [010] direction, oxygen atoms are colored red. (b) Isosceles triangles of Fe-ions.

All the atoms present in the crystal structure occupy general positions, which include three different iron and lithium sites, six vanadium sites, and 21 oxygen sites. The FeO_6

octahedra indicate Fe-O bond distances between 1.91 and 2.13 Å, similar to a previous report [5]. All FeO_6 are surrounded by five VO_4 tetrahedra, Fe2 shares the sixth corner with the VO_5 trigonal bipyramid while the corner-sharing Fe1 and Fe3 share adjacent edges of VO_5 trigonal bipyramid, as can be seen in the crystal structure (Figure 6.4(a)). The Fe^{3+} ions in octahedral coordination (FeO_6) occupy three independent crystallographic sites and forms isosceles tringles and render this compound magnetically frustrated. The magnetic exchange interactions between adjacent Fe^{3+} ions occur through VO_4 and VO_5 network, and a corner shared oxygen between Fe1 and Fe3 ions.

Table 6.1 Crystallographic parameters of $LiFeV_2O_7$ from the refinement of NPD data collected at 10 K.

Atom	Wyckoff position	*x*	*y*	*z*	B_{iso} (Å^2)	Occ.
Fe1	4*a*	0.48729	0.8029(4)	0.36898	0.24(1)	1.0
Fe2	4*a*	0.8388(4)	0.8270(2)	0.5456(3)	0.24(1)	1.0
Fe3	4*a*	0.6866(2)	0.3004(4)	0.7130(2)	0.24(1)	1.0
V1	4*a*	0.412(6)	1.031(9)	0.173(5)	0.10(2)	1.0
V2	4*a*	0.704(4)	1.013(6)	0.343(4)	0.10(2)	1.0
V3	4*a*	0.566(4)	0.462(7)	0.495(4)	0.10(2)	1.0
V4	4*a*	0.612(5)	0.959(7)	0.563(4)	0.10(2)	1.0
V5	4*a*	0.264(5)	0.964(9)	0.400(5)	0.10(2)	1.0
V6	4*a*	0.394(4)	0.464(6)	0.247(4)	0.10(2)	1.0
O1	4*a*	0.4629(4)	0.3232(6)	0.4804(4)	0.19(5)	1.0
O2	4*a*	0.3082(4)	1.1520(6)	0.1488(4)	0.17(5)	1.0
O3	4*a*	0.2232(5)	0.9806(5)	0.2852(5)	0.37(6)	1.0
O4	4*a*	0.3841(5)	0.4866(6)	0.1219(4)	0.38(6)	1.0
O5	4*a*	0.4085(4)	0.6460(6)	0.2965(4)	0.26(6)	1.0
O6	4*a*	0.2787(4)	1.1593(6)	0.4497(5)	0.13(5)	1.0
O7	4*a*	0.5136(5)	0.8803(7)	0.6223(5)	0.47(7)	1.0
O8	4*a*	0.6078(3)	0.7905(5)	0.3016(4)	0.30(5)	1.0
O9	4*a*	0.5731(4)	0.9737(6)	0.4480(4)	0.13(5)	1.0
O10	4*a*	0.6676(4)	1.1275(5)	0.3087(4)	0.56(6)	1.0
O11	4*a*	0.6489(4)	1.1401(6)	0.6075(4)	0.17(5)	1.0
O12	4*a*	0.6612(5)	0.3803(6)	0.4540(5)	0.27(6)	1.0
O13	4*a*	0.2805(4)	0.3632(6)	0.2792(4)	0.28(5)	1.0
O14	4*a*	0.4937(4)	0.3401(5)	0.2730(4)	0.16(5)	1.0
O15	4*a*	0.4386(4)	1.0071(5)	0.2950(4)	0.16(5)	1.0
O16	4*a*	0.5285(5)	0.6429(7)	0.4634(5)	0.74(9)	1.0
O17	4*a*	0.3909(5)	0.8442(9)	0.1217(6)	2.10(1)	1.0
O18	4*a*	0.7768(5)	0.9959(7)	0.4507(5)	1.39(9)	1.0
O19	4*a*	0.5977(5)	0.4549(6)	0.6366(5)	1.20(1)	1.0
O20	4*a*	0.3693(4)	0.8501(7)	0.4323(5)	0.50(7)	1.0
O21	4*a*	0.7063(4)	0.8126(6)	0.5931(4)	0.18(5)	1.0
Li1	4*a*	0.6684(8)	0.686(1)	0.7090(8)	0.30(2)	1.0
Li2	4*a*	0.3124(9)	0.299(1)	0.0202(8)	0.60(2)	1.0
Li3	4*a*	0.5612(9)	0.178(2)	0.3517(9)	0.72(2)	1.0

Space group: *Cc*; a = 13.4515(2) Å, b = 8.1691(1) Å, c = 14.3653(2) Å, β = 96.5967(7)°. Vol.: 1568.11(4) Å^3; Reliability factors: GOF = 1.97, Bragg R-factor = 0.87 (%), R_{wp}– factor = 2.12 (%), R_{exp}– factor = 1.08 (%).

6.3.1.2 DC magnetization

Temperature variation of the zero-field-cooled (ZFC) and field-cooled (FC) magnetization was carried out under a magnetic field of 100 Oe. Magnetization and heat capacity data confirm that Fe^{3+}-ions order antiferromagnetically around 5 K, as shown in Figure 6.5(a). The slight increase of magnetization below 3 K could be due to the different magnetic moments of three Fe^{3+} ions, as discussed in the magnetic structure section. Applied magnetic fields shifted the magnetic ordering to low temperature and suppressed below 2 K at above 4 T, as shown in the magnetization and heat capacity data. Isothermal magnetization curve at 2 K shows field induced transition around 1 T that can be seen in the derivative curve as shown

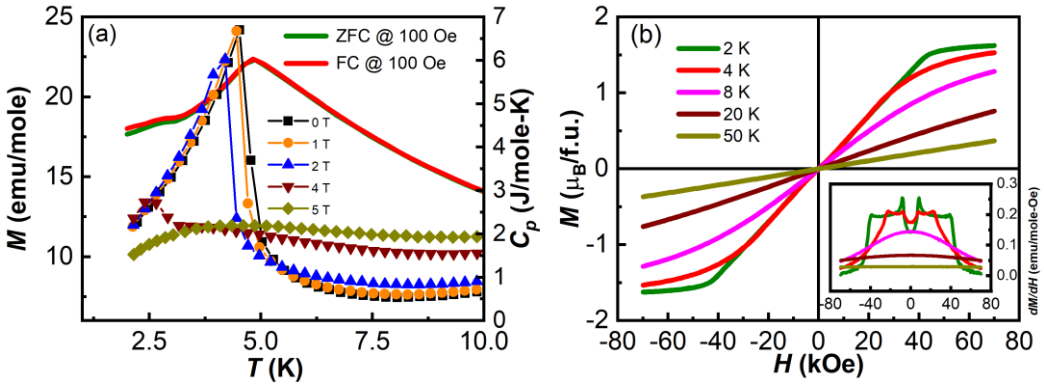

Figure 6.5 (a) DC magnetization as a function of temperature under ZFC and FC condition with 100 Oe field and temperature dependent heat capacity data (C_p) with different fields 0 – 5 T. (b) magnetic field dependent magnetization $M(H)$ and dM/dH in the inset.

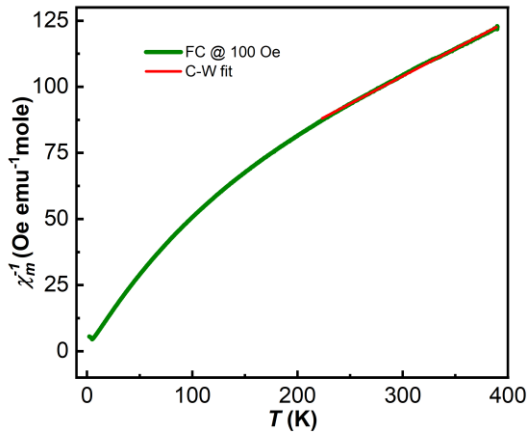

Figure 6.6 Temperature dependent inverse susceptibility data fitted to Curie-Weiss law at higher paramagnetic region.

in the inset of Figure 6.5(b). With further increase of field, the magnetization increases linearly and show a plateau at 4.3 T with one-third of saturation magnetization. Such magnetization plateau has been reported in low dimensional frustrated antiferromagnets. For example, the system $R_2V_2O_7$ (R = Ni, Co) shows a similar magnetization plateau and a field induced ferroelectricity [13]. The Curie-Weiss fit was performed to the inverse susceptibility data at the high temperature paramagnetic region (shown in Figure 6.6). The effective magnetic moment obtained from the fit is 6.2 μ_B/f.u. which is close to the calculated paramagnetic moment of 5.9 μ_B/f.u. The Curie-Weiss temperature (θ_{CW}) is -199 K indicating the dominant antiferromagnetic interactions. The estimated frustration parameter (f = 40) is remarkably high for $LiFeV_2O_7$. The frustration parameter ($f = |\theta_{CW}|/T_N$) greater than five means the system is highly frustrated. This could be due to competing exchange interactions between three different Fe^{3+} ions in the system. Further, theoretical investigations are required on this new high entropy material to understand the nature of geometrical and spin frustrations.

6.3.1.3 Magnetocaloric effect

Considering the field induced metamagnetic transition and saturation behavior of *M vs. H* curves at low temperatures, we have studied the magnetocaloric effect in $LiFeV_2O_7$. To calculate the magnetic entropy change (ΔS), one quadrant magnetic field dependent isothermal magnetization has been measured from 0-7 T in 2 K intervals between 2-20 K, and the corresponding plot is shown in Figure 6.7(a). The curves gradually display linear behavior, which indicates the increasing paramagnetic contribution above magnetic ordering temperature. Before we discuss the magnetocaloric effect (MCE), we point out the nature of magnetic transition with the help of Arrot plots. According to the Banerjee criterion, if the slope of *H/M vs.* M^2 curves (Arrott plot) is negative, then the magnetic transition is of first order, while a positive slope indicates second-order transition [14]. From Figure 6.7(b), it is clear that the slope of the Arrot plots is positive around T_N, revealing the second-order magnetic phase transition of this compound. However, the negative slope of the 2 K curve (inset of Figure 6.7(b)) may be due to the first-order transition from the AFM-FM transition associated with the metamagnetic transition of $LiFeV_2O_7$.

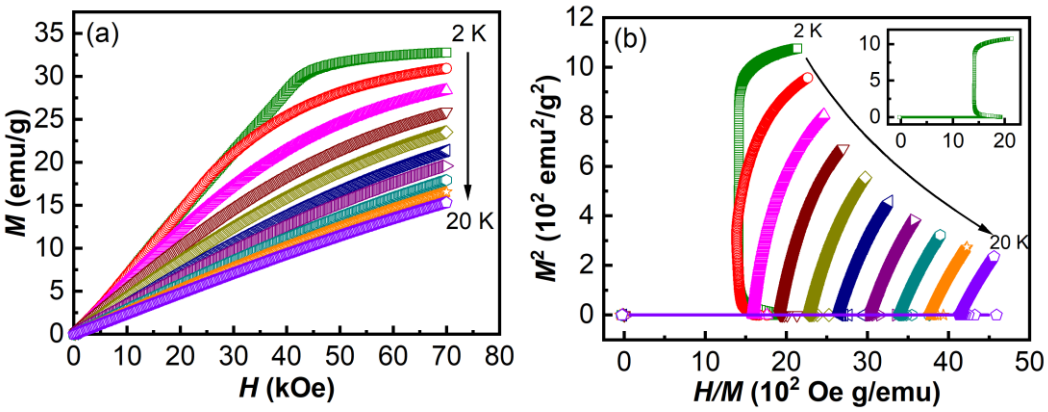

Figure 6.7 (a) Magnetic field dependent magnetization measured up to 7 T between isothermal temperature 2-20 K in the interval of 2 K. (b) M^2 *vs*. *H/M* plot at different temperatures around magnetic ordering temperature. Inset: Arrott plot at 2 K.

The magnetocaloric effect was estimated using Maxwell's thermodynamic relation:

$$\Delta S(T,H) = \int_0^H \left(\frac{\partial M}{\partial T}\right)_H dH$$

The isothermal magnetic entropy change under magnetic fields from 5-70 kOe is given in Figure 6.8(a). A magnetic entropy change ($-\Delta S$) showed a maximum value around T_N with the maximum value of $-\Delta S$ ~ 9 J/kg.K under a magnetic field of 70 kOe, which is relatively high in the oxide system. The magnetic entropy (ΔS) changes its sign at a lower temperature below 30 kOe, and this behavior is related to field induced transition observed in the magnetization measurements. Furthermore, the magnetic entropy change was calculated from the heat capacity data by the equation below,

$$\Delta S = \int_0^T \frac{C_p(T)}{T}\, dT$$

As seen in Figure 6.8(b), the calculated $-\Delta S$ from the heat capacity (C_p) follows the same trend as that obtained from *M vs*. *H* data. On the whole, these results indicate that $LiFeV_2O_7$ exhibits second-order magnetic phase transition, and it is a good candidate for the magnetocaloric effect.

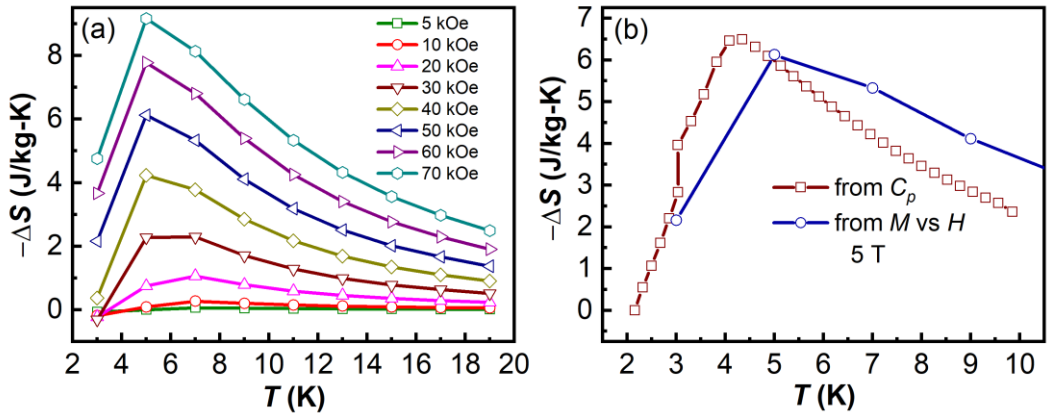

Figure 6.8 (a) Temperature variation of entropy changes (ΔS) under various magnetic fields obtained from isothermal field dependent magnetization data. (b) Comparison of magnetic entropy change obtained from both *M vs*. *H* and heat capacity (C_p) data at 5 T, respectively.

6.3.1.4 Electrical studies

An apparent dielectric anomaly is seen in $\varepsilon_r(T)$ at the magnetic ordering temperature in the absence of a magnetic field, as shown in Figure 6.9(a), and with increasing applied magnetic field, the dielectric anomaly is shifted to lower temperature. The absence of a dielectric peak at 5 T could be due to the shift of the anomaly further below 2 K, which might be related to a change in the spin structure under applied magnetic fields, as indicated by heat capacity data and magnetic field dependent magnetization. Frequency dependent dielectric constant against temperature showed dielectric anomaly at $T_{N,}$ and it is not associated with any relaxation phenomenon as shown in Figure 6.9(b). Isothermal field dependent dielectric constant showed the magnetodielectric effect, corresponding to magnetization data as shown in Figure 6.10.

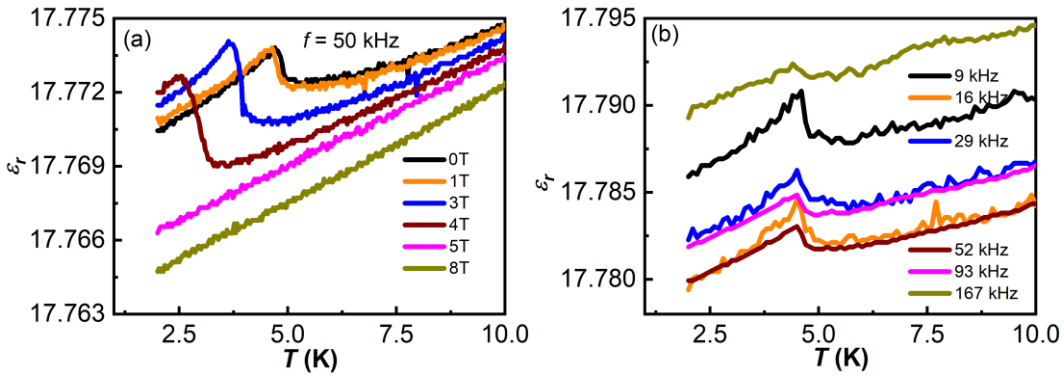

Figure 6.9 (a, b) Temperature dependent dielectric constant $\varepsilon_r(T)$ measured at various magnetic fields and frequencies.

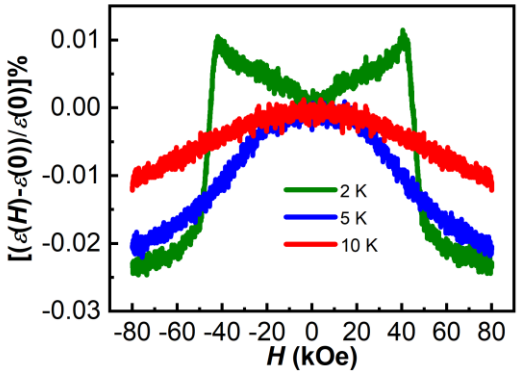

Figure 6.10 Isothermal field dependent dielectric constant $\varepsilon(H)$ at various temperatures, normalized by the expression $[(\varepsilon(H)-\varepsilon(0))/\varepsilon(0)]\%$.

Pyroelectric current measurements did not show an anomaly below magnetic ordering temperature. However, temperature dependent dc-bias current measurement showed a broad positive polarization peak followed by a sharp negative depolarization current peak, as shown in Figure 6.11(a) at 0 - 4 T, confirming the ferroelectricity of this compound below magnetic ordering temperature. The dc-bias signal shifted to a lower temperature with an increasing magnetic field similar to the dielectric anomaly. DC-bias current measurement is a well-known method to distinguish between intrinsic polarization from thermally stimulated free charge carriers [15,16]. During this measurement, the current is recorded while warming the sample by applying the dc electric field without prior poling. The change in polarization obtained by integrating the depolarization peak of the dc-bias signal is shown in Figure 6.11(b). The observed dc-bias current signal at the magnetic ordering temperature confirmed the multiferroic properties of this compound. Further, we have measured the electric field dependent polarization $P(E)$ loops at 77 K with a high field of about 350 kV/cm which showed lossy dielectric behavior, as shown in Figure 6.12.

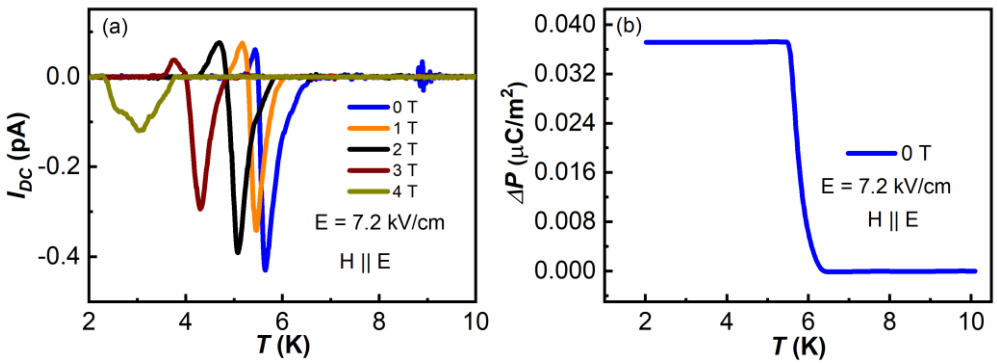

Figure 6.11 Temperature variation of dc-biased current at 0 – 4 T with an electric field of E = 7.2 kV/cm.

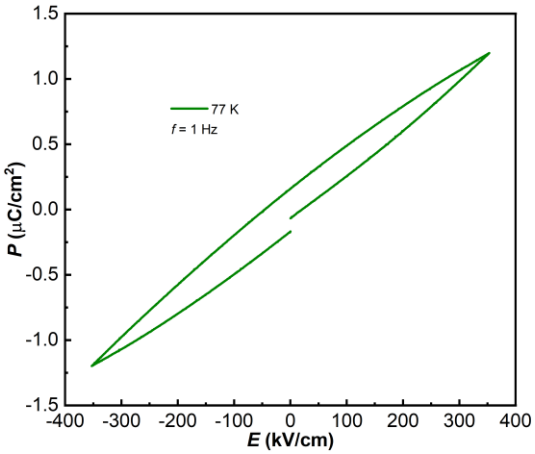

Figure 6.12 Electric field dependent polarization measured at 77 K.

6.3.1.5 Magnetic structure

Neutron powder diffraction (NPD) studies were carried out to determine the magnetic structure and understand the magnetoelectric coupling of the $LiFeV_2O_7$ compound. The NPD data were collected at 10 K and 2 K to determine the crystal and magnetic structures. The magnetic reflections at 2 K can be indexed with **k** = (0, 1, 0). The Rietveld refinement of NPD data at 2 K, performed using TOPAS Academic V. 5.0, is shown in Figure 6.13, and asterisks indicate the intense magnetic peaks. Group-theoretical calculations were performed by the ISODISTORT program to identify the magnetic space group. Out of the two irreducible representations, mY1 and mY2, the former with origin (0, 0, 0) and magnetic space group P_Cc fit the experimental data well. Various combinations of moments were tried, and a better fit is obtained by refining the moment values along the *b*-axis for all the three Fe atoms. The magnetic structure is shown in Figure 6.14. It has moment components of My = 1.2(9) μ_B for Fe1, 3.4(2) μ_B for Fe2, and 1.4(9) μ_B for Fe3, respectively. It should be noted that the chemical environment of Fe2 is different from Fe1 and Fe3, as discussed in the structural part. The magnetic structure of this compound is collinear, and it does not induce individual polarization. The observed magnetoelectric coupling of this compound could be due to spin-lattice coupling, and further studies on a single crystal of $LiFeV_2O_7$ could be helpful to realize magnetoelastic coupling as studied in $LiFeP_2O_7$ [6]. The magnetic structure of $LiFeP_2O_7$ is simple with **k** = (0, 0, 0). Thermal expansion experiments on $LiFeP_2O_7$ single crystal revealed the macroscopic distortion of the lattice below T_N, which confirmed the presence of significant spin-lattice coupling associated with the reported magnetoelectricity. Also, the multiferroicity due to magnetoelastic coupling is reported in other classes of compounds in the literature [17,18–20].

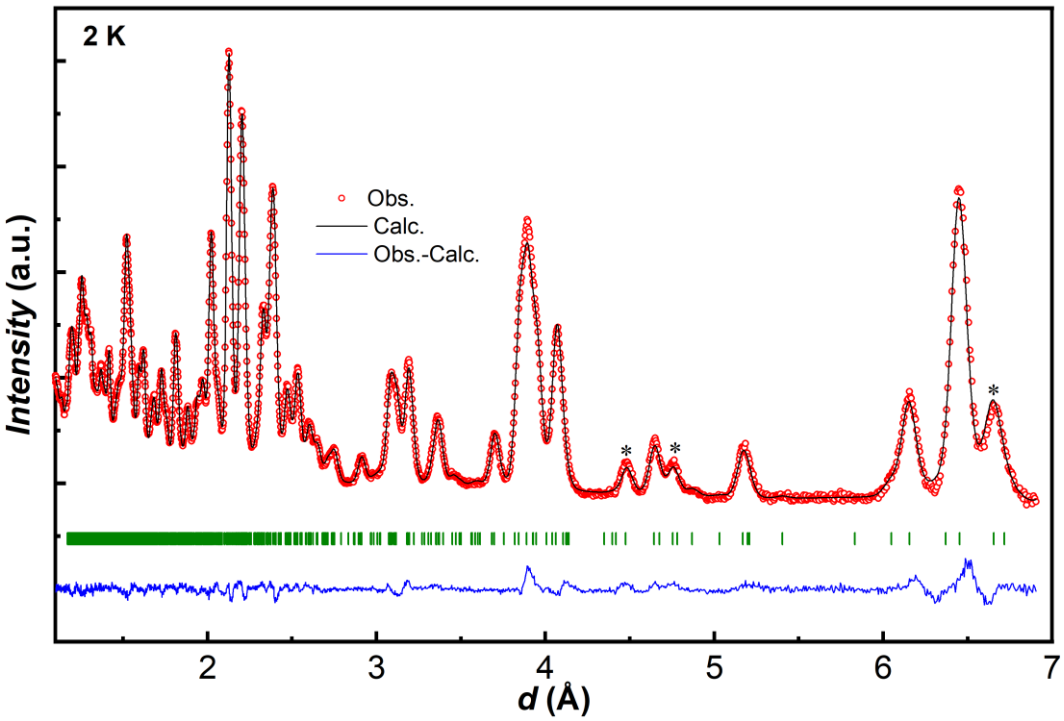

Figure 6.13 Rietveld refinement result of the time-of-flight (TOF) NPD pattern collected on GEM at 2θ = 34.96º and 2 K for $LiFeV_2O_7$ compound.

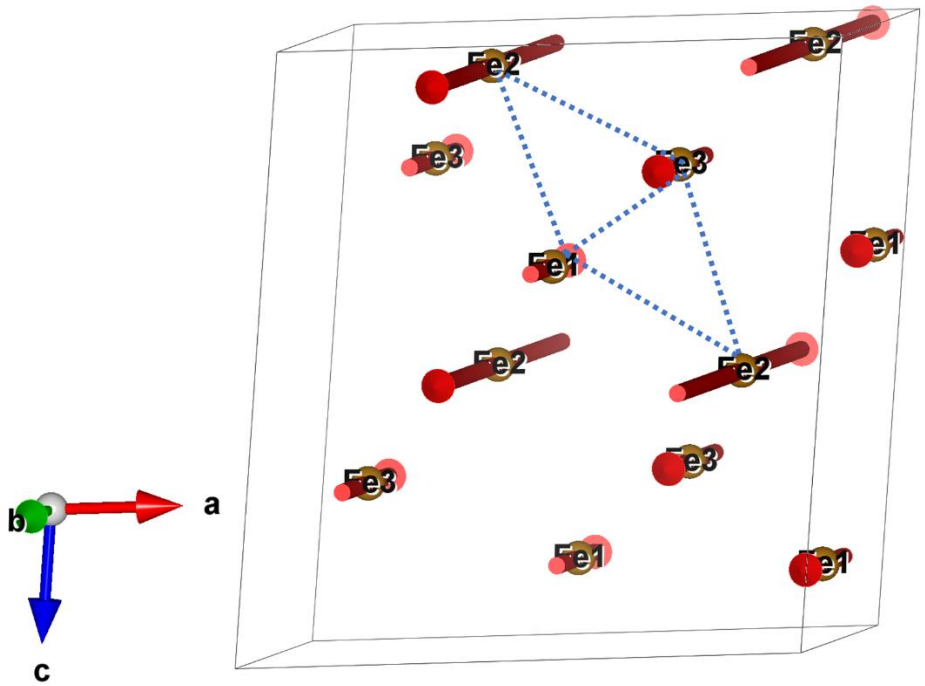

Figure 6.14 Magnetic structure of $LiFeV_2O_7$ with magnetic moments plotted on the Fe atoms and dotted lines represent isosceles triangles.

6.3.2 Results on $LiCrAs_2O_7$

6.3.2.1 Structural analysis

The powder X-ray diffraction (PXRD) data indicates that $LiCrAs_2O_7$ is pure and well crystallized. The PXRD data was refined with space group *C*2 (Figure 6.15), and the absence of the inversion centre is confirmed by SHG measurement, as shown in Figure 6.16. The resulting crystallographic parameters and reliability factors from the Rietveld refinement of PXRD data are given in Table 6.2. The crystal structure is shown in Figure 6.17, where the CrO_6 octahedron shares its corners with six diarsenate As_2O_7 groups. The Cr-O bond distances are in the range of 1.97 to 2.08 Å, indicating Cr ion is present at the middle of the O_6 octahedron [7]. In this structure, super-super-exchange type interactions take place through As_2O_7 units between Cr atoms.

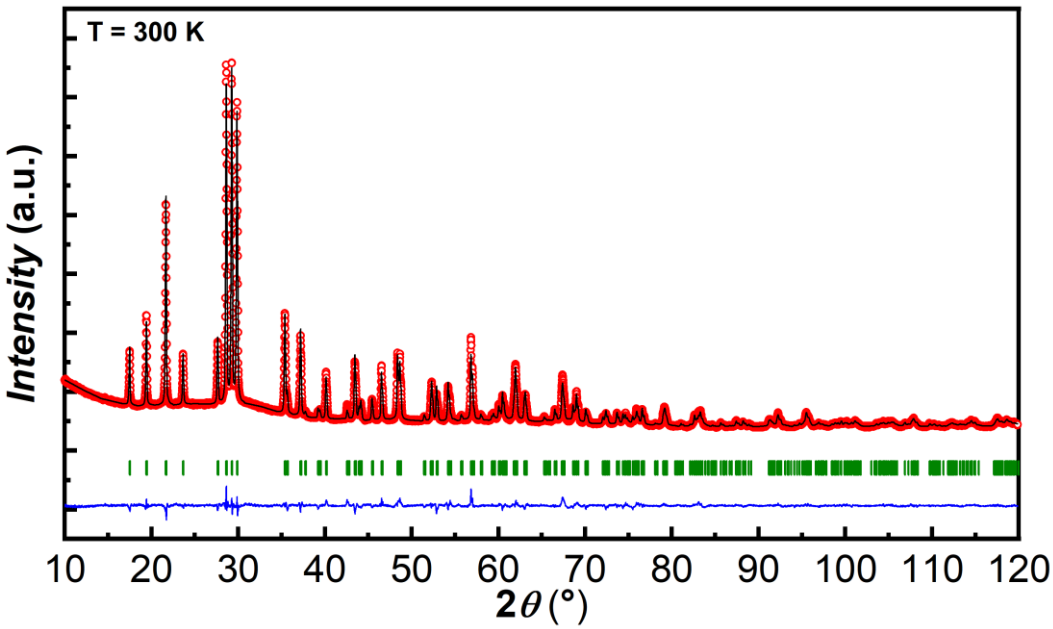

Figure 6.15 Rietveld refined fit of $LiCrAs_2O_7$ where calculated and experimental intensities are plotted as a continuous black line and red circles, respectively. The olive-green tick marks correspond to Bragg positions of space group *C*2, and the difference in intensities are shown in the blue line.

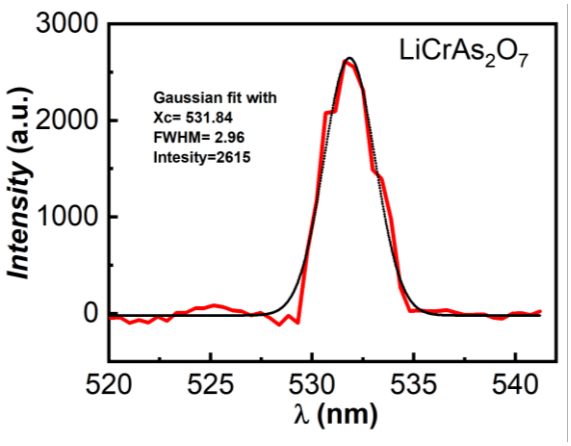

Figure 6.16 The SHG signal from spectrometer data, which is processed by baseline subtraction and five-point average to get clear SHG data. The data is fitted with a Gaussian curve to see the mean value with full width half maxima.

Table 6.2 Crystallographic parameters of $LiCrAs_2O_7$ from the refinement of PXRD data collected at room temperature.

Atom	Wyckoff position	*x*	*y*	*z*	B_{iso} (Å^2)	Occ.
Li	2*a*	0.0000	0.628(2)	0.0000	1.0000	0.5
Cr	2*a*	0.0000	0.0000	0.0000	0.89(4)	0.5
As	4*c*	0.7852(2)	0.3388(2)	0.5916(3)	0.70(6)	1.0
O1	4*c*	0.7623(6)	0.5025(6)	0.8439(9)	1.0000	1.0
O2	4*c*	0.8272(6)	0.1583(6)	0.7318(9)	1.0000	1.0
O3	4*c*	0.5994(6)	0.2966(5)	0.2603(9)	1.0000	1.0
O4	2*b*	0.0000	0.4397(7)	0.5000	1.0000	0.5

Space group: *C*2; a = 6.6414(2) Å, b = 8.2007(3)Å, c = 4.7026(1) Å, β = 103.734(3)°. Vol.: 248.797(4)Å^3; Reliability factors: χ^2 = 5.71, Bragg *R*-factor = 5.38 (%), R_f – factor = 5.76 (%).

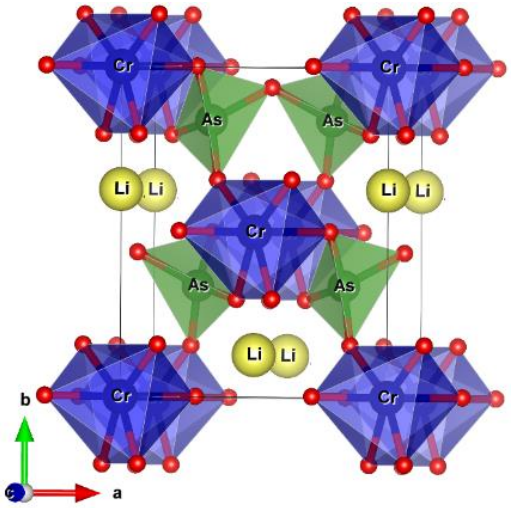

Figure 6.17 Crystal structure of $LiCrAs_2O_7$ viewed along [001] direction, oxygen atoms are colored red.

6.3.2.2 Magnetic and electrical properties

Temperature dependent dc magnetization under zero-field-cooled (ZFC) and field-cooled (FC) conditions with a magnetic field of 100 Oe is shown in Figure 6.18(a). The inset of Figure 6.18(a) shows *dM/dT* at 100 Oe underlying the antiferromagnetic transition temperature of this compound around 5.5 K, which is confirmed by heat capacity (C_p) data as shown in the right axis of Figure 6.18(a). Magnetization is increasing below magnetic ordering temperature could be due to spin canting. Unlike $LiFeV_2O_7$, applied magnetic fields during heat capacity measurement did not show any effect on the magnetic ordering temperature of this compound. Isothermal magnetization curve below magnetic ordering temperature at 2 K showed non-linearity related to field induced transition as seen in Figure 6.18(b). The Curie-Weiss fit was performed at a high-temperature paramagnetic region, as shown in Figure 6.19. The effective magnetic moment procured from the fit is 4.1 μ_B/f.u. which is close to the calculated paramagnetic moment of 3.9 μ_B/f.u. The Curie-Weiss temperature (θ_{CW}) is -18.9 K indicating the dominant antiferromagnetic interactions.

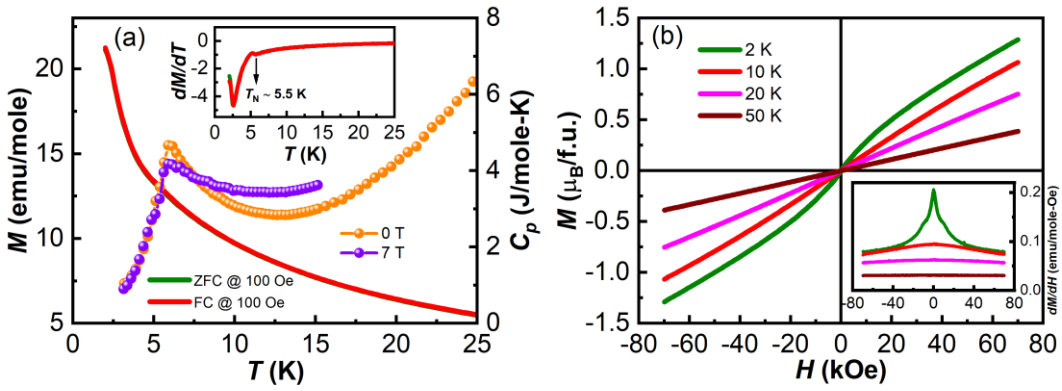

Figure 6.18 (a) DC magnetization as a function of temperature under ZFC and FC condition with 100 Oe field and temperature dependent heat capacity data (C_P) with different fields 0 and 7 T. (b) Magnetic field dependent magnetization $M(H)$ at various temperatures.

Despite having long-range magnetic ordering, this compound does not exhibit dielectric anomaly around magnetic ordering temperature. The absence of dielectric anomaly suggests that the coupling between order parameters could be so weak that it cannot be observed experimentally. Also, this compound is expected to show ferroelectricity owing to the polar nature of this compound, but the measured ferroelectric hysteresis loops yielded a linear dependence of the polarization (P) on the electric field (E) at 77 K, as shown in Figure 6.20. We have investigated the multiferroic properties of polar $LiFeAs_2O_7$ considering its previous

studies of its structural, magnetic, and incommensurate magnetic structure, but the electrical measurements failed to detect any electrical anomaly to confirm the ferroelectricity below magnetic ordering temperature [8].

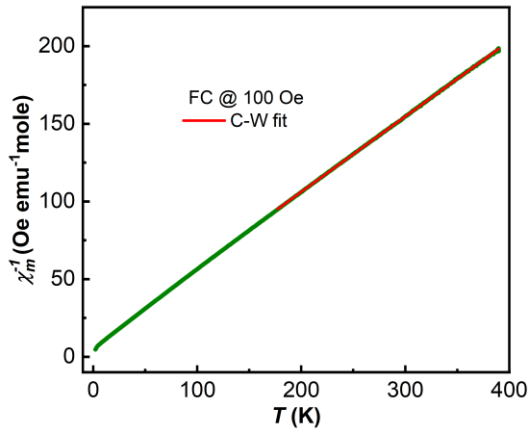

Figure 6.19 Temperature dependent inverse susceptibility data fitted to Curie-Weiss law at higher paramagnetic region.

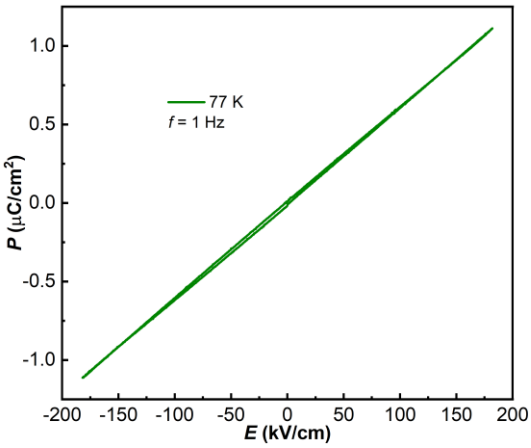

Figure 6.20 Electric field dependent polarization measured at 77 K.

6.4 Conclusion

Polycrystalline samples of $LiFeV_2O_7$ and $LiCrAs_2O_7$ have been synthesized by solid-state and wet chemical methods, respectively. The structural investigation by PXRD and NPD data and the SHG studies revealed a monoclinic *Cc* space group for $LiFeV_2O_7$ and *C*2 for $LiCrAs_2O_7$. The magnetic and heat capacity measurements confirmed the antiferromagnetic ordering of these compounds around 5 K. $LiFeV_2O_7$ showed field induced transition and, additionally, a significant magnetocaloric effect around T_N, which is reasonably high compared

to other antiferromagnetic oxides. The magnetic structure of $LiFeV_2O_7$ is collinear with **k** = (0, 1, 0). The observed dc-bias signal below magnetic ordering temperature confirmed the multiferroic properties of the $LiFeV_2O_7$. However, $LiCrAs_2O_7$ failed to show any electrical anomaly below magnetic ordering temperature despite having a polar structure. These studies open up a way to explore multiferroic and many other interesting properties of polar compounds.

References

[1] K. H. Lii, Y. P. Wang, Y. B. Chen, and S. L. Wang, J. Solid State Chem. **86**, 143 (1990).

[2] D. Riou, N. Nguyen, R. Benloucif, and B. Raveau, Mater. Res. Bull. **25**, 1363 (1990).

[3] A. K. Padhi, K. S. Nanjundaswamy, and J. B. Goodenough, J. Electrochem. Soc. **144**, 1188 (1997).

[4] C. Wurm, M. Morcrette, G. Rousse, L. Dupont, and C. Masquelier, Chem. Mater. **14**, 2701 (2002).

[5] Y. Benabed, L. Castro, N. Penin, J. Darriet, and M. Dollé, Chem. Mater. **29**, 9292 (2017).

[6] K. C. Liang, W. Zhang, B. Lorenz, Y. Y. Sun, P. S. Halasyamani, and C. W. Chu, Phys. Rev. B - Condens. Matter Mater. Phys. **86**, 1 (2012).

[7] E. Pachoud, W. Zhang, J. Tapp, K. C. Liang, B. Lorenz, P. C. W. Chu, and P. S. Halasyamani, Cryst. Growth Des. **13**, 5473 (2013).

[8] G. Rousse, J. Rodríguez-Carvajal, C. Wurm, and C. Masquelier, Phys. Rev. B - Condens. Matter Mater. Phys. **88**, 1 (2013).

[9] G. Rousse, J. Rodríguez-Carvajal, C. Wurm, and C. Masquelier, Solid State Sci. **4**, 973 (2002).

[10] H. M. Rietveld, J. Appl. Crystallogr. **2**, 65 (1969).

[11] Coelho, A. A. TOPAS-Academic. (accessed Oct 20, 2014)..

[12] B. J. Campbell, H. T. Stokes, D. E. Tanner, and D. M. Hatch, J. Appl. Crystallogr. **39**, 607 (2006).

[13] R. Chen, J. F. Wang, Z. W. Ouyang, Z. Z. He, S. M. Wang, L. Lin, J. M. Liu, C. L. Lu, Y. Liu, C. Dong, C. B. Liu, Z. C. Xia, A. Matsuo, Y. Kohama, and K. Kindo, Phys. Rev. B **98**, 1 (2018).

[14] B. K. Banerjee, Phys. Lett. **12**, 16 (1964).

[15] C. De, S. Ghara, and A. Sundaresan, Solid State Commun. **205**, 61 (2015).

[16] N. Terada, Y. S. Glazkova, and A. A. Belik, Phys. Rev. B **93**, 155127 (2016).

[17] R. Shankar P N, F. Orlandi, P. Manuel, W. Zhang, P. S. Halasyamani, and A. Sundaresan, Chem. Mater. **32**, 5641 (2020).

[18] M. R. Li, E. E. McCabe, P. W. Stephens, M. Croft, L. Collins, S. V. Kalinin, Z. Deng, M. Retuerto, A. Sen Gupta, H. Padmanabhan, V. Gopalan, F. Orlandi, P. Manuel, W. M. Li, C. Q. Jin, D. Walker, and M. Greenblatt, Nat. Commun. **8**, 2037 (2017).

[29] M. Chandra, S. Yadav, R. J. Choudhary, R. Rawat, A. K. Sinha, M.-B. Lepetit, and K. Singh, Phys. Rev. B **98**, 104427 (2018).

[20] A. Gauzzi, F. P. Milton, V. Pascotto Gastaldo, M. Verseils, A. J. Gualdi, D. Von Dreifus, Y. Klein, D. Garcia, A. J. A. De Oliveira, P. Bordet, and E. Gilioli, Appl. Phys. Lett. **115**, (2019).

Summary of the thesis

For pursuing the quest for magnetoelectric multiferroics, it is important to design new materials and understand the various mechanisms of combining ferroelectricity and magnetism for future new technological applications. In this thesis, we focused on exploring a new class of multiferroic materials based on polar magnetic oxides where the polar structure results from chemical ordering. This class of multiferroics is promising because they do not necessarily involve complex magnetic structures arising from spin frustration, and therefore one can combine appropriate magnetic ions with the polar structure to achieve a magnetoelectric effect at room temperature. Initially, we have worked on a series of doubly ordered perovskites Na*Ln*$NiWO_6$ (*Ln* =Y, Dy – Lu) in which polar structure arises because of the combined cation ordering in both the sites and octahedral tilting. Our attempt to measure typical ferroelectric polarization versus electric field loop was unsuccessful. However, switchable polarization is observed below magnetic ordering temperature. $NaYNiWO_6$ manifested an unconventional spin density wave with **k** = (0.47, 0, 0.49) near magnetic ordering temperature (T_N), and it changes to a collinear magnetic structure with **k** = (0.5, 0, 0.5) below 18 K. Subsequently, we have investigated larger sized rare-earth cation compounds Na*Ln*$NiWO_6$ (*Ln* = La, Pr-Tb). These compounds showed only a magnetodielectric effect without measurable change in electric polarization around T_N. Further, we have extended our studies on doubly ordered perovskites with different transition magnetic cations (Co, Mn, and Fe). Non-switchable polarization is discovered in Na*Ln*$CoWO_6$ (*Ln* = Y, Er-Lu) and $NaLuMnWO_6$ indicating the pyroelectric nature of these compounds. Interestingly, switchable polarization is found in isostructural $NaLuCoWO_6$ similar to the Ni series. In contrast to the $NaYNiWO_6$, the $NaYCoWO_6$ exhibit only collinear magnetic structure with **k** = (0.5, 0, 0.5). Clear magnetodielectric behavior is probed in Na*Ln*$FeWO_6$ (*Ln* = Y, Ho). Miserably, we could not measure the polarization because of the conducting nature of these compounds. Apart from doubly ordered perovskites, we have explored the structural and physical properties of other polar oxides, $LiFeV_2O_7$ and $LiCrAs_2O_7$. $LiFeV_2O_7$ is a highly frustrated antiferromagnet (frustration parameter = 40) that exhibits a magnetization plateau with one-third of the saturation moment at 4.3 T. We found multiferroicity in $LiFeV_2O_7$, and further the magnetic structure of this compound with **k** = (0, 1, 0) suggest that the change in polarization below T_N could be due to magnetoelastic coupling. $LiCrAs_2O_7$, another polar antiferromagnet, has been investigated, in which multiferroicity is not observed.

Summary of compounds reported in the present thesis.

Compound	Space group	Transition temperature in K (T_N)	Property	Results
Chapter 3				
$NaYNiWO_6$	$P2_1$	21	Multiferroic	These compounds exhibit double peak in heat capacity data corresponding to incommensurate (AFM-SDW) with **k** = (0.47, 0, 0.49) and collinear magnetic structure with **k** = (0.5, 0, 0.5) Exhibit switchable polarization below T_N
$NaDyNiWO_6$		23		
$NaHoNiWO_6$		22		
$NaErNiWO_6$		21		
$NaTmNiWO_6$		20		
$NaYbNiWO_6$		20		
$NaLuNiWO_6$		18		
Chapter 4				
$NaLaNiWO_6$	$P2_1$	30	Magnetodielectric	$NaLaNiWO_6$ exhibit only collinear magnetic structure with **k** = (0.5, 0, 0.5) Polarization (ΔP) is not observed in these compounds
$NaPrNiWO_6$		30		
$NaNdNiWO_6$		30		
$NaSmNiWO_6$		27		
$NaEuNiWO_6$		26		
$NaGdNiWO_6$		24		
$NaTbNiWO_6$		23		
Chapter 5				
$NaYCoWO_6$	$P2_1$	7	Multiferroic	The magnetic structure of $NaYCoWO_6$ is collinear with **k** = (0.5, 0, 0.5) Na*Ln*$CoWO_6$ (*Ln* = Y, Er, Tm, Yb) and $NaLuMnWO_6$ exhibit non-switchable polarization below T_N, whereas polarization is switchable in $NaLuCoWO_6$ Pyrocurrent and dc-bias current peaks of Fe compounds are dominated by leakage currents
$NaErCoWO_6$		7		
$NaTmCoWO_6$		7		
$NaYbCoWO_6$		7		
$NaLuCoWO_6$		7		
$NaLuMnWO_6$		8		
$NaYFeWO_6$		13		
$NaHoFeWO_6$		15		
Chapter 6				
$LiFeV_2O_7$	*Cc*	5	Multiferroic	DC-bias signal below T_N confirmed the multiferroicity
$LiCrAs_2O_7$	*C*2	6	Antiferromagnetic	No electrical anomaly below T_N

Appendix 1

Chapter 3 Structural, magnetic, multiferroic properties of Na*Ln*NiWO$_6$ (*Ln* = Y, Dy-Lu) and unconventional spin density wave (SDW) structure of NaYNiWO$_6$

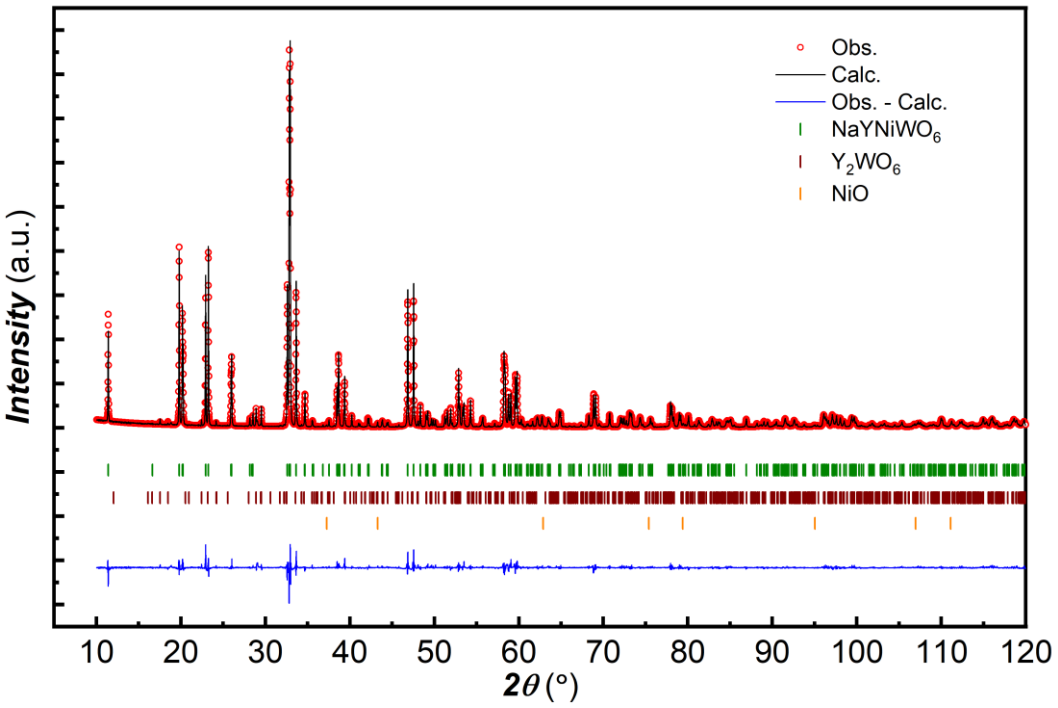

Figure A-1.3.1 Rietveld refined powder X-ray diffraction data of NaYNiWO$_6$ sample recorded at room temperature.

Table A-1.3.1 Structural parameters of NaYNiWO$_6$ from the PXRD pattern refinement. Space group: $P2_1$; a = 5.3226(2) Å, b = 5.4894(2) Å, c = 7.7499(2) Å, β = 90.202(9)º, Vol.: 225.55(1) Å^3; χ^2 = 4.50, Bragg R-factor = 4.88 (%), R_f – factor = 3.93 (%).

Atom	Wyckoff position	x	y	z	B_{iso} (Å^2)	Occ.
Na	2*a*	0.243(2)	0.215(3)	0.004(1)	2.6(4)	1.0
Y	2*a*	0.2654(5)	0.3132(5)	0.4994(3)	0.66(9)	1.0
Ni	2*a*	0.7500(8)	0.27(0)	0.2488(4)	0.1(1)	1.0
W	2*a*	0.7608(3)	0.2500	0.7664(1)	0.48(3)	1.0
O(1)	2*a*	0.546(4)	0.538(4)	0.698(2)	1.0	1.0
O(2)	2*a*	0.543(3)	0.552(4)	0.303(2)	1.0	1.0
O(3)	2*a*	-0.052(3)	-0.051(3)	0.217(2)	1.0	1.0
O(4)	2*a*	-0.084(4)	-0.040(3)	0.794(2)	1.0	1.0
O(5)	2*a*	0.845(2)	0.222(4)	0.499(1)	1.0	1.0
O(6)	2*a*	0.675(2)	0.276(5)	-0.008(1)	1.0	1.0

Details of DFT calculations

Spin-polarized DFT calculations were carried out by using the Vienna ab Initio Simulation Package (VASP) [1,2], the projector augmented wave (PAW) method and the PBE exchange-correlation functionals [3]. The electron correlation associated with the 3d states of Ni was taken into consideration by performing the DFT+U calculations with the effective on-site repulsion $U_{eff} = U - J$ on magnetic ions [4]. For the ionic relaxation, DFT+U calculations (with U_{eff} = 4 eV) were performed using a set of (6×6×4) k-points and the criterion of 10^{-3} eV/Å for ionic relaxation. All our DFT+U calculations (with U_{eff} = 3, 4, and 5 eV) for extracting the spin-exchange parameters employed the (2a, 4b, 2c) supercell, the plane wave cutoff energy of 450 eV, the threshold of 10^{-6} eV for self-consistent-field energy convergence and a set of (4×2×4) k-points. The preferred spin direction of Ni^{2+} cation was determined by DFT+U+SOC calculations employed a set of (6×6×4) k-points and the threshold of 10^{-7} eV for self-consistent-field energy convergence [5].

Table A-1.3.2 Geometrical parameters associated with the nine spin-exchange paths based on the crystal structure determined by neutron diffraction refinement at 100 K.[a,b]

	Ni…Ni	Ni-O	O…O	∠Ni-O…O, ∠O…O-Ni
J_1	5.4166	2.0593, 2.0495	2.8311	112.0, 147.9
		2.0495, 2.1259	2.8177	153.9, 103.4
J_2	5.4630	2.0441, 2.0495	2.7745	146.3, 115.5
		2.0495, 2.0765	2.7339	135.9, 116.3
J_3	5.4223	2.1259, 2.0631	2.6998	160.6, 105.0
		2.0593, 2.0631	2.6472	145.8, 109.9
J_4	5.4420	2.0631, 2.0441	2.6328	151.8, 107.8
		2.0631, 2.0765	2.6923	146.5, 117.7
J_a	5.3135	2.0441, 2.0593	2.5825	149.9, 107.5
		2.0765, 2.1259	2.7951	105.2, 140.6
J_b	5.4864	2.0441, 2.0765	2.7275	107.2, 162.4
		2.0593, 2.1259	2.6726	152.3, 115.1
J_c	7.7371	2.0495, 2.0631		
J_{ab}	7.6377	2.0593, 2.0765		
$J_{ab'}$	7.6377	2.1259, 2.0441		

[a] Space group: $P2_1$

[b] Cell parameters: a = 5.31349 Å, b = 5.48641 Å, c = 7.73727 Å, α = 90.0°, β = 90.2029°, γ = 90.0°.

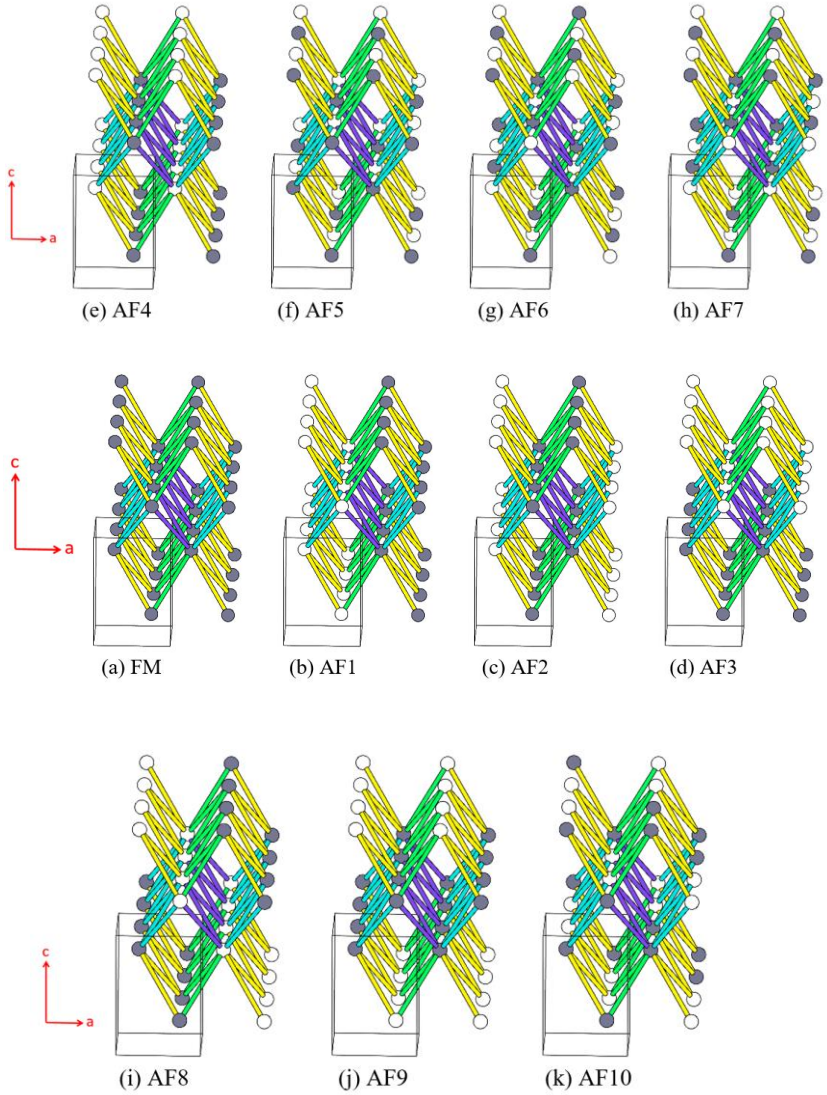

Figure A-1.3.2 Ordered spin states of $NaYNiWO_6$, where the J_a, J_b, J_{ab}, and J_c paths are not indicated in the diagrams. The grey and white circles indicate up and down spin sites, respectively.

The total spin exchange energies of the 11 ordered spin states per formula unit can be expressed as

$$E = \sum_{i=1}^{9} n_i J_i S^2 \qquad (1)$$

where S refers to the spin of the Ni^{2+} ion (i.e., S = 1). The values of n_i (i = a, b, c, ab, ab′, 1, 2, 3, 4) found for the 11 spin states are listed in Table A-1.3.3. We obtain the values of the

Table A-1.3.3 Energies of the 11 ordered spin states in terms of the nine spin-exchange parameters

	J_a	J_c	J_b	J_{ab}	J_{ab}'	J_1	J_2	J_3	J_4
E_{FM}	-32	-32	-32	-32	-32	-32	-32	-32	-32
E_{AF1}	32	-32	-32	32	32	-32	32	-32	32
E_{AF2}	32	-32	-32	32	32	32	-32	32	-32
E_{AF3}	-32	32	-32	-32	-32	32	-32	-32	32
E_{AF4}	-32	-32	-32	-32	-32	32	32	32	32
E_{AF5}	-32	-32	32	32	32	0	0	0	0
E_{AF6}	32	32	32	-32	-32	0	0	0	0
E_{AF7}	-32	32	32	32	32	0	0	0	0
E_{AF8}	32	32	-32	32	32	32	32	-32	-32
E_{AF9}	-32	32	-32	-32	-32	-32	32	32	-32
E_{AF10}	0	-32	0	-32	32	0	16	0	16

spin exchanges by energy-mapping analysis [6–8], in which the relative energies from the DFT+U calculations are mapped onto the corresponding energies expected from the spin exchange energies. The values of the nine spin exchanges are related to the relative energies of the ordered spin states as follows:

$$J_c = (1/64)(1/S^2)[E_{AF7} - E_{AF5}] \quad (2a)$$

$$J_3 = (1/128)[\{(E_{AF2} - E_{AF8}) - (E_{AF3} - E_{AF4})\}(1/S^2) + 128J_c] \quad (2b)$$

$$J_2 = (1/64)[(E_{AF4} - E_{AF3})(1/S^2) + 64J_c - 128J_3] \quad (2c)$$

$$J_1 = (1/128)[\{(E_{AF4} - E_{FM}) - (E_{AF1} - E_{AF2})\}(1/S^2) - 128J_3] \quad (2d)$$

$$J_4 = (1/128)[\{(E_{AF1} - E_{AF2}) - (E_{FM} - E_{AF4})\}(1/S^2) - 128J_2] \quad (2e)$$

$$J_a = (1/128)[\{(E_{AF1} - E_{AF9}) - (E_{AF5} - E_{AF6})\}(1/S^2) + 64J_3 - 64J_4] \quad (2f)$$

$$J_b = (1/64)[(E_{AF5} - E_{AF2})(1/S^2) + 64J_a + 32J_1 - 32J_2 + 32J_3 - 32J_4] \quad (2g)$$

$$J_{ab} = (1/64)[(E_{AF5} - E_{AF10})(1/S^2) + 32J_a - 32J_b + 16J_2 + 16J_4] \quad (2h)$$

$$J_{ab}' = (1/64)[(E_{AF10} - E_{AF6})(1/S^2) + 32J_a + 64J_c + 32J_b - 16J_2 - 16J_4] \quad (2i)$$

The values of the spin exchanges as described above from our DFT+U calculations with U_{eff} = 3, 4 and 5 eV are summarized in Table A-1.3.4.

Table A-1.3.4 Values of the spin exchanges (in K) obtained from DFT+U calculations of $NaYNiWO_6$

	U_{eff} = 3 eV	U_{eff} = 4 eV	U_{eff} = 5 eV
J_a	-4.80	-3.77	-2.94
J_b	-6.89	-5.33	-4.09
J_c	-18.65	-14.48	-11.16
J_{ab}	-11.98	-9.26	-7.09
J_{ab}'	-12.11	-9.38	-7.17
J_1	-8.75	-6.78	-5.22
J_2	0.96	0.72	0.56
J_3	0.70	0.50	0.34
J_4	-1.31	-1.06	-0.86

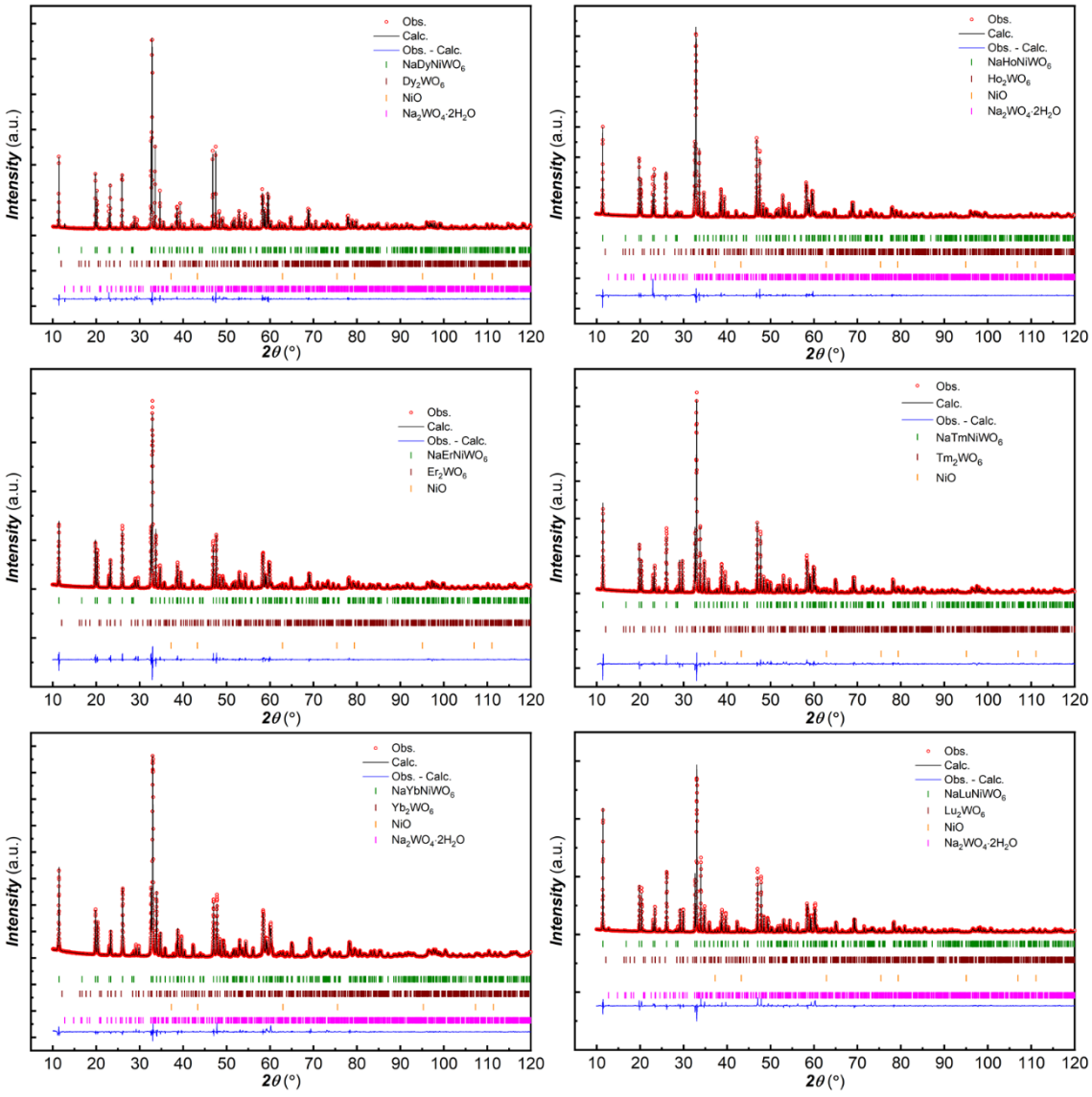

Figure A-1.3.3 Rietveld refined powder X-ray diffraction data of Na*Ln*$NiWO_6$ (*Ln* = Dy-Lu) recorded at room temperature.

Table A-1.3.5 Structural parameters of $NaDyNiWO_6$ from the PXRD pattern refinement. Space group: $P2_1$; a = 5.3379(3) Å, b = 5.4874(3) Å, c = 7.7578(5) Å, β = 90.246(4)º, Vol.: 227.234(2) Å^3; χ^2 = 7.0, Bragg R-factor = 3.22 (%), R_f-factor = 2.55 (%).

Atom	Wyckoff position	x	y	z	B_{iso} (Å^2)	Occ.
Na	2*a*	0.255(3)	0.210(2)	0.005(2)	1.4(3)	1.0
Dy	2*a*	0.2655(5)	0.3099(9)	0.5001(3)	0.1(1)	1.0
Ni	2*a*	0.752(2)	0.253(4)	0.2496(7)	0.7(2)	1.0
W	2*a*	0.7602(4)	0.25000	0.7652(2)	0.1(3)	1.0
O(1)	2*a*	0.556(4)	0.538(4)	0.713(3)	1.0	1.0
O(2)	2*a*	0.561(4)	0.538(4)	0.286(3)	1.0	1.0
O(3)	2*a*	-0.044(4)	-0.064(4)	0.200(3)	1.0	1.0
O(4)	2*a*	-0.046(4)	-0.057(4)	0.798(3)	1.0	1.0
O(5)	2*a*	0.868(3)	0.218(4)	0.463(2)	1.0	1.0
O(6)	2*a*	0.668(3)	0.190(3)	-0.008(2)	1.0	1.0

Table A-1.3.6 Structural parameters of $NaHoNiWO_6$ from the PXRD pattern refinement. Space group: $P2_1$; a = 5.3271(3) Å, b = 5.4912(4) Å, c = 7.7499(2) Å, β = 90.239(2)º, Vol.: 226.853(3) Å^3; χ^2 = 6.47, Bragg R-factor = 3.56 (%), R_f-factor = 3.11 (%).

Atom	Wyckoff position	x	y	z	B_{iso} (Å^2)	Occ.
Na	2*a*	0.249(2)	0.277(2)	0.015(1)	0.9(2)	1.0
Ho	2*a*	0.2677(3)	0.3074(4)	0.5017(2)	0.1(3)	1.0
Ni	2*a*	0.7527(9)	0.2275(9)	0.2457(4)	0.04(7)	1.0
W	2*a*	0.7607(3)	0.2500	0.7655(11)	0.04(7)	1.0
O(1)	2*a*	0.554(3)	0.507(3)	0.729(2)	1.0	1.0
O(2)	2*a*	0.564(3)	0.509(3)	0.276(2)	1.0	1.0
O(3)	2*a*	-0.099(3)	-0.098(3)	0.197(2)	1.0	1.0
O(4)	2*a*	-0.085(3)	-0.098(3)	0.795(2)	1.0	1.0
O(5)	2*a*	0.860(2)	0.198(3)	0.465(2)	1.0	1.0
O(6)	2*a*	0.680(2)	0.183(3)	-0.010(2)	1.0	1.0

Table A-1.3.7 Structural parameters of $NaErNiWO_6$ from the PXRD pattern refinement. Space group: $P2_1$; a = 5.3089(2) Å, b = 5.4858(2) Å, c = 7.7429(2) Å, β = 90.215(2)º, Vol.: 225.50(1) Å^3; χ^2 = 8.02, Bragg R-factor = 4.39 (%), R_f-factor = 3.43 (%).

Atom	Wyckoff position	x	y	z	B_{iso} (Å^2)	Occ.
Na1	2*a*	0.240(2)	0.219(2)	0.004(1)	2.5(4)	0.97(1)
Er2	2*a*	0.240(2)	0.219(2)	0.004(1)	2.5(4)	0.03(1)
Er1	2*a*	0.2679(3)	0.3153(4)	0.4998(2)	0.45(4)	0.97(1)
Na2	2*a*	0.2679(3)	0.3153(4)	0.4998(2)	0.45(4)	0.03(1)
Ni	2*a*	0.749(1)	0.266(1)	0.2472(4)	0.35(9)	1.0
W	2*a*	0.7615(3)	0.2500	0.7659(1)	0.80(3)	1.0
O1	2*a*	0.527(3)	0.532(3)	0.707(3)	1.0	1.0
O2	2*a*	0.547(3)	0.570(4)	0.286(3)	1.0	1.0
O3	2*a*	-0.055(3)	-0.056(3)	0.207(2)	1.0	1.0
O4	2*a*	-0.092(3)	-0.065(3)	0.797(2)	1.0	1.0
O5	2*a*	0.853(3)	0.209(3)	0.495(2)	1.0	1.0
O6	2*a*	0.674(2)	0.266(3)	-0.010(2)	1.0	1.0

Table A-1.3.8 Structural parameters of $NaTmNiWO_6$ from the PXRD pattern refinement. Space group: $P2_1$; a = 5.2951(2) Å, b = 5.4797(2) Å, c = 7.7345(2) Å, β = 90.221(2)º, Vol.: 224.42(3) Å^3; χ^2 = 9.5, Bragg R-factor = 6.15 (%), R_f-factor = 4.21 (%).

Atom	Wyckoff position	x	y	z	B_{iso} (Å^2)	Occ.
Na1	2*a*	0.257(2)	0.200(2)	-0.0006(9)	2.2(5)	0.93(1)
Tm2	2*a*	0.257(2)	0.200(2)	-0.0006(9)	2.2(5)	0.07(1)
Tm1	2*a*	0.2686(3)	0.3177(5)	0.5001(2)	0.30(4)	0.93(1)
Na2	2*a*	0.2686(3)	0.3177(5)	0.5001(2)	0.30(4)	0.07(1)
Ni	2*a*	0.7439(9)	0.265(2)	0.2469(4)	0.15(9)	1.0
W	2*a*	0.7616(3)	0.2500	0.7665(1)	0.91(3)	1.0
O1	2*a*	0.529(3)	0.567(3)	0.708(2)	1.0	1.0
O2	2*a*	0.589(3)	0.557(3)	0.277(2)	1.0	1.0
O3	2*a*	-0.054(3)	-0.038(3)	0.200(2)	1.0	1.0
O4	2*a*	-0.086(4)	-0.071(3)	0.806(2)	1.0	1.0
O5	2*a*	0.846(3)	0.194(3)	0.492(2)	1.0	1.0
O6	2*a*	0.665(3)	0.259(3)	-0.001(2)	1.0	1.0

Table A-1.3.9 Structural parameters of $NaYbNiWO_6$ from the PXRD pattern refinement. Space group: $P2_1$; a = 5.2834(5) Å, b = 5.4792(5) Å, c = 7.7284(8) Å, β = 90.209(7)º. Vol.: 223.728(4) Å^3; χ^2 = 6.95, Bragg R-factor = 3.70 (%), R_f-factor = 2.76 (%).

Atom	Wyckoff position	x	y	z	B_{iso} (Å^2)	Occ.
Na	2*a*	0.257(3)	0.229(2)	0.012(1)	1.5(2)	1.0
Yb	2*a*	0.2624(4)	0.3156(7)	0.5023(2)	0.16(3)	1.0
Ni	2*a*	0.752(1)	0.256(3)	0.2435(5)	0.40(3)	1.0
W	2*a*	0.7628(4)	0.2500	0.7655(2)	0.01(7)	1.0
O(1)	2*a*	0.546(3)	0.560(4)	0.673(2)	1.0	1.0
O(2)	2*a*	0.597(3)	0.545(3)	0.273(2)	1.0	1.0
O(3)	2*a*	-0.054(3)	-0.061(3)	0.181(2)	1.0	1.0
O(4)	2*a*	-0.099(3)	-0.099(4)	0.853(2)	1.0	1.0
O(5)	2*a*	0.871(3)	0.184(3)	0.475(2)	1.0	1.0
O(6)	2*a*	0.640(3)	0.184(3)	-0.012(2)	1.0	1.0

Table A-1.3.10 Structural parameters of $NaLuNiWO_6$ from the PXRD pattern refinement. Space group: $P2_1$; a = 5.271(1) Å, b = 5.4777(2) Å, c = 7.725(1) Å, β = 90.192(1)º, Vol.: 223.06(5) Å^3; χ^2 = 10.2, Bragg R-factor = 7.13 (%), R_f-actor = 3.76 (%).

Atom	Wyckoff position	x	y	z	B_{iso} (Å^2)	Occ.
Na1	2*a*	0.241(2)	0.208(2)	0.011(1)	1.3(2)	1.0
Lu1	2*a*	0.2678(3)	0.3199(3)	0.5006(2)	0.39(3)	1.0
Ni	2*a*	0.749(1)	0.267(1)	0.2483(4)	0.02(9)	1.0
W	2*a*	0.762(3)	0.2500	0.7655(1)	0.19(2)	1.0
O1	2*a*	0.572(3)	0.549(3)	0.715(2)	1.0	1.0
O2	2*a*	0.528(3)	0.550(3)	0.298(2)	1.0	1.0
O3	2*a*	-0.073(3)	-0.058(3)	0.218(2)	1.0	1.0
O4	2*a*	-0.116(4)	-0.054(3)	0.784(2)	1.0	1.0
O5	2*a*	0.829(3)	0.212(3)	0.501(2)	1.0	1.0
O6	2*a*	0.673(3)	0.269(3)	-0.019(2)	1.0	1.0

Table A-1.3.11 The proportions of main and impurity phases are given as wt % from the Rietveld refinement of PXRD data of Na*Ln*NiWO$_6$ (*Ln* = Y, Dy-Lu).

Compound	Main phase purity (%)	Impurities (%)
$NaYNiWO_6$	96.1(3)	Y_2WO_6: 3.0(5), NiO: 0.9(6)
$NaDyNiWO_6$	94.3(3)	Dy_2WO_6: 3.9(1), NiO: 1.0(1), $Na_2WO_4{\cdot}2H_2O$: 0.9(2)
$NaHoNiWO_6$	97.3(3)	Ho_2WO_6: 1.7(4), NiO: 0.5(2), $Na_2WO_4{\cdot}2H_2O$: 0.5(2)
$NaErNiWO_6$	94.2(3)	Er_2WO_6: 4.7(2), NiO: 1.1(2)
$NaTmNiWO_6$	91.4(3)	Tm_2WO_6: 6.7(2), NiO: 1.9(2)
$NaYbNiWO_6$	95.8(3)	Yb_2WO_6: 3.3(2), NiO: 0.5(2), $Na_2WO_4{\cdot}2H_2O$: 0.4(2)
$NaLuNiWO_6$	90.3(2)	Lu_2WO_6: 6.5(2), NiO: 1.8(2), $Na_2WO_4{\cdot}2H_2O$: 1.4(1)

References

[1] G. Kresse and J. Furthmüller, Mater. Sci. **6**, 15 (1996).

[2] G. Kresse and D. Joubert, Phys. Rev. B **59**, 1758 (1999).

[3] J. P. Perdew, K. Burke, and M. Ernzerhof, Phys. Rev. Lett. **77**, 3865 (1996).

[4] S. L. Dudarev, G. A. Botton, S. Y. Savrasov, C. J. Humphreys, and A. P. Sutton, Phys. Rev. B **57**, 1505 (1998).

[5] J. Kuneš, P. Novák, R. Schmid, P. Blaha, and K. Schwarz, Phys. Rev. B **64**, 153102 (2001).

[6] H. Xiang, C. Lee, H. J. Koo, X. Gong, and M. H. Whangbo, Dalt. Trans. **42**, 823 (2013).

[7] M.-H. Whangbo, H.-J. Koo, and D. Dai, J. Solid State Chem. **176**, 417 (2003).

[8] M.-H. Whangbo and H. Xiang, Handbook of Solid State Chemistry, **10,** 285 (2017).

Appendix 2

Chapter 4 Structural, magnetic and electrical properties of Na*Ln*NiWO$_6$ (*Ln* = La, Pr, Nd, Sm, Eu, Gd, and Tb)

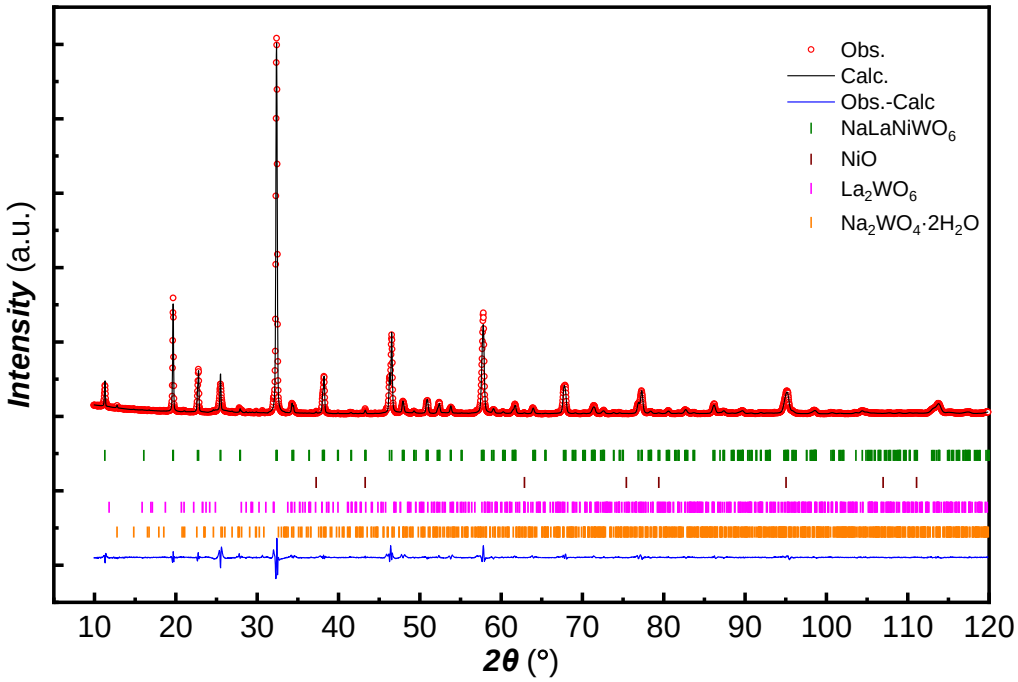

Figure A-2.4.1 Rietveld refinement on powder X-ray diffraction (PXRD) data of NaLaNiWO$_6$ sample recorded at room temperature.

Table A-2.4.1 Crystallographic parameters obtained from the Rietveld refinement on PXRD data of NaLaNiWO$_6$ at room temperature. Reliability factors: χ^2 = 8.9, Bragg *R*-factor = 5.41 (%), R_f – factor = 4.44 (%).

Atom	Wyckoff position	*x*	*y*	*z*	B_{iso} (Å^2)	Occ.
Na1	2*a*	0.252(8)	0.253(5)	-0.002(11)	1.01(7)	0.824(4)
La2	2*a*	0.252(8)	0.253(5)	-0.002(11)	1.01(7)	0.176(4)
La1	2*a*	0.250(2)	0.268(1)	0.50012(2)	0.30(5)	0.824(4)
Na2	2*a*	0.250(2)	0.268(1)	0.50012(2)	0.30(5)	0.176(4)
Ni	2*a*	0.749(5)	0.2500	0.2451(9)	0.60(1)	1.0
W	2*a*	0.7498(15)	0.2500	0.7652(3)	0.36(4)	1.0
O1	2*a*	0.489(19)	0.50(2)	0.714(8)	1.0	1.0
O2	2*a*	0.49(2)	0.488(18)	0.251(9)	1.0	1.0
O3	2*a*	-0.013(18)	-0.016(16)	0.264(9)	1.0	1.0
O4	2*a*	-0.061(11)	-0.083(9)	0.812(3)	1.0	1.0
O5	2*a*	0.774(13)	0.245(8)	0.50047	1.0	1.0
O6	2*a*	0.714(15)	0.220(17)	0.005(3)	1.0	1.0

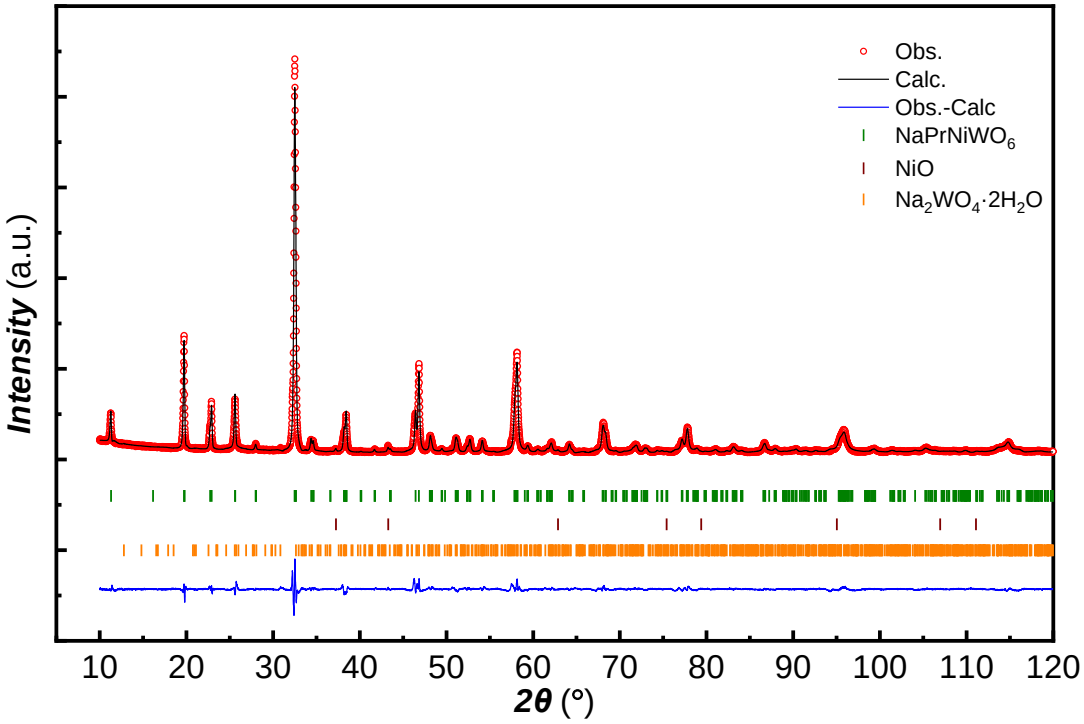

Figure A-2.4.2 Rietveld refinement on powder X-ray diffraction (PXRD) data of $NaPrNiWO_6$ sample recorded at room temperature.

Table A-2.4.2 Crystallographic parameters obtained from the Rietveld refinement on PXRD data of $NaPrNiWO_6$ at room temperature. Reliability factors: χ^2 = 6.82, Bragg *R*-factor = 4.63 (%), R_f – factor = 5.17 (%).

Atom	Wyckoff position	*x*	*y*	*z*	B_{iso} (Å^2)	Occ.
Na1	2*a*	0.239(5)	0.272(5)	0.005(6)	1.48(1)	0.84(1)
Pr2	2*a*	0.239(5)	0.272(5)	0.005(6)	1.48(1)	0.16 (1)
Pr1	2*a*	0.253(2)	0.277(1)	0.5061(9)	0.73(4)	0.84(1)
Na2	2*a*	0.253(2)	0.277(1)	0.5061(9)	0.73(4)	0.16(1)
Ni	2*a*	0.745(3)	0.25000	0.2415(8)	0.23(6)	1.0
W	2*a*	0.7538(10)	0.25000	0.7673(3)	0.70(2)	1.0
O1	2*a*	0.515(11)	0.512(12)	0.680(4)	1.0	1.0
O2	2*a*	0.482(13)	0.513(12)	0.252(6)	1.0	1.0
O3	2*a*	0.008(14)	-0.003(13)	0.252(6)	1.0	1.0
O4	2*a*	0.016(7)	-0.089(5)	0.841(4)	1.0	1.0
O5	2*a*	0.813(11)	0.197(10)	0.489(2)	1.0	1.0
O6	2*a*	0.716(11)	0.214(10)	-0.002(2)	1.0	1.0

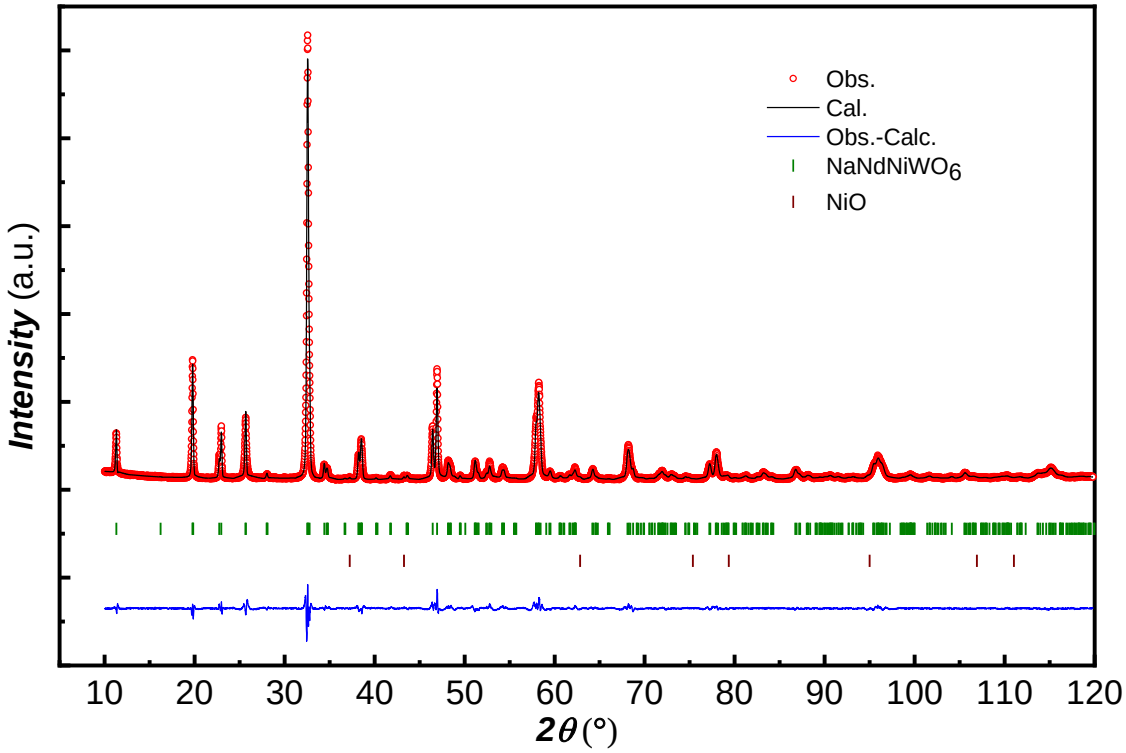

Figure A-2.4.3 Rietveld refinement on powder X-ray diffraction (PXRD) data of $NaNdNiWO_6$ sample recorded at room temperature.

Table A-2.4.3 Crystallographic parameters obtained from the Rietveld refinement on PXRD data of $NaNdNiWO_6$ at room temperature. Reliability factors: χ^2 = 6.28, Bragg *R*-factor = 4.80 (%), R_f – factor = 4.94 (%).

Atom	Wyckoff position	*x*	*y*	*z*	B_{iso} (Å^2)	Occ.
Na1	2*a*	0.243(5)	0.265(4)	-0.002(4)	1.1(4)	0.862(1)
Nd2	2*a*	0.243(5)	0.265(4)	-0.002(4)	1.1(4)	0.138 (1)
Nd1	2*a*	0.253(2)	0.277(1)	0.503(1)	0.71(1)	0.862(1)
Na2	2*a*	0.253(2)	0.277(1)	0.503(1)	0.71(1)	0.138 (1)
Ni	2*a*	0.741(2)	0.2500	0.2426(7)	0.40(1)	1.0
W	2*a*	0.7614(6)	0.2500	0.7667(2)	0.78(5)	1.0
O1	2*a*	0.503(8)	0.523(8)	0.712(5)	1.0	1.0
O2	2*a*	0.537(6)	0.517(7)	0.263(6)	1.0	1.0
O3	2*a*	-0.032(8)	-0.007(8)	0.252(5)	1.0	1.0
O4	2*a*	0.008(7)	-0.053(6)	0.866(4)	1.0	1.0
O5	2*a*	0.821(5)	0.202(6)	0.489(2)	1.0	1.0
O6	2*a*	0.672(4)	0.218(7)	0.014(3)	1.0	1.0

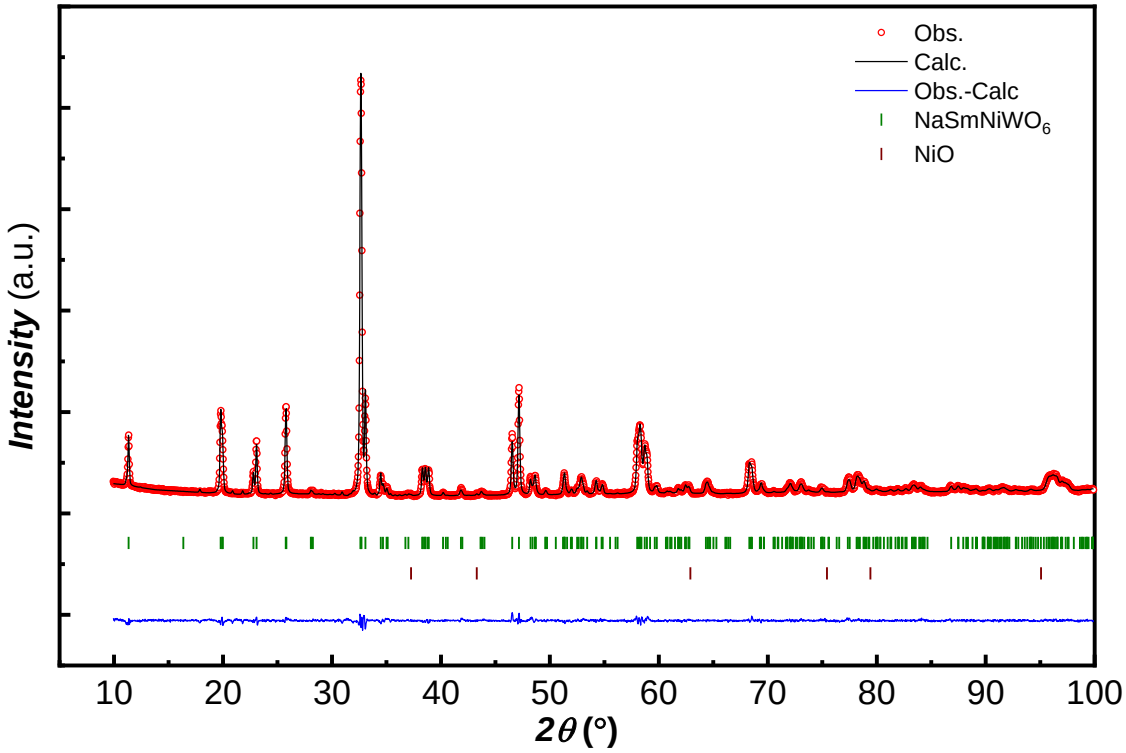

Figure A-2.4.4 Rietveld refinement on powder X-ray diffraction (PXRD) data of $NaSmNiWO_6$ sample recorded at room temperature.

Table A-2.4.4 Crystallographic parameters obtained from the Rietveld refinement on PXRD data of $NaSmNiWO_6$ at room temperature. Reliability factors: $\chi^2 = 4.37$, Bragg *R*-factor = 3.17 (%), R_f – factor = 4.1 (%).

Atom	Wyckoff position	*x*	*y*	*z*	B_{iso} (Å^2)	Occ.
Na1	2*a*	0.248(7)	0.253(5)	0.002(5)	2.6(3)	0.902(3)
Sm2	2*a*	0.248(7)	0.253(5)	0.002(5)	2.6(3)	0.098(3)
Sm1	2*a*	0.255(2)	0.290(8)	0.501(1)	0.17(6)	0.902(3)
Na2	2*a*	0.255(2)	0.290(8)	0.501(1)	0.17(6)	0.098(3)
Ni	2*a*	0.748(4)	0.2500	0.240(1)	0.99(2)	1.0
W	2*a*	0.757(1)	0.2500	0.767(3)	0.33(3)	1.0
O1	2*a*	0.501(1)	0.516(11)	0.709(6)	1.0	1.0
O2	2*a*	0.467(10)	0.457(10)	0.247(9)	1.0	1.0
O3	2*a*	-0.071(8)	-0.063(9)	0.230(7)	1.0	1.0
O4	2*a*	0.014(9)	-0.039(8)	0.904(4)	1.0	1.0
O5	2*a*	0.830(5)	0.238(9)	0.491(4)	1.0	1.0
O6	2*a*	0.670(5)	0.265(12)	0.005(4)	1.0	1.0

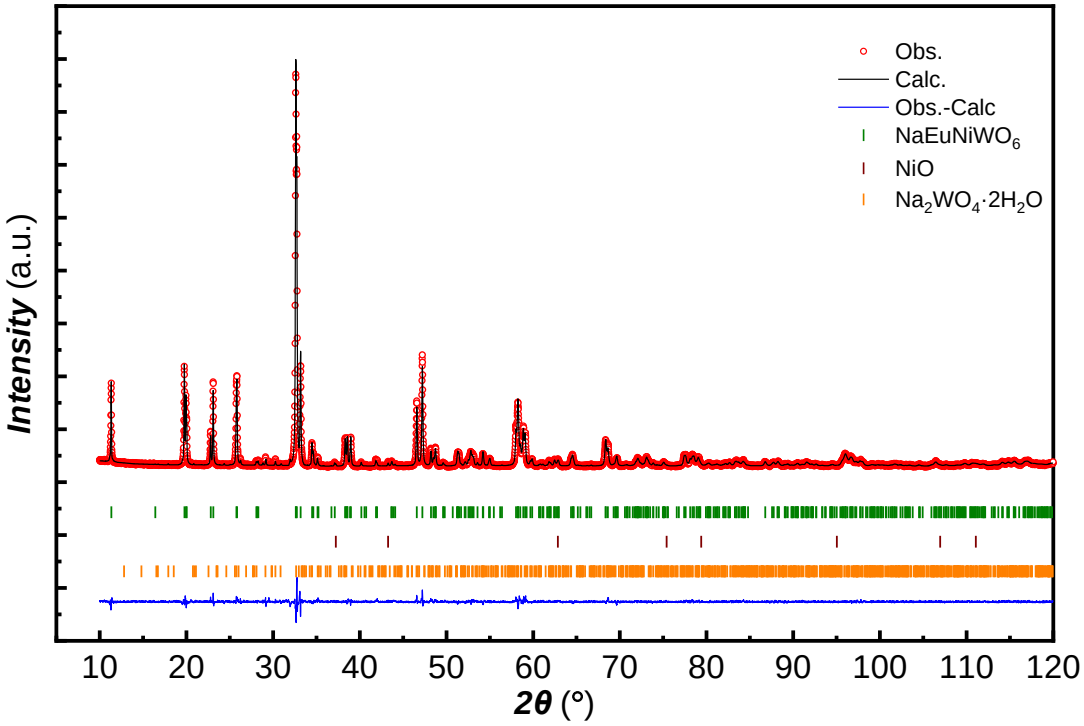

Figure A-2.4.5 Rietveld refinement on powder X-ray diffraction (PXRD) data of $NaEuNiWO_6$ sample recorded at room temperature.

Table A-2.4.5 Crystallographic parameters obtained from the Rietveld refinement on PXRD data of $NaEuNiWO_6$ at room temperature. Reliability factors: χ^2 = 3.41, Bragg *R*-factor = 6.98 (%), R_f – factor = 5.51 (%).

Atom	Wyckoff position	*x*	*y*	*z*	B_{iso} (Å^2)	Occ.
Na1	2*a*	0.228(2)	0.2217(16)	0.0081(14)	1.7(2)	0.888(1)
Eu2	2*a*	0.228(2)	0.2217(16)	0.0081(14)	1.7(2)	0.112(1)
Eu1	2*a*	0.2566(7)	0.3018(4)	0.5021(5)	0.62(4)	0.888(1)
Na2	2*a*	0.2566(7)	0.3018(4)	0.5021(5)	0.62(4)	0.112(1)
Ni	2*a*	0.7503(16)	0.25000	0.2402(6)	0.25(7)	1.0
W	2*a*	0.7589(5)	0.25000	0.7681(2)	0.73(3)	1.0
O1	2*a*	0.520(5)	0.539(5)	0.706(5)	1.0	1.0
O2	2*a*	0.528(4)	0.526(5)	0.291(5)	1.0	1.0
O3	2*a*	-0.048(4)	-0.036(5)	0.229(4)	1.0	1.0
O4	2*a*	-0.030(5)	-0.039(4)	0.816(3)	1.0	1.0
O5	2*a*	0.835(3)	0.183(4)	0.491(2)	1.0	1.0
O6	2*a*	0.668(3)	0.236(4)	0.002(2)	1.0	1.0

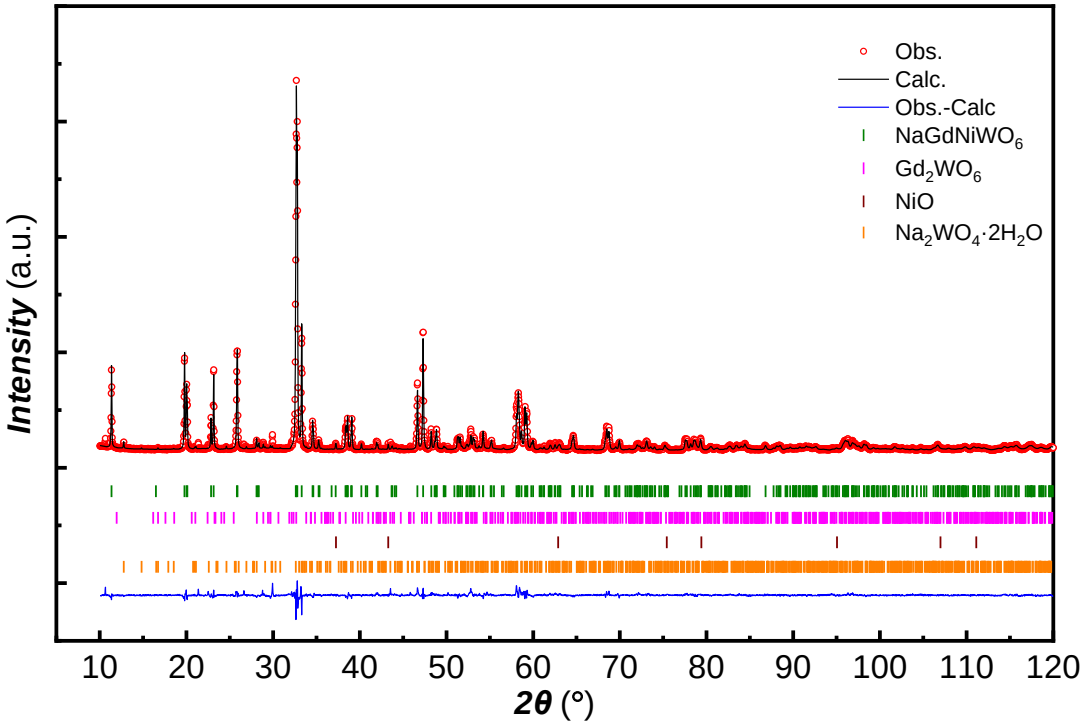

Figure A-2.4.6 Rietveld refinement on powder X-ray diffraction (PXRD) data of $NaGdNiWO_6$ sample recorded at room temperature.

Table A-2.4.6 Crystallographic parameters obtained from the Rietveld refinement on PXRD data of $NaGdNiWO_6$ at room temperature. Reliability factors: χ^2 = 5.38, Bragg *R*-factor = 5.92 (%), R_f – factor = 4.85 (%).

Atom	Wyckoff position	*x*	*y*	*z*	B_{iso} (Å^2)	Occ.
Na1	2*a*	0.240(4)	0.217(2)	0.003(2)	1.7(2)	0.918(2)
Gd2	2*a*	0.240(4)	0.217(2)	0.003(2)	1.7(2)	0.082(2)
Gd1	2*a*	0.2612(9)	0.3032(5)	0.5000(6)	0.17(6)	0.918(2)
Na2	2*a*	0.2612(9)	0.3032(5)	0.5000(6)	0.17(6)	0.082(2)
Ni	2*a*	0.754(2)	0.2500	0.2422(9)	0.41(10)	1.0
W	2*a*	0.7612(6)	0.2500	0.7679(3)	0.65(4)	1.0
O1	2*a*	0.504(7)	0.534(6)	0.710(9)	1.0	1.0
O2	2*a*	0.518(7)	0.517(6)	0.286(9)	1.0	1.0
O3	2*a*	-0.047(6)	-0.044(5)	0.212(6)	1.0	1.0
O4	2*a*	-0.038(6)	-0.050(5)	0.800(6)	1.0	1.0
O5	2*a*	0.836(4)	0.205(4)	0.487(3)	1.0	1.0
O6	2*a*	0.653(4)	0.357(5)	0.005(4)	1.0	1.0

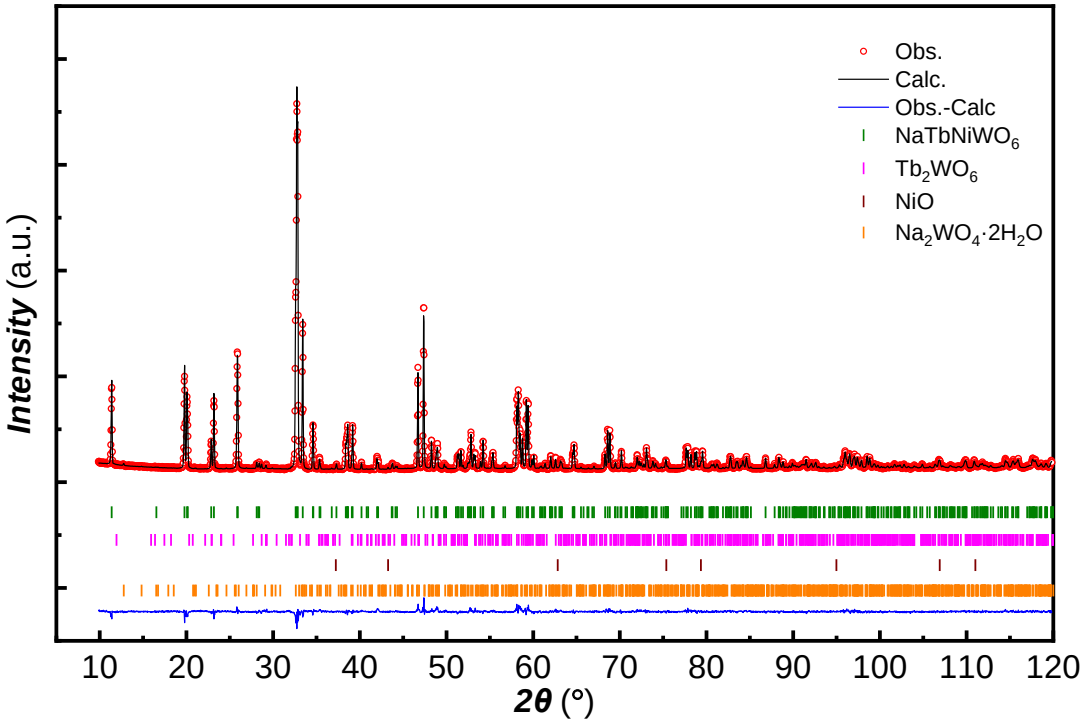

Figure A-2.4.7 Rietveld refinement on powder X-ray diffraction (PXRD) data of $NaTbNiWO_6$ sample recorded at room temperature.

Table A-2.4.7 Crystallographic parameters obtained from the Rietveld refinement on PXRD data of $NaTbNiWO_6$ at room temperature. Reliability factors: χ^2 = 2.84, Bragg *R*-factor = 5.87 (%), R_f – factor = 4.48 (%).

Atom	Wyckoff position	*x*	*y*	*z*	B_{iso} (Å^2)	Occ.
Na1	2*a*	0.239(2)	0.2045(2)	0.0310	2.4(2)	0.922(2)
Tb2	2*a*	0.239(2)	0.2045(2)	0.003(1)	2.4(2)	0.077(2)
Tb1	2*a*	0.2610(5)	0.3052(4)	0.5003(3)	0.12(3)	0. 922 (2)
Na2	2*a*	0.2610(5)	0.3052(4)	0.5003(3)	0.12(3)	0.077 (2)
Ni	2*a*	0.752(1)	0.2500	0.2446(5)	0.11(9)	1.0
W	2*a*	0.7607(3)	0.2500	0.7674(2)	0.08(4)	1.0
O1	2*a*	0.534(4)	0.545(4)	0.702(3)	1.0	1.0
O2	2*a*	0.555(4)	0.548(4)	0.289(3)	1.0	1.0
O3	2*a*	-0.051(4)	-0.038(4)	0.206(3)	1.0	1.0
O4	2*a*	-0.058(5)	-0.062(4)	0.804(3)	1.0	1.0
O5	2*a*	0.848(3)	0.204(4)	0.493(2)	1.0	1.0
O6	2*a*	0.672(3)	0.264(5)	0.001(2)	1.0	1.0

Table A-2.4.8 The proportions of main and impurity phases are given as wt % from the Rietveld refinement of PXRD data of Na*Ln*NiWO$_6$ (*Ln* = La, Pr, Nd, Sm, Eu, Gd, and Tb).

Compound	Main phase purity (%)	Impurities (%)
NLaNiWO$_6$	97.4(6)	La$_2$WO$_6$: 0.5(1), NiO: 1(1), Na$_2$WO$_4$·2H$_2$O: 1(1)
NaPrNiWO$_6$	97.3(3)	NiO: 2.4(1), Na$_2$WO$_4$·2H$_2$O: 0.3(1)
NaNdNiWO$_6$	99(3)	NiO: 1(1)
NaSmNiWO$_6$	99.5(5)	NiO: 0.5(1)
NaEuNiWO$_6$	98.8(2)	NiO: 0.9(2), Na$_2$WO$_4$·2H$_2$O: 0.4(2)
NaGdNiWO$_6$	96.5(3)	Gd$_2$WO$_6$: 0.8(2), NiO: 1.3(1), Na$_2$WO$_4$·2H$_2$O: 1.5(1)
NaTbNiWO$_6$	98.3(2)	Tb$_2$WO$_6$: 0.80(2), NiO: 0.4(2), Na$_2$WO$_4$·2H$_2$O: 0.5(2)

Appendix 3

Chapter 5 Switchable, nonswitchable polarization in Na*Ln*CoWO$_6$ (*Ln* = Y, Er, Tm, Yb, and Lu), NaLuMnWO$_6$, and magnetodielectric properties of Na*Ln*FeWO$_6$ (*Ln* = Y, Ho)

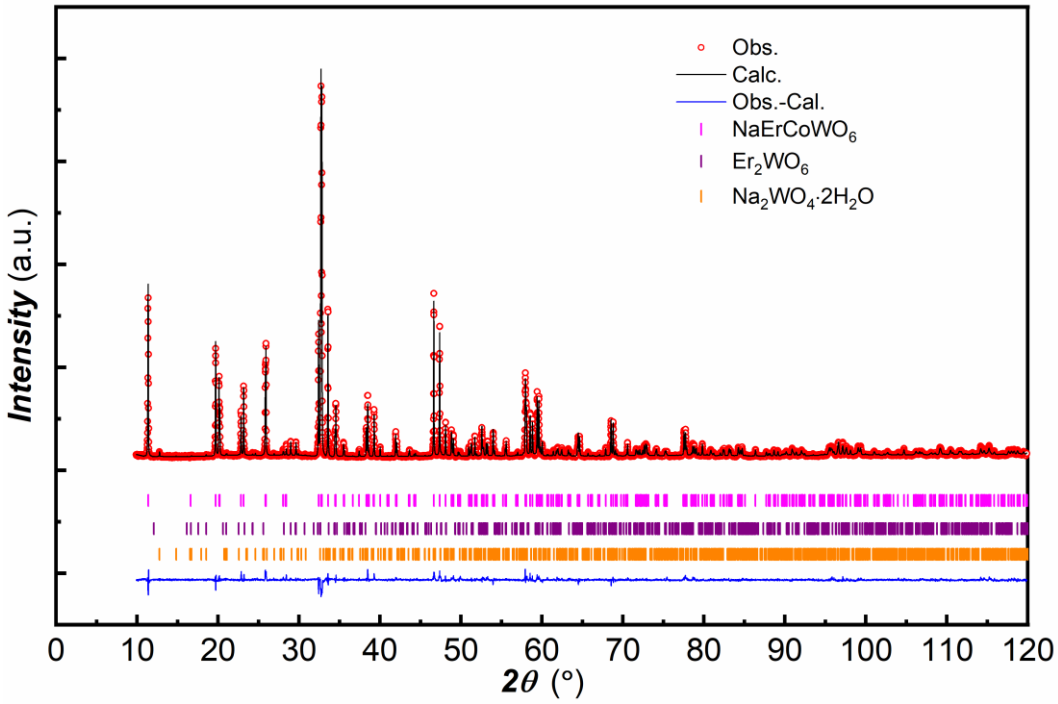

Figure A-3.5.1 Rietveld refined powder x-ray diffraction data collected at room temperature.

Table A-3.5.1 Structural parameters of NaErCoWO$_6$ obtained from the Rietveld refinement. Reliability factors: χ^2 = 3.24, Bragg *R*-factor = 7.46 (%), R_f – factor = 8.82 (%).

Atom	Wyckoff position	*x*	*y*	*z*	B_{iso} (Å^2)	Occ.
Na1	2*a*	0.231(2)	0.208(2)	0.008(1)	2.01(5)	0.95(1)
Er2	2*a*	0.231(2)	0.208(2)	0.008(1)	2.01(5)	0.05(1)
Er1	2*a*	0.2653(5)	0.3190(5)	0.5007(3)	0.08(4)	0.95(1)
Na2	2*a*	0.2653(5)	0.3190(5)	0.5007(3)	0.08(4)	0.05(1)
Co	2*a*	0.753(1)	0.269(2)	0.2435(5)	0.31(1)	1.0
W	2*a*	0.7632(4)	0.25000	0.7647(2)	0.69(3)	1.0
O1	2*a*	0.545(4)	0.558(4)	0.720(3)	1.0	1.0
O2	2*a*	0.533(4)	0.540(4)	0.282(3)	1.0	1.0
O3	2*a*	-0.076(4)	-0.061(3)	0.216(2)	1.0	1.0
O4	2*a*	-0.098(4)	-0.049(3)	0.791(2)	1.0	1.0
O5	2*a*	0.845(3)	0.183(3)	0.499(2)	1.0	1.0
O6	2*a*	0.682(3)	0.265(4)	-0.012(2)	1.0	1.0

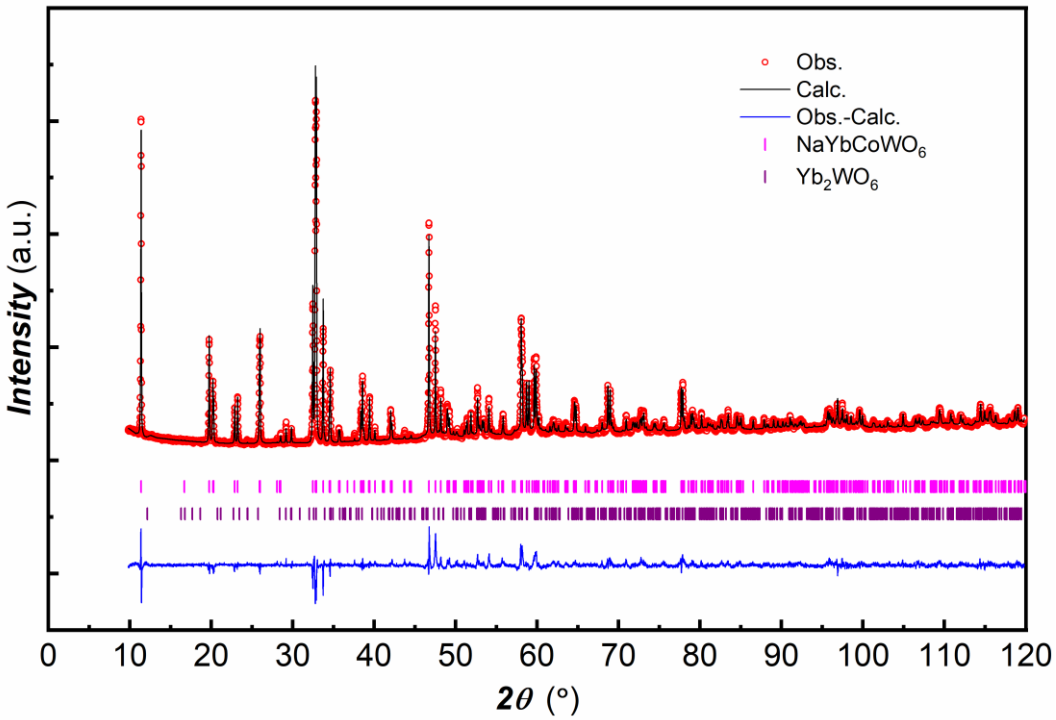

Figure A-3.5.2 Rietveld refined powder x-ray diffraction data collected at room temperature.

Table A-3.5.2 Structural parameters of $NaYbCoWO_6$ obtained from the Rietveld refinement. Reliability factors: $\chi^2 = 5.87$, Bragg *R*-factor = 13.5 (%), R_f – factor = 12.0 (%).

Atom	Wyckoff position	*x*	*y*	*z*	B_{iso} (Å^2)	Occ.
Na1	2*a*	0.216(4)	0.211(3)	0.015(2)	0.91(1)	0.96(1)
Yb2	2*a*	0.216(4)	0.211(3)	0.015(2)	0.91 (1)	0.04(1)
Yb1	2*a*	0.2622(8)	0.3144(6)	0.5023(5)	0.23(8)	0.96(1)
Na2	2*a*	0.2622(8)	0.3144(6)	0.5023(5)	0.23(8)	0.04(1)
Co	2*a*	0.752(3)	0.2476	0.243(1)	0.24(6)	1.0
W	2*a*	0.7634(7)	0.2500	0.7622(3)	0.27(7)	1.0
O1	2*a*	0.548(6)	0.5584(6)	0.716(4)	1.0	1.0
O2	2*a*	0.611(5)	0.582(5)	0.276(4)	1.0	1.0
O3	2*a*	-0.0755(7)	-0.0605(4)	0.214(4)	1.0	1.0
O4	2*a*	-0.0436(7)	-0.0579(4)	0.790(4)	1.0	1.0
O5	2*a*	0.830(5)	0.234(6)	0.498(4)	1.0	1.0
O6	2*a*	0.676(5)	0.259(7)	-0.003(3)	1.0	1.0

Table A-3.5.3 Structural parameters of $NaTmCoWO_6$ obtained from the Rietveld refinement. Reliability factors: $\chi^2 = 5$, Bragg *R*-factor = 9.29 (%), R_f – factor = 11.2 (%).

Atom	Wyckoff position	*x*	*y*	*z*	B_{iso} (Å^2)	Occ.
Na1	2*a*	0.226(3)	0.181(2)	0.011(2)	2.28(6)	0.93(1)
Tm2	2*a*	0.226(3)	0.181(2)	0.011(2)	2.28(6)	0.07(1)
Tm1	2*a*	0.2633(6)	0.314(1)	0.5016(3)	0.47(4)	0.93(1)
Na2	2*a*	0.2633(6)	0.314(1)	0.5016(3)	0.47(4)	0.07(1)
Co	2*a*	0.755(2)	0.255(5)	0.2403(7)	0.52(8)	1.0
W	2*a*	0.7643(4)	0.2500	0.7640(2)	0.54(3)	1.0
O1	2*a*	0.538(4)	0.561(4)	0.729(3)	1.0	1.0
O2	2*a*	0.560(4)	0.560(4)	0.266(3)	1.0	1.0
O3	2*a*	-0.095(5)	-0.061(4)	0.199(2)	1.0	1.0
O4	2*a*	-0.096(5)	-0.075(4)	0.801(2)	1.0	1.0
O5	2*a*	0.853(4)	0.193(4)	0.498(2)	1.0	1.0
O6	2*a*	0.685(3)	0.271(5)	-0.009(2)	1.0	1.0

Table A-3.5.4 Structural parameters of $NaLuCoWO_6$ obtained from the Rietveld refinement. Reliability factors: $\chi^2 = 3.86$, Bragg *R*-factor = 6.43 (%), R_f – factor = 6.18 (%).

Atom	Wyckoff position	*x*	*y*	*z*	B_{iso} (Å^2)	Occ.
Na1	2*a*	0.219(3)	0.211(2)	0.009(2)	1.70(2)	0.90(1)
Lu2	2*a*	0.219(3)	0.211(2)	0.009(2)	1.70(2)	0.10(1)
Lu1	2*a*	0.2596(8)	0.3181(5)	0.5017(5)	0.48(5)	0.90(1)
Na2	2*a*	0.2596(8)	0.3181(5)	0.5017(5)	0.48(5)	0.10(1)
Co	2*a*	0.751(2)	0.2500	0.241(1)	0.42(2)	1.0
W	2*a*	0.7654(6)	0.2500	0.7636(3)	0.19(3)	1.0
O1	2*a*	0.561(5)	0.621(5)	0.733(4)	1.0	1.0
O2	2*a*	0.582(6)	0.549(5)	0.269(4)	1.0	1.0
O3	2*a*	-0.090(7)	-0.0605	0.202(4)	1.0	1.0
O4	2*a*	-0.072(6)	-0.0487	0.815(4)	1.0	1.0
O5	2*a*	0.844(5)	0.190(5)	0.489(4)	1.0	1.0
O6	2*a*	0.666(4)	0.272(6)	-0.009(4)	1.0	1.0

Table A-3.5.5 Structural parameters of $NaLuMnWO_6$ obtained from the Rietveld refinement. Reliability factors: $\chi^2 = 10.7$, Bragg *R*-factor = 12.3 (%), R_f – factor = 9.14 (%).

Atom	Wyckoff position	*x*	*y*	*z*	B_{iso} (Å^2)	Occ.
Na1	2*a*	0.23067	0.208(3)	0.009(2)	1.70(2)	0.91(1)
Lu2	2*a*	0.23067	0.208(3)	0.009(2)	1.70(2)	0.09(1)
Lu1	2*a*	0.2657(6)	0.3166(6)	0.5034(4)	0.48(5)	0.91(1)
Na2	2*a*	0.2657(6)	0.3166(6)	0.5034(4)	0.48(5)	0.09(1)
Mn	2*a*	0.748(2)	0.2500	0.237(1)	0.42(2)	1.0
W	2*a*	0.7673(7)	0.2500	0.7574(4)	0.19(3)	1.0
O1	2*a*	0.530(7)	0.51868	0.736(4)	1.0	1.0
O2	2*a*	0.557(6)	0.53297	0.266(4)	1.0	1.0
O3	2*a*	-0.132(6)	-0.078(4)	0.222(3)	1.0	1.0
O4	2*a*	-0.074(7)	-0.0487	0.796(3)	1.0	1.0
O5	2*a*	0.836(5)	0.240(6)	0.498(3)	1.0	1.0
O6	2*a*	0.665(5)	0.276(7)	-0.003(3)	1.0	1.0

Table A-3.5.6 The proportions of main and impurity phases are given as wt % from the Rietveld refinement of PXRD data of Na*Ln*$CoWO_6$ (*Ln* = Er, Tm, Yb, and Lu) and $NaLuMnWO_6$.

Compound	Main phase purity (%)	Impurities (%)
$NErCoWO_6$	96.6(3)	Er_2WO_6: 2.4(1), $Na_2WO_4{\cdot}2H_2O$: 1.0(1)
$NaTmCoWO_6$	93.3(3)	Tm_2WO_6: 3.6(2), CoO: 0.5(2), $Na_2WO_4{\cdot}2H_2O$: 2.6(2)
$NaYbCoWO_6$	97.5(4)	Yb_2WO_6: 2.5(1)
$NaLuCoWO_6$	95.7(5)	Lu_2WO_6: 3.7(2), $Na_2WO_4{\cdot}2H_2O$: 0.6(1)
$NaLuMnWO_6$	91.6(4)	Lu_2WO_6: 8.2(1), $Na_2WO_4{\cdot}2H_2O$: 0.2(2)

Table A-3.5.7 Structural parameters of $NaYFeWO_6$ obtained from the Rietveld refinement. Reliability factors: $\chi^2 = 3.07$, Bragg *R*-factor = 2.57 (%), R_f – factor = 2.31 (%).

Atom	Wyckoff position	*x*	*y*	*z*	B_{iso} (Å^2)	Occ.
Na1	2*a*	0.2534(1)	0.217(2)	0.008(1)	2.7(3)	0.905(3)
Y2	2*a*	0.253(2)	0.217(2)	0.008(1)	2.7(3)	0.095(3)
Y1	2*a*	0.2666(6)	0.3119(9)	0.5014(4)	0.77(8)	0.905(3)
Na2	2*a*	0.2666(6)	0.3119(9)	0.5014(4)	0.77(8)	0.095(3)
Fe	2*a*	0.752(1)	0.260(4)	0.2440(6)	0.88(9)	1.0
W	2*a*	0.7644(3)	0.25000	0.7617(2)	1.23(2)	1.0
O1	2*a*	0.500(3)	0.572(3)	0.696(2)	1.0	1.0
O2	2*a*	0.564(2)	0.567(3)	0.293(2)	1.0	1.0
O3	2*a*	-0.037(3)	-0.050(3)	0.220(2)	1.0	1.0
O4	2*a*	-0.097(3)	-0.042(2)	0.784(2)	1.0	1.0
O5	2*a*	0.876(2)	0.197(3)	0.489(2)	1.0	1.0
O6	2*a*	0.701(2)	0.258(3)	-0.003(2)	1.0	1.0

Table A-3.5.8 Structural parameters of $NaHoFeWO_6$ obtained from the Rietveld refinement. Reliability factors: $\chi^2 = 3.77$, Bragg *R*-factor = 4.85 (%), R_f – factor = 4.01 (%).

Atom	Wyckoff position	*x*	*y*	*z*	B_{iso} (Å^2)	Occ.
Na1	2*a*	0.245(2)	0.234(1)	0.007(1)	2.1(3)	0.869(1)
Ho2	2*a*	0.245(2)	0.234(1)	0.007(1)	2.1(3)	0.131(1)
Ho1	2*a*	0.2640(6)	0.3152(3)	0.5015(4)	0.81(9)	0.869(1)
Na2	2*a*	0.2640(6)	0.3152(3)	0.5015(4)	0.81(9)	0.131(1)
Fe	2*a*	0.743(1)	0.2500	0.2394(6)	0.40(8)	1.0
W	2*a*	0.7667(3)	0.2500	0.7617(2)	0.61(3)	1.0
O1	2*a*	0.520(4)	0.552(3)	0.706(4)	1.0	1.0
O2	2*a*	0.546(3)	0.535(3)	0.282(4)	1.0	1.0
O3	2*a*	-0.081(3)	-0.062(3)	0.222(3)	1.0	1.0
O4	2*a*	-0.077(4)	-0.068(3)	0.795(3)	1.0	1.0
O5	2*a*	0.857(4)	0.166(3)	0.486(2)	1.0	1.0
O6	2*a*	0.692(3)	0.259(3)	0.002(2)	1.0	1.0

Table A-3.5.9 The proportions of main and impurity phases are given as wt % from Rietveld refinement of PXRD data of $NaYFeWO_6$ and $NaHoFeWO_6$.

Compound	Main phase purity (%)	Impurities (%)
$NYFeWO_6$	87.4(2)	Y_2WO_6: 11.2(1), KCl: 1.4(1)
$NaHoFeWO_6$	89.0(2)	Ho_2WO_6: 9.2(1), KCl: 1.8(1)

Appendix 4

Chapter 6 Magnetization plateau, magnetocaloric and multiferroic properties of $LiFeV_2O_7$

Table A-4.6.1 Crystallographic parameters of $LiFeV_2O_7$ from the refinement of PXRD data collected at room temperature.

Atom	Wyckoff position	*x*	*y*	*z*	B_{iso} (Å^2)	Occ.
Fe1	4*a*	0.502(7)	0.804(2)	0.376(6)	0.53(1)	1.0
Fe2	4*a*	0.853(7)	0.823(1)	0.545(7)	0.92(6)	1.0
Fe3	4*a*	0.703(7)	0.308(2)	0.715(6)	0.11(7)	1.0
V1	4*a*	0.428(7)	1.025(2)	0.183(6)	1.0000	1.0
V2	4*a*	0.712(7)	0.965(1)	0.361(6)	1.0000	1.0
V3	4*a*	0.572(6)	0.467(2)	0.523(6)	1.0000	1.0
V4	4*a*	0.633(7)	0.950(2)	0.576(6)	1.0000	1.0
V5	4*a*	0.276(6)	0.974(2)	0.411(6)	1.0000	1.0
V6	4*a*	0.409(7)	0.461(2)	0.245(6)	1.0000	1.0
O1	4*a*	0.485(7)	0.315(6)	0.477(7)	1.0000	1.0
O2	4*a*	0.331(7)	1.149(7)	0.154(6)	1.0000	1.0
O3	4*a*	0.235(7)	0.982(6)	0.300(7)	1.0000	1.0
O4	4*a*	0.404(7)	0.490(6)	0.128(7)	1.0000	1.0
O5	4*a*	0.426(7)	0.638(6)	0.292(7)	1.0000	1.0
O6	4*a*	0.289(8)	1.163(6)	0.461(7)	1.0000	1.0
O7	4*a*	0.522(7)	0.900(5)	0.625(6)	1.0000	1.0
O8	4*a*	0.620(7)	0.792(6)	0.313(7)	1.0000	1.0
O9	4*a*	0.591(7)	0.976(5)	0.447(7)	1.0000	1.0
O10	4*a*	0.687(8)	1.150(6)	0.300(6)	1.0000	1.0
O11	4*a*	0.660(8)	1.142(7)	0.604(6)	1.0000	1.0
O12	4*a*	0.666(9)	0.379(4)	0.451(7)	1.0000	1.0
O13	4*a*	0.302(7)	0.362(5)	0.288(6)	1.0000	1.0
O14	4*a*	0.516(7)	0.368(6)	0.274(7)	1.0000	1.0
O15	4*a*	0.458(7)	1.002(6)	0.302(7)	1.0000	1.0
O16	4*a*	0.536(7)	0.642(7)	0.485(7)	1.0000	1.0
O17	4*a*	0.397(7)	0.847(7)	0.139(6)	1.0000	1.0
O18	4*a*	0.794(7)	1.004(6)	0.461(7)	1.0000	1.0
O19	4*a*	0.615(8)	0.455(6)	0.643(7)	1.0000	1.0
O20	4*a*	0.381(8)	0.859(5)	0.427(7)	1.0000	1.0
O21	4*a*	0.718(7)	0.823(7)	0.596(7)	1.0000	1.0
Li1	4*a*	0.685(1)	0.699(6)	0.699(8)	1.0000	1.0
Li2	4*a*	0.341(7)	0.307(7)	0.040(6)	1.0000	1.0
Li3	4*a*	0.549(6)	0.181(8)	0.379(7)	1.0000	1.0

Space group: *Cc*; a = 13.4560(2) Å, b = 8.1875(2)Å, c = 14.3796(1) Å, β = 96.551(1)°. Vol.: 1573.87(2)Å^3; Reliability factors: χ^2 = 2.94, Bragg *R*-factor = 3.91 (%), R_f – factor = 3.52 (%).